UNIVERSITY OF SOUTHAMPTON

FACULTY OF ENGINEERING AND THE ENVIRONMENT

Development of Non-Destructive Damage Detection Approach using Vibrational Power Flow

by

Ponprot Boonpratpai

Thesis for the degree of Doctor of Philosophy

March 2017

UNIVERSITY OF SOUTHAMPTON

ABSTRACT

FACULTY OF ENGINEERING AND THE ENVIRONMENT

Doctor of Philosophy

Development of Non-Destructive Damage Detection Approach using Vibrational Power Flow

By Ponprot Boonpratpai

Catastrophic structural failures are very harmful to humans' lives. Theses failures can be created by minor damages, such as cracks, which can be propagated due to external loading and lead to the loss of structural integrity and stability. It is, therefore, worthwhile to have a reliable non-destructive damage detection (NDD) technique capable of detecting early-age damages on structures. Once the damages are discovered, repair or replacement can be made before their enlargement.

In this thesis, investigations of the power flow in the plates containing single open crack are firstly performed. It is shown that the pattern and magnitude of the power flow are significantly changed only at the crack location. This trend also happens in the cases of the double- and triple-cracked plates. An NDD technique for plate structures based on these local changes of the power flow due to damages is introduced. The technique can effectively reveal damage location and severity using three power flow data measured from the tested plate as inputs for the reverse step.

The characteristics of the nonlinear power flow induced by single and multiple breathing fatigue cracks on the cracked cantilever beam, namely super-harmonic resonance, are studied. The degree of nonlinearity of the power flow is shown to be dependent on the crack location, crack severity and amount of crack on the beam. This degree is used in conjunction with the surface fitting to determine the approximate location and severity of a crack on the beam. An NDD technique that can detect multiple-cracked cantilever beams is also proposed. This technique employs the power flow damage indices (DIs) obtained from the time-domain power flow plot to pinpoint the crack locations. The application capabilities of above three NDD techniques are presented through several numerical case studies. Effects of noise on each technique are also discussed.

Contents

List of Figures

List of Tables

Declarations of Authorship

I, Ponprot Boonpratpai, declare that the thesis entitled *"Development of non-destructive damage detection approach using vibrational power flow"* and the work presented in the thesis are both my own, and have been generated by me as the result of my own original research. I confirm that:

- this work was done wholly or mainly while in candidature for a research degree at this University;
- where any part of this thesis has previously been submitted for a degree or other qualification at this University or any other institution, this has been clearly stated;
- where I have consulted the published work of others, this is always clearly attributed;
- where I have quoted from the work of others, the source is always given. With the exception of such quotations, this thesis is entirely my own work
- I have acknowledged all main sources of help;
- where the thesis is based on work done by myself jointly with others, I have made clear exactly what was done by others and what I have contributed myself;
- parts of this work have been published as given in the list of publication.

Signed: ……*Ponprot Boonpratpai*……...

Date: ……..……*6 March 2017*…….....

Acknowledgements

Firstly, I would like to acknowledge the financial support from the Royal Thai Navy for the tuition fees of my PhD course and the living expenses during past few years of my studies.

I wish to express my deepest gratitude to Associate Professor Yeping Xiong and Dr Zhi-min Chen, who are my research supervisors, for their persistent scientific guidance from the beginning of my research. Without their helpful guidance, this thesis would not have materialised. I also wish to show my greatest appreciation to Professor Philip A Wilson for his personal help and valuable advice since my master degree.

I would like to offer my special thanks to Dr Khemapat Tontiwattanakul, Rittirong Ariyatanapol, and Kantapon Tanakitkorn for their technical support throughout my doctoral studies. Special thanks also to all of the colleagues in the Fluid Structure Interactions Research Group for making the office a great place to work, and to the friends in Southampton and my home country for their consistent friendship and emotional support.

The last but not least, my PhD journey would not happen without the great support and inspiration of my family. I feel I am so fortunate to have such loving and supportive parents, sister and brother. I am also deeply grateful to my lovely girlfriend, Jessica Lam, who always stands by me and gives me the encouragement.

Acronyms

CL	clamped plate boundary
CNDD	classical non-destructive damage detection
DI	damage index
DNPF	dimensionless net power flow
FDM	finite difference method
FEM	finite element method
FR	free plate boundary
LDV	scanning laser Doppler vibrometer
NAD	negative amplitude difference
NAH	nearfield acoustic holography
NDD	non-destructive damage detection
PAD	positive amplitude difference
PF	time-averaged vibrational power flow per unit length (Chapters 4-6)/instantaneous net power flow (Chapters 7 and 8)
SNR	signal to noise ratio
SPD	difference of peaks of super-harmonic and primary resonance
SS	simply-supported plate boundary
TPF	time-average net power flow
VNDD	vibration-based non-destructive damage detection
WGN	white Gaussian noise

Nomenclature

A_{nh}	higher negative amplitude
A_{nl}	lower negative amplitude
$\bar{B}$	standard Bayesian average
$\mathbf{C}$	damping matrix
D	thickness of beam/diagonal scaling matrix
d	damage depth (Chapter 6)
E	Young's modulus
ER_f	error function of dimensionless net power flow
$\mathbf{F}$	external force vector
F	force amplitude
f	force
f_b	bilinear frequency
f_c	closed-crack natural frequency
f_e	excitation frequency
f_n	n^{th} natural frequency
f_o	open-crack natural frequency
g	gap of contact point, gradient
H	thickness of plate
I	instantaneous power flow
J	Jacobi
$\mathbf{K_T}$	tangent stiffness matrix
K_n	polynomial coefficient
L	length of beam/plate

l length of crack on plate

$\mathbf{M}$ mass matrix

$\widetilde{M}$ complex amplitude of bending/twisting moment

M_n polynomial coefficient

$\widetilde{N}$ complex amplitude of axial force

N_n polynomial coefficient

$\boldsymbol{P}$ magnitude of power flow per unit length

P instantaneous power flow per unit area (in beam)/per unit length (in plate)

$\bar{P}$ time-averaged net power flow (in beam)/time-averaged power flow per unit length (in plate)

P_d net power flow obtained from damaged plate (Chapter 6)

P_f dimensionless net power flow at each location on plate (Chapter 6)

P_h peak of primary resonance

P_{int} net power flow obtained from intact plate (Chapter 6)

P_l peak of super-harmonic resonance

P_f^m dimensionless net power flow obtained from damaged plate (Chapter 6)

p instantaneous power flow

$\bar{p}$ time-averaged power flow

$\tilde{Q}$ complex amplitude of shear force

R traction at contact point

$\mathbb{R}^2$ two dimensional real coordinate space

r radius of curvature

s trial step

T time period

$\tilde{T}$ complex amplitude of torque

t time

$\mathbf{U}$	nodal displacement
$\tilde{U}$	complex amplitude of displacement in x direction
u	displacement of contact point
$\dot{u}$	velocity in x direction
V	velocity amplitude
$\tilde{V}$	complex amplitude of displacement in y direction
v	velocity
$\dot{v}$	velocity in y direction
W	width of beam/plate
$\tilde{W}$	complex amplitude of displacement in z direction
$\dot{w}$	velocity in z direction
α	dimensionless crack location (beam/plate)
α_{lb}	lower bound of crack location
α_r	real crack location
α_{ub}	upper bound of crack location
β	dimensionless crack location (plate)
ζ	dimensionless damage depth (Chapter 6)/dimensionless crack severity (Chapters 7 and 8)
ζ_{lb}	lower bound of crack severity
ζ_r	real crack severity
ζ_{ub}	upper bound of crack severity
σ	normal stress
τ	shear stress
ν	Poisson's ratio
$\tilde{\Theta}$	complex amplitude of angular displacement
θ	phase angle

ω radian frequency

$\langle . \rangle_t$ time average

Chapter 1

General introduction

1.1 Research background and motivation

1.1.1 Non-destructive damage detection

Damages can destruct integrities and stabilities of structures. They will reduce structural performances, or lead to structural failures which are very dangerous to humans' lives. Table 1.1 contains the examples of the past structural failures that killed a huge number of people. These hazardous incidents motivate researchers to invent methods to prevent them from occurring again. Structural damages are customarily considered as one of the main culprits of the losing above.

Table 1.1: Examples of past structure failures.

Year	Structure	Location	Killed	Reference
1845	Yarmouth Bridge	UK	79	Barber (2013)
1907	Quebec Bridge	Canada	75	Pearson and Delatte (1987)
1959	Vega de Tera	Spain	144	de Wrachien and Mambretti (2011)
1986	Hotel New World	Singapore	33	Kayat (2012)
2002	China Airline Flight 611	Taiwan	225	Gittings (2002)
2003	Space Shuttle Columbia	USA	7	Dowling (2015)

The causes of damages in structures may be categorised into loads from the environment, such as waves, winds, and vibrations generated by earthquakes, and human errors, including accidents and manufacturing or constructing mistakes. Structures collapse as the result of the severe damages induced by the critical loads from a natural catastrophe or an accident. These serious damages occur instantly, so it is beyond our abilities to repair and prevent the structures from failures. Some past structural failures due to the critical loads are shown in Figure 1.1. As indicated in the figure, the structures collapsed due to the strong hurricane and typhoon.

The other external loads, called cyclic loads, usually have significantly less severity than the critical loads mentioned previously. However, these cyclic loads can also initiate damages in structures and create structural failures if those structures are continually subjected to them for a long period. This weakness of structures caused by the cyclic loads is called fatigue. The examples of the incidents of the structural failures owing to fatigue are shown in Figure 1.2. The damages from fatigue, such as cracks, are initially small and hard to be spotted by human's naked eyes. Their extents can be continuously enlarged by the cyclic loads, and consequently, they may give rise to structural failures, as stated before, if they are not detected early enough. Hence, it is very important to have a reliable damage detection technique to pinpoint the damages at their early stages. The damaged structures should be repaired before the damages are enlarged.

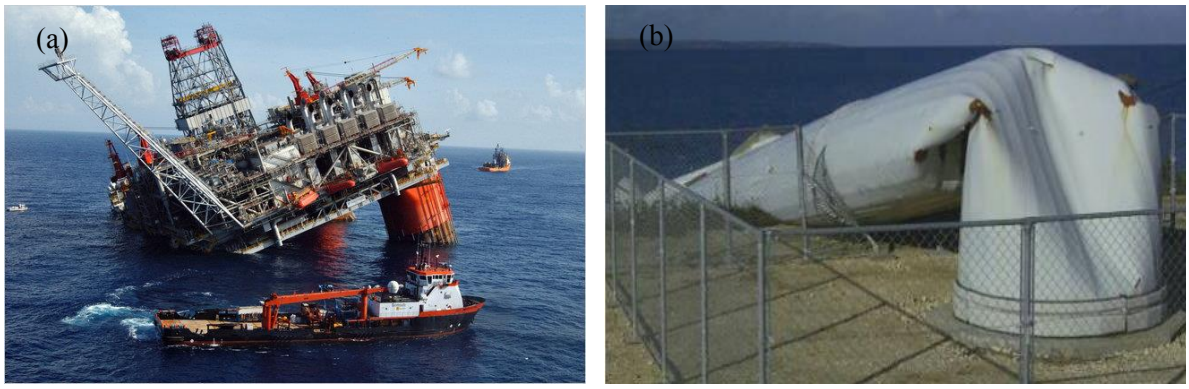

Figure 1.1: Structural failures due to critical load: (a) Thunder Horse platform damaged by Hurricane Dennis in 2005(see, Lyall (2010)); (b) Wind energy facilities on Miyakojima Island damaged by Typhoon Maemi in 2003(see, Tamura (2009)).

In manufacturing processes of structures, destructive testing (DT) is employed to investigate structural behaviours and performances under different loads. The structures are tested to obtain the information, such as geometrical aspects of deformations and yield points. The tests are usually carried on until structural failures occur, so the DT is suitable for mass-produced structures, some of which can be destroyed without giving negative effects on the profits. The purpose of using the DT is to prevent damages from occurring in structures when they are being operated, rather than to detect damages that have already occurred.

Non-destructive damage detection (NDD) is a group of techniques used to assess the properties of structures without destruction of the tested structures. It plays a crucial role in

assuring structural reliability and safety. According to Rytter (1993), the NDD techniques are classified based on their performances into four levels as follows:

Level 1: Detection of the occurrence of damage

Level 2: Determination of the geometric location of the damage

Level 3: Evaluation of the severity of the damage

Level 4: Prediction of remaining service life of the damaged structure.

The theory of the fracture mechanics is required to take part in the process of the NDD to obtain results of Level 4.

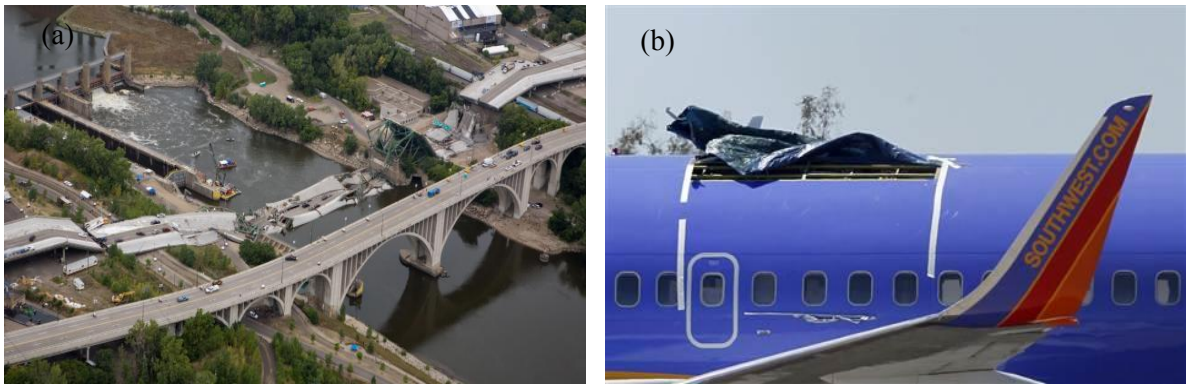

Figure 1.2: Structural failures due to cyclic load: (a) I-35W bridge collapse in 2007(see, Jones (2014)); (b) Aircraft structure failure (see, Xu (2011)).

The classical non-destructive damage detection (CNDD) techniques, such as liquid penetrant testing, eddy current testing, ultrasonic testing, and acoustic emission testing, can complete Levels 1 and 2. These techniques rely on chemical substances, electrical currents, and acoustic waves used as damage indicators. Even though the classical techniques can effectively detect both the presence the location of the damage, they still contain general limitations which are the need of the approximated damage location to be known before starting the tests and the accessible clean surface of the tested structure. Due to these limitations, the CNDD techniques are not suitable for dealing with damages in large structures. Also, for some techniques, such as ultrasonic testing and eddy current testing, skilful operators are required. Thus the effectiveness of the techniques is highly dependent on skill and experience of the operators.

Vibration-based non-destructive damage detection (VNDD) is one more option for using in damage detection activities. Unlike the CNDD, the VNDD relies on changes in inherent vibration characteristics of structures because of damages. One advantage of the VNDD over the CNDD is that the estimated damage locations are not required before the tests. It

means that the working ranges of the VNDD are wider than those of the classical techniques. Thus, the properties of global structures may conveniently be evaluated within a test by the VNDD.

A number of the VNDD techniques have been introduced by researchers at the moment. Their abilities to detect damages are generally up to Level 3. Changes in natural frequencies and vibration mode shapes may be the damage indicators that start to be used in the earliest stage of the VNDD development (see, for example, Gudmundson (1982); Cawley and Adam (1979); Pandey et al. (1991) and Ratcliffe (1997)). Natural frequencies cannot work solely to obtain damage locations and severities since they are global properties of a structure, so their changes due to damages located at different locations of the structure may be the same. Vibration mode shapes can reveal both occurrences of damages and locations, but their measurement accuracy relies on positions and amounts of the sensors.

Following these two early-stage damage indicators, several new vibration-based damage indicators were introduced, such as strain energy (see, for example, Shi et al. (1998) and Hu and Wu (2009)), structural stiffness/flexibility (see, for example, Pandey and Biswas (1994) and Yan and Golinval (2005)), frequency response functions (FRFs) (see, for example, Sampaio et al. (1999) and Park and Park (2003)), wavelets (see, for example, Wang and Deng (1999) and Zhu and Law (2006)), and vibrational power flow (see, for example, Li et al. (2001) and Li et al. (2009)). Each of these damage indicators contains intrinsic limitations when directly applied to damage detection, so it is a challenging task for researchers to seek methods that can enhance their capability and feasibility of detecting all types of damages in all practical structures. The literature reviews informing the details and developments of the aforementioned damage indicators for the VNDD are presented in Chapter 2.

1.1.2 Damage types and modelling

As stated earlier, damages will reduce structural stiffness and may cause structural failures if they are not discovered early enough. Modelling damages in structures is one of the crucial parts in the research of damage detection. More realistic damages will produce results that more alike to those obtained from real situations. In some previous works of the VNDD, the damages were simply modelled by reducing the structural stiffness at the damage locations (see, for example, Wong et al. (2009) and Reddy and Swarnamani

(2012)). This stiffness reduction method is generally based on the finite element method (FEM).

Damages in structures are also modelled as cracks. The cracks in the previous works of the VNDD may be categories, according to their effects on dynamic behaviours of the cracked structures, to linear and nonlinear cracks. Both crack types have started to take part in the research of the VNDD since before last two decades (see, Dimarogonas (1996)). The linear cracks are assumed open constantly, although the cracked structures are subjected to a dynamic force, so they are usually called *open cracks*. The open cracks can be modelled in structures by introducing a constant local flexibility at their location as a massless spring. This flexibility is a function of crack depth, and it will change structural stiffness. This technique is used widely to model cracked beams (see, for example, Rizos et al. (1990); Chinchalkar (2001); Lele and Maiti (2002) and Zhu et al. (2006)) and cracked plates (see, for example, Khadem and Rezaee (2000); Douka et al. (2004) and Li et al. (2009)) for the research of the VNDD.

The open cracks can also be modelled numerically using the FEM by reducing the structural stiffness of the elements at the crack location. For commercial finite element codes, the open cracks are simulated by generating small gaps to disconnect the coincident nodes (see, Aderson (2005)). The gaps should be much smaller than the crack lengths. The previous works employing this crack modelling method are, for example, Lee et al. (2006) and Boonpratpai and Xiong (2015). At the vicinity of the crack tips, the sizes of the elements may be made finer, or the special elements called *singular elements* may be used to determine stress concentration at the tips based on the theory of fracture mechanics (see, Anderson (2005)).

The nonlinear cracks are the cracks that make dynamic responses of the cracked structures nonlinear. They can be called *breathing cracks* since they can be open and closed depending on the dynamic force input to the cracked structures. The nonlinearity in structural responses occurs due to abrupt changes in the structural stiffness during opening and closing of the cracks. Breathing crack modelling is similar to that of the open cracks, except that local flexibility at the crack locations is not constant (see, Ruotolo et al. (1996) and Giannini et al. (2013)). Furthermore, for commercial finite element codes, the contact and target elements may be used at the crack faces to obtain responses when two crack faces contact each other (see, Andreaus et al. (2007) and Bouboulas and Anifantis (2010)).

The breathing cracks generally represent fatigue cracks at their early stage. These cracks are more realistic than the open cracks when used in the research of the VNDD that aim to detect early-stage cracks in structures. Nonlinearity of structural responses induced by the breathing cracks can be used as a tool to detect cracks.

1.1.3 Vibrational power flow

Vibrational power flow is the rate of energy exchange in a structure due to wave propagation. After Noiseux successfully measured the power flow in a beam and plate using the one-point transducer method in the year 1970 (see, Noiseux, (1970)), and Goyder and White demonstrated the fundamental ideas of the power transmission from machines into built-up structures (see, Goyder and White (1980a, 1980b and 1980c)), a number of theoretical approaches for power flow analysis in structures, such as the dynamic stiffness method (see, Langley (1989)), the mobility method (see, Cuschieri (1990)), the travelling wave approach (see, Langley (1992)), the finite element method for power flow analysis (see, Mace and Shorter (2000)), the progressive approach (see, Xiong et al. (2001)) and the power flow boundary element approach (see, Kwon et al. (2011)) were subsequently proposed. Several experimental measurement methods of the power flow in both near and far fields were also introduced (see, for example, Pavić (1976); Williams et al. (1985) and Arruda and Mas (1998)).

The power flow analysis can be employed to predict vibration characteristics and transmissions of structures in both low- and high-range frequencies (see, Yang (2013)). It was applied to various fields of vibration analysis (more details in Chapter 3). One of the power flow applications is to be a damage indicator for the VNDD, as stated earlier. Since the power flow is a dot product of force and velocity components, its changes induced by the damages on structures are more significant than those of the separate force and velocity. In other words, it is more sensitive to damage existence than solely force or velocity. Both magnitude and direction of the power flow have high potential to indicate damage locations and geometries.

Among the damage indicators for the VNDD mentioned in Section 1.1.1, the power flow is the most recent one that starts to get involved in the field of damage detection. At this moment, there are still little publications connected with the VNDD using the power flow as a damage indicator. Most of the available published works dealt with the damages and the structural boundary conditions that may not be practical in reality. Moreover, the

technique based on the power flow capable of detecting damages in the forms of breathing cracks, or fatigue cracks at their early stages, has not been proposed yet. These breathing cracks can generate slight nonlinearity in dynamic responses of the cracked structures. As a result, the power flow in the domains is also nonlinear. On account of the reasons stated formerly, the research on the application of the power flow to the VNDD is still having gaps waiting to be filled.

1.2 Aim and objectives

The research primarily aims to design and develop the methods that can enhance the capability of vibrational power flow to nondestructively assess structural properties, and provide the results up to Level 3 stated before in Section 1.1.1. These NDD techniques are meant to detect damage(s) in common substructures, such as beams and plates. In the thesis, linear and nonlinear characteristics of the power flow in beam and plate structures when through-thickness and breathing cracks occur in the structures are also intended to present.

To reach the targets mentioned above, several objectives are required to be completed. These objectives are as follows:

- To investigate linear power flow behaviours in cracked plate structures having several boundary conditions; single and multiple cracks in the structures are assumed open constantly
- To investigate nonlinear power flow behaviours in beam structures induced by single and multiple breathing cracks that can be open and closed depending on excitation forces
- To show the applications of the linear and nonlinear power flows to the VNDD; changes in the linear and nonlinear power flow behaviours in structures due to the occurrence of damage(s) are used as damage indicators
- To develop techniques that can corroborate with the changes in the linear and nonlinear power flows due to damage to detect the presence of damage, and pinpoint damage location and severity in beam and plate structures.

1.3 Novel contribution of the research

As mentioned earlier, there are only a few works connected to the vibrational power flow for damage detection in the literature. Therefore, the studies of the application capability of the power flow to detect structural damages are required to be carried out further. Based on the aim and objectives given in the previous section, the findings obtained from the research will contribute to the field of the VNDD in several ways as follows:

- The characteristics of the power flow, i.e. power flow patterns and magnitudes, in intact and damaged plates with different types of boundary conditions are studied, so the power transmission paths and the global and local changes in the power flow due to the damages can be observed;
- The behaviours of the nonlinear power flow induced by single and multiple breathing cracks on beam structures are analysed. These breathing cracks can represent early-age fatigues cracks that usually occur on structures in reality. The relationship of the breathing crack location and severity and the degree of power flow nonlinearity is disclosed;
- New VNDD techniques using the advantages of the changes in linear and nonlinear power flow due to the occurrence of single and multiple damages are developed.

1.4 Outline of the thesis

The thesis is composed of 9 chapters which can be categorised into four parts. The first part, Chapters 1, 2 and 3, contains the thesis introduction and the general background and concepts of the research required to be known before getting into the main details. The second part, Chapters 4, 5 and 6, provides the investigation of linear power flow behaviour in damaged structures and its applications to the NDD. The third part, Chapter 7 and 8, is the investigation of nonlinear power flow due to single and multiple breathing cracks, and its benefit to early-stage crack detection. The final part, Chapter 9, is the conclusions and future research. More details of what are in each chapter are provided in the following paragraphs.

In Chapter 2, the literature reviews of the CNDD and VNDD techniques are presented. The advantages and limitations of each technique are also given in the final section of the chapter. The basic concepts of the vibrational power flow are discussed in Chapter 3. This

chapter includes the general idea of the power flow, applications of the power flow, methods to determine the power flow, and the power flow formulation.

Chapter 4 examines the power flow behaviours in plate structures containing single through-thickness crack. The cracked plates are modelled using the FEM implemented by the finite element code, ANSYS. The vibration responses obtained from the cracked plate models are processed by MATLAB to compute the power flow. The behaviours of the power flow in the vicinity of the crack and the other locations on the plates are displayed on the vector field and surface plots. The investigation is also extended to the plates containing multiple cracks and presented in Chapter 5. In Chapter 6, a technique to detect damage location and severity in plate structures using linear power flow contours is introduced. The effectiveness of the damage detection technique is shown through several numerical case studies with and without noise contamination.

In Chapter 7, the nonlinearity of the power flow in a cantilever beam induced by a breathing crack is firstly studied. The relationship between the degree of the power flow nonlinearity and the location and severity of the breathing crack is presented. A crack detection technique based on the benefit of this relationship and surface fitting is also proposed. The numerical case studies show the successfulness of the technique in revealing approximate crack location and severity of the breathing crack in the cantilever beams.

Chapter 8 proposes the novel damage indices based on time-domain nonlinear power flow for crack detection in cantilever beams. This technique can deal with beams containing both single and multiple breathing cracks. The behaviours of the nonlinear power flow in a beam containing multiple cracks are compared to those of the beams with the single crack in Chapter 7. The numerical case studies show that these damage indices are sensitive to small cracks, and can still work well in noisy environments.

Finally, in Chapter 9, some conclusions are drawn and the future work is provided.

Chapter 2

Literature review of non-destructive damage detection techniques

2.1 Introduction

A number of the NDD techniques have been introduced in the literature. In the present chapter, the literature review of those NDD techniques is presented. As stated in the previous chapter, the majority of the NDD techniques are generally classified into the CNDD and the VNDD. Each of them has advantages and limitations. The review of this chapter is therefore divided into three sections: classical damage detection testing, vibration-based damage detection techniques and a summary of benefits and limitations of the techniques.

2.2 Classical non-destructive damage detection

2.2.1 Liquid penetrant testing

The liquid penetrant testing is an inspection method used to reveal locations of surface-breaking flaws in nonporous materials by the penetrant. This technique is simpler and economical than the other techniques. The process of this technique is basically started with the application of the penetrant on the tested surface. The surface must be free of substances, such as water, grease, and dust, which may prevent the penetrant from penetrating the flaws. The penetrant is then left on the surface for the length recommended by the manufacturer. Following that, the penetrant is removed from the surface, and the developer is used to pull up the penetrant confined in the flaws to the surface. The locations of the flaws are finally revealed.

Deutsch (1979) studied some fluid-mechanic aspects of the liquid penetrant testing. The author used an open-ended capillary tube to demonstrate surface tension that influences the

flow of penetrant into flaws. The time of penetration and the effects of trapped air on penetration were also discussed deeply. The ergonomics and human factors in using the liquid penetrant testing were discussed in the work of Luk and Chan (2007).

2.2.2 Eddy current testing

Eddy current testing is a technique used to inspect defects on surfaces of conductive materials. Its function is based on the principle of electromagnetic induction. Eddy currents are swirling electrical currents generated within conductors or tested conductive materials by magnetic fields from eddy current probes. Defects in structures, such as cracks, can be detected by changes in the eddy current magnitudes and patterns. The signals of these changes are then sent to an eddy-current instrument to produce the test results.

The principle and applications of the eddy current technique to damage detection were rigorously reviewed in the work of Martín et al. (2011). Although this technique can detect small surface cracks effectively, it is still limited to only conductive materials, and skill and training are needed in the operations of the technique.

2.2.3 Radiographic testing

This testing deploys X-rays or gamma rays to check the quality of structures. The process is similar to that of medical radiography for humans. The basic principle of the testing is that the energetic rays are radiated through the tested structures, and, as a result, the interior of the structures will be shown on the films. This testing is, therefore, able to detect internal defects of structures and welds. The structural regions containing defects have low material density. These low-density areas can absorb less energy than the others, and they will present in the films with higher-darkness colour.

Due to the technological development, the conventional testing that uses films to present the results is replaced by digital radiography using a computer system. The digital radiography can improve image quality, the time consumption and the accuracy (see, Wang and Liao (2002)). Liao and Ni (1996) introduced a methodology for extracting welds from digitised radiographic images. The results obtained in this work were then used to detect flaws in the welds in the work of Liao and Li (1998). This flaw detection consists of four steps, which are pre-processing, curve fitting, profile-anomaly detection, and post-processing. Aoki and Suga (1999) applied an artificial neural network to the X-ray radiographic testing to discriminate the defect type. Shafeek et al. (2004) developed

software named AutoWDA that can enhance the quality of images obtained from radiographic films, and illustrate defect information, such as area, shape, width and length.

The significant disadvantage of the radiographic testing is hazardous radiation which is very dangerous to humans' health (see, Cawley (2001)). Unfortunately, the X-rays and gamma rays are invisible to humans' naked eyes, so proper area and radiation screens are required for operations.

2.2.4 Ultrasonic/ultrasound testing

Presently, several methods of the ultrasonic testing have been introduced. It can gain more interest of the researchers than the other NDD techniques because of its advantages compared to the others, including higher depth of wave penetration for damage detection, higher sensitivity to both surface and subsurface discontinuities in the materials even concretes, and less part preparation required for testing.

The ultrasonic testing basically employs ultrasonic waves to detect damage in structures. Discontinuity in a structure due to damage will lead to a reflection of the ultrasonic waves. These reflected waves are transformed to signals illustrated on the monitor. The waves commonly used for this technique were categorised by Alobaidi et al. (2015) into longitudinal waves (see, Lucassen and Tempel (1972)), shear waves (see, Lysmer and Waas (1972)), Rayleigh waves (see, Masserey (2006)) and Lamb waves (see, Alleyne and Cawley (1992)).

The review of the ultrasonic testing for detecting the welding flaws was completed by Manjula et al. (2014). This paper details several methods of the ultrasonic testing using the waves mentioned formerly. The applications of the ultrasonic testing to various flaw inspection tasks and their merits and limitations were reviewed in the work of Muthumari and Singh (2011). It is noticed from the paper that the technology of the instruments for showing the defects visually is also important, and still needs development simultaneously with that of the other parts of the testing, such as sensors.

The nonlinear ultrasonic techniques were also introduced in many papers in the literature. These techniques are more sensitive to small damage than the conventional linear counterparts. Jhang (2011) conducted the review of nonlinear ultrasonic techniques for detection of microdamage. In this review, the author categorised the nonlinear ultrasonic techniques, based on the nonlinear acoustic phenomena induced in materials, into higher

harmonic generation, sub-harmonic generation, shift of resonance frequency and mixed frequency response. Chillara and Lissenden (2016) did a review in term of nonlinear ultrasonic guided waves for the NDD. The theories, numerical simulations and experimental measurements of those nonlinear guided waves were presented.

2.2.5 Acoustic emission testing

Acoustic emission testing is the analysis of acoustic wave radiation induced by energy released, as a result of crack propagation or plastic deformation, at a region in the material subjected to an external load. It can be stated that damage in the material behaves as a source of acoustic emission wave, and this source is detected by a sensor to give us notice of damage occurrence and its location. To sum up, the process of the acoustic emission testing fundamentally composes of three parts which are emission waves generated by defects, transducers used to capture those waves, and instruments for interpreting and illustrating the collected data (see, Nair and Cai, 2010).

Two distinct merits of this technique, when compared to the other NDD techniques, are that it can work with structures which are operating, so the conditions of the structures can be monitored round the clock, and the defects can consequently be detected at their early stages; and it does not depend on structural geometry. However, it is also subject to one drawback which is from contamination of noise. The uses of the acoustic emission testing for the health monitoring of bridges were discussed in the work of Nair and Cai (2010). In this work, the principle of the acoustic emission, review of available data processing techniques and the case studies of the real bridges constructed using concrete, steel, and fibre reinforced polymer (FRP) were clearly demonstrated.

Gholizadeh et al. (2015) divided the applications of the acoustic emission testing into the applications to the quality control in manufacturing operations (see, Chen and Li (2007) and Jemielniak and Arrazola (2008)), civil engineering (see, Ai et al. (2010) and Keshtgar and Modarres (2013)), aerospace engineering (Hensman et al., 2011), and material engineering (see, Ohno and Ohtsu (2010) and Aggelis and Matikas (2012)). Each of these applications mainly uses the acoustic emission testing to monitor, in real time, the qualities of materials or structures.

Recently, the acoustic emission testing was also combined with other techniques to enhance its ability. The combination of the acoustic emission and the infrared

thermography was introduced by Dassios et al. (2014). This combined technique could successfully illustrate the extent of the crack and its real-time growth rate in the composite structures. Aggelis et al. (2009) employed both the acoustic emission and ultrasonic to characterise damage in reinforced concrete beams. The damage which is too small for the acoustic emission could be detected by the ultrasonic. Kral et al. (2013) conducted experiments to identify crack propagation in flat aluminium plates using the acoustic emission sensors coupled with the artificial neural networks. In the experiments, the data of the strain waves released from the crack was collected by the acoustic emission sensors, and then the artificial neural networks estimated crack length.

2.3 Vibration-based damage detection techniques

2.3.1 Natural frequencies

Natural frequencies are inherent properties of all structures, which can be measured easily without dependence on measured positions. A number of research papers showing the benefits of natural frequencies on damage detection have been proposed in the literature. An early review of the detection techniques using natural frequencies as damage indicators was completed by Salawu (1997). This review contains the details of the techniques introduced before last two decades, and the factors and limitations needed to concern when using the techniques.

Gudmundson (1982) introduced a first-order perturbation method to determine changes in natural frequencies of beams containing a crack, notch, and hole. The method called Rank-ordering of eigenfrequency shifts was invented by Armon et al. (1994). This method, however, can only predict the approximate region of the beam that contains the damage. Tanaka and Bercin (1998) formulated the equations showing the relationship between changes in natural frequency and local flexibility at the crack location in a cantilever beam. By substituting three natural frequencies measured from the damaged and intact beams to the equations, the crack location on the beam was obtained.

The methods of Gudmundson (1982) and Armon et al. (1994) were combined and used in conjunction with the finite element method by Lee and Chung (2000). This combination could create the technique capable of detecting both location and severity of the crack in a beam structure. Kim et al. (2003) proposed a single damage indicator (DI), generated from one to three fraction changes in natural frequencies, for detecting the crack location in a

beam. The DI of every section of the beam was evaluated, and the crack was on the section that had the maximum DI. The authors also formulated an equation for estimating crack size from the Gudmundson's equation.

Apart from one-dimensional structures, the damage detection technique using natural frequencies was also used for two-dimensional structures. Cawley and Adams (1979) employed the similar method to that in the work of Kim et al. (2003) to assess the plates. Their method was successfully dealt with the single damaged plate, but not the case of the plate with multiple damages. Yang et al. (2013) recently proposed the inverse and forward problems based on three measured natural frequencies to predict both damage location and severity in a plate.

Although natural frequencies are easy to be measured accurately, their sensitivity to small damage or damage at an early stage is low. A structure containing the damage at different locations may have the same natural frequencies. Thus, natural frequencies usually work cooperatively with another damage indicator, such as local stiffness of structures, to detect damage location.

2.3.2 Vibration mode shapes

Each vibration mode of structures has its own natural frequency and mode shape, so these two parameters are usually measured together. When compared mode shapes to natural frequencies, the previous one is more difficult to be measured accurately than the latter. However, mode shapes can reveal more information about damage than natural frequencies.

Pandey et al. (1991) successfully located damage in cantilever and simply supported beams using changes in curvature mode shapes. The curvature mode shapes of the intact and damaged beams were numerically computed using a central difference approximation, and the absolute differences between the curvature mode shapes for the intact and damaged beams were plotted to demonstrate the location of the damage. The method of Pandey et al. (1991) was recently extended to be used with plate structures by Zhong and Yang (2016). Ratcliffe (1997) employed the modified Laplacian operator and mode shape data to pinpoint the location of damage. The main advantage of this technique claimed by the author is it can operate without knowledge of the intact beam.

Khoo et al. (2004) used pole shifts in the s-plane plots to illustrate the effect of damage on structural mode shapes. These plots could reveal that the mode shapes are not affected equally by the occurrence of the damage so that the authors could select the ones highly sensitive to the damage. The modal residue and stiffness drop techniques were then used to detect damage location. Rucevskis and Wesolowski (2010) proposed the technique of mode shape curvature squares which can detect both damage location and size. Rucevskis et al. (2016) introduced the damage index, established from the absolute difference between measured curvature of the damaged structure and the smoothed polynomial representing the corresponding intact structure. They also deployed the concept of the statistical hypothesis testing technique to enhance the contrast of the damage index plot at damage location.

2.3.3 Modal strain energy

Modal strain energy is a product of the modulus of elasticity and the second power of the mode shape (see, Shi et al. (1998)). The Modal Strain Energy Change Ratio (MSECR) was created by Shi et al. (1998) to locate single or multiple damages in a structure. The MSECR is the summation of modal strain energy ratios of intact and damaged structures at each position collected from several vibration modes. This algorithm was later improved by the same group of the authors (see, Shi et al. (2002)) to reduce the number of vibration modes required for detecting damage. Cornwell et al. (1999) built damage indices based on local one- and two-dimensional modal strain energy at each location on perfect and damaged structures. The damage index of one-dimensional energy can also be used for two-or three-dimensional structures by splitting the structures into several parts of beam-like structures.

Hu and Wu (2009) combined modal strain energy and the idea of the traditional scanning damage detection techniques, such as X-ray and ultrasonic, to make the scanning damage index method (SDIM). The tested structure was scanned by moving a small local area, containing a number of measurement grid points, throughout its body. This approach was successfully applied to damaged plates. It also works well with a curve shell structure (see, Hu et al. (2011)) if the gap between each grid point is sufficiently small, and the effect of the curvature can be neglected.

2.3.4 Structural stiffness/flexibility

Stiffness has an inverse relationship with flexibility. Both of them are obtained from normalised mode shapes and corresponding natural frequencies. Stiffness matrices of structures can usually provide more information of damage than mass matrices (see, Yan et al. (2007)). Pandey and Biswas (1994) proposed a damage index based on flexibility changes capable of detecting occurrence and location of damage. The flexibilities were determined from the principle of normalised mode shapes of intact and damaged structures. Comparing to the stiffness matrix determination showed that the flexibility matrices could be accurately predicted using only a few of the lower frequency modes. The damages located on the structures at the regions where higher bending moment occurs could more easily be identified than at the other places.

The higher sensitivity of the modal flexibility to damage when compared to those of natural frequencies and mode shapes was presented through various case studies in the work of Zhao and DeWolf (1999). Lu et al. (2002) investigated the performances of the changes in flexibility and flexibility curvature techniques for detecting multiple damages. Only first three modes were used to determine the flexibility matrix. The authors found that the sensitivity of the changes in flexibility technique to small damage is high, but it cannot clearly illustrate locations of two damages located close to each other. The flexibility curvature technique can, on the other hand, work well with two damages near each other. However, it cannot deal effectively with small damage. The combining technique of flexibility and stiffness was proposed by Yan and Golinval (2005). In this work, the modal parameters were determined by using the covariance-driven subspace identification technique. The method to estimate and scale the flexibility obtained from the use of ambient force as an input excitation was presented. The corresponding stiffness matrix was then determined by a pseudo inversion of the flexibility matrix. The changes in the flexibility and stiffness matrices were perceived together to locate locations of the damages, so the reference data from the intact structure was not needed.

2.3.5 Frequency response functions (FRFs)

A frequency response function (FRF) is a quantity representing the relationship between input and output of a system. Sampaio et al. (1999) proposed damage identification method using FRF curvatures. The difference between FRF curvatures of damaged and perfect

structures was evaluated without the needs of modal data and natural frequencies. Thus modal analysis was ignored from the process. Lee and Shin (2002) derived the equation of FRF (inertance), generated by a harmonic point force, for detecting single and multiple damages in a beam. The damage influence matrix and the algorithm composing of three steps were introduced to search and remove damage-free regions of the beam from the domain of calculation. Then the left-over regions, which contain damage, were assessed to obtain damage severity.

The incomplete FRF method for detecting damage location in structures was presented by Park and Park (2003). This method has the advantage over the conventional methods as it does not need an analytical model. However, it requires a number of experiments and a suitable operating frequency range have to be selected. Otherwise, its performance may be worsened. Park and Park (2005) later proposed a similar detection method capable of reducing an experimental load by dividing the tested structure into several sub-structures.

A statistical damage detection method was proposed by Furukawa et al. (2006). Unlike the works mentioned previously, in this work, the authors used changes in both total stiffness and damping matrices to model damage. The hypothesis testing based on the boot strap method was employed to detect undamaged elements of a frame structure by checking decrease in stiffness and increase in damping due to damage. Once the undamaged elements were excluded, the severity of damages in the other elements was evaluated. Lin et al. (2012) proposed a substructure-based FRF approach with a damage location index (SubFRFDI) whose excitation force is from an earthquake. The SubFRFDI was then experimentally tested with the developed Imote2.Net-based wireless sensing system and the six-story steel structure subjected to base excitation. This wireless sensor could be deployed efficiently to measure the required data and real-timely send it to the authors.

2.3.6 Vibrational power flow

Power flow is another vibration characteristic that can be advantageous to damage detection. Since power flow is a dot product of force and velocity components, the change of it due to damage will be more than that of solely force or velocity. The potentials of power flow to apply to damage detection in semi-infinite structures were demonstrated by Li et al. (2001), Li et al. (2004), Zhu et al. (2006), Zhu et al. (2007), and Li et al. (2009). In these works, the ratios of power flows and input powers in the damaged structures were compared with those of the corresponding intact structures to show the changes in the

power flow when the cracks appear in the structures. The results of these works can guarantee the high potential of power flow to function as a damage indicator. However, the semi-infinite structures are still not practical in the real world.

Diversion of power flow and its magnitude changed at the crack tips and close region in a cracked plate were shown in the work of Lee et al. (2006). The cracked plate was assumed undamped, so a damping dashpot was used as the sink of the system, and also used to control the power flow path. This work indicates a high sensitivity of power flow to damage, although the power flow was generated by low-range excitation frequency.

Huh et al. (2011) proposed a damage index created from the ratio of change in power flow due to damage and maximum power flow in the finite intact beam. The damage was done on the beam as a saw cut. The index could effectively predict the location of the damage. This work did not include the effect of reflection of waves at the boundaries of the beam. This index was later extended to two-dimensional one for plate structures by Huh et al. (2015). The method to identify the damage direction was also introduced in this work. Again, the boundaries of the plate were assumed not to induce reflected waves.

2.3.7 Nonlinear dynamic responses

All of the works reviewed in the previous sections assumed that the damage is constantly open, so the dynamic behaviours of the damaged structures are linear. As mentioned earlier, nonlinear dynamic behaviours of structures can be created by several reasons. One of those reasons is a sudden change in structural stiffness due to contact. An early-stage crack in a structure is open and closed depending on the input force. When the crack is open, the structural stiffness is decreased. The stiffness is, on the other hand, increased when the crack becomes closed and two crack faces contact each other. This nonlinearity induces super- and sub-harmonic resonances, which will be beneficial to damage detection, when the cracked structure is excited by a bilinear frequency (see, Chati et al. (1997); Andreaus et al. (2007) and Carneiro and Ribeiro (2015)).

Nonlinear behaviour of cracked beams analysed for the purpose of damage detection was demonstrated in the work of Saavedra and Cuitiño (2001). The occurrence of a crack in a free-free beam and U-frame structure was detected by the super-harmonic resonance appeared in the acceleration responses of the structures. The concept of nonlinear output frequency response functions (NOFRFs) for damage detection was introduced by Peng et

al. (2007). The results of the experiment showed that the NOFRFs can report the occurrence of the crack in the tested beam, but the information of crack location is still missing. One more technique capable of detecting the presence of a crack in a cantilever beam was presented by Yan et al. (2013). The free vibration response of the beam was divided into two parts based on the beam stiffness when the crack is fully open and closed, and then the frequency of each part was compared to each other. If the beam contains a crack or more than that, these two frequencies will be different.

Super-harmonic signals were numerically used to locate a crack on the beam by Semperlotti et al. (2009a). The technique to detect the crack location in this work is based on the algorithm to obtain the location of a source of a dispersive pulse. From the results presented in their work, the maximum error of the technique using the Hilbert-Transform approach as the data post-processing tool is still as high as 20%. The damage detection technique was later experimentally validated by Semperlotti et al. (2009b). In this work, they used sub-harmonic signals instead of the superharmonics because the piezoelectric transducers deployed in the experiment also generated superharmonics, and these could interfere the signals induced by the crack.

Andreaus and Baragatti (2011) presented different types of super- and sub-harmonic acceleration responses when a crack in a cantilever beam is located at a different location and has different severity. From the acceleration responses, it can be stated that the degree of system nonlinearity relies on location and severity of the crack. This relationship was employed to build a damage detection technique for cantilever beams based on curve fitting of acceleration responses. The authors subsequently performed experiments to validate the technique, and the results were shown in Andreaus and Baragatti (2012).

Giannini et al. (2013) detected crack location and severity in a cantilever beam by the maximum ratio of two peaks of Fourier spectrum plots created by the driving frequency and super- or sub-harmonic frequency components. These maximum values were then processed using the Bayesian method and plotted in a surface plot to illustrate the location and severity of the crack. Andreaus and Casini (2015) recently introduced a damage index that could successfully reveal locations and sizes of multiple open and fatigue cracks in a cantilever beam. The damage index was built from the ratio between the maximum wavelet coefficient and the curvature of the intact beam at the same location.

There are not many NDD techniques associated with nonlinear power flow in the literature. Semperlotti and Conlon (2010) proposed the nonlinear power flow in a plate induced by the damage created using a riveted joint with loosened fasteners. Their power flow intensity map revealed that the contact between the joint and the plate body behaves like another source of power. The interaction between the joint and the plate body is similar to clapping of the crack faces of a breathing crack. This concept was then extended to deal with homogeneous and composite airframe structures containing damage modelled in the same way by Romano et al. (2013).

2.4 Advantages and limitations of the techniques

This section summarises the advantages and limitations of the NDD techniques mentioned in the former sections. It is noted that these advantages and limitations are considered from the inherent ability of each damage indicator, without any supplementary technique to enhance its performance of damage detection. The section will start with the advantages and limitations of the CNDD techniques, and this is followed by those of the VNDD techniques.

2.4.1 Classical non-destructive damage detection

Liquid penetrant testing

Advantages	Limitations
• High sensitivity to small defects • Low cost • Can be used with all materials • Equipment is portable	• Can detect only surface defects • Limited to nonporous surfaces • Tested surface must be clean and dry

Eddy current testing

Advantages	Limitations
• High sensitivity to small defects • Can deal with both surface and near-surface defects • Equipment is portable	• Can be used with only conductive materials • Require trained and skilful operators • Material surface has to be accessible to probe

Radiographic testing

Advantages	Limitations
• High sensitivity to both surface and sub-surface defects • Results can be kept permanently on films • Available reference standards	• Danger from radiation • Require trained and skilful operators • Equipment is expensive

Ultrasonic/ultrasound testing

Advantages	Limitations
• High sensitivity to both surface and sub-surface defects • High depth penetration for defect detection • Results illustrated through images	• Material surface has to be accessible to transmit ultrasonic • Require trained and skilful operators • Not suitable for coarse-grained materials i.e. cast iron due to its low sound transmission

Acoustic emission

Advantages	Limitations
• Can work while structures are in operation • Sensors can be fixed at one place and do not need to be moved frequently to scan the whole structure	• Sensitive to noise • Difficulty of calibrations • Cannot reveal geometries of defects

2.4.2 Vibration-based damage detection techniques

Natural frequencies

Advantage	Limitations
• High accuracy and convenience of measurements	• Low sensitivity to small damage (changes in natural frequencies due to small damage may be insignificant) • Lack of information for damage detection, i.e. damage location (damage at different locations may give the same natural frequency) • Need data of corresponding intact structures to compare

Vibration mode shapes

Advantage	Limitations
• Mode shape curvatures can predict damage location	• Measurement errors due to amount of sensors and their distribution may occur, especially for higher vibration modes • May need data of corresponding intact structures to compare • Need higher vibration modes to detect small damage • Mode shapes may need to be scaled • Not sensitive to damage located at node

Modal strain energy

Advantages	Limitation
• No requirement of knowledge of undamaged state • Need only a few lower vibration modes to complete damage detection • No need to scale mode shapes	• Accuracy is heavily dependent on measured mode shapes

Structural stiffness/flexibility

Advantage	Limitations
• Need only a few lower vibration modes to complete damage detection	• Not sensitive to small damage • Need many sensors with good distribution to detect small damage

Frequency response functions (FRFs)

Advantages	Limitations
• No requirement of analytical model • No requirement of modal data	• Need many experimental measurements • High sensitivity to noise

Vibrational power flow

Advantages	Limitation
• Very high sensitivity to small damage • No requirement of knowledge of undamaged state	• Need vibration responses from more than one measurement point to compute power flow

Chapter 3

Concepts of vibrational power flow

3.1 Introduction

As stated earlier in Chapter 1, vibrational power flow is used as a damage indicator for the NDD in this research. This chapter will present the concepts of the power flow that should be known before applying it to the NDD. The chapter starts with the general idea of the power flow, and this is followed by the power flow application history, which includes the information of the power flow applied to several engineering fields from the past. The other two sections will provide the details of how to obtain the power flow in structures, such as beams, plates, and shells. The power flow determinations in the previous research associated with the NDD using power flow are also discussed.

3.2 General idea of power flow

For the investigation of structural-borne sound, power flow is an important index that can illustrate the magnitude of vibratory power at an observed location in a structure, power sources and sinks, and power transmission paths. It will allow engineers to deal with problems caused by structural vibration more easily. The power flow is, consequently, the rate of energy transmission at an observed point. It can also be in the form of structural intensity or power flow per unit area.

According to the law of the conservation of energy, energy cannot be destroyed, but it can be converted to another form. Thus, the vibratory power input to a system will be equal to power output if the system has no internal loss factor that can convert the power to heat. The power converted to heat by the internal damping is called dissipated power. This activity can be represented by the power balance equation (see, Hambric (1990)) which can be given as

$$p_{in} = p_{dis} + p_{out}. \tag{3.1}$$

The diagram explaining the power balance equation is shown in Figure 3.1. It is assumed that this system contains a small internal damping. The system is subjected to the input power, p_{in}, at the location of the power source. The power is out of the system, p_{out}, at the power sink. The arrows show the direction of power transmission, and their lengths represent the magnitudes of the power flow. The power transmits from the source to the sink which is the mounting consisting of a spring and damping dashpot. On the way from the source to the sink, its magnitude also decreases continuously due to the internal damping of the system.

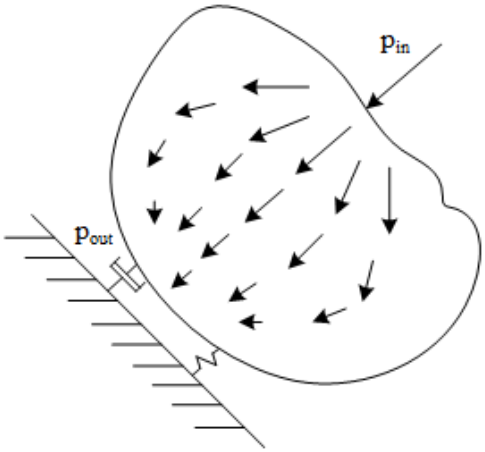

Figure 3.1: Diagram of power flow

3.3 Power flow applications history

Investigation of vibration behaviour on a structure may be simply completed by measuring dynamic responses of the structure i.e. displacement, velocity, and acceleration. However, these responses are still not able to clearly reveal some important information such as vibration sources and sinks and vibration propagating paths. Vibrational power flow is the power transmitted in structures by wave propagation. Thus, it can be used to characterise vibration characteristics including the aforementioned vibration transmitting paths and their sources and sinks. The power flow in structures is usually measured as structural intensity or power flow per unit area cross section. Apart from damage detection, the power flow is also applied to several research fields. Some of them are stated below.

3.3.1 Prediction of vibration transmission

Vibratory power will transmit from its source to sink, so the path of the vibration, locations of the source and sink of the power can be inspected. The study of the power flow path was started as early as before 1970. Noiseux (1970) successfully measured the direction and quantity of the power flow in a plate and studied power flow behaviour. He also found the relationship between the far-field power flow and the plate damping. Arruda and Mas (1998) demonstrated the power flow path and the source and sink of the power using the gradient and divergence plots. Li and Lai (2000) determined the mobility of a plate using the analysis of the power flow. The power flow in a coupled plate-cylindrical shell was studied by Wang et al. (2004). The authors showed that the coupling edges behave as other sinks of the system. They also showed the power flow paths in both substructures. Xu et al. (2004) analysed the power flow in the stiffened plates and illustrated the changes in the power flow pattern due to the existence of the stiffeners. Li et al. (2010) employed the streamline maps to demonstrate the power flow paths in the coupled plates.

3.3.2 Vibration control

The goal of vibration control is to minimise the vibration in a structure using active, passive or hybrid controllers. Since vibration characteristics in a structure can be characterised by the power flow, minimising the power transmission into or within the structure will reduce the structural vibration. Heretofore, many researchers have successfully employed the power flow as indicators in vibration isolation; for example, Goyder and White (1980c), Pinnington and White (1981), Xiong et al. (2000), Xiong et al. (2005a), Choi et al. (2009), and Yang et al. (2013).

Xiong et al. (2005b) proposed a damping-based power flow mode theory that can be applied to vibration control. According to the theory, the input time-averaged power flow of a system is equal to the dissipated power due to its damping. The theory was established based on the well-known knowledge of the unchanged kinetic and potential energies in the systems of harmonic motions or stationary random processes after every cycle. The damping and mode control factors of the system were adjusted to obtain high dissipated power that could reduce the power flow in the system.

Power flow can also be used as an indicator in vibration absorption. Chen and Wang (2014) decreased the power flow in the sandwich structures using the internal vibration

absorbers. Yang et al. (2015) recently proposed the study of the power flow behaviour of the nonlinear vibration absorber coupled to a nonlinear oscillator. They concluded that the nonlinear absorber could work well with the linear oscillator. However, for the nonlinear oscillator, the performance of the absorber is reduced when the hardening stiffness absorber is coupled to the hardening stiffness oscillator, and it is also the same for the case of the softening stiffness.

3.3.3 Energy harvesting

Even though there are many available works of energy harvesting in the literature nowadays (see, for example, Mitcheson et al. (2008), Truitt and Mahmoodi (2013), Santhosh et al. (2015)), it still has limited works employing power flow analysis to investigate the performance of the harvesting systems. Yang et al. (2013) used power flow analysis to investigate a nonlinear energy harvesting system composing of a flapping foil coupled with an electromagnetic generator. This system produces energy by using incompressible quasi-steady air flows. Based on the power balance equation, they found that the energy harvesting system requires more power input to drive the system than the flapping foil without the electromagnetic generator since the generator functions as another damping. Li and Xiong (2015) recently introduced a nonlinear model for harvesting energy using the interaction between a smooth and discontinuous oscillator (SD oscillator) and an electromagnetic generator. The authors concluded that its performance is higher than the linear counterpart in term of the efficiency of broadband vibration energy harvesting.

3.3.4 Damage detection

The applications of the power flow to damage detection have been discussed in Section 2.3.6 of Chapter 2.

3.4 Power flow determinations for damage detection

In this section, the techniques to compute or measure power flow in structures are reviewed. The section is divided into three sub-sections which are analytical methods, computational methods, and experimental measurement. It is noted that the review particularly focuses on the previous works in the literature related to damage detection using power flow. More details of the methods to determine the power flow in structures

can be found in the works of Mandal and Biswas (2005) and Shepherd et al. (2012) which are more specific to power flow-based damage detection.

3.4.1 Analytical methods

For the previous works of damage detection, power flow in a damaged structure was, generally, computed using the basic power flow equation (see, Pavić (1976) and Xing and Price (1999)) in conjunction with vibration responses, i.e. force and velocity, obtained from the analytical solution of the structure based on the wave approach. Therefore, more attention was paid to the derivation of the analytical solutions to determine vibration responses of damaged structures. More practical damage in a structure requires a more complicated analytical solution to solve its governing equation (see, Khadem and Rezaee (2000) and Israr et al. (2009)).

There are several works of power flow-based damage detection completed by the analytical methods in the literature. Li et al. (2001) studied the power flow in an infinite damaged Euler beam. They modelled a surface crack in the beam as a jointed rotational spring based on the relation between the strain energy and stress intensity factor in fracture mechanics. The beam was divided into multiple sections with the boundary conditions at each side of each section. The crack was located on one of these sections. The effect of the cracks was added to the slope angle of the beam section through the boundary conditions at the crack joints. This additional slope was calculated from the local flexibility of the spring and the bending moment to which the spring is subjected. The vibration responses of every section of the cracked beams were obtained using the state vector and transfer matrix satisfying all of the boundary conditions, and the theory of periodic structures. The responses were then used to predict the power flow.

The power flow in an infinite cracked Timoshenko beam was analysed by Zhu et al. (2006). The same technique as the one mentioned in the former paragraph was used to model a crack in the beam. The beam was divided into three sections, and the responses of each section were computed using the wave solutions of Timoshenko beams and the boundary conditions.

Li et al. (2009) proposed the power flow analysis in a damaged semi-infinite plate. The plate has the finite width and simple supports along two opposite sides. The damage was modelled as an all-over part-through surface crack lying parallel to the plate width using a

rotational spring. The Kirchhoff's plate equation was solved to obtain the power flow by the wave approach in conjunction with the valid boundary conditions at the location of the crack affected by the additional slope due to the presence of the crack. This slope discontinuity along the crack was previously introduced by Rice and Levy (1972). The analytical power flow investigations in cracked circular plate and cylindrical shell using the similar methods as stated before were also presented by Li et al. (2004) and Zhu et al. (2007), respectively.

3.4.2 Computational methods

A computational method, such as the finite element method (FEM), can ease the difficulty of solving equations of damaged structures. Additionally, it allows us to model more complicated and realistic damage in more complex structures. However, we need to bear in mind that the FEM is an approximation method, so its accuracy is lower than the analytical method, and the accuracy will be highly dependent of element sizes.

The power flow equations for beams, plates and shells based on the FEM were presented by Hambric (1990) and Gavrić and Pavić (1993). These equations were later popular among the researchers who did the research on power flow in structures modelled using the FEM. Lee et al. (2006) employed the FEM implemented by ABAQUS to model a through-thickness crack in the middle of a simply-supported plate. The element type used in this modelling is shell element. At the vicinity of the crack, the elements were made finer to provide the better estimations of the results. They assumed no structural damping but a damping dashpot attached at the specific location on the plate. The power flow was calculated from the vibration responses obtained from the FEM. The power flow vector was then plotted to assess the power flow path and the diversion and increase of the power flow at the crack tips. This vector plot could also illustrate the locations of the source and sink of the power.

Huh et al. (2011) modelled a damaged beam using the beam elements in MSC/NASTRAN. The damage is in the form of a saw cut. The material of the beam was assumed undamped. The springs and dashpots were attached at two ends of the beam to behave as damping of the system. Therefore, the power transmitted from the source to these ends, which are the sinks, and no reflected power occurred at both ends. The authors also showed that the beam stiffness decreases significantly at the location of the damage. The instantaneous and time-averaged power flows were computed from the vibration responses of the beam

model. A cracked plate was also modelled using MSC/NASTRAN by Huh et al. (2015). The boundary condition of the plate was the same as that of the beam mentioned before. The behaviour of the power flow at the crack tips seen in the vector plot was similar to that presented in the work of Lee et al. (2006). The details of the power flow experimental measurement are presented in the next section.

3.4.3 Experimental measurements

An experimental measurement of the power flow is an important part of damage detection since it is the way to practically obtain power flow values from a tested structure that may contain damage. The experimental measurement techniques of the power flow may be categorized into contact and non-contact types (see, Mandal and Biswas (2005)).

Contact measurement

The contact measurement deployed sensors such as accelerometers to measure vibration responses for power flow calculation. The sensors have to be attached on the surface of the tested structure, so this is the reason why it is called contact measurement. The contact measurement of the power flow was firstly performed by Noiseux (1970). The biaxial accelerometer, which composes of the transverse and rotational accelerometers, was used to measure the power flow at the far field of a plate.

Pavić (1976) extended the technique of Noiseux (1970) to the technique called *transducer array technique* that relies on only the vertical displacements of the structure and the finite difference method (FDM). This technique can measure both one-and two-dimensional power flows in respectively beams and plates using only a few transverse accelerometers.

For the one-dimensional power flow in beams, a four-point transducer array is used. The array with four sensors is shown in Figure 3.2(a). The power flow is measured at the beam cross section shown by the dashed line. The finite difference equation for computing the power flow from the vertical displacement measured by each sensor was introduced by Pavić (1976) as

$$\bar{P}_x = \frac{EI}{\Delta^3}\langle 4\dot{w}_2 w_3 - \dot{w}_2 w_4 - \dot{w}_1 w_3 \rangle_T \tag{3.2}$$

where $\bar{P}_x$ is the time-averaged net power flow in the x direction (direction parallel to the length of the beam) at the measurement point; E is the Young's modulus; Δ is the distance

between sensors; w_i is the vertical displacement at point i; $\langle\ \rangle_T$ represents the time-averaged term; I is the second moment of area of the beam which is equal to $bh^3/12$; b is the width of the beam and h is the height of the beam. The net power flow is defined as the amount of power transmitted through a cross section of the beam.

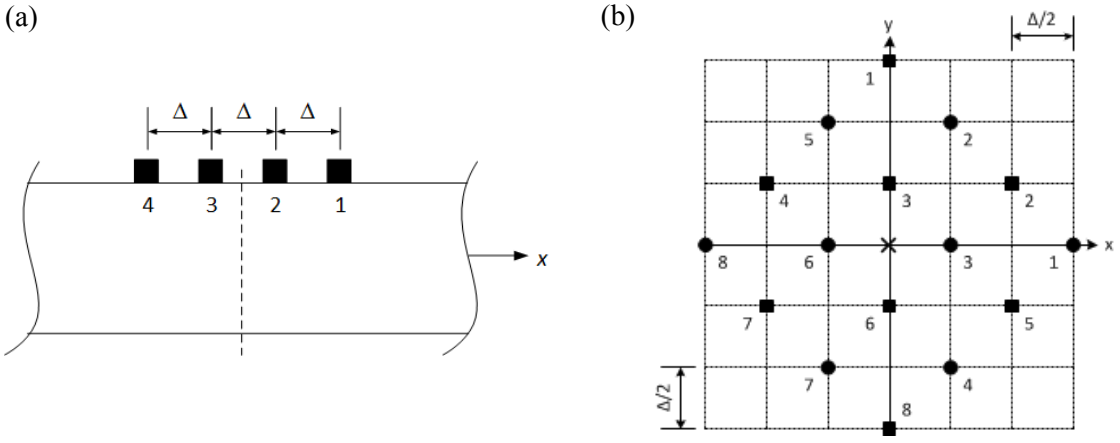

Figure 3.2: Measurement array: (a) four point; (b) eight point.

Huh et al. (2011) presented the finite difference equation in the frequency domain for broadband signals as

$$P_x(\omega) \cong \frac{EI}{\Delta^3 \omega^3} \Im\{4\tilde{G}_{23}(\omega) - \tilde{G}_{24}(\omega) - \tilde{G}_{13}(\omega)\} \tag{3.3}$$

where $P_x(\omega)$ is the spectral density of the net power flow at the measurement point; ω is the radian frequency; $\Im$ denotes the imaginary part of a complex number and $\tilde{G}_{ij}$ is the cross spectrum of the accelerations at points i and j which is equal to

$$\tilde{G}_{ij}(\omega) = \tilde{H}_{Fi}^*(\omega)\tilde{H}_{Fj}(\omega)\tilde{G}_{FF}(\omega) \tag{3.4}$$

where $\tilde{H}_{Fi}$ is the frequency response function (FRF) of the force and acceleration signals at point i; $\tilde{H}_{Fj}$ is the FRF of the force and acceleration signals at point j; $\tilde{G}_{FF}$ is the auto spectrum of the force signal; * denotes the complex conjugate and ~ denotes the complex number. The time-averaged net power flow of the beam can be obtained by integrating the values of the spectral density in Equation (3.3) over all frequencies (see, Linjama and Lahti (1992)).

The eight-point transducer array is used for the two-dimensional power flow in plate structures. The grid of the eight-point measurement array is shown in Figure 3.2(b). The

array measures the power flow at the location shown by the cross. The circles represent the points of the power flow in the x direction, while that in the y direction is shown by the squares. The finite difference equation for the power flow in the x direction is given as (see, Pavić (1976) and Huh el al. (2015))

$$\begin{aligned}\bar{P}_x \cong \frac{D}{4\Delta^3}\langle -8(3+\nu)w_3\dot{w}_6 + 4w_1\dot{w}_6 + 4w_3\dot{w}_8 \\ + (1-\nu)(2w_2\dot{w}_3 - w_2\dot{w}_5 + w_2\dot{w}_7 - w_3\dot{w}_4 + w_4\dot{w}_5 - w_4\dot{w}_7 \\ - 2w_5\dot{w}_6 + 2w_6\dot{w}_7) + 2(1+\nu)(w_3\dot{w}_5 + w_3\dot{w}_7 + w_2\dot{w}_6 + w_4\dot{w}_6)\rangle_T\end{aligned} \tag{3.5}$$

where $\bar{P}_x$ is the time-averaged power flow per unit length of the plate; D is the flexural rigidity of the plate which is equal to $Eh^3/12(1-\nu^2)$; h is the plate thickness and ν is the Passion's ratio.

The power flow per unit length in the x direction of the plate can also be obtained from the frequency domain finite difference equation which is

$$\begin{aligned}P_x(\omega) = \frac{D}{4\Delta^3\omega^3}\Im\big[-8(3+\nu)\tilde{G}_{36} + 4\tilde{G}_{16} + 4\tilde{G}_{38} \\ + (1-\nu)\big(2\tilde{G}_{23} - \tilde{G}_{25} + \tilde{G}_{27} - \tilde{G}_{34} + \tilde{G}_{45} - \tilde{G}_{47} - 2\tilde{G}_{56} \\ + 2\tilde{G}_{67}\big) + 2(1+\nu)(\tilde{G}_{35} + \tilde{G}_{37} + \tilde{G}_{26} + \tilde{G}_{46}\big]\end{aligned} \tag{3.6}$$

where $P_x(\omega)$ is the spectral density of the power flow per unit length in the x direction of the plate and $\tilde{G}_{ij}$ can be obtained using Equation (3.4). An integral of the spectral density values obtained from Equation (3.6) over all frequencies will generate the time-averaged power flow per unit area. The power flow in the y direction of the plate can be measured by the similar way to that of the power flow in the x direction stated above.

Since the contact measurement is based on the FDM, the distance between sensors, Δ, has to be small to achieve accurate results. However, too small Δ will lead to phase mismatch errors (see, Mandal (2006)). Thus, the suitable Δ has to be determined. An example of the method to determine the suitable Δ is presented in the work of Huh et al. (2011). Moreover, the selection of the sensors is also needed to be concerned since mass of the sensors can cause measurement errors, especially for the case of eight-point measurement array.

Non-contact measurement

For the non-contact measurement, the approaches such as a scanning laser Doppler vibrometer (LDV) and a nearfield acoustic holography (NAH) are employed to measure vibration responses for power flow calculation instead of sensors. It can eliminate phase mismatch errors and errors due to the mass of sensors that may occur to the contact measurement. However, the devices used in the measurement are more costly than sensors of the contact counterpart.

Similar to the contact measurement, the measurement points of vibration responses are arranged as a measurement array, and the FDM is then used to compute the power flow from those measured vibration responses. Therefore, the four-point and eight-point arrays as mentioned previously in the contact measurement section can also be used with the LDV and NAH.

Arruda and Mas (1998) used the LDV to localise energy sources and sinks in plates. The authors compared the results obtained from the three-point, five-point and nine-point measurement arrays, and they found that the array with more measurement points can yield better results. Daley and Hambric (2005) later introduced the technique of thirteen-point measurement array that can work well with both the near-field and far-field power flows.

The NAH employs microphones placed close to the surface of the tested structure to obtain pressure generated by structural vibration (see, Williams et al. (1985)). The pressure is then transformed to velocity for the power flow computation. Again, the measurement points of the pressure are arranged as a measurement array, and the power flow is calculated using the FDM.

3.5 Power flow formulation

3.5.1 Basic equation of power flow

Power is defined as the rate of work done per unit time. Thus the equation of the power at time t is written mathematically as

$$p(t) = f(t)\mathrm{v}(t) \tag{3.7}$$

where f denotes the force; and v is the velocity. This power at the specific time is designated as instantaneous power.

In vibration analysis, the terms f and v are physically in the forms of real harmonic functions which compose of their amplitudes, F and V, radian frequency, ω, phase angle, θ, and time, t. These functions are expressed as

$$f(t) = F\cos\omega t \tag{3.8}$$

$$\mathrm{v}(t) = \mathrm{V}\cos(\omega t + \theta). \tag{3.9}$$

Alternatively, these harmonic functions can also be in complex forms. Only the real part of a complex variable contains a physical meaning (see, Xing and Price (1998)), so $f(t)$ and $\mathrm{v}(t)$ can also be written as

$$f(t) = \Re\{\tilde{F}e^{i\omega t}\} \tag{3.10}$$

$$\mathrm{v}(t) = \Re\{\tilde{\mathrm{V}}e^{i\omega t}\} \tag{3.11}$$

where $\Re$ denotes the real part; e is the exponential function; i equals to $\sqrt{-1}$; ~ denotes the complex variable. The complex amplitudes $\tilde{F}$ and $\tilde{\mathrm{V}}$ are generally equal to F and $\mathrm{V}e^{i\theta}$, respectively.

When a power response is in a harmonic form, the power can be averaged over one period of time, T, to yield a quantity defined as time-averaged power flow. The equation of the time-averaged power flow is

$$\bar{p} = \frac{1}{T}\int_0^T \Re\{\tilde{F}e^{i\omega t}\}\ \Re\{\tilde{\mathrm{V}}e^{i\omega t}\}dt. \tag{3.12}$$

If $T = 2\pi/\omega$, Equation (3.7) can be transformed to

$$\bar{p} = \frac{1}{2}\Re\{\tilde{F}\tilde{\mathrm{V}}^*\} = \frac{1}{2}\Re\{\tilde{F}^*\tilde{\mathrm{V}}\} \tag{3.13}$$

where $*$ is the complex conjugate.

From Equation (3.13), it is seen clearly that only the real part is selected to show the quantity of the time-averaged power flow. This real part is usually called active power flow which is a mechanical power flow.

3.5.2 Power flow in continuous structures

In continuous structures, such as beams, plates, and shells, the power flow may be measured as structural intensity or power flow per unit area at each point on a cross-section of the structures. Integration of the power flow per unit area at every point on a cross section yields a rate of the power transmitting through that cross-section or net power flow (see, Pavić (1987)).

The equations of the power flows per unit area in three directions based on Cartesian coordinates are given as (see, Pavić (1987))

$$P_x = -\sigma_{xx}u - \tau_{xy}v - \tau_{xz}w \tag{3.14}$$

$$P_y = -\sigma_{yy}v - \tau_{yx}u - \tau_{yz}w \tag{3.15}$$

$$P_z = -\sigma_{zz}w - \tau_{zx}u - \tau_{zy}v \tag{3.16}$$

where P is the instantaneous vibrational power flow per unit area; σ and τ are the direct and shear stresses; u, v and w are the velocities; and the subscripts x, y and z show the directions in the Cartesian coordinates. The positive direction of the stress components are presented in Figure 3.3.

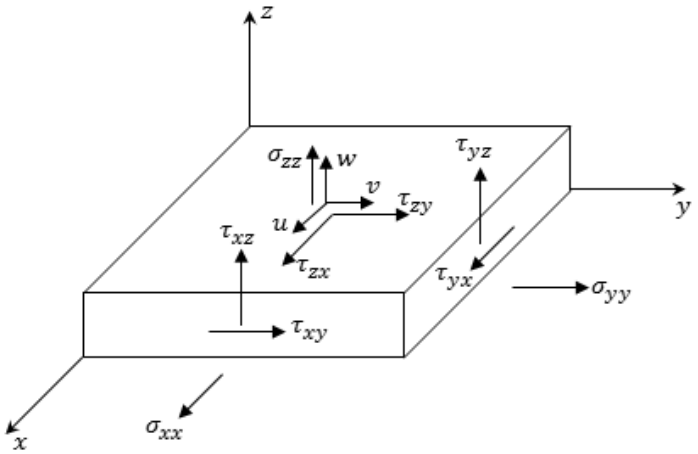

Figure 3.3: Positive direction of stress components.

Equations (3.14)-(3.16) are the fundamental equations of the power flows per unit area at an observed point on a cross section of any continuous structures. For thin structures such as beams and plates having the z axis parallel to their thicknesses, the power flow in the z direction is frequently negligible when compared to those in the other two directions. Equations (3.14)-(3.16) can be transformed to the specific power flow equations for each type of structures. These equations are presented in the following sections.

3.5.3 Power flow in beams

For beam structures, only the power flow in the x direction which is parallel to the length of beams is focused on. The equation of the time-average net power flow when a beam is excited by single harmonic frequency, ω, is expressed as (see, Gavrić and Pavić (1993))

$$\bar{P}_x = -\frac{\omega}{2}\Im\{\tilde{N}\tilde{U}^* + \tilde{Q}_y\tilde{V}^* + \tilde{Q}_z\tilde{W}^* + \tilde{T}\tilde{\Theta}_x^* + \tilde{M}_y\tilde{\Theta}_y^* + \tilde{M}_z\tilde{\Theta}_z^*\} \tag{3.17}$$

where $\bar{P}$ is the time-averaged net power flow; $\Im$ denotes the imaginary part; $\tilde{N}$ is the complex amplitude of the axial force; $\tilde{Q}$ is the complex amplitude of shear force; $\tilde{T}$ is the complex amplitude of torque; $\tilde{M}$ is the complex amplitude of bending moment; $\tilde{U}$, $\tilde{V}$ and $\tilde{W}$ are the complex amplitudes of displacements in the x, y and z directions, respectively; and $\tilde{\Theta}$ is the complex amplitude of angular displacement. The positive direction of the displacements, forces, moments and torque are shown in Figure 3.4(a).

The quantity obtained from this equation is the time-averaged net power flow at an observed cross section. The velocities in the equation are replaced by the displacements using the theory of the complex algebra.

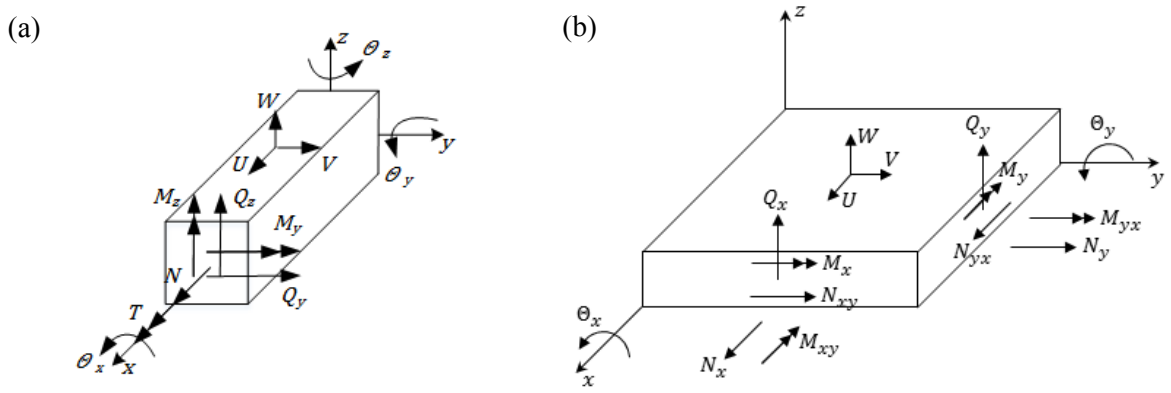

Figure 3.4: Positive direction of displacements, forces, moments and torque: (a) beams; (b) plates

3.5.4 Power flow in plates

Unlike the power flow of beams obtained from Equation (3.17), the power flow in plates is usually obtained in the form of time-average power flow per unit length. Not only the power flow in the x direction but also the one in the y direction are paid attention to. The power flow in plates is mainly dependent on shear force and bending moment components. It is also subjected to in-plane forces, but the contribution is low when compared to the aforementioned parameters. The equations of the power flows in the x and y directions are given as (see, Gavrić and Pavić (1993))

$$\bar{P}_x = -\frac{\omega}{2}\Im\{\tilde{N}_x\tilde{U}^* + \tilde{N}_{xy}\tilde{V}^* + \tilde{Q}_x\tilde{W}^* + \tilde{M}_x\tilde{\Theta}_y^* - \tilde{M}_{xy}\tilde{\Theta}_x^*\} \tag{3.18}$$

$$\bar{P}_y = -\frac{\omega}{2}\Im\{\tilde{N}_y\tilde{V}^* + \tilde{N}_{yx}\tilde{U}^* + \tilde{Q}_y\tilde{W}^* - \tilde{M}_y\tilde{\Theta}_x^* + \tilde{M}_{yx}\tilde{\Theta}_y^*\} \tag{3.19}$$

where $\bar{P}$ is the time-averaged power flow per unit length; $\tilde{N}_x$ and $\tilde{N}_y$ are the complex amplitudes of membrane forces per unit length; $\tilde{N}_{xy} = \tilde{N}_{yx}$ is the complex amplitude of tangential membrane force per unit length; $\tilde{Q}_x$ and $\tilde{Q}_y$ are the complex amplitudes of shear forces per unit length; $\tilde{M}_x$ and $\tilde{M}_y$ are the complex amplitudes of bending moments per unit length; and $\tilde{M}_{xy} = \tilde{M}_{yx}$ is the complex amplitude of twisting moments per unit length. The positive direction of the displacements, forces and moments are given in Figure 3.4(b).

The contributions of $\tilde{N}_x$, $\tilde{N}_y$, $\tilde{N}_{xy}$ and $\tilde{N}_{yx}$ to the power flow magnitudes are significantly less than those of the other forces and moments. Therefore, in some works, such as the one of Arruda and Mas (1998), Equations (3.18) and (3.19) are reduced to

$$\bar{P}_x = -\frac{\omega}{2}\Im\{\tilde{Q}_x\tilde{W}^* + \tilde{M}_x\tilde{\Theta}_y^* - \tilde{M}_{xy}\tilde{\Theta}_x^*\} \tag{3.20}$$

$$\bar{P}_y = -\frac{\omega}{2}\Im\{\tilde{Q}_y\tilde{W}^* - \tilde{M}_y\tilde{\Theta}_x^* + \tilde{M}_{yx}\tilde{\Theta}_y^*\}. \tag{3.21}$$

3.5.5 Power flow in curved shells

The power flow equations of curved shells are similar to those of thin plates. In each equation, two more terms are added due to the effect of the curvature of shells. The power flow of shells can be determined by (see, Gavrić and Pavić, 1993))

$$\bar{P}_x = -\frac{\omega}{2}\Im\left\{\widetilde{N}_x\tilde{U}^* + \widetilde{N}_{xy}\tilde{V}^* + \tilde{Q}_x\widetilde{W}^* + \widetilde{M}_x\tilde{\theta}_y^* - \widetilde{M}_{xy}\tilde{\theta}_x^* + \widetilde{M}_x\left(\frac{\tilde{U}^*}{r_x}\right) + \widetilde{M}_{xy}\left(\frac{\tilde{V}^*}{r_y}\right)\right\} \quad (3.22)$$

$$\bar{P}_y = -\frac{\omega}{2}\Im\left\{\widetilde{N}_y\tilde{V}^* + \widetilde{N}_{yx}\tilde{U}^* + \tilde{Q}_y\widetilde{W}^* + \widetilde{M}_y\tilde{\theta}_x^* - \widetilde{M}_{yx}\tilde{\theta}_y^* + \widetilde{M}_y\left(\frac{\tilde{V}^*}{r_y}\right) + \widetilde{M}_{yx}\left(\frac{\tilde{U}^*}{r_x}\right)\right\} \quad (3.23)$$

where r_x and r_y are the radii of curvature of shells; and the other parameters are the same as those of the equations of thin plates. It should be noted that for these two equations, $\widetilde{N}_{xy} \neq \widetilde{N}_{yx}$ and $\widetilde{M}_{xy} \neq \widetilde{M}_{yx}$.

Chapter 4

Power flow characteristics of thin plates with single crack

4.1 Introduction

The main purpose of this chapter is to study the behaviours of the vibrational power flow in damaged structures with different boundary conditions, and the potential of the power flow to be used for damage detection. Thin plate structures are used to fulfil the aforementioned purpose. The time-averaged power flow per unit length at every location in intact and damaged plates will be computed. The damage is in the form of a through-thickness crack oriented parallel and perpendicular to the coordinate x axis of the plate. The time-averaged power flow is generated by a unit point force. The power flow patterns are presented through vector field and power distribution plots. The trend of the net power flow, which is the integrated value of the time-averaged power flow through the length of cross section, around the input force and crack tips is also investigated and discussed.

4.2 Finite element modelling of intact and cracked plates

4.2.1 Validation of power flow computation using FEM

A plate having the geometry and material properties the same as those in the work of Li and Lai (2000) is remodelled using ANSYS. The plate has the length, width, and thickness of $0.707\,m$, $0.5\,m$ and $0.003\,m$, respectively, and it is simply supported along the short edges. The Young's modulus is $70\,GPa$. The Poisson ratio and density are 0.3 and $2100\,kg/m^3$. The FEM is employed to determine the time-average power flow per unit length in this plate. The plate is discretised into 560 eight-node shell elements. The plate also contains structural damping ratio of 0.005. This damping ratio is equal to half of the loss

factor of the structure, and it represents the ratio of the actual damping coefficient to the critical damping coefficient. To generate power flow, a unit point harmonic force with the excitation frequencies of 14 Hz and 128 Hz is at the centre of the plate. The time-average power flow per unit length is determined using Equations (3.18) and (3.19).

The time-average power flow per unit length generated by these two excitation frequencies are presented through the vector field plots in Figures 4.1. It can be seen from the figure that the power transmits outwards from the location of the excitation force, and its direction depends on the excitation frequency. These vector plots of power agree well with those presented in the work of Li and Lai (2000).

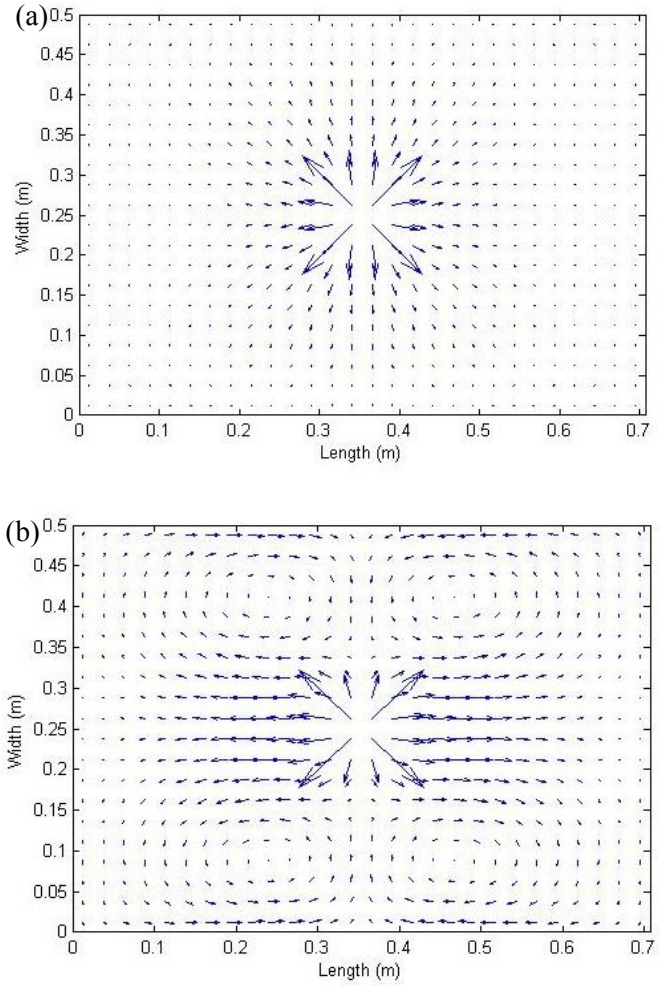

Figure 4.1: PF vector plot of plate: (a) excitation force 14 Hz; (b) excitation force 128 Hz.

The power flow shown in Figure 4.1 is in the form of the time-average power flow per unit length. In order to determine net power transmitting through a cross section of the plate, integration of the time-average power flow per unit length along the length of that cross-

section is required. Since the finite element models of the plates are composed of a number of discrete elements, and the time-average power flow per unit length is calculated at each element centroid, the integration cannot be carried out analytically. The numerical integration method, Trapezoidal rule, is, therefore, advantageous to this computation. For the sake of convenience, the time-average power flow per unit length and the time-average net power propagating through a cross section of the plate obtained from the numerical integration will be, respectively, labelled as *power flow (PF)* and *net power flow (net PF)*, from now on, for this chapter.

To confirm the validity of the numerical integration method for using with the FEM, the finite element model of the plate proposed in the work of Gavrić and Pavić (1993) is remodelled using ANSYS. The plate is discretised into 510 square-shaped elements. Its length, width, and thickness are 3 m, 1.7 m and 0.01 m. Young's modulus, Poisson's ratio and mass density are 210 GPa, 0.3 and 7800 kg/m^3, respectively. A damping dashpot with the damping coefficient of 100 Ns/m is attached to the plate. The plate is assumed free of structural damping. A 100 N point force with the frequency of 50 Hz is used as an external load. The vector plot of the power flow is given in Figure 4.2(a). The locations of the excitation force and damping dashpot which are the source and sink of the power flow can be seen clearly from the vector plot. The power propagates smoothly from the source to the sink. This vector plot has good agreement with the original one in the work of Gavrić and Pavić (1993).

Since the plate does not contain the structural damping, the net power flow from the integration of the closed curve around the excitation force is identical to the power injected by the excitation force. The injected power calculated analytically by Gavrić and Pavić (1993) using 100 integration points in a circle, with the position of the source at its centre, is 1.246 $Watt$. The integration path of the Trapezoidal rule integration is shown by the red dashed line in Figure 4.2(b). As seen from the figure, four discrete points are taken part in the integration.

Table 4.1 contains the results of the injected powers, or the net power flows around the excitation force, obtained from the analytical integration by Gavrić and Pavić (1993) and from the numerical (Trapezoidal rule) integration by the author of the thesis. It is seen that the injected power obtained from the numerical integration in the 510-element plate as

presented in Figure 4.2 is slightly larger than that from the analytical integration. The size of each element in this 510-element plate is $0.1\,m \times 0.1\,m$. When the element size is reduced to $0.0\dot{3}\,m \times 0.0\dot{3}\,m$, and hence the amount of the elements used to model the plate is increased to 4590 elements, the injected power becomes very close to the value from analytical computation. Once the element size is sufficiently small, a similar result to the one obtained from the analytical solution can be determined by FEM. However, it should be borne in mind that the finer the element size, the higher the costs of computation.

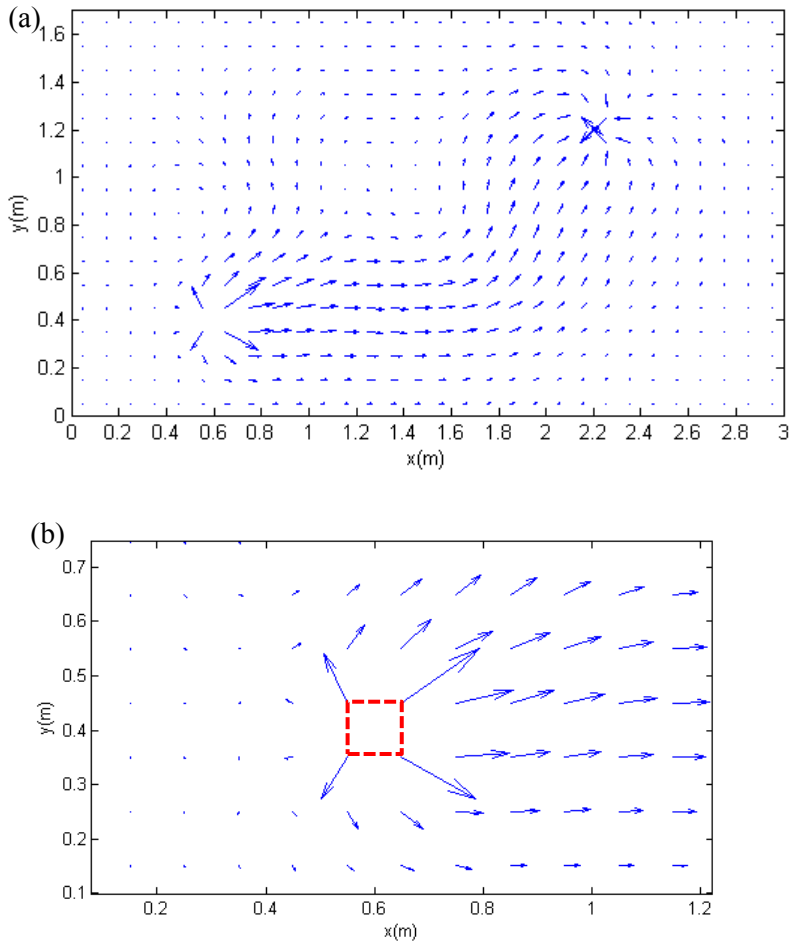

Figure 4.2: PF vector field plot in undamped plate with damping dashpot: (a) vector field of the whole plate; (b) integration path at the power source.

Table 4.1: Injected power obtained from analytical and numerical integrations.

Injected power obtained from analytical integration by Gavrić and Pavić (1993) (Watt)	Injected power obtained from numerical integration in 510-element plate (Watt)	Injected power obtained from numerical integration in 4590-element plate (Watt)
1.246	1.295	1.248

4.2.2 Validation of crack modelling method

Crack modelling in a plate is a crucial part to obtain accurate results of the power flow patterns at the crack location. The crack that will be used in this chapter is in the form of a through-thickness crack. The cracked plate is discretised into a number of eight-node shell elements. This element type can provide more accurate results than the four-node shell element when the computation is relevant to fracture analysis (see, Anderson (2005)). At the area close to the crack tips, the order of mesh refinement is higher. The effects of the order of mesh refining at the region around through-thickness cracks on the accuracy of the computation are rigorously discussed in the work of Vafai and Estekanchi (1999). A small gap between two crack faces is created to avoid coincident of the nodes. This gap must be very small when compared to the crack length (see, Anderson (2005)).

Before using this crack modelling method to model a cracked plate for the power flow investigation in this chapter, validation is required to confirm the validity of the modelling method. The cracked plate in the work of Vafai and Estekanchi (1999) is remodelled using ANSYS. This plate has Young's modulus, Poisson ratio and mass density of 68.95 GPa, 0.33 and 2700 kg/m^3, respectively. The plate dimensions are 2 m length, 2 m width and 0.01 m thickness. The size of the square-shaped elements is 0.1×0.1 m. The crack having the length of 0.4 m is located at the centre parallel to one side of the plate. This crack is modelled using the mesh refinement method with the order of mesh refinement of 4. A membrane stress of 1000 N/m is applied to two sides of the plate parallel to the crack. Due to the symmetry, the computation is carried out for only one-fourth of the plate.

The membrane forces in the x and y directions at the region close to the crack tip obtained from ANSYS are presented in Figure 4.3(a). These results have a good agreement with those predicted by Vafai and Estekanchi (1999) presented in Figure 4.3(b). The crack tip is at the position of 0.2 m (the x coordinate of the graph in Figure 4.3). Based on the theory of fracture mechanics, the membrane forces in the x and y directions at a crack tip on a plate which behave elastically are close to infinity due to the singularity of stress components (see, Anderson, (2005)). The values of stresses then decrease exponentially from those at the crack tip until those at the edge of the one-fourth plate. This is the reason why the results of stresses at this crack tip obtained from the FEM will always be lower than those from the theory.

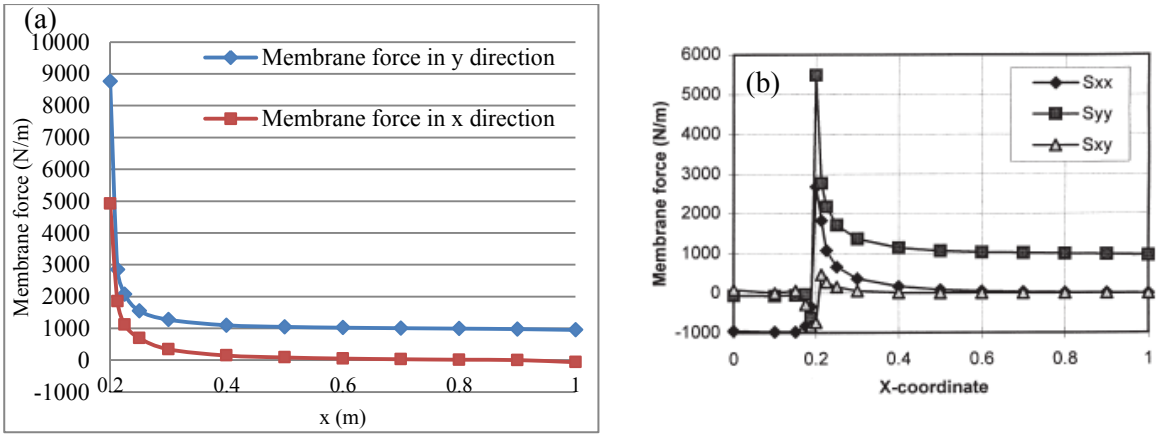

Figure 4.3: Membrane forces at crack region: (a) the results predicted by the author using ANSYS; (b) the results shown in Vafai and Estekanchi (1999) (S_{xx} is the membrane force in the x direction, S_{yy} is the membrane force in the y direction).

The mesh refinement method with the order of 8 from the square-shaped element size of $0.02 \times 0.02\,m$ will be employed to model through-thickness cracks on the plates for the power flow investigation in this chapter. Smaller elements at the crack tips can provide more details of the changes in power flow characteristics at the vicinity of the tips.

4.2.3 Finite element model of cracked plate

The plate that will be used in the power flow analysis has $1.2\,m$ length (L), $1.0\,m$ width (W) and thickness (H) of $0.01\,m$. The width and the length of the plate are respectively parallel and perpendicular to the coordinate x axis. Young's modulus, Poisson ratio and density of the steel plate are 210 GPa, 0.31, and 7800 kg/m^3, respectively. These material properties of a steel plate are taken from the table of material properties given in Cremer et al. (2005).

As stated in the previous section, the damage on this plate is in the form of a through-thickness crack. The through-thickness cracks parallel and perpendicular to the x axis of the model coordinates are firstly assumed to be located at the position $x = 0.5\,m$ and $y = 0.9\,m$ of the plate. This crack position is taken from the middle point of the crack line, and it may be written in a bracket as (0.5, 0.9) for being more convenient. The length of the crack (l) is firstly fixed at 0.01 and $0.04\,m$, and the crack is assumed not to propagate. These cracks are modelled using the method mentioned in the previous section, and the order of meshing refining at the region around the crack tips is 8. The finite element

models of the cracked plates are shown schematically in Figures 4.4. The z coordinate axis points outwards the paper.

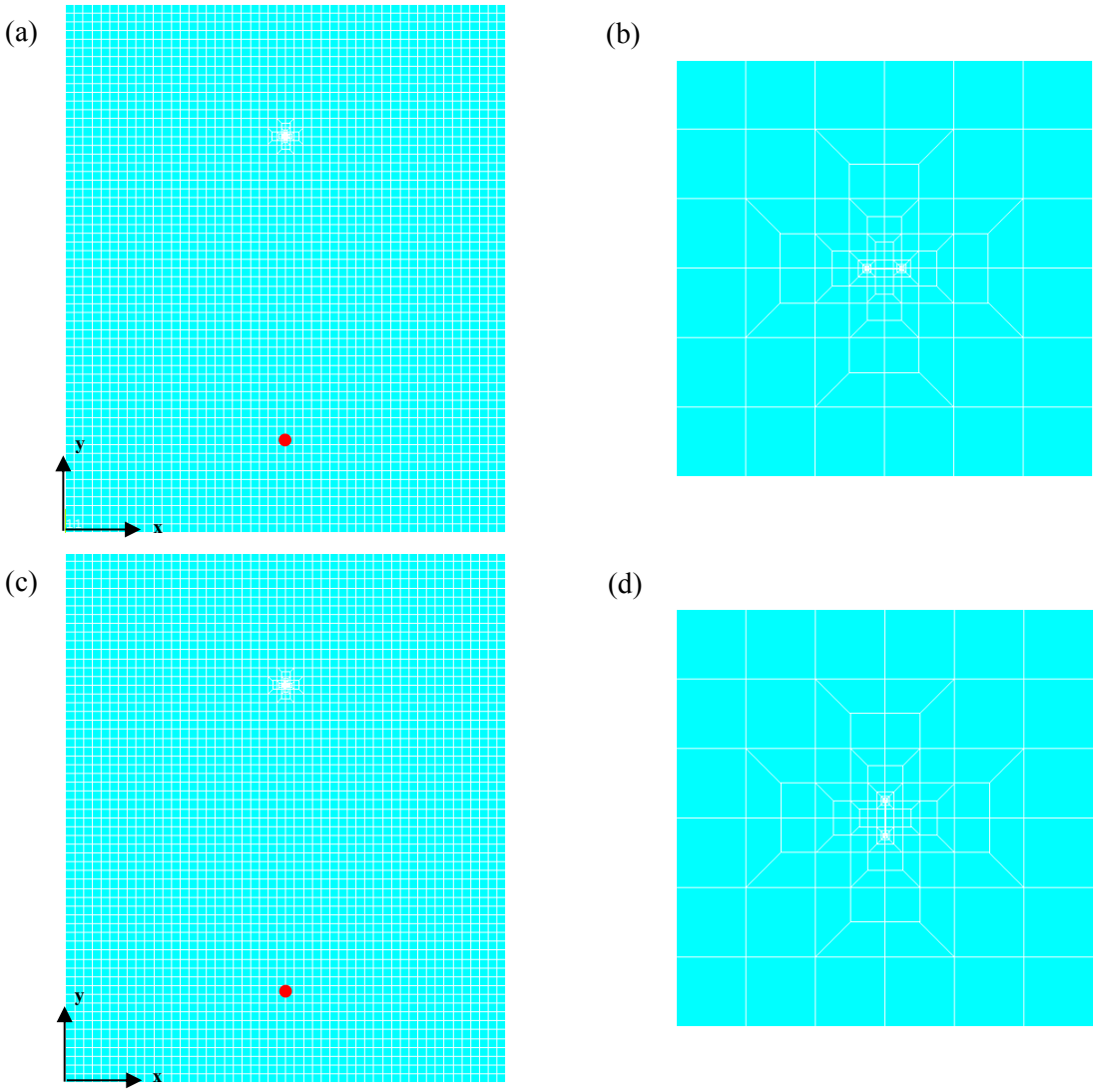

Figure 4.4: Finite element model of cracked plates ($0.01\ m$ crack length): (a) crack parallel to the x axis; (b) zoomed-in version at location of crack parallel to the x axis at its location; (c) crack perpendicular to the x axis; (d) zoomed-in version at location of crack perpendicular to the x axis at its location.

The source of the power flow is a vertical unit point force parallel to the z coordinate axis located on the plate at the position (0.5, 0.2) which is shown in the models by the red dots. The constant structural damping ratio of 0.005 is applied to the model. These input force and structural damping will act as the energy source and sink of the plate vibration system. The types of the boundary conditions of the plates are given in Figure 4.5.

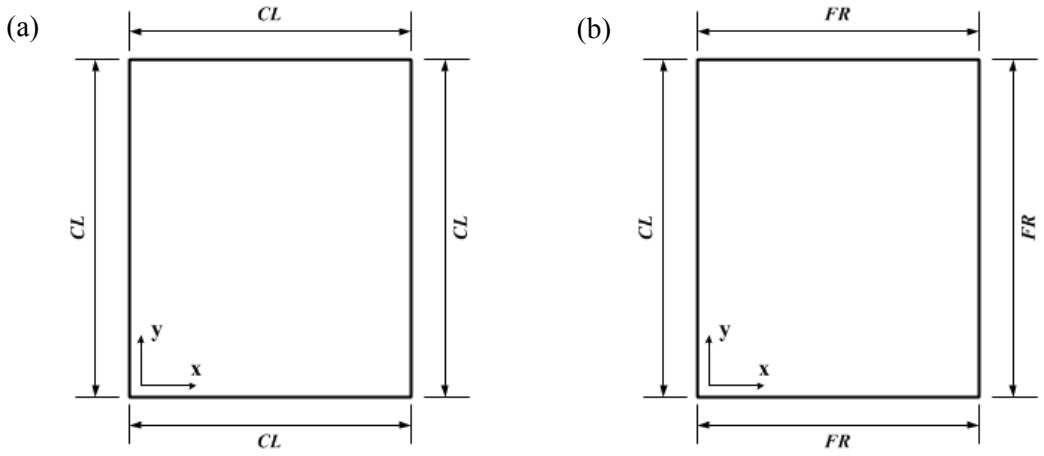

CL = Clamped, *FR* = Free

Figure 4.5: Plate boundary conditions: (a) all edge clamped; (b) cantilever.

4.2.4 Natural frequencies of intact and cracked plates

Every structure has modes of vibration, and each mode behaves as a single degree of freedom, and it has its own natural frequency. In this section, the natural frequencies of the cracked plates are determined from the modal analysis in ANSYS. Since the constant structural damping ratio is very small, it is omitted in this modal analysis. The natural frequencies of the intact and cracked plates are presented in Tables 4.2 and 4.3.

Table 4.2: Natural frequencies of intact plates and plates with crack parallel to the *x* axis.

Set	Natural frequency of intact clamped plate (Hz)	Natural frequency of clamped plate with crack parallel to x (Hz)		Natural frequency of intact cantilever plate (Hz)	Natural frequency of cantilever plate with crack parallel to x (Hz)	
		l = 0.04m	l = 0.01m		l = 0.04m	l = 0.01m
1	77.038	77.027	77.037	8.711	8.711	8.711
2	139.220	139.010	139.210	18.532	18.530	18.532
3	173.230	173.220	173.220	48.341	48.335	48.340
4	230.440	230.430	230.440	56.227	56.216	56.226
5	239.330	238.880	239.290	70.763	70.759	70.762
6	320.390	320.350	320.390	114.200	114.190	114.190
7	325.920	325.900	325.910	115.620	115.500	115.610
8	374.150	373.840	374.130	152.960	152.960	152.960
9	375.790	375.770	375.790	168.110	168.090	168.110
10	458.190	458.140	458.180	183.680	183.530	183.660

It is seen that the natural frequencies are decreased when the cracks occur in the plates. When the length of the cracks is increased, the natural frequencies are also reduced. This change in the natural frequency can be used as an indicator to detect the occurrence of

damage on the plate. However, it cannot be used solely to predict the location and severity of damage, and change in the natural frequency is very small even in the higher mode.

Table 4.3: Natural frequencies of intact plates and plates with crack perpendicular to the x axis.

Set	Natural frequency of intact clamped plate (Hz)	Natural frequency of clamped plate with crack perpendicular to x (Hz)		Natural frequency of intact cantilever plate (Hz)	Natural frequency of cantilever plate with crack perpendicular to x (Hz)	
		l = 0.04m	l = 0.01m		l = 0.04m	l = 0.01m
1	77.038	77.005	77.035	8.711	8.709	8.711
2	139.220	139.130	139.220	18.532	18.530	18.532
3	173.230	173.220	173.220	48.341	48.331	48.340
4	230.440	230.430	230.440	56.227	56.167	56.222
5	239.330	239.230	239.320	70.763	70.717	70.759
6	320.390	320.050	320.360	114.200	114.190	114.190
7	325.920	325.900	325.910	115.620	115.600	115.620
8	374.150	373.640	374.120	152.960	152.960	152.960
9	375.790	375.550	375.760	168.110	168.090	168.110
10	458.190	458.140	458.180	183.680	183.620	183.670

4.2.5 Effect of number of elements on power flow

The clamped plates containing the crack parallel to the x axis with the length of $0.04\ m$ are modelled with two different mesh refinements (Figure 4.6). These plates have the same geometry and material properties as those mentioned in Section 4.2.3. The cracked plate model on the left consists of 3216 elements and 25728 nodes. The one on the right is the model with the 12168 finer elements and 97344 nodes. The geometry and the location of two cracks on these plates are exactly the same, but their mesh refinements are different. Only the elements around the crack tips of both models are kept consistent. Both cracked plates are excited by the unit excitation force with the frequency of 20 and $100\ Hz$. The location of the excitation force, which is mentioned in the Section 4.2.3, is at the red dot on each model as shown in Figure 4.6. The power flows at the same positions around the crack tips of these two models are integrated using the Trapezoidal rule. The integration path is presented by the black dashed line in Figure 4.7. The results obtained from the integrations are the net power flows around the crack tips.

The net power flows around the crack tips of the cracks on the aforementioned plates are given in Table 4.6. The unit of the net power flows is decibel (dB) with the reference power of $10^{-12}\ W$. The last column of the table is the percentage difference where the net power flows obtained from the plate modelled by 3216 elements are used as the references.

It can be observed from the table that the differences of the net power flows around the crack tips on those two plate models are very small. Thus, it may be proved that the results obtained from the model composing of 3216 elements are sufficiently accurate.

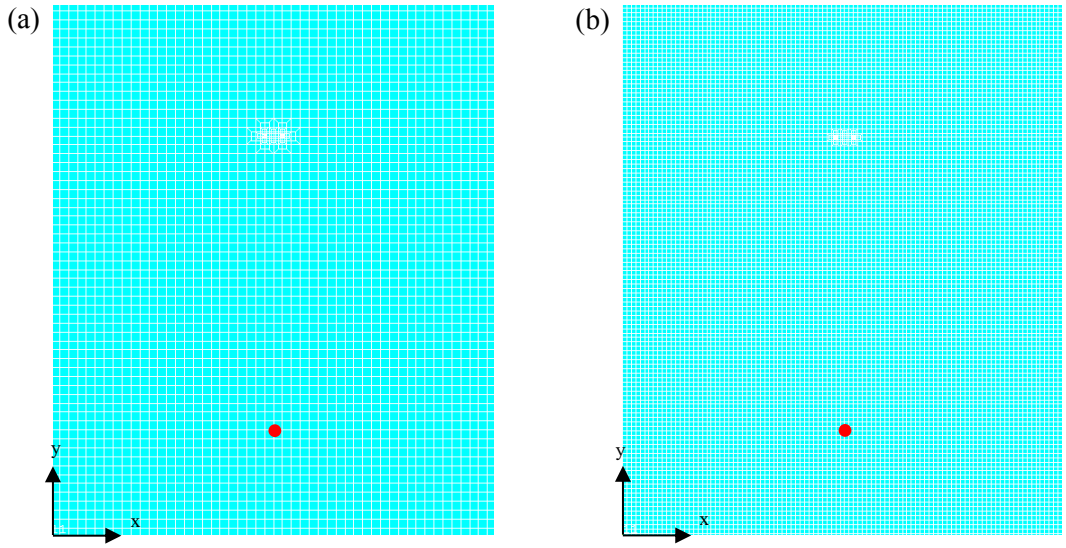

Figure 4.6: Cracked plates modelled with different mesh refinements: (a) 3216 elements; (b) 12168 elements.

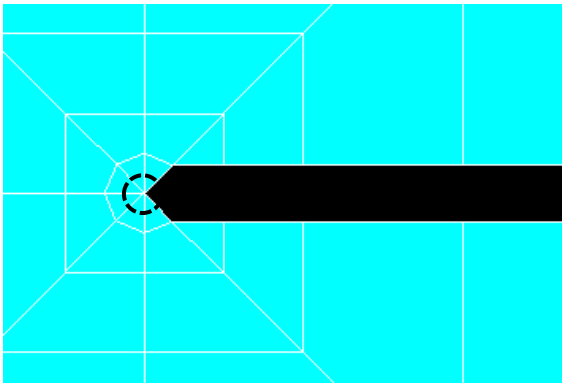

Figure 4.7: Integration path at crack tips.

Table 4.4: Net PF around crack tips of cracked plates modelled by different mesh refinements.

Excitation frequency (Hz)	Plate modelled by 3216 elements (dB)	Plate modelled by 12168 elements (dB)	Percentage difference
20	-1.10269	-1.10252	0.01542%
100	33.46273	33.46310	0.03700%

4.3 Power flow in intact and cracked plates

4.3.1 Power flow in intact plate

In this section, the patterns of the power flow in the intact clamped and cantilever plates are determined and presented through vector field plots. These vector plots are also accompanied by power flow distribution plots illustrating power flow distribution and magnitude at each location of the plates. The plates are subjected to the unit point force with the excitation frequencies of 20 and 100 Hz. These plots are displayed in Figures 4.8 and 4.9.

It can be seen from each vector field plot that the power transmits out of the source or the location of the excitation force, and spreads out to the other locations in the plate. This propagation path of the power is illustrated by the vector arrows. The paths of power transmission in the clamped and cantilever plates are different. For the cantilever plate, the power propagates towards the nearest free edges, and travels along these edges. The power in the clamped plates, in contrast, spreads outward from the source to the whole plates, and most of the power transmits along the centre line of the plate that is perpendicular to the coordinate x axis.

The length of each arrow in each vector plot indicates the magnitude of the power flow. It is noted that the scales of the vector arrows used in the vector plots are not the same. Thus, only the lengths of the arrows in the same plot can be compared to each another. The lengths of the vector arrows of each plate will decrease when the number of the elements used in finite element modelling is increased (see, Cieślik, (2004)). Due to the huge differences between the magnitudes of the power flow at the power sources and those at the other locations of the plates, the directions of the vector arrows at some locations in Figures 4.8 and 4.9, especially those near the plate boundaries far away from the sources, cannot be seen clearly. The zoomed-in versions at the plate boundaries of Figures 4.8 and 4.9 are given in Appendix A.

The magnitudes of the power flow can be observed from the power flow distribution plots. The unit of the magnitudes shown in the colour bars is dB/m with the reference power of $10^{-12}\,W$. The magnitudes of the power flow in both clamped and cantilever plates are highest at the locations of the input forces or the sources of power. The magnitudes

become lower at the distance far away from the sources, due to the structural damping of the plates. For the clamped plates, the high power flow magnitudes are in the middle regions of the plates, and the power flow distributions are symmetric about the centre line perpendicular to the coordinate x axis. The magnitudes of the power flow at the free edges of the cantilever plate are considerably larger than those at the regions near the clamped edges.

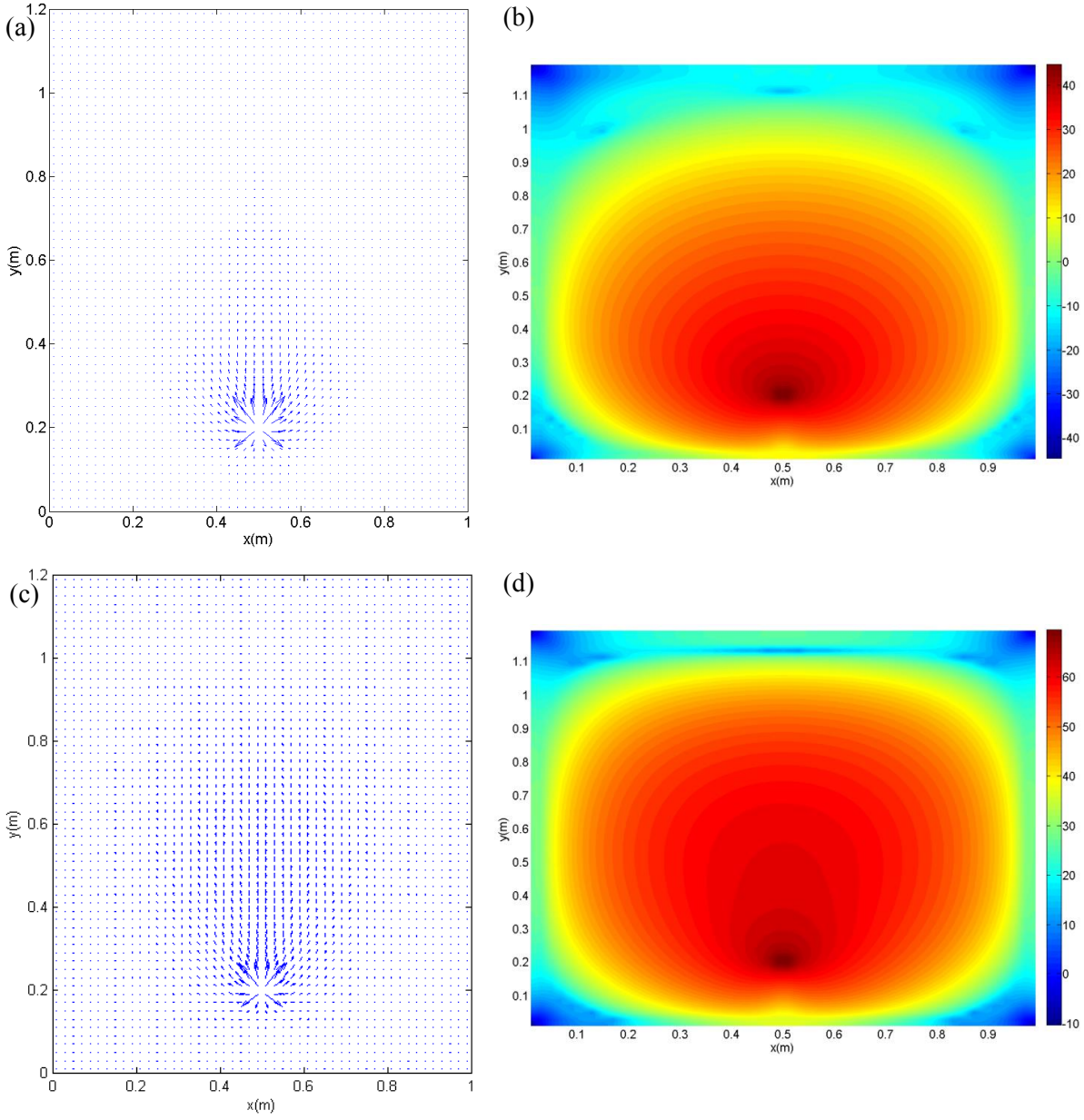

Figure 4.8: PF in the intact clamped plate: (a) PF vector field when $f_e = 20Hz$; (b) PF distribution and magnitude when $f_e = 20Hz$ with colour bar in the unit dB/m with the reference power of $10^{-12}\ W$; (c) PF vector filed when $f_e = 100Hz$; (d) PF distribution and magnitude when $f_e = 100Hz$ with colour bar in the unit dB/m with the reference power of $10^{-12}\ W$.

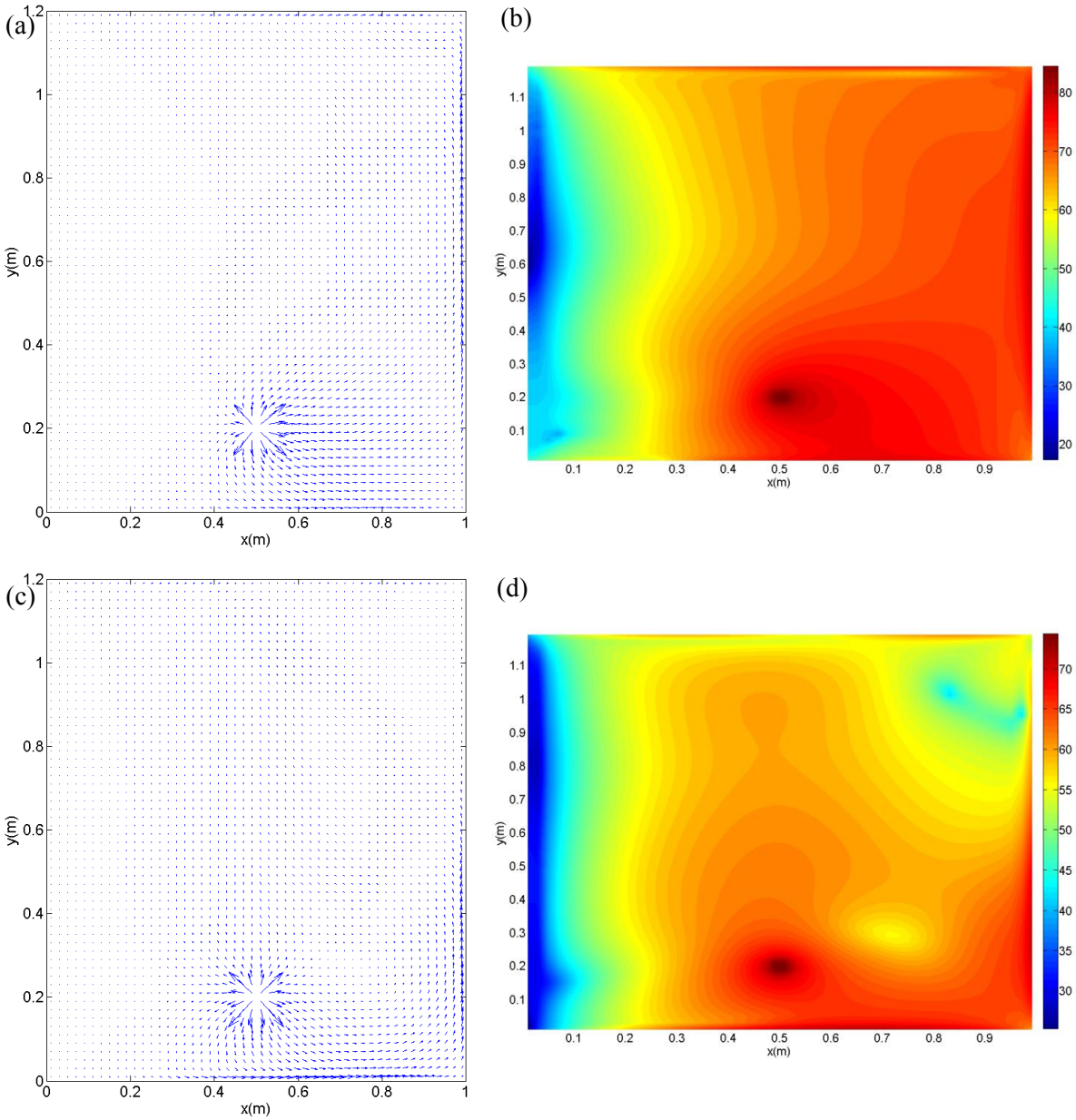

Figure 4.9: PF in the intact cantilever plate: (a) PF vector field when $f_e = 20Hz$; (b) PF distribution and magnitude when $f_e = 20Hz$ with colour bar in the unit dB/m with the reference power of $10^{-12}\ W$; (c) PF vector filed when $f_e = 100Hz$; (d) PF distribution and magnitude when $f_e = 100Hz$ with colour bar in the unit dB with the reference power of $10^{-12}\ W$.

It is also seen that the maximum power flow magnitude of the clamped plate excited by the $20\,Hz$ excitation force is smaller than that of the clamped plate subjected to the $100\,Hz$ force. On the other hand, the highest power flow magnitude in the case of the $20\,Hz$ excitation frequency of the cantilever plate is larger than that of the other. The reason of this can be known when going back to see Tables 4.2 and 4.3. The $20\,Hz$ excitation frequency is close to the second natural frequency of the cantilever plate which is $18.532\,Hz$. Thus, it can produce more power flow than $100\,Hz$ force. For the clamped plates, both 20 and $100\,Hz$ frequencies are off resonance, so the higher frequency can inject more power to the plate.

4.3.2 Power flow in plate with crack parallel to the coordinate x axis

In this section, the through-thickness crack parallel to the coordinate x axis of the plate model is occurred on the plates at the location (0.5, 0.9) as shown in Figure $4.4(a)$. The length of the crack (l) is fixed at $0.01\,m$. The power flow is generated by the excitation frequencies of 20 and $100\,Hz$. The power flow vector filed plots and the power flow distribution plots of the cracked clamped plates are illustrated in Figures 4.10 and 4.11, while those of the cantilever cracked plates are in Figures 4.12 and 4.13. Comparing these vector field plots and the distribution plots of the cracked plates and those of the intact counterparts shows that there are the significant changes in the power flow patterns and magnitudes at the locations of the cracks. However, the patterns and magnitudes of the power flow at the other locations are almost the same. The zoomed-in versions at the plate boundaries of Figures $4.10 - 4.13$ that illustrate the similarities of the power flow directions in intact and cracked plates are given in Appendix A.

The plots (b) in Figures $4.10 - 4.13$ display the zoomed-in versions of the vector field plots at the location of the cracks. It is seen that the power propagates towards the crack tips which are the highest-stress regions, and then propagates out of the tips with the higher magnitudes. The power flow patterns at both tips of each crack in the clamped plate are consistent, whereas those in the cantilevered plate are different. This is due to symmetry of the boundary conditions of the clamped plates, and the positions of the excitation forces.

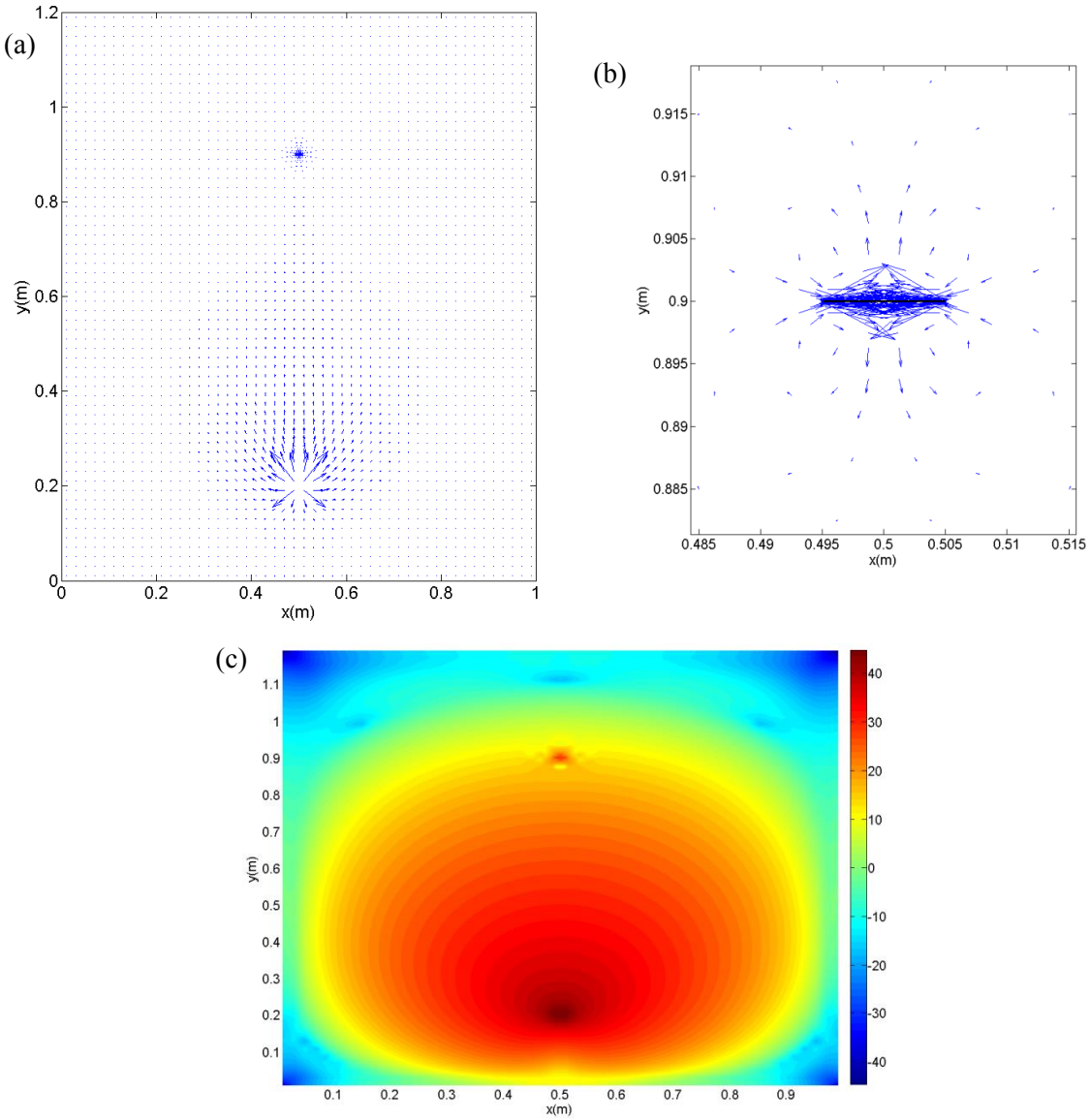

Figure 4.10: PF in the clamped plate with crack parallel to the x axis at $f_e = 20\ Hz$: (a) PF vector filed plot; (b) zoomed-in version at crack location; (c) distribution plot of PF magnitude with colour bar in the unit dB/m with the reference power of $10^{-12}\ W$.

The magnitudes of the net power flow at the cross section around the excitation force and those around the tips of the cracks are given in Tables 4.5 and 4.6. For the cracks parallel to the coordinate x axis, the crack tips will be labelled as the *left* and *right crack tips*, hereinafter. When observing the results in Table 4.5, it is seen that the presence of the cracks does not highly affect the magnitudes of the net power flow around the excitation force, since the values of the net power flow in the intact and cracked plates are approximately the same.

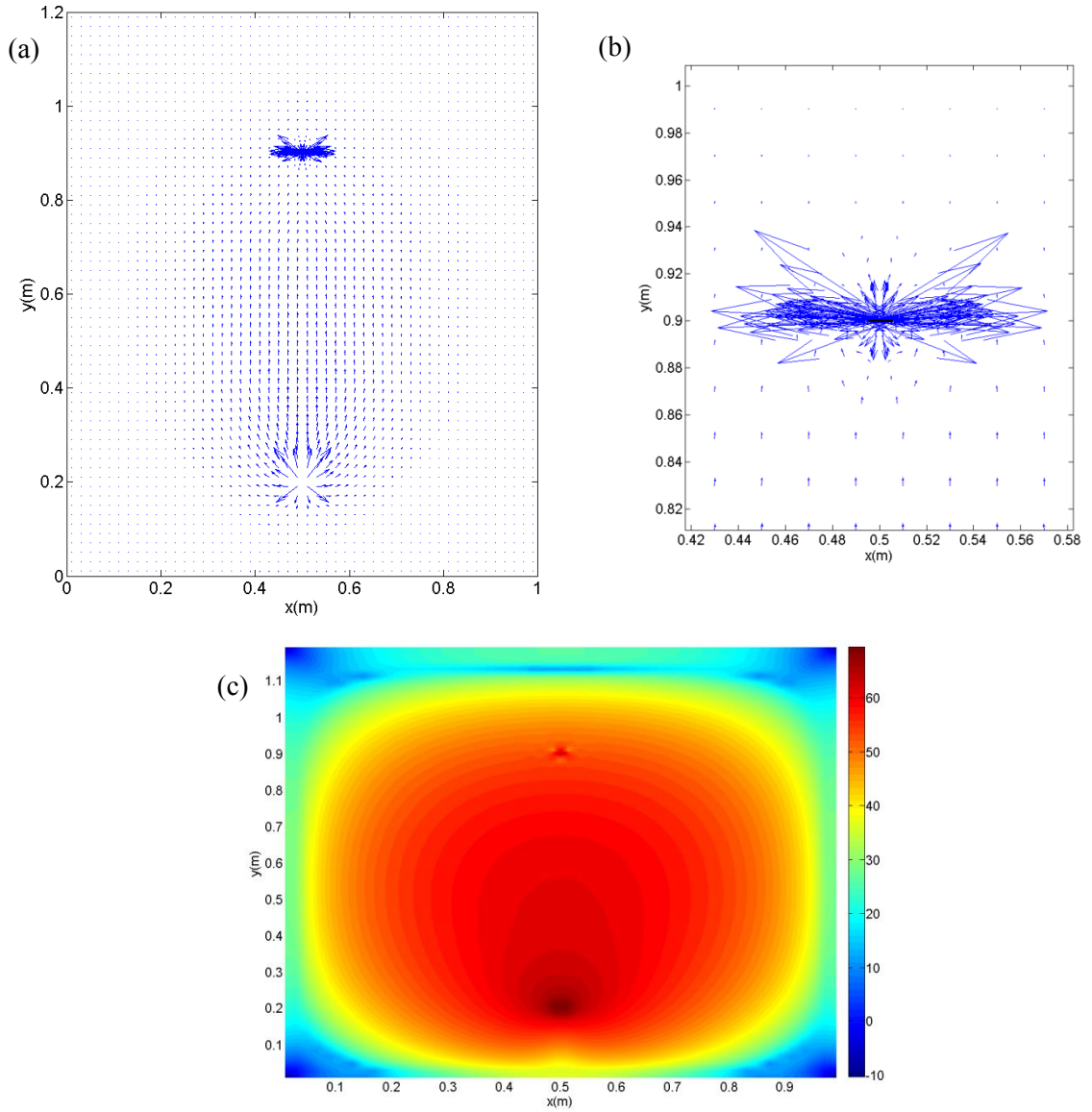

Figure 4.11: PF in the clamped plate with crack parallel to the x axis when $f_e = 100\ Hz$: (a) PF vector field plot; (b) zoomed-in version at crack location; (c) distribution plot of PF magnitude with colour bar in the unit dB/m with the reference power of $10^{-12}\ W$.

Table 4.5: Net PF around excitation force of intact plates and plates with crack parallel to the x axis.

Excitation frequency	**Net PF in clamped plate (dB)**		**Net PF in cantilever plate (dB)**	
	Intact	**l = 0.01m**	**Intact**	**l = 0.01m**
20 Hz	33.015	33.016	72.876	72.886
100 Hz	57.702	57.693	62.966	62.956

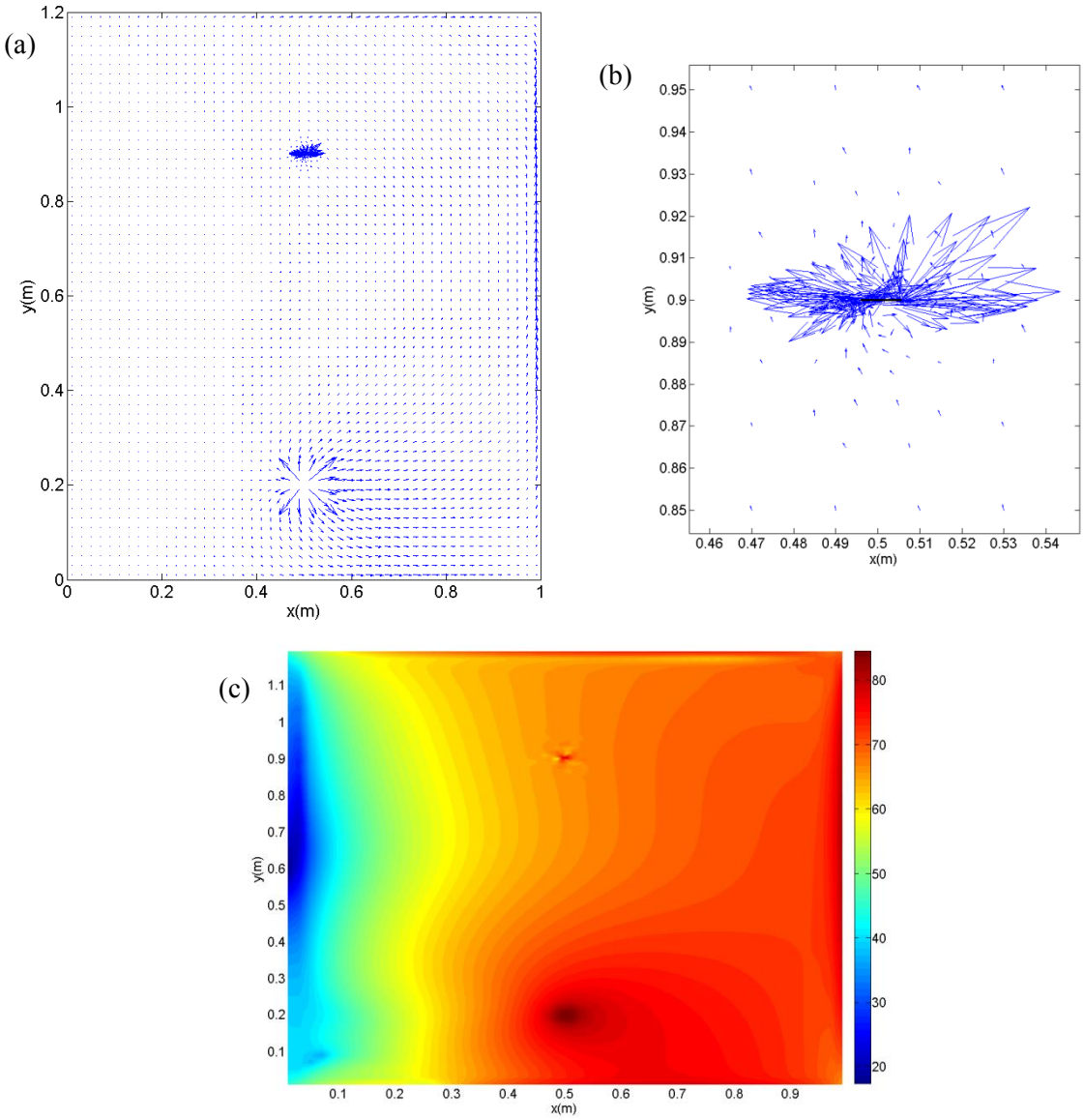

Figure 4.12: PF in the cantilever plate with crack parallel to the x axis when $f_e = 20\ Hz$: (a) PF vector field plot; (b) zoomed-in version at crack location; (c) distribution plot of PF magnitude with colour bar in the unit dB/m with the reference power of $10^{-12}\ W$.

Table 4.6 indicates that the net power flow at the left and the right crack tips of the clamped plates excited by both excitation frequencies are the same, due to the symmetries of the plate boundary condition and the locations of the input forces as stated before. The net power flow at the left and the right tips of the cantilever plates are, on the other hand, not the same. The values of the net power flow calculated at the same locations as those of the crack tips are given in Table 4.7. It is seen that these values are smaller than those of the cracked plates shown in Table 4.6. Thus, these local changes of the net power flow can also be used to pinpoint the crack locations.

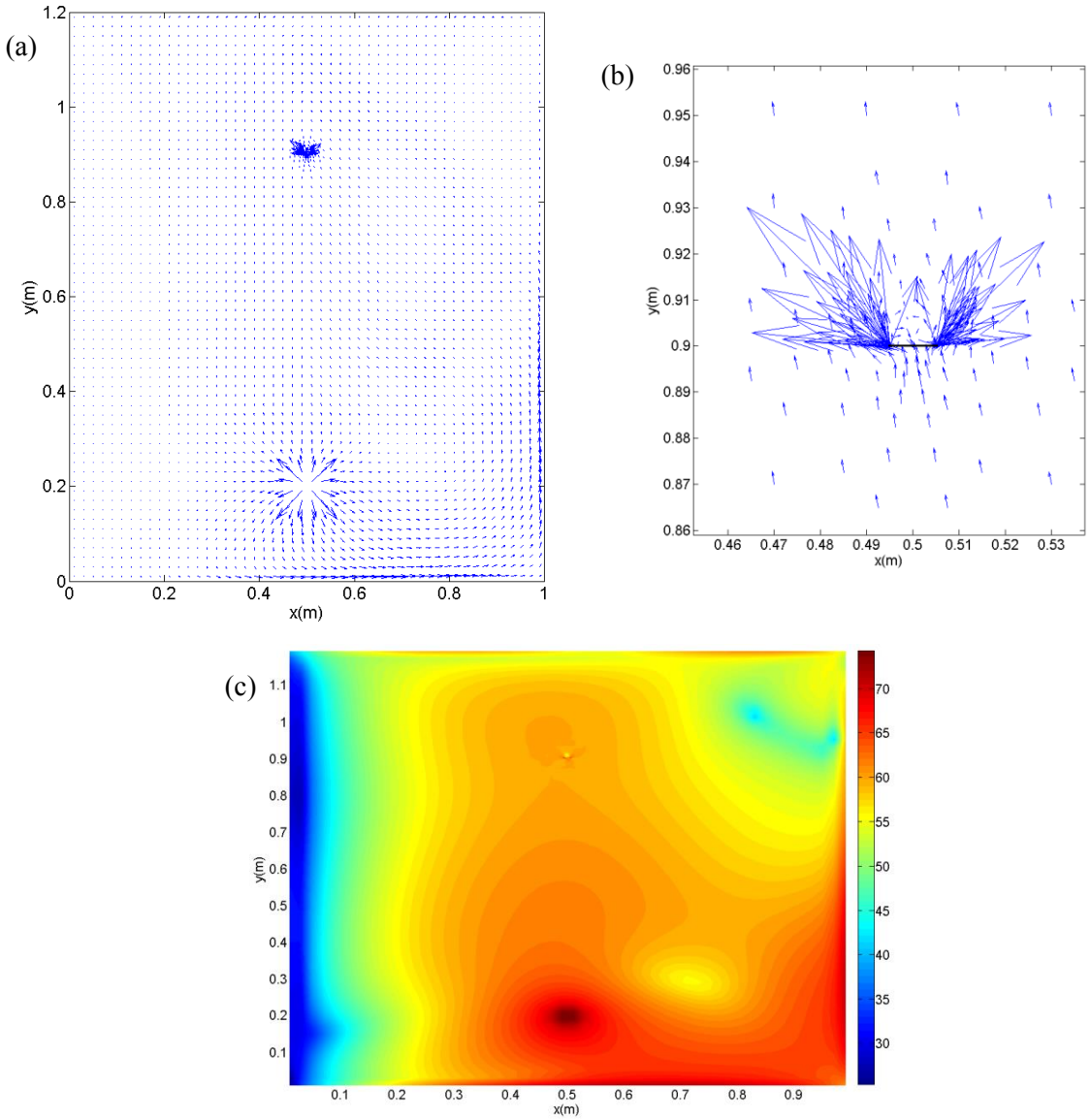

Figure 4.13: PF in the cantilever plate with crack parallel to the x axis when $f_e = 100\ Hz$: (a) PF vector field plot; (b) zoomed-in version at crack location; (c) distribution plot of PF magnitude with colour bar in the unit dB/m with the reference power of $10^{-12}\ W$.

Table 4.6: Net PF around crack tips of plates with crack parallel to the x axis: left and right values in bracket are power flows at left and right crack tips.

Excitation frequency	Net PF in clamped plate (dB)		Net PF in cantilever plate (dB)	
	Left tip	Right tip	Left tip	Right tip
20 Hz	-4.282	-4.282	38.460	42.189
100 Hz	30.282	30.282	32.604	31.702

Table 4.7: Net PF in intact plates computed at the same locations as those of crack tips (crack parallel to the x axis)

Excitation frequency	Net PF in clamped plate (dB)		Net PF in cantilever plate (dB)	
	Left tip location	**Right tip location**	**Left tip location**	**Right tip location**
20 Hz	-24.007	-24.007	29.004	29.171
100 Hz	15.615	15.615	22.746	22.714

4.3.3 Power flow in plate with crack perpendicular to coordinate x axis

The orientation of the $0.01\,m$ cracks is now changed to being perpendicular to the coordinate x axis of the plates. The orders of the mesh at the region around the cracks are analogous to those of the cracks parallel to the x axis in Section 4.5.2. The location of the unit force with the frequencies of 20 and 100 Hz is fixed at the same place as before. The vector and power distributions plots of the power flows are displayed in Figures 4.14 – 4.17.

Similar to the results of the cracks parallel to the x axis, the patterns of the power flow shown in the vector filed and the power distribution plots change considerably at the location of the cracks. From the vector field plots, it is observed that the power propagates to both crack tips of each crack and then propagates out of the tips with higher magnitudes. The power flow patterns at the regions far from the cracks of the clamped and cantilever plates are not significantly changed when compared to those of the intact counterparts. Comparing the zoomed-in versions of the vector filed plots of the cracks parallel and perpendicular to the x axis show that the changes in the power flow patterns can be inspected more clearly when the cracks are parallel to the x axis.

The net power flow around the input forces is given in Table 4.8. The value of each case is approximately the same as those of the intact plate and the plate with the crack parallel to the x axis. Table 4.9 presents the net power flow around the crack tips of the clamped and cantilever plates. Two crack tips of the crack perpendicular to the x axis are designated as *lower* and *upper crack tips*. The lower crack tip of each clamped plates, which is closer to the excitation force, has the larger net power flow than that belonging to the upper tip. The net power flow of both upper and lower tips of the same crack on each cantilever plate are comparable. This is due to the power flow paths of the clamped and cantilever plates which are different. The power propagation paths of the clamped plates excited by both 20 and 100 Hz forces are perpendicular or parallel to the crack lines. In contrast, the power in the

cantilever plates does not directly go to the locations of the cracks. It transmits out of the sources and goes along the nearest free boundaries before propagating to the crack locations.

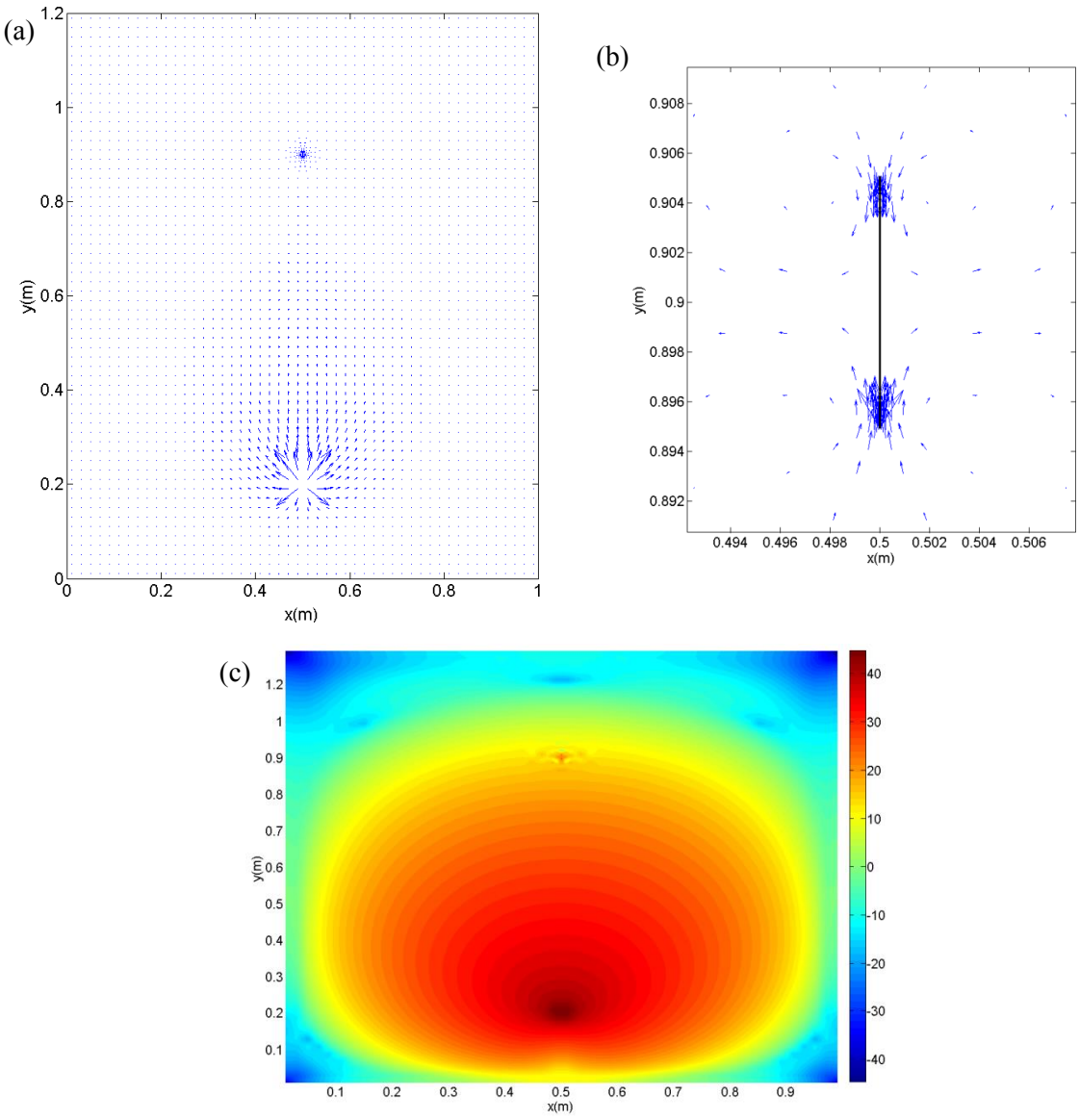

Figure 4.14: PF in the clamped plate with crack perpendicular to the x axis when $f_e = 20\ Hz$: (a) PF vector field plot; (b) zoomed-in version at crack location; (c) distribution plot of PF magnitude with colour bar in the unit dB/m with the reference power of $10^{-12}\ W$.

Table 4.8: Net PF around excitation force of plates with crack perpendicular to the x axis.

Excitation frequency	Net PF in clamped plate (dB)	Net PF in cantilever plate (dB)
20 Hz	33.016	72.886
100 Hz	57.369	62.955

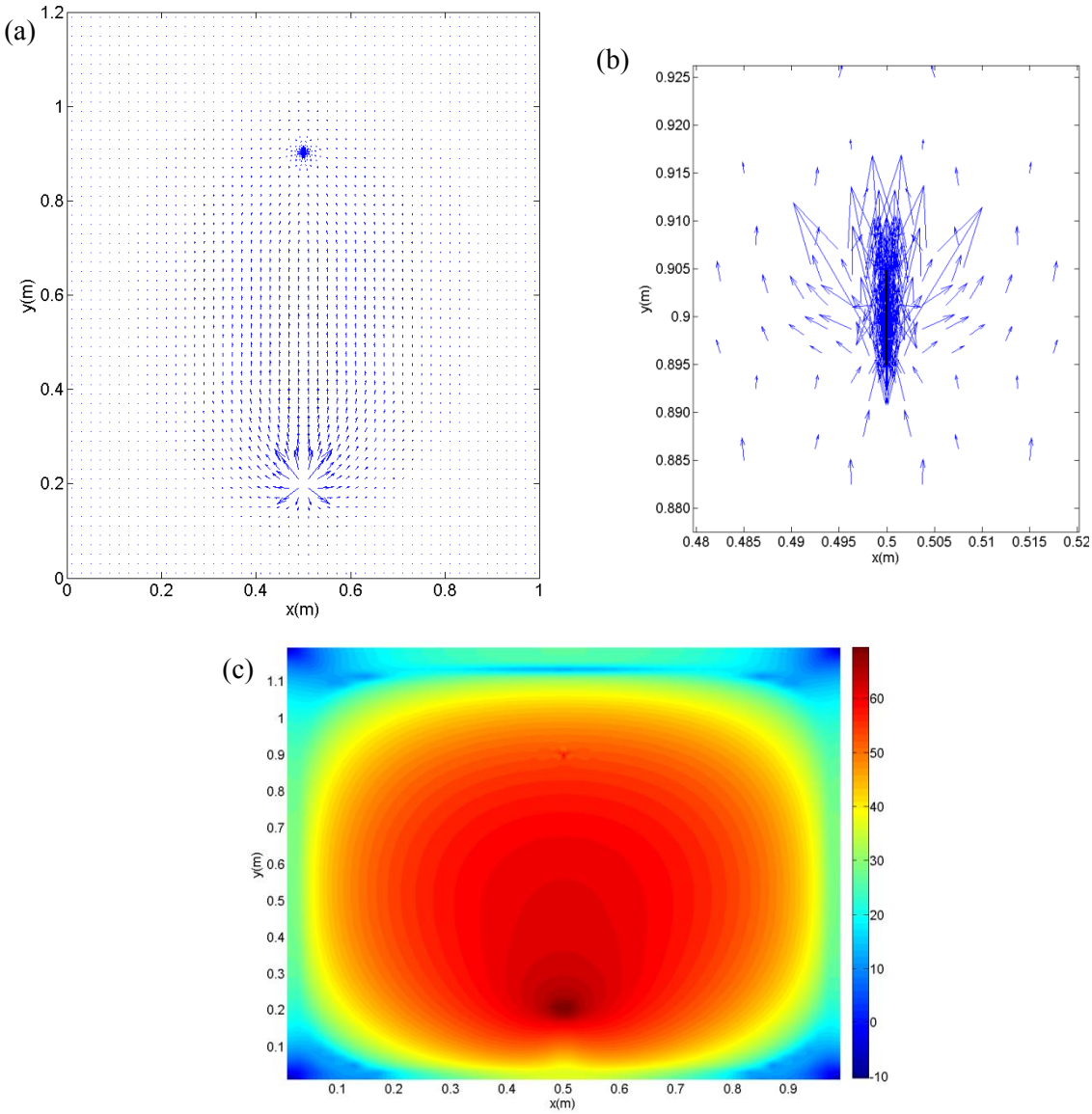

Figure 4.15: PF in the clamped plate with crack perpendicular to the x axis when $f_e = 100\ Hz$: (a) PF vector field plot; (b) zoomed-in version at crack location; (c) distribution plot of PF magnitude with colour bar in the unit dB/m with the reference power of $10^{-12}\ W$.

Table 4.9: Net PF around crack tips of plates with crack perpendicular to the x axis.

Excitation frequency	Net PF in clamped plate (dB)		Net PF in cantilever plate (dB)	
	Lower tip	Upper tip	Lower tip	Upper tip
20 Hz	-10.000	-12.663	44.154	43.916
100 Hz	25.262	21.791	27.886	26.732

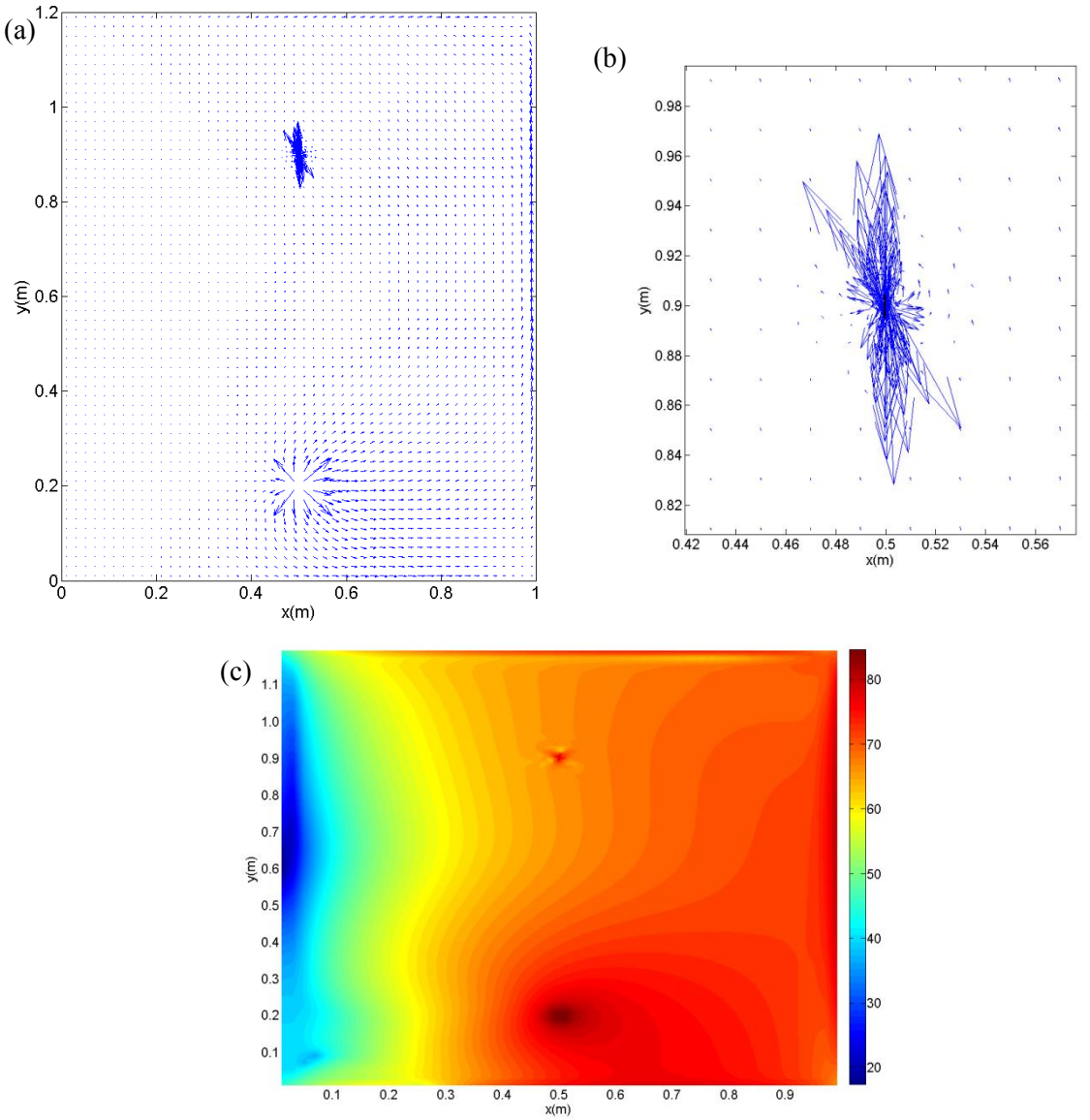

Figure 4.16: PF in the cantilever plate with crack perpendicular to the x axis when $f_e = 20\ Hz$: (a) PF vector field plot; (b) zoomed-in version at crack location; (c) distribution plot of PF magnitude with colour bar in the unit dB/m with the reference power of $10^{-12}\ W$.

Table 4.10: Net PF in intact plates computed at the same locations as those of crack tips (crack perpendicular to the x axis)

Excitation frequency	Net PF in clamped plate (dB)		Net PF in cantilever plate (dB)	
	Lower tip location	Upper tip location	Lower tip location	Upper tip location
20 Hz	-23.831	-24.280	29.050	29.152
100 Hz	15.831	15.385	22.728	22.736

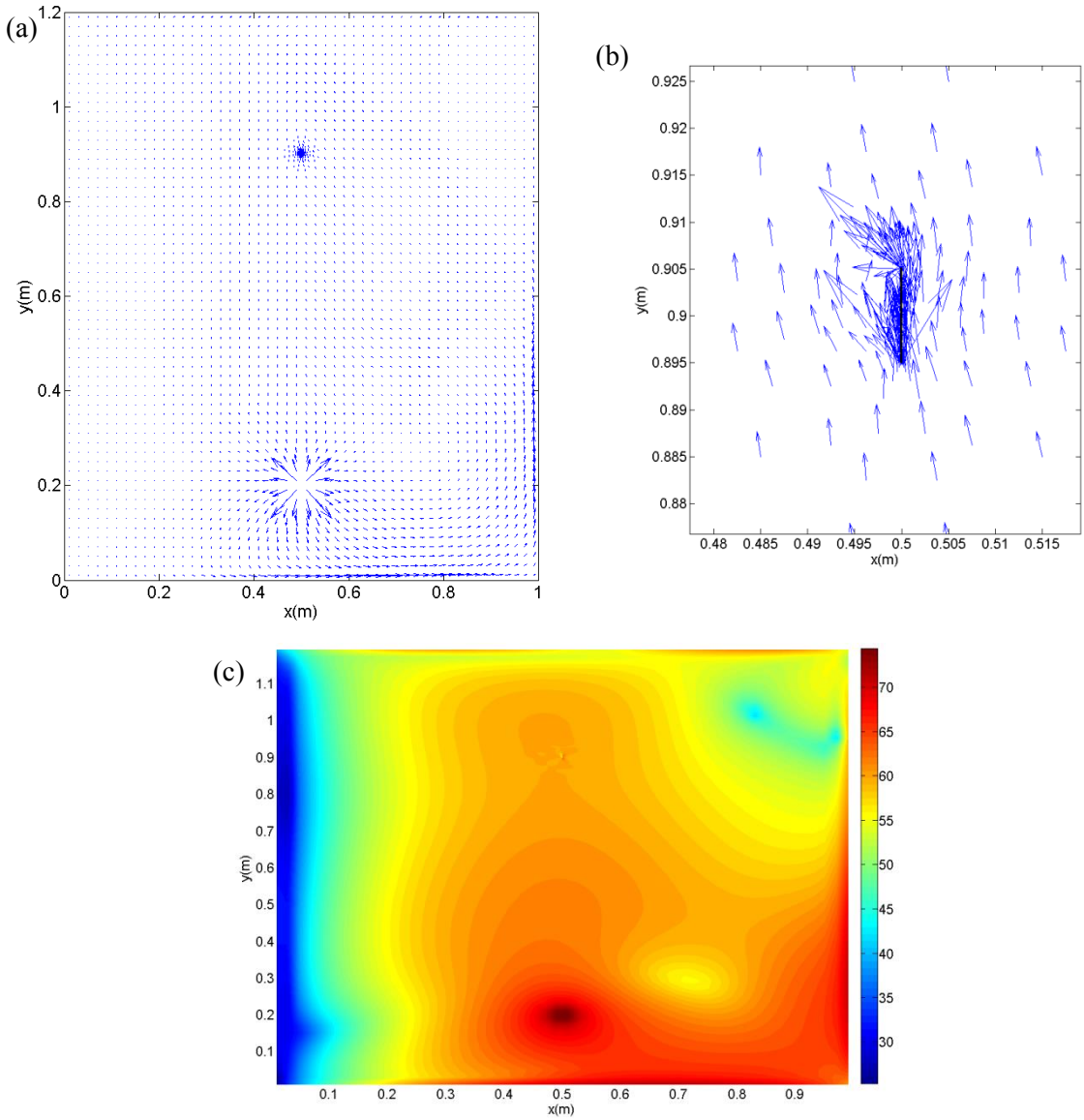

Figure 4.17: PF in the cantilever plate with crack perpendicular to the x axis when $f_e = 100\ Hz$: (a) PF vector field plot; (b) zoomed-in version at crack location; (c) distribution plot of PF magnitude with colour bar in the unit dB/m with the reference power of $10^{-12}\ W$.

Table 4.10 shows the values of the net power flow in the intact plates computed at the same locations to those of the crack tips of the cracks perpendicular to the x axis. It can be seen that these values are less than those of the cracked plates given in Table 4.9, so the crack locations can be known by these local changes of the net power flow, apart from the power flow plotted in the vector and surface plots as shown in Figures $4.14 - 4.17$.

4.3.4 Effect of excitation frequency on magnitude of net power flow

Previously, the power flow results are obtained from the cracked plates subjected to two fixed excitation frequencies of 20 and 100 Hz. In this section, the net power flow around the input forces and around the crack tips, when the clamped and cantilever plates are excited by the unit force with the excitation frequency varied from 0 to 150 Hz, are computed. This aims to observe the trends of the net power flow when the excitation frequency is varied.

As indicated in Figure 4.18, the net power flow is large when the plates are excited by the frequency equal to one of the natural frequencies. There are two modes of the clamped plate and seven modes of the cantilever plate in the range of the frequencies from 0 to 150 Hz. The 6^{th} and 7^{th} modes of the cantilever plates are close to each other as seen from Tables 4.2 and 4.3. It is also shown in the figure that the differences between the net power flow around the input forces of the intact and cracked plates are very small. These results can prove that the net power flow around the input forces is not affected much by the presence of the cracks.

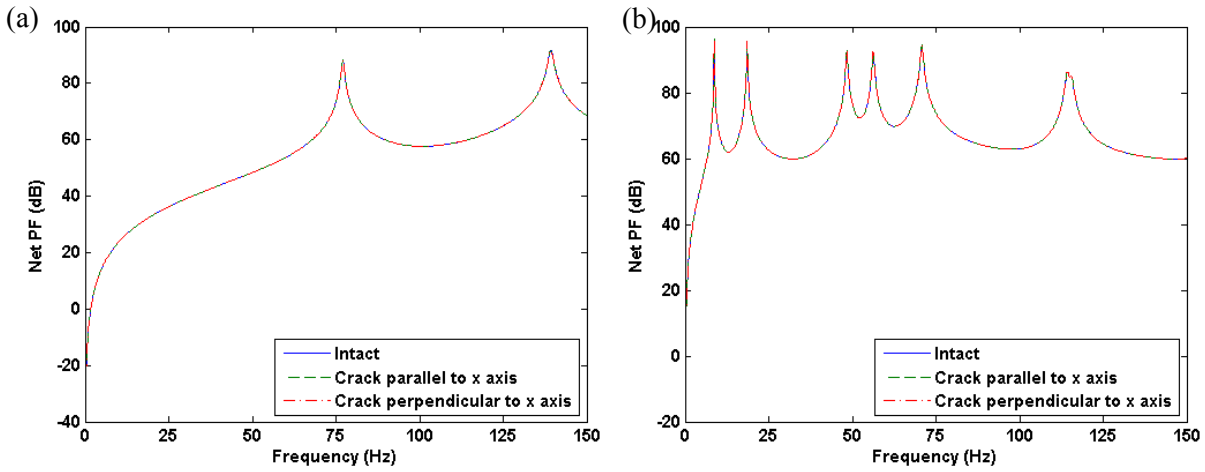

Figure 4.18: Net PF around excitation force when $f_e = 0 - 150\ Hz$: (a) clamped plate; (b) cantilever plate.

Figures 4.19 and 4.20 illustrate the net power flow around the crack tips of the cracked clamped and cantilever plates, respectively. The trends of the net power flow when the excitation frequency increases from 0 to 150 Hz are similar to those around the input forces mentioned previously. The highest net power flow around the crack tips of each mode occur at the excitation frequencies equal to the natural frequencies of that mode. This can show the reason why the power flow generated by the 20 Hz force in the cantilever plate,

presented in Sections 4.3.2 and 4.3.3, are larger than those created by the force with the frequency of $100\,Hz$. The $20\,Hz$ excitation frequency is close to the second natural frequency of the cantilever plates as shown in the graph.

It can be observed from Figure 4.19 that at every excitation frequency, the net power flow around the tip of the crack parallel to the x axis is largest. This is followed by that of the lower tip of the crack perpendicular to the x axis. The smallest one is of the upper tip of the crack perpendicular to the x axis which locates farthest from the power source. If the direction of the power flow is used as a reference for the crack orientation instead of the coordinate x axis, we can state that the crack perpendicular to the power propagation direction (parallel to the x axis) has higher net power flow at the tips than the one parallel to the power propagation direction (perpendicular to the x axis).

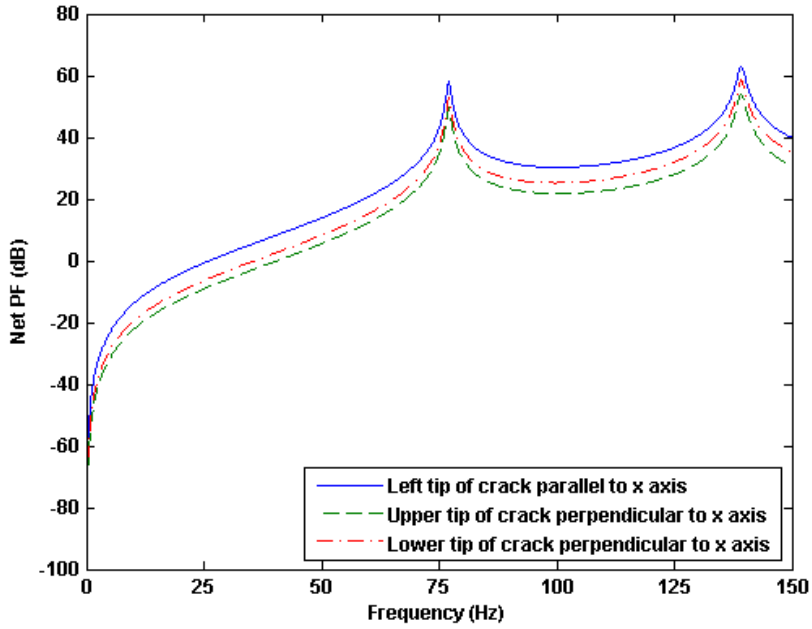

Figure 4.19: Net PF around crack tips of clamped plates when $f_e = 0 - 150\,Hz$.

As detailed in Figure 4.20, at the very low frequencies, the net power flow of all crack tips are almost equal. After the first natural frequency, the magnitudes of the net power flow around the tips of the cracks in both orientations are more or less than each other depending on the excitation frequency and mode shape. This is different from the net power flow around the tips of the clamped plates, which have the consistency of the trends through the range of the excitation frequencies.

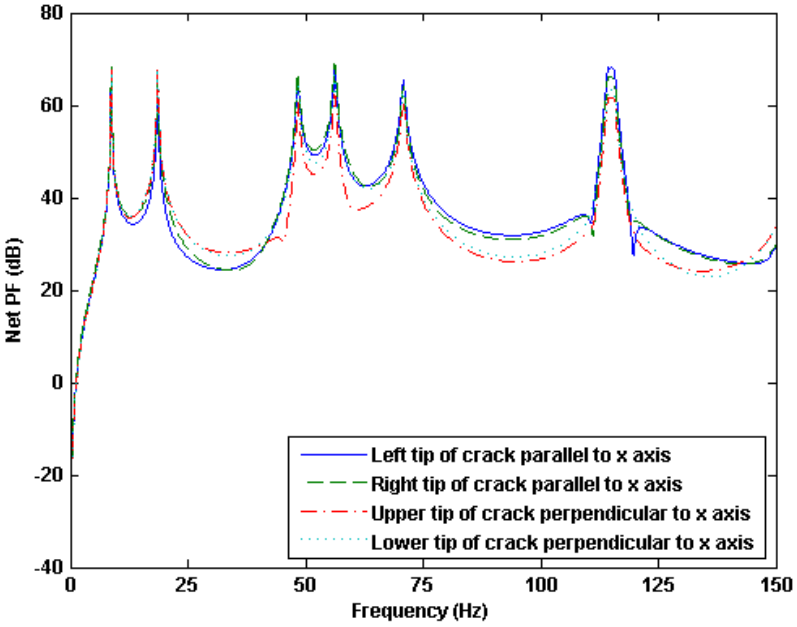

Figure 4.20: Net PF around crack tips of cantilever plates when $f_e = 0 - 150\ Hz$.

4.3.5 Effects of crack length on power flow at crack tips

In this section, the investigation of how the length of the crack can affect the net power flow at the crack tips is presented. The positions of the cracks, orientated parallel and perpendicular to the x coordinate of the plate, and the excitation force are fixed at (0.5, 0.9) and (0.5, 0.2), respectively. The lengths of the cracks (l) are $0.01\,m$, $0.04\,m$ and $0.12\,m$. The finite element models of the plates containing $0.12\,m$ cracks parallel and perpendicular to the x axis are presented in Figure 4.21. The excitation frequencies of the unit input force are varied from 0 to 150 Hz.

It can be observed from Figure 4.22 that the tips of the $0.12\,m$ crack parallel to the x axis have the larger net power flow than the other two. The lowest net power flow is of the $0.01\,m$ crack, which is the shortest one. This trend also occurs for the case of the cracks perpendicular to the x axis presented in Figures 4.23 and 4.24. Some of the numerical values of the net power flow at these crack tips are presented in Tables 4.11 and 4.12.

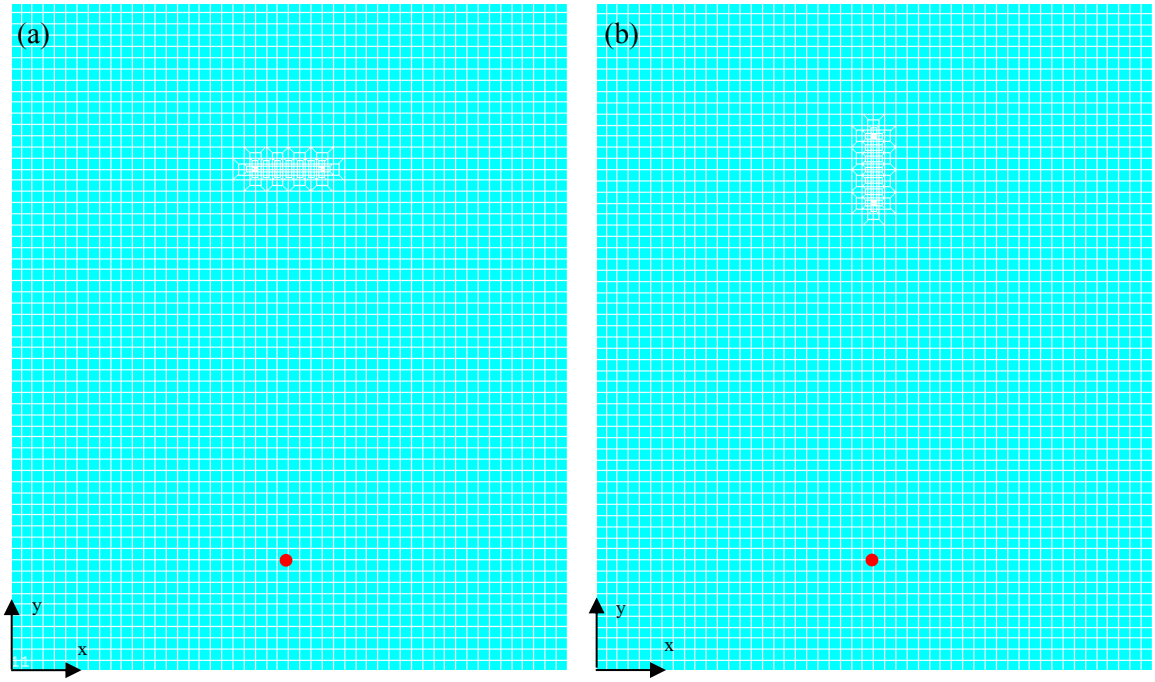

Figure 4.21: Model of plate containing 0.12 m cracks: (a) crack parallel to the x axis; (b) crack perpendicular to the x axis.

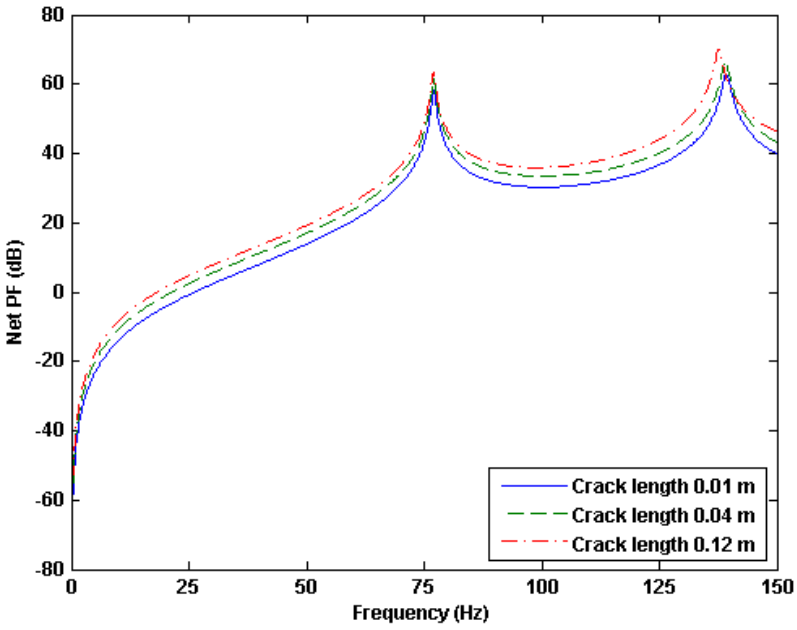

Figure 4.22: Net PF around crack tips of 0.01 m, 0.04 m and 0.12 m cracks parallel to the x axis on clamped plates when $f_e = 0 - 150\ Hz$.

Table 4.11: Net PF around crack tips on clamped plate when crack length is varied (crack parallel to the x axis).

Crack length (m)	Crack tip	Net PF around crack tip of crack parallel to the x axis (dB)						
		20 Hz	**77 Hz**	**100 Hz**	**139 Hz**	**150 Hz**	**173 Hz**	**200 Hz**
0.01	Left	-4.282	58.306	30.282	62.751	39.990	32.815	33.493
0.01	Right	-4.282	58.306	30.282	62.751	39.990	32.815	33.493
0.04	Left	-1.103	61.467	33.463	66.548	43.396	36.741	37.944
0.04	Right	-1.103	61.467	33.463	66.548	43.396	36.741	37.944
0.12	Left	1.182	63.570	59.441	63.183	46.545	41.375	43.428
0.12	Right	1.182	63.570	59.441	63.183	46.545	41.375	43.428

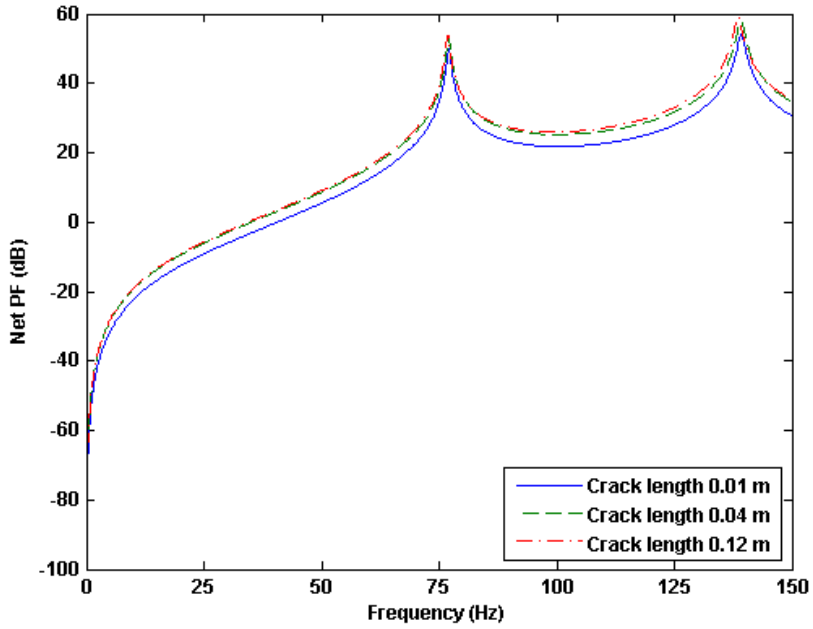

Figure 4.23: Net PF around upper tips of 0.01 m, 0.04 m and 0.12 m cracks perpendicular to the x axis on clamped plates when $f_e = 0 - 150\ Hz$.

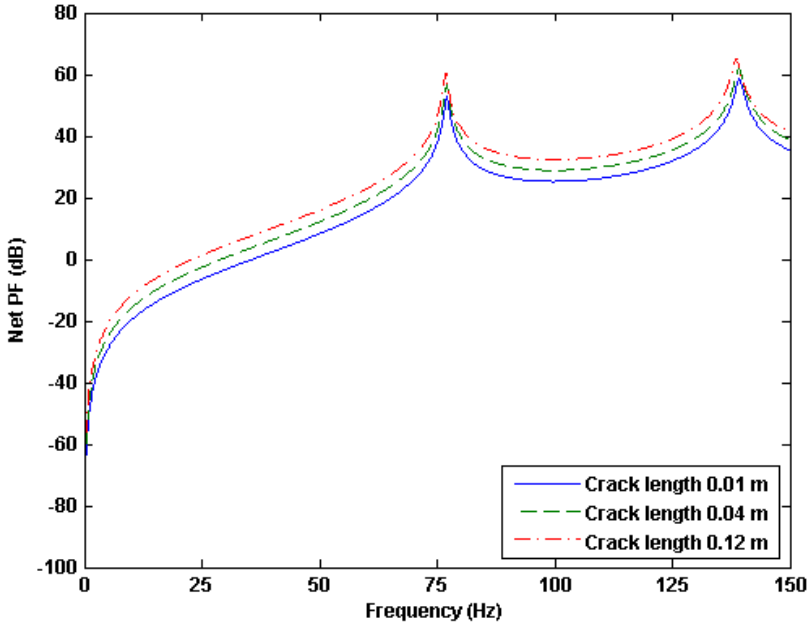

Figure 4.24: Net PF around lower tips of 0.01 m, 0.04 m and 0.12 m cracks perpendicular to the x axis on clamped plates when $f_e = 0 - 150\ Hz$.

Table 4.12: Net PF around crack tips on clamped plate when crack length is varied (crack perpendicular to the x axis).

Crack length (m)	Crack tip	Net PF around at crack tip of crack perpendicular to the x axis (dB)						
		20 Hz	77 Hz	100 Hz	139 Hz	150 Hz	173 Hz	200 Hz
0.01	Upper	-12.663	49.913	21.791	53.730	30.748	22.681	21.121
0.01	Lower	-10.000	53.022	25.262	58.093	35.445	28.283	28.684
0.04	Upper	-9.598	53.230	25.233	57.845	34.701	27.136	26.655
0.04	Lower	-6.113	56.788	28.872	61.735	38.700	31.457	31.720
0.12	Upper	-9.228	52.695	26.005	57.607	35.520	28.627	28.846
0.12	Lower	-2.227	59.299	32.355	63.524	41.329	34.280	34.553

4.4 Summary

This chapter investigates the characteristics and the behaviours of the power flow in the intact plates and the plates containing a through-thickness crack. From all of the results presented in the chapter, it can be summarised as follows:

- The power transmits outward from the source at the location of the excitation force
- The direction of the power transmission path is dependent on the excitation frequency and plate boundary condition.
- The power transmits smoothly throughout the intact plate. The pattern of the power flow is dependent on plate boundary conditions
- When the cracks occur on the plates, the patterns and magnitudes of the power flow at the regions around the cracks change considerably from those of the intact counterparts, while those at the other regions show only the very small changes.
- The power transmits to the crack tip and propagates out of the tips with a higher magnitude.
- The transmission path of the power can affect the patterns and magnitudes of the power flow at the crack locations. The diversion of power flow at the crack tips can be inspected more clearly when the transmission path is perpendicular to the crack.
- The length of the crack can affect the magnitude of the power flow at the crack tips.
- The power flow is large when the plates are excited by one of the natural frequencies.

The results obtained from this chapter can confirm the potential of the power flow to detect damage on a structure.

Chapter 5

Power flow characteristics of thin plates with multiple cracks

5.1 Introduction

This chapter investigates the pattern and magnitude of the power flow when more than one crack appears on the plates. Similar to Chapter 4, the vector field and power distribution plots are employed as tools to display the power flow patterns and magnitudes at the locations of the cracks and the others on the plates. The trends of the net power flow, when the excitation frequency is varied are also studied. Differences in the power flow in single- and multiple-cracked plates are discussed.

5.2 Power flow patterns and distributions

5.2.1 Cracks parallel to coordinate *x* axis

Two identical cracks parallel to the coordinate x axis are simulated on the plate at the positions (0.5, 0.9) which is designated as *first crack* and (0.5, 1.06) which is *second crack*. The first crack is located at the same position as that of the single-cracked plates (Figure 4.4). The locations of the cracks are taken from the middle points of the crack lines. The plate geometry, material properties, and location of the excitation force are analogous to those used in Chapter 4. The model of the plate containing these two cracks are given in Figure 5.1. The same as those used in Chapter 4, the word *power flow (PF)* will represent the time-average power flow per unit length, and the word *net power flow (net PF)* will be the net power transmitting through the cross section of the plate obtained from the numerical integration through the length of the cross section.

The vector and power distribution plots of the clamped plate containing two cracks parallel to the x axis is shown in Figure 5.2. The plate is excited by the $20\ Hz$ force. It is seen that the locations of both cracks can be revealed by the power flow. From (b) and (c) of Figure 5.2 which are the zoomed-in versions of the vector plot, we can inspect the lengths of the power flow vectors and their propagation directions in the regions near the cracks. The behaviours of the power flow vectors around the first crack are almost the same as that of the single crack plate illustrated in Figure 4.10. The zoom-in levels of (b) and (c) are equal, so the lengths of the vector arrows representing the magnitude of the power flow in these plots can be compared to each other. From the comparison, it is clear that the magnitude of the power flow at each point in the area close to the first crack is larger than that of the second crack. These trends also happen when the same plate is subjected to the $100\ Hz$ force (Figure 5.3). The zoom-in level of (c) in Figure 5.3 is higher than that of (b) of the same figure, so the vector arrow at each point shown in (c) is longer than that in (b). However, when we inspect (a) in Figure 5.3, it can be seen clearly that the length of the vector arrow at each point around the first crack is much larger than that around the second crack.

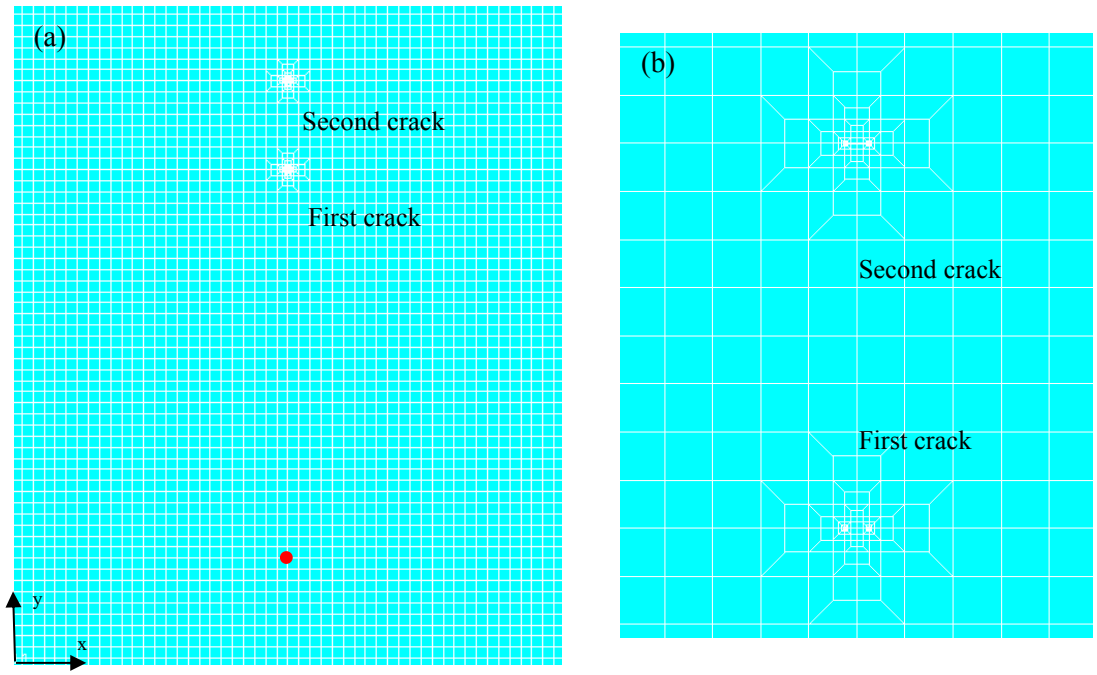

Figure 5.1: Model of plate with two cracks parallel to the x axis: (a) overall plate with red dot representing location of excitation force; (b) at crack locations (higher-order mesh refinement).

The magnitudes of the net power flow around the input force and the crack tips of the cases mentioned above are given in Tables 5.1 and 5.2. Unsurprisingly, the values of the net

power flow around the first crack are larger than those at the second crack. When comparing the results in Table 5.1 and 5.2 to those of the single cracked plate in Tables 4.5 and 4.6, it is seen that magnitudes of the net power flow around the input forces of single- and double-cracked plates are the same. The magnitudes of the net power flow around the tips of the first crack and those around the tips of the crack in the single cracked plates are slightly different.

The power flow calculation is also performed in the case of the cantilever plate containing two identical cracks parallel to the x axis. The results are presented in Figure 5.4 for the 20 Hz excitation force and Figure 5.5 for the 100 Hz force. It is revealed by the vector plots and their zoomed-in versions that the difference of the power flow magnitudes in the regions close to the first and second cracks is small when compared to that of the clamped plates. Inspection of (a), (b) and (c) in Figures 5.4 and 5.5 also indicates that the propagation paths of the power flow are not symmetric, so the power flow at the crack tips of each crack is not uniform. The differences of the net power flow values around the tips of the first and second cracks are small. Comparing the results in Tables 5.3 and 5.4 to those of the cantilever plates in Tables 4.5 and 4.6 shows that the magnitude of the net power flow around the input force and around the crack tips of the cantilever plates with one and two cracks are marginally different.

The zoomed-in versions at the plate boundaries of the vector plots in Figures 5.2 – 5.5 are displayed in Appendix A. It can be seen that only the power flow directions at the areas close to the second cracks are changed. At the other regions in these plots, the power flow directions are approximately the same as those in the corresponding intact plates.

Table 5.5 contains the results of the net power flow in the intact clamped and cantilever plates computed at the same locations as those of the tips of the second cracks at the location (0.5, 1.06). It can be observed when comparing these results to those in Tables 5.1 – 5.4 that the values of the net power flow at the crack tips are higher than those at the same locations on the corresponding intact plates. The values of the net power flow calculated at the same locations as those of the tips of the first cracks were previously presented in Table 4.7. The changes of the net power flow at the crack tips can also be used to locate the crack location, besides the power flow presented through the vector and power distribution plots.

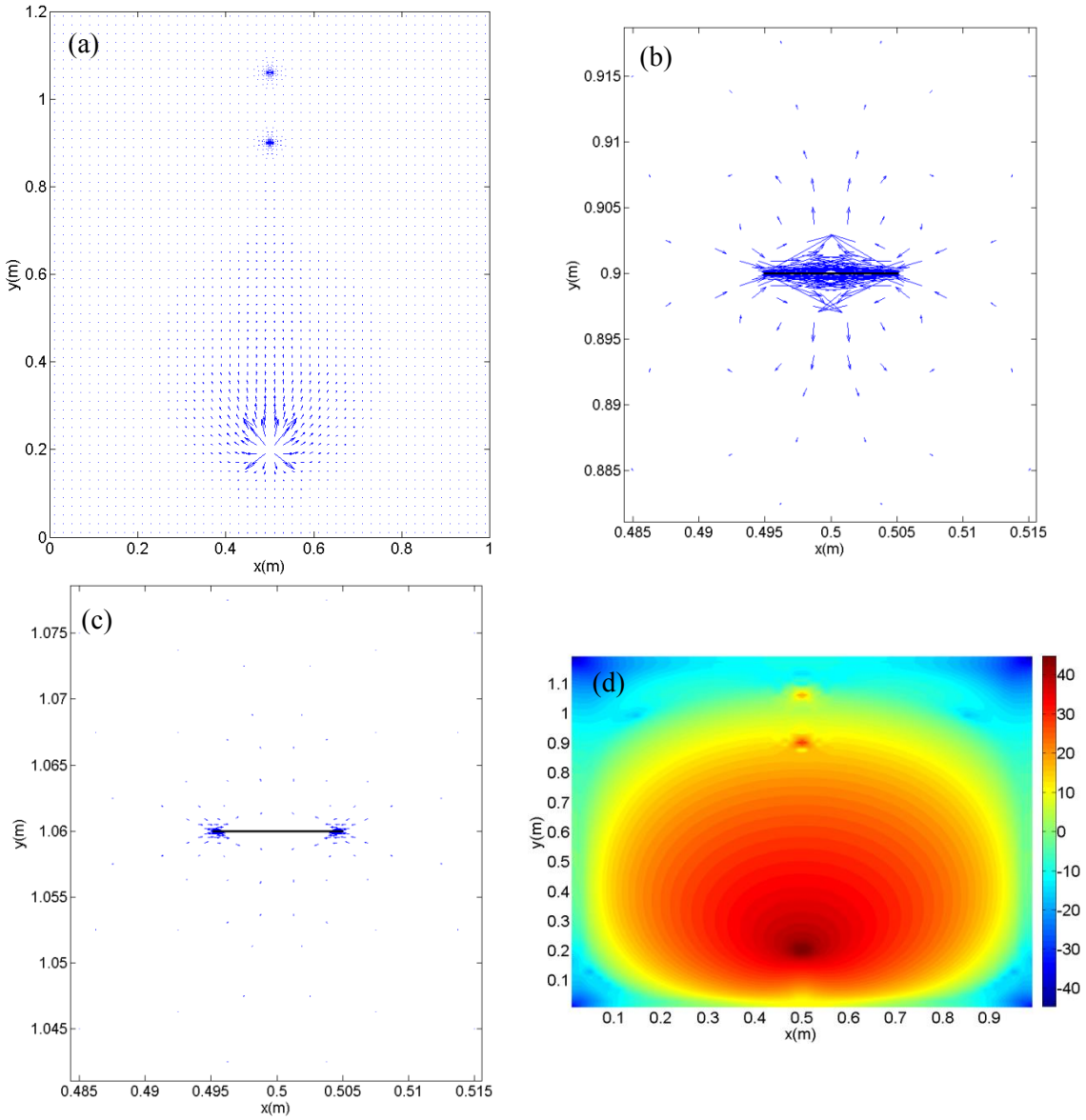

Figure 5.2: PF in the clamped plate with two cracks parallel to the x axis at $f_e = 20\ Hz$: (a) PF vector plot; (b) zoomed-in version at first crack; (c) zoomed-in version at second crack; (d) power distribution plot of PF magnitude and colour bar in the unit dB/m with the reference power of $10^{-12}\ W$.

Table 5.1: Net PF around excitation force and crack tips of clamped plate with two cracks excited by 20 Hz force (cracks parallel to the x axis).

Measurement location	**Net PF (dB)**
Around excitation force	33.016
Around tip of the first crack	-4.274
Around tip of the second crack	-14.381

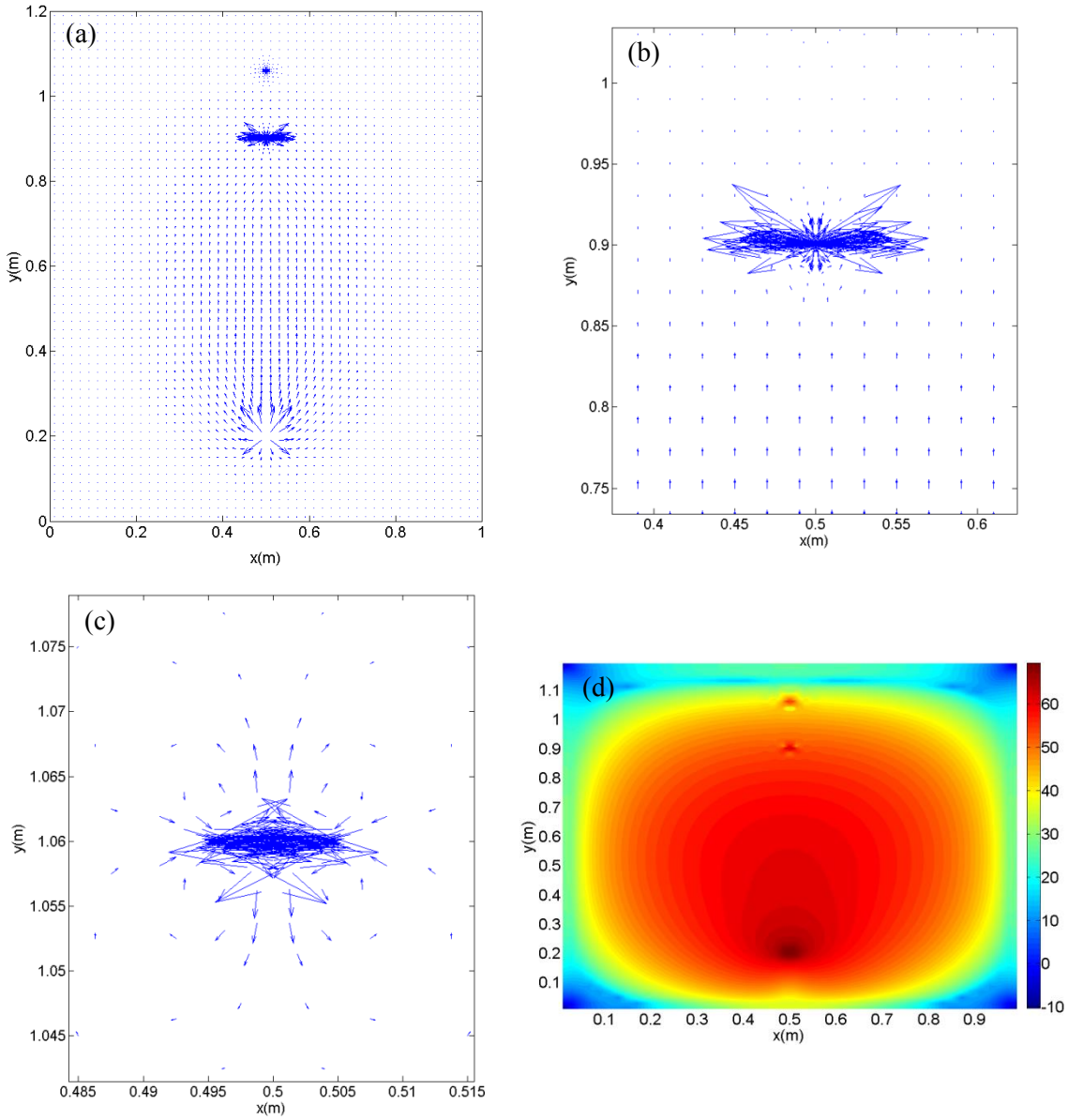

Figure 5.3: PF in the clamped plate with two cracks parallel to the x axis at $f_e = 100\ Hz$: (a) PF vector plot; (b) zoomed-in version at first crack; (c) zoomed-in version at second crack; (d) power distribution plot of PF magnitude and colour bar in the unit dB/m with the reference power of $10^{-12}\ W$.

Table 5.2: Net PF around excitation force and crack tips of clamped plate with two cracks excited by 100 Hz force (cracks parallel to the x axis).

Measurement location	**Net PF (dB)**
Around excitation force	57.693
Around tip of the first crack	30.279
Around tip of the second crack	21.847

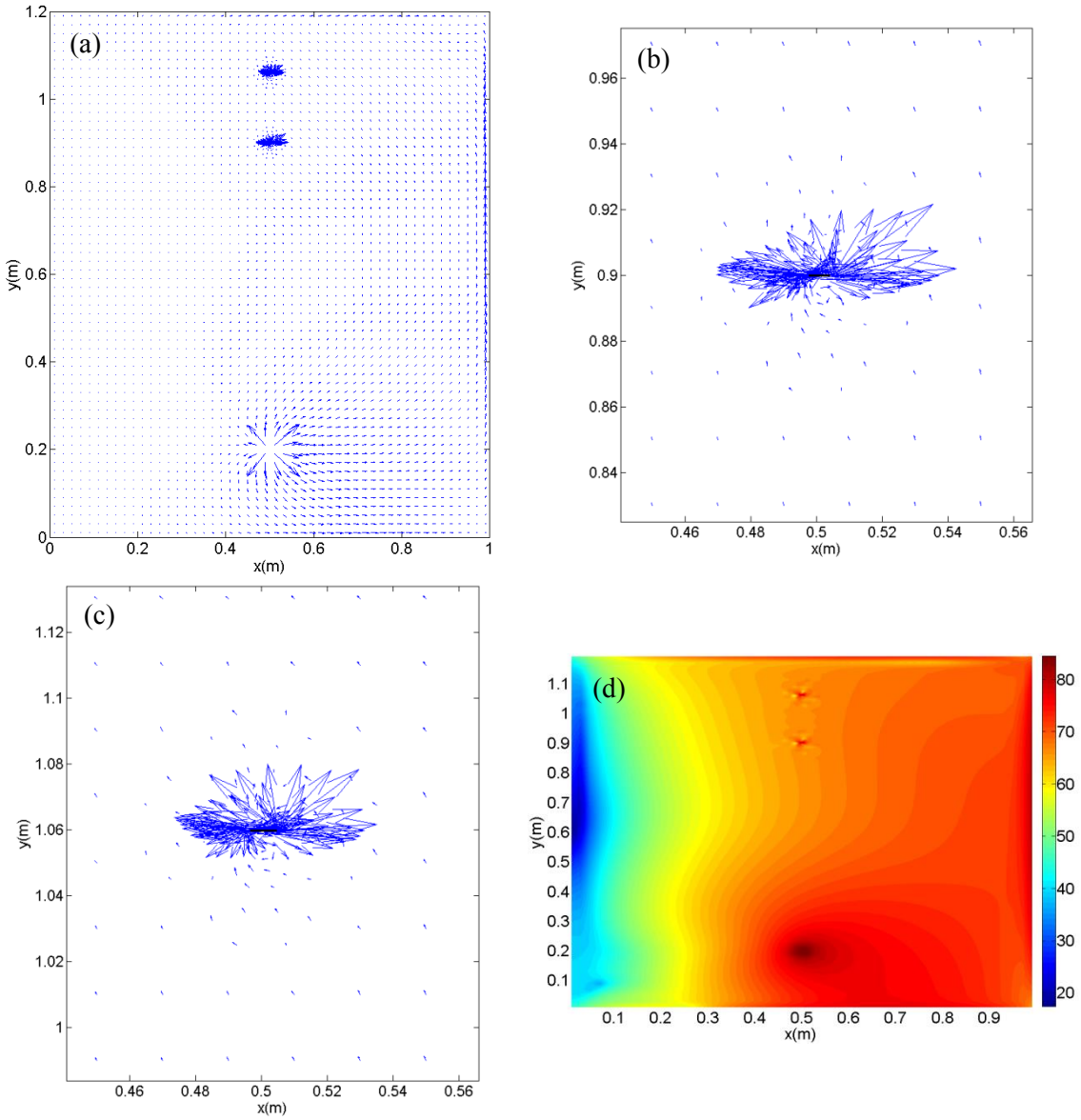

Figure 5.4: PF in the cantilever plate with two cracks parallel to the x axis at $f_e = 20\ Hz$: (a) PF vector plot; (b) zoomed-in version at first crack; (c) zoomed-in version at second crack; (d) power distribution plot of PF magnitude and colour bar in the unit dB/m with the reference power of $10^{-12}\ W$.

Table 5.3: Net PF around excitation force and crack tips of cantilever plate with two cracks excited by 20 Hz force (cracks parallel to the x axis).

Measurement location	**Net PF (dB)**
Around excitation force	72.884
Around left tip of the first crack	38.395
Around right tip of the first crack	42.186
Around left tip of the second crack	38.399
Around right tip of the second crack	42.084

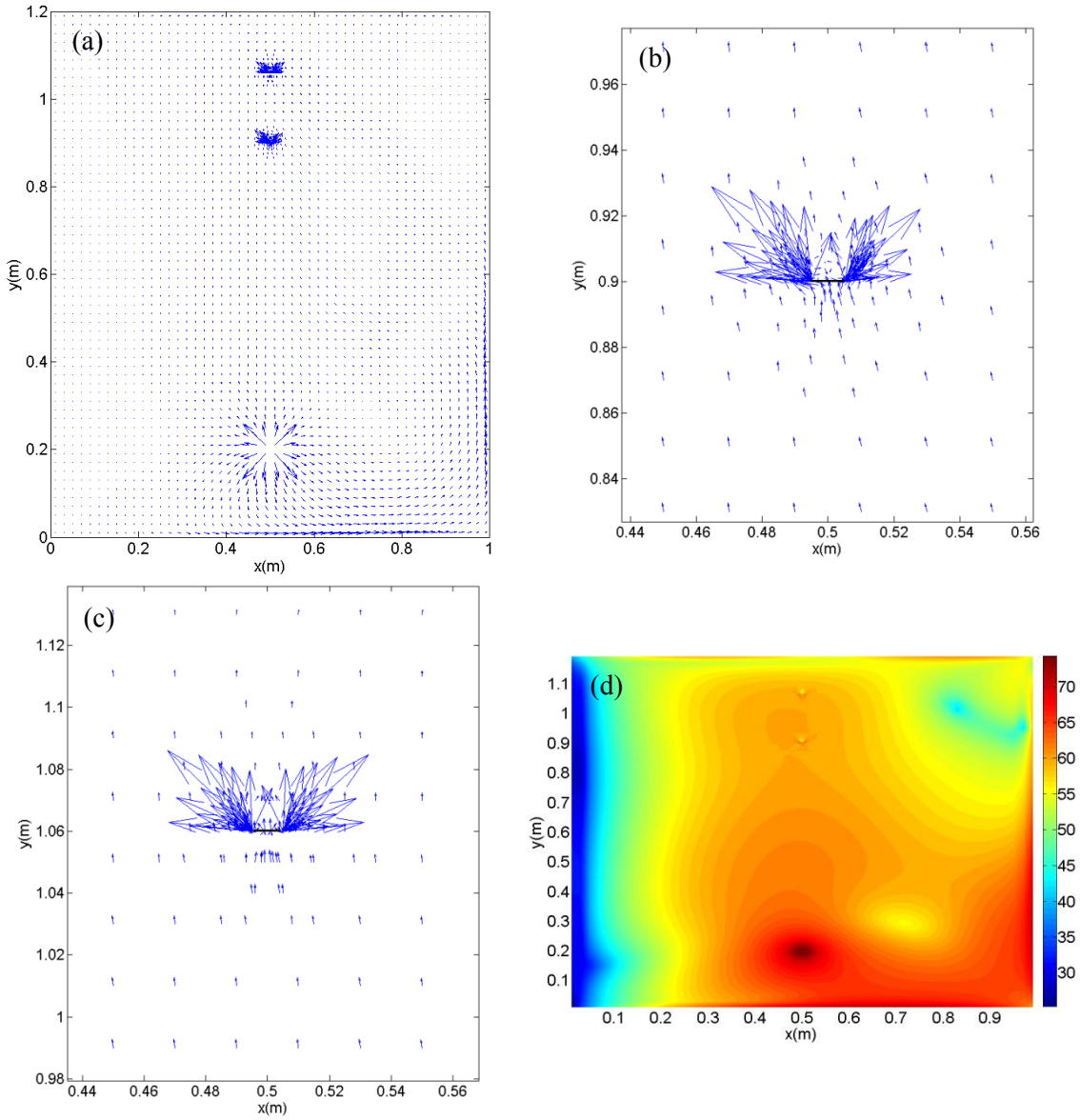

Figure 5.5: PF in the cantilever plate with two cracks parallel to the x axis at $f_e = 100\ Hz$: (a) PF vector plot; (b) zoomed-in version at first crack; (c) zoomed-in version at second crack; (d) power distribution plot of PF magnitude and colour bar in the unit dB/m with the reference power of $10^{-12}\ W$.

Table 5.4: Net PF around excitation force and crack tips of cantilever plate with two cracks excited by 100 Hz force (cracks parallel to the x axis).

Measurement location	**Net PF (dB)**
Around excitation force	62.956
Around left tip of the first crack	32.627
Around right tip of the first crack	31.701
Around left tip of the second crack	32.107
Around right tip of the second crack	32.124

Table 5.5: Net PF in intact plates computed at the same locations as those of crack tips (the second crack parallel to the x axis located at (0.5, 1.06)).

Excitation frequency	Net PF in clamped plate (dB)		Net PF in cantilever plate (dB)	
	Left tip location of the second crack	Right tip location of the second crack	Left tip location of the second crack	Right tip location of the second crack
20 Hz	-38.549	-38.549	29.152	29.252
100 Hz	2.392	2.392	22.281	22.244

The plates containing double cracks are modelled again. However, this time, the second cracks moved from the position (0.5, 1.06) to the position (0.5, 0.74). The first cracks are still at the same position. This model of the plate containing cracks parallel to the x axis are shown in Figure 5.6. The geometries of both cracks are kept consistent with those presented in Figures 5.1 (b). The unit excitation point force is applied to the plates at the position (0.5, 0.2). The frequencies of this force are 20 and 100 Hz.

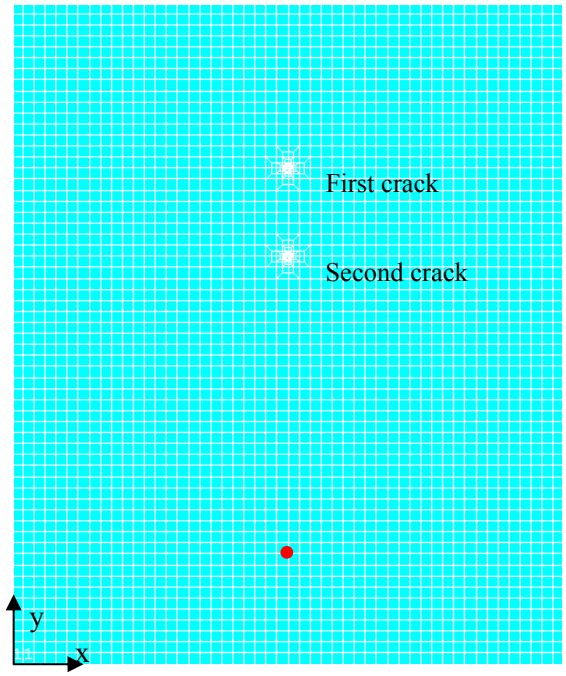

Figure 5.6: Model of plate with two cracks parallel to the x axis when the second crack is moved to (0.5, 0.74).

The vector and power distribution plots of this case studies are presented in Figures 5.7 – 5.10. The first two figures belong to the clamped plates, while the other two are of the cantilever plates. It can be observed from these figures that the patterns of the power flow in the regions around the first cracks and at the areas far from the cracks in both clamped and cantilever plates are still comparable to those shown in Figures 5.2 – 5.5. The patterns of the power flow around the second cracks located at the new position are in the

similar manners as those of the first and the second cracks of the previous cases. The locations of both two cracks are presented clearly on the power distribution plots in (d) of Figures $5.7 - 5.10$.

The magnitudes of the net power flow at the input forces and the crack tips are given in Tables $5.6 - 5.9$. When comparing the results in these tables to those in Tables $5.1 - 5.4$, it can be seen that the magnitudes of the net power flow around the input forces and at the first crack tips are slightly changed after the second cracks are moved to the new location. For the clamped plates excited by 20 and $100\ Hz$ forces, the magnitudes of the net power flow at the tips of the second cracks located at $(0.5,\ 0.74)$ are greatly higher than those counterparts when they are at the position $(0.5,\ 1.06)$. In contrast, the values of the net power flow at the tips of the second cracks on the cantilever plates are almost the same for the positions $(0.5,\ 0.74)$ and $(0.5,\ 1.06)$. These occur due to the directions of the power propagation. As seen before, the transmission paths of the power in the clamped plates are perpendicular to the crack lines, while the powers in the cantilever plates transmit along the free edges before going to reach the cracks.

The magnitudes of the net power flow around the tips of the second cracks mentioned previously in this section are also compared to those of the corresponding intact plates computed at the same locations given in Table 5.10. The magnitudes of the net power flow around the crack tips are higher than those of the intact plates.

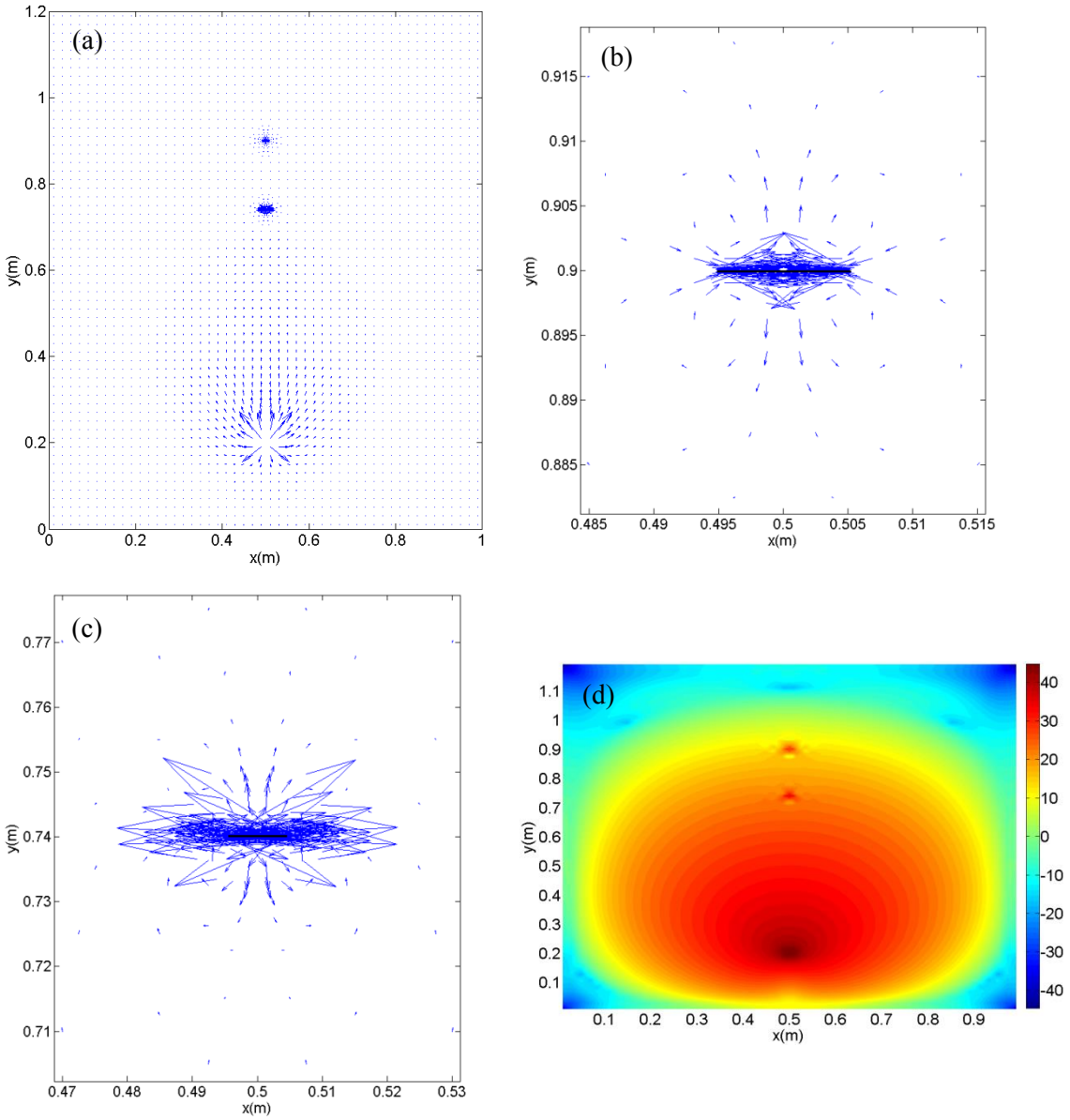

Figure 5.7: PF in the clamped plate with two cracks parallel to the x axis at $f_e = 20\ Hz$ when the second crack is at (0.5, 0.74): (a) PF vector plot; (b) zoomed-in version at first crack; (c) zoomed-in version at second crack; (d) power distribution plot of PF magnitude and colour bar in the unit dB/m with the reference power of $10^{-12}\ W$.

Table 5.6: Net PF around excitation force and crack tips of clamped plate with two cracks excited by 20 Hz force when the second crack is at (0.5, 0.74) (cracks parallel to the x axis).

Measurement location	**Net PF (dB)**
Around excitation force	33.016
Around tip of the first crack	-4.278
Around tip of the second crack	1.087

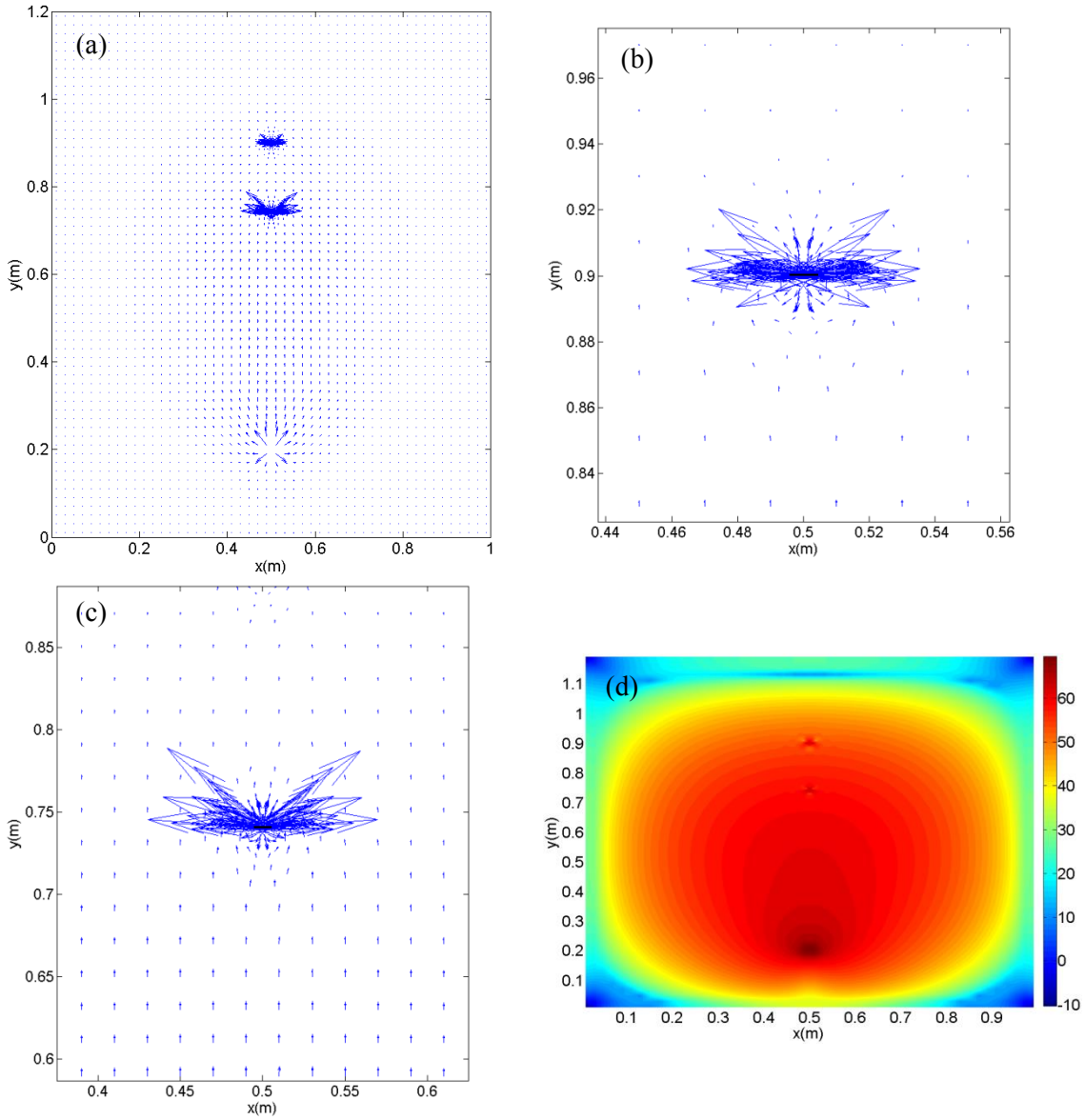

Figure 5.8: PF in the clamped plate with two cracks parallel to the x axis at $f_e = 100\ Hz$ when the second crack is at (0.5, 0.74): (a) PF vector plot; (b) zoomed-in version at first crack; (c) zoomed-in version at second crack; (d) power distribution plot of PF magnitude and colour bar in the unit dB/m with the reference power of $10^{-12}\ W$.

Table 5.7: Net PF around excitation force and crack tips of clamped plate with two cracks excited by 100 Hz force when the second crack is at (0.5, 0.74) (cracks parallel to the x axis).

Measurement location	**Net PF (dB)**
Around excitation force	57.693
Around tip of the first crack	30.280
Around tip of the second crack	32.806

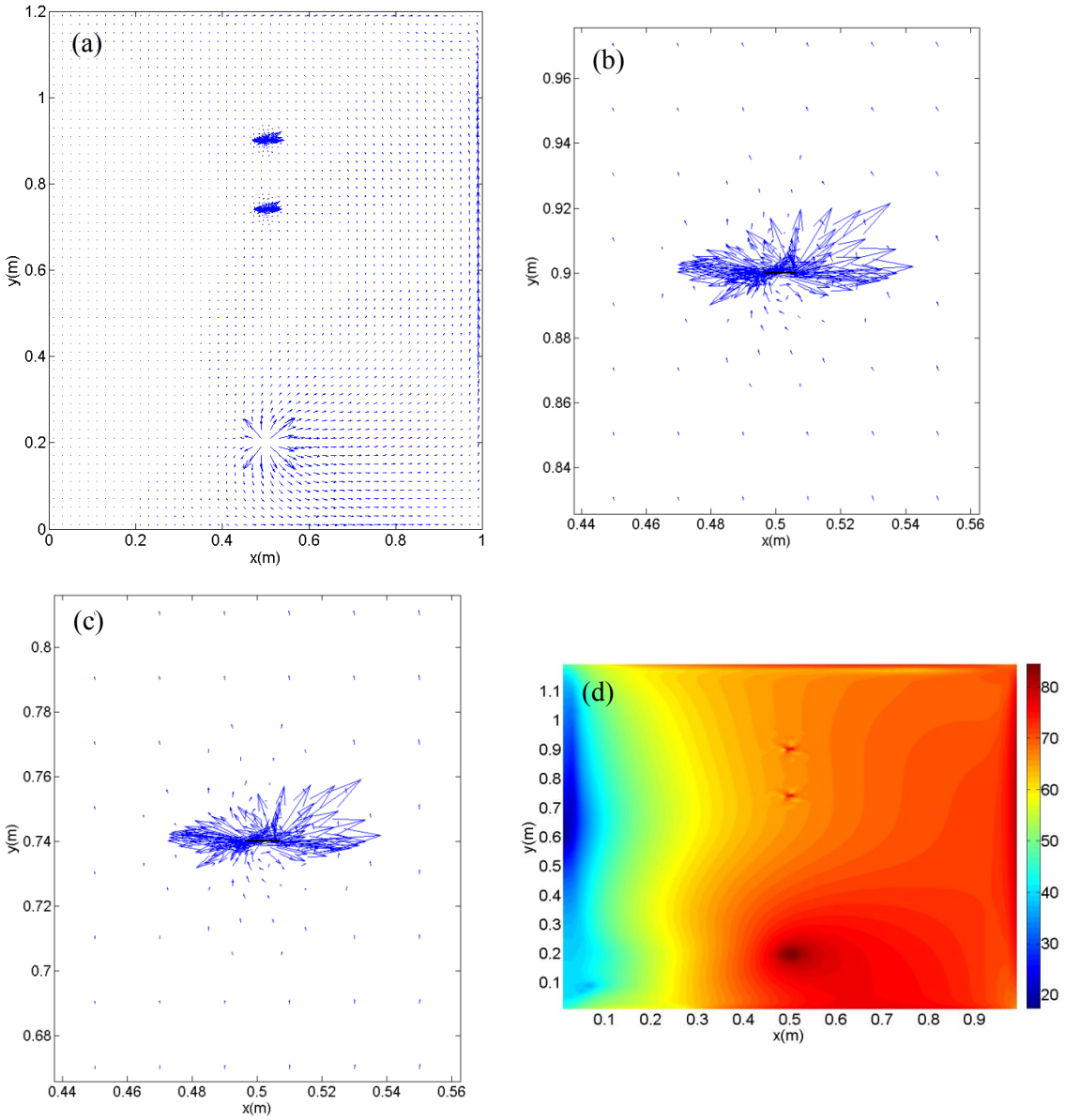

Figure 5.9: PF in the cantilever plate with two cracks parallel to the x axis at $f_e = 20\ Hz$ when the second crack is at (0.5, 0.74): (a) PF vector plot; (b) zoomed-in version at first crack; (c) zoomed-in version at second crack; (d) power distribution plot of PF magnitude and colour bar in the unit dB/m with the reference power of $10^{-12}\ W$.

Table 5.8: Net PF around excitation force and crack tips of cantilever plate with two cracks excited by 20 Hz force when the second crack is at (0.5, 0.74) (cracks parallel to the x axis).

Measurement location	**Net PF (dB)**
Around excitation force	72.884
Around left tip of the first crack	38.395
Around right tip of the first crack	42.184
Around left tip of the second crack	37.766
Around right tip of the second crack	41.586

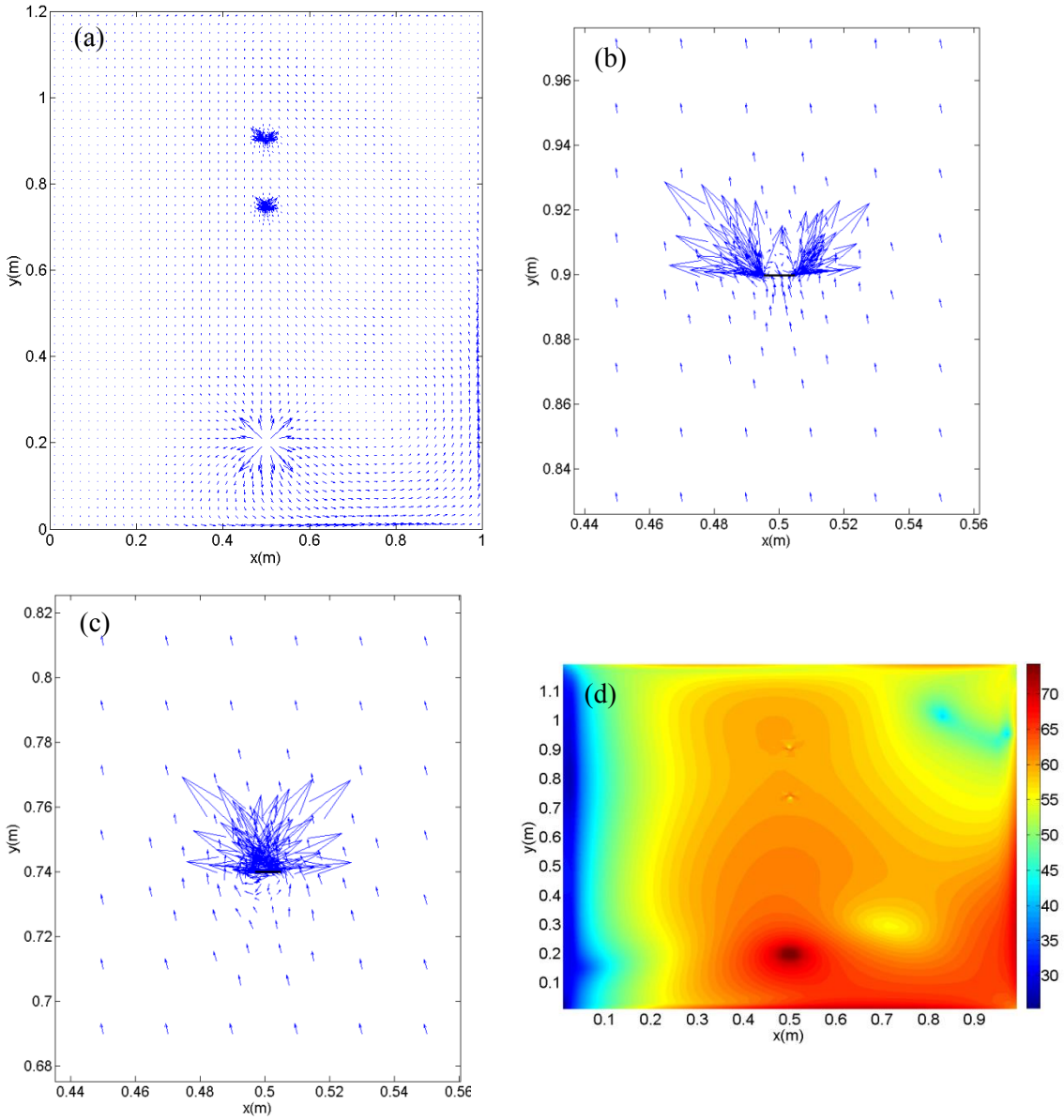

Figure 5.10: PF in the cantilever plate with two cracks parallel to the x axis at $f_e = 100\ Hz$ when the second crack is at (0.5, 0.74): (a) PF vector plot; (b) zoomed-in version at first crack; (c) zoomed-in version at second crack; (d) power distribution plot of PF magnitude and colour bar in the unit dB/m with the reference power of $10^{-12}\ W$.

Table 5.9: Net PF around excitation force and crack tips of cantilever plate with two cracks excited by 100 Hz force when the second crack is at (0.5, 0.74) (cracks parallel to the x axis).

Measurement location	**Net PF (dB)**
Around excitation force	62.958
Around left tip of the first crack	32.630
Around right tip of the first crack	31.704
Around left tip of the second crack	32.760
Around right tip of the second crack	32.415

Table 5.10: Net PF in intact plates computed at the same locations as those of crack tips (the second crack parallel to the x axis located at (0.5, 0.74)).

Excitation frequency	Net PF in clamped plate (dB)		Net PF in cantilever plate (dB)	
	Left tip location of the second crack	Right tip location of the second crack	Left tip location of the second crack	Right tip location of the second crack
20 Hz	-15.356	-15.356	28.627	28.833
100 Hz	21.218	21.218	23.063	23.050

5.2.2 Cracks perpendicular to coordinate x axis

The finite element model of the plate with two identical cracks perpendicular to the x axis is displayed in Figure 5.11. All parameters, except the orientations of the cracks, are the same as those used in Section 5.2.1. The positions of the first and second cracks and the excitation force are identical to those in the previous section.

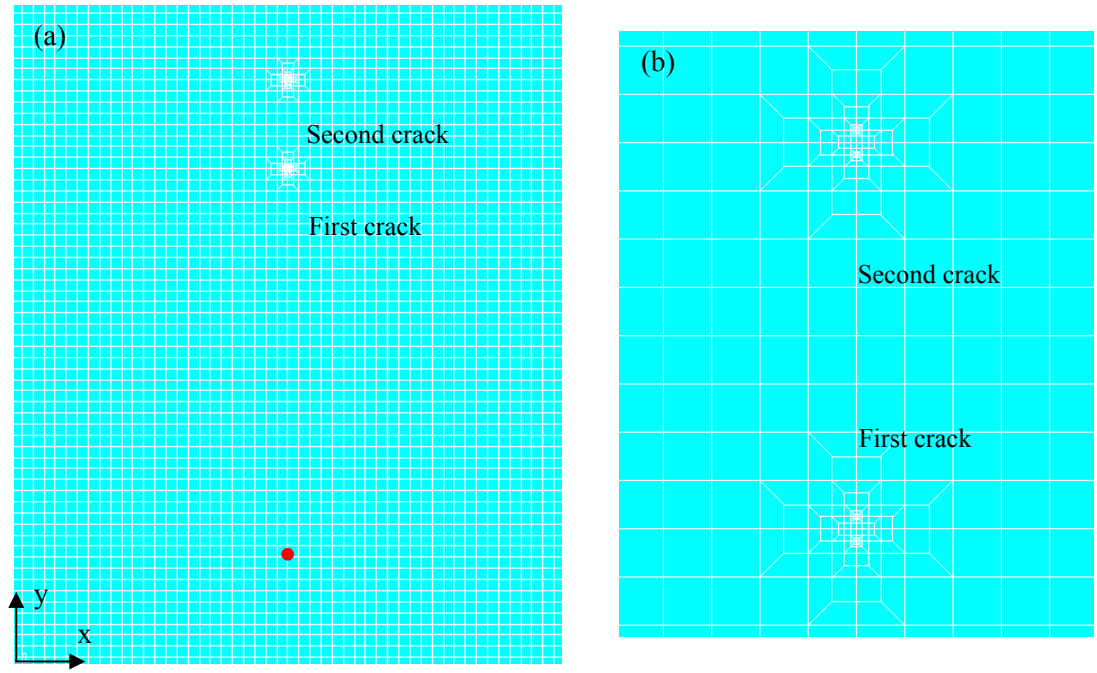

Figure 5.11: Model of plate with two cracks perpendicular to the x axis: (a) overall plate with red dot representing location of excitation force, (b) at crack locations (higher mesh refinement).

Figures 5.12 and 5.13 display the vector and power distribution plots of the clamped plates which are excited by the 20 and 100 Hz forces. The locations of both cracks are shown in the plots by the changes of the power flow patterns at those positions. The magnitudes of the net power flow around the input force and crack tips are given in Tables 5.11 and 5.12. It is seen when comparing the results in these tables to those of the clamped plates of Tables 4.8 and 4.9 that the presence of the second crack inconsiderably affect the net power flow around the excitation force and the tips of the first crack, since the differences of the

net power flow magnitudes before and after the existence of the second crack are negligible. The magnitudes of the net power flow around the tips of both cracks perpendicular to the x axis are less than those of the cracks parallel to the x axis shown in the previous section.

The vector and power distribution plots of the power flow in the cantilever plate with double cracks perpendicular to the x axis is presented in Figures 5.14 and 5.15. The locations of both cracks are revealed owing to the changes of the power flow patterns at those locations. The magnitudes of the net power flow around the excitation force and the first crack tips of the double cracked plates given in Tables 5.13 and 5.14 are comparable to those of the single-cracked counterparts (Tables 4.8 and 4.9). Due to the propagation paths of the power in the cantilever plates, the second cracks can have the larger net power flow magnitudes at their tips than the first cracks that are closer to the excitation force or the source of power. By cause of this, the magnitudes of the net power flow around the tips generated by the $20\ Hz$ force of the cracks perpendicular to the x axis are bigger than those of the cracks in the other orientation, whereas the trend of the net power flow at the tips created by the $100\ Hz$ force is the same as that of the clamped plates, but the differences are lower.

The values of the net power flow in the intact clamped and cantilever plates computed at the same locations as those of the tips of the second cracks perpendicular to the x axis are shown in Tables 5.15. Comparing these values to those in Tables $5.6 - 5.9$ indicates that the values of the net power flow at the crack tips are larger than those of the intact plates.

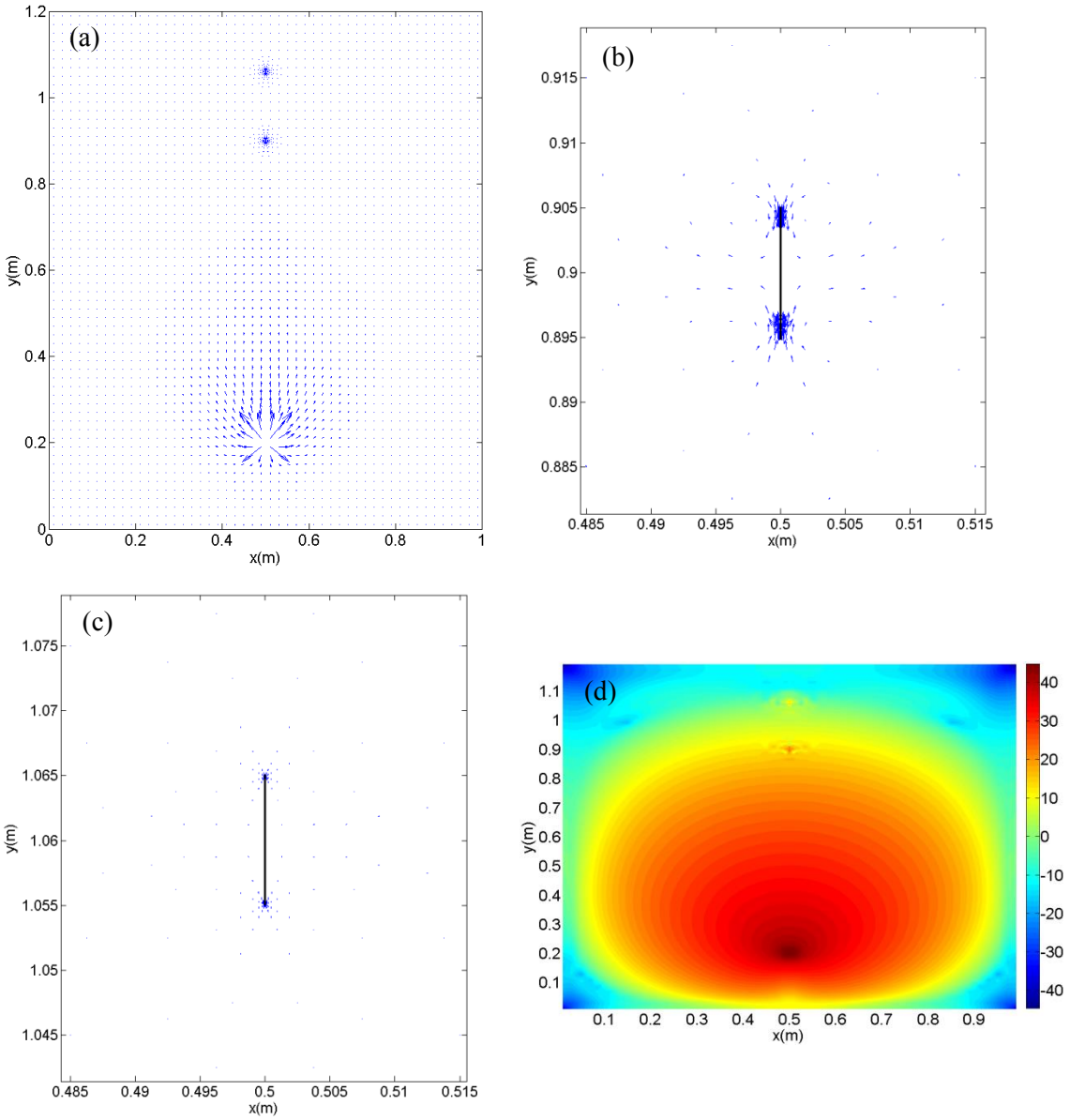

Figure 5.12: PF in the clamped plate with two cracks perpendicular to the x axis at $f_e = 20\ Hz$: (a) PF vector plot; (b) zoomed-in version at first crack; (c) zoomed-in version at second crack; (d) power distribution plot of PF magnitude and colour bar in the unit dB/m with the reference power of $10^{-12}\ W$.

Table 5.11: Net PF around excitation force and crack tips of clamped plate with two cracks excited by 20 Hz force (cracks perpendicular to the x axis).

Measurement location	**Net PF (dB)**
Around excitation force	33.016
Around upper tip of the first crack	-12.661
Around lower tip of the first crack	-9.996
Around upper tip of the second crack	-22.826
Around lower tip of the second crack	-20.022

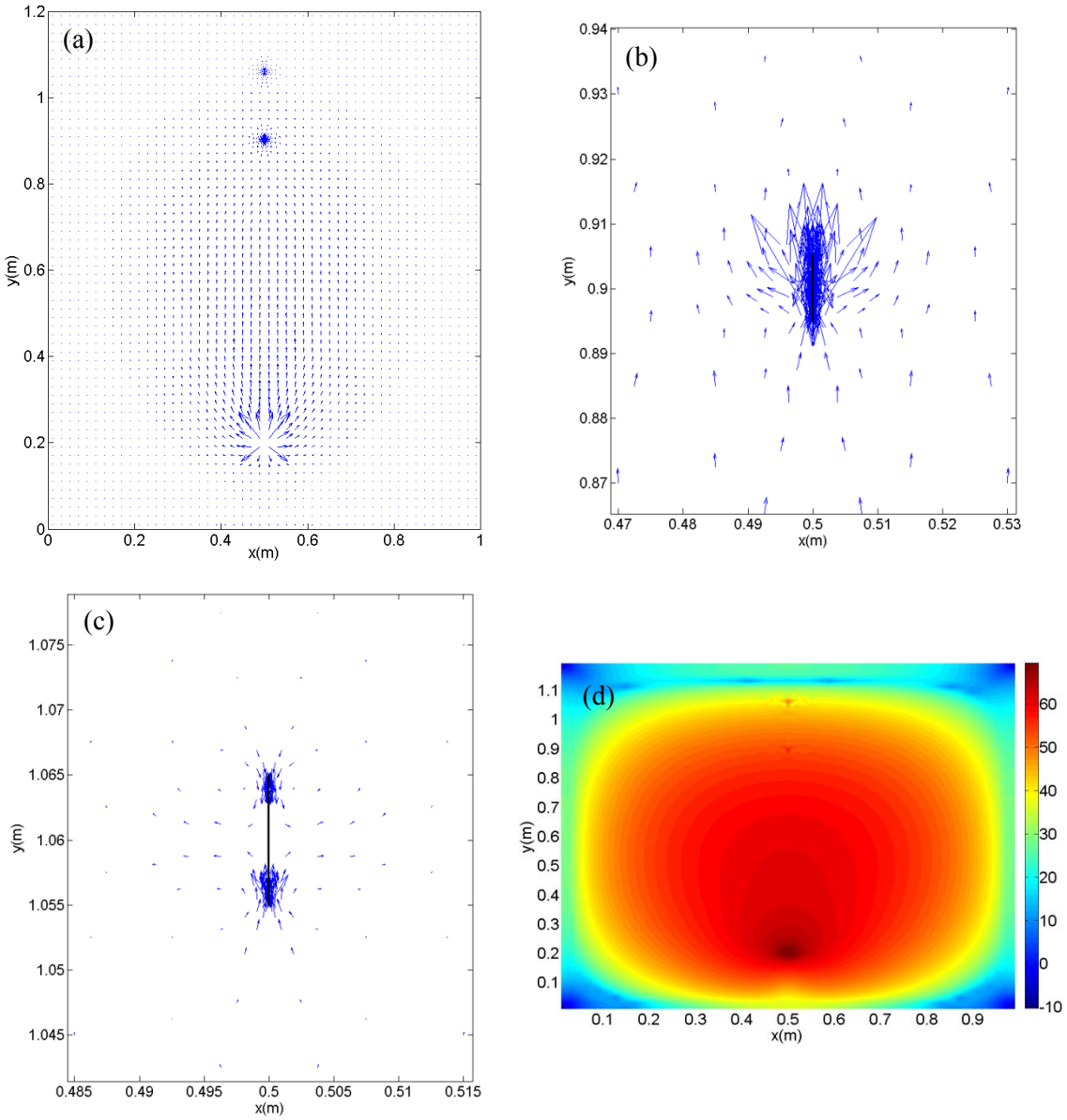

Figure 5.13: PF in the clamped plate with two cracks perpendicular to the x axis at $f_e = 100\ Hz$: (a) PF vector plot; (b) zoomed-in version at first crack; (c) zoomed-in version at second crack; (d) power distribution plot of PF magnitude and colour bar in the unit dB/m with the reference power of $10^{-12}\ W$.

Table 5.12: Net PF around excitation force and crack tips of clamped plate with two cracks excited by 100 Hz force (cracks perpendicular to the x axis).

Measurement location	**Net PF (dB)**
Around excitation force	57.692
Around upper tip of the first crack	21.793
Around lower tip of the first crack	25.264
Around upper tip of the second crack	13.815
Around lower tip of the second crack	16.848

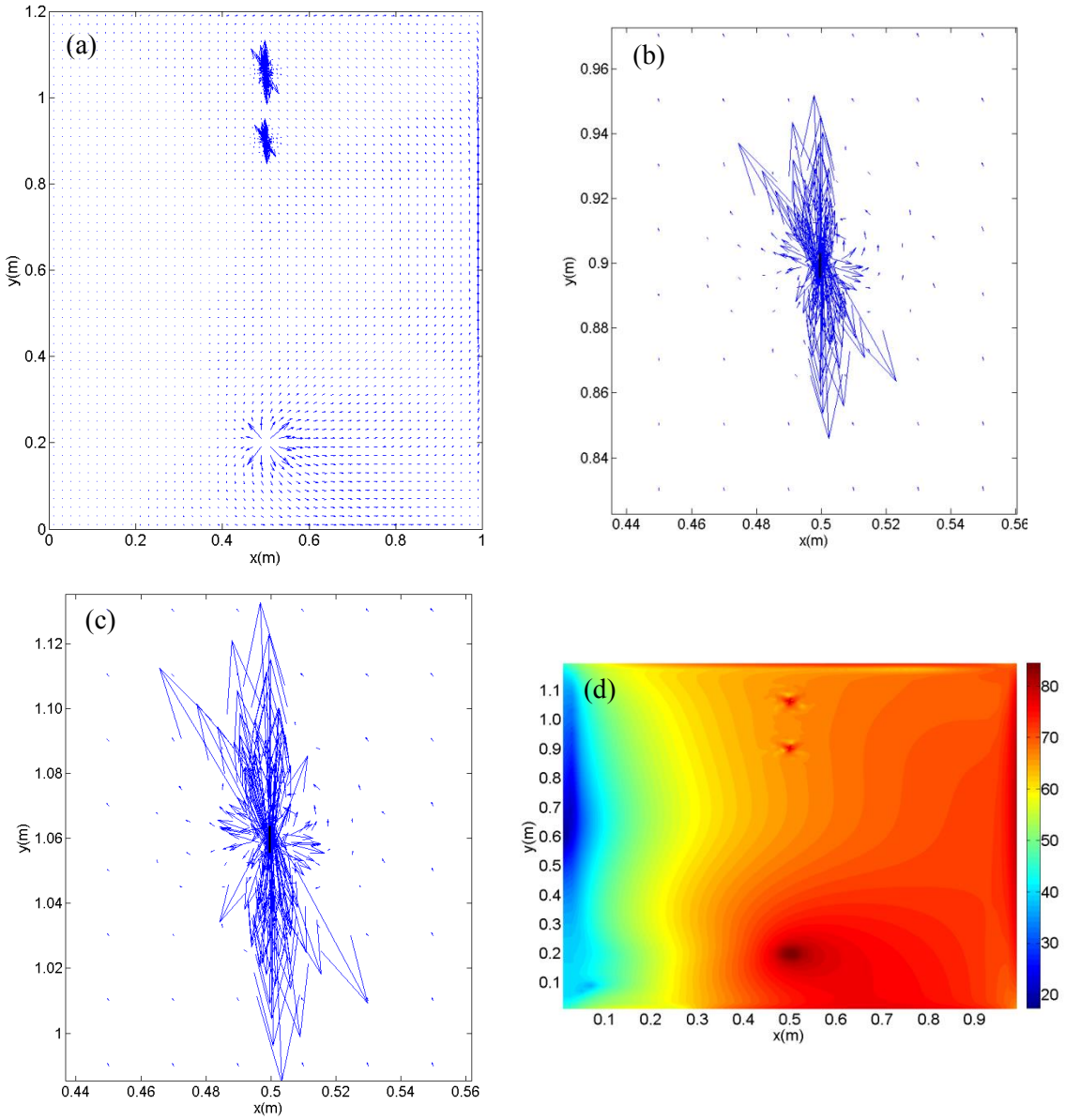

Figure 5.14: PF in the cantilever plate with two cracks perpendicular to the x axis at $f_e = 20\ Hz$: (a) PF vector plot; (b) zoomed-in version at first crack; (c) zoomed-in version at second crack; (d) power distribution plot of PF magnitude and colour bar in the unit dB/m with the reference power of $10^{-12}\ W$.

Table 5.13: Net PF around excitation force and crack tips of cantilever plate with two cracks excited by 20 Hz force (cracks perpendicular to the x axis).

Measurement location	**Net PF (dB)**
Around excitation force	72.884
Around upper tip of the first crack	43.919
Around lower tip of the first crack	44.156
Around upper tip of the second crack	45.541
Around lower tip of the second crack	45.734

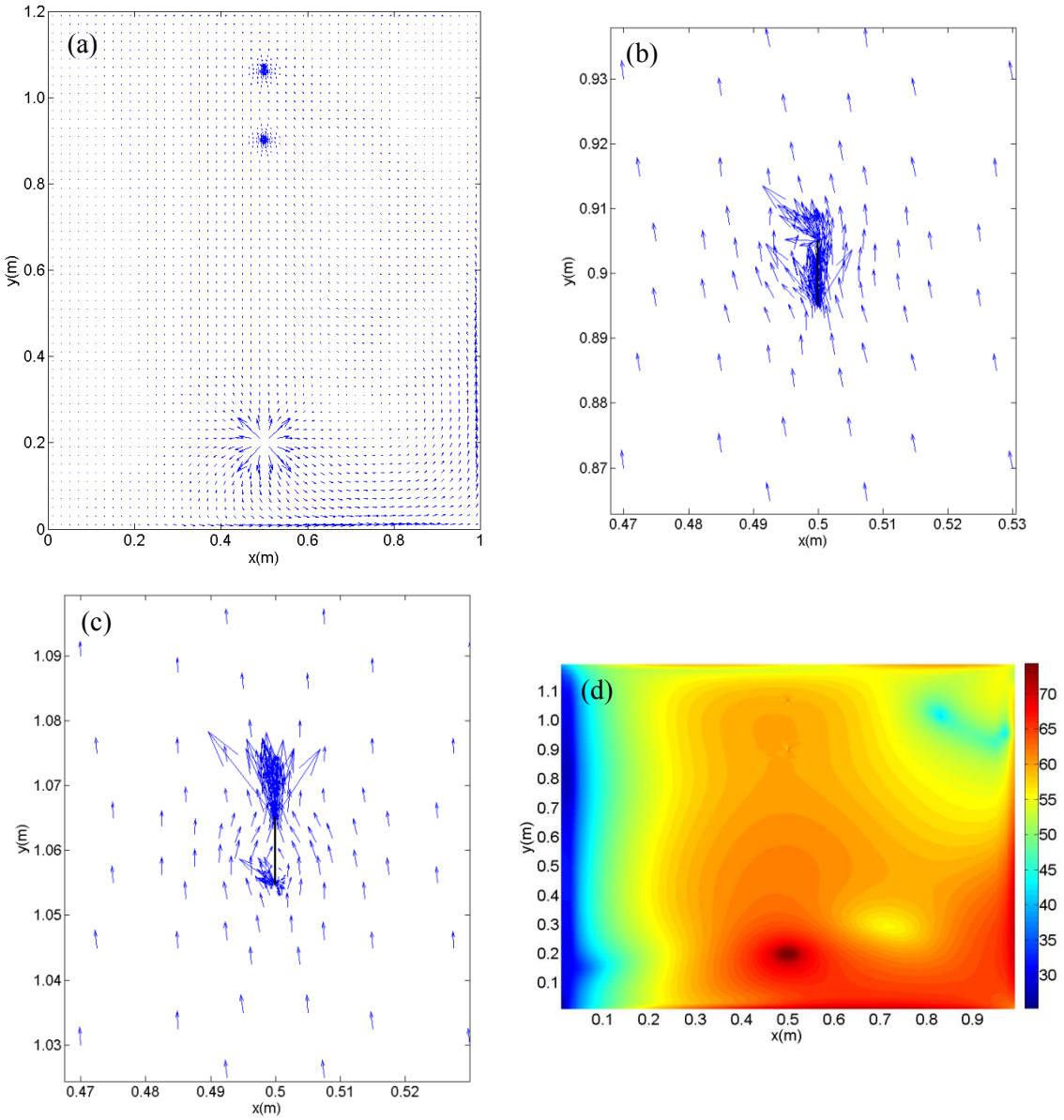

Figure 5.15: PF in the cantilever plate with two cracks perpendicular to the x axis at the $f_e = 100\ Hz$: (a) PF vector plot; (b) zoomed-in version at first crack; (c) zoomed-in version at second crack; (d) power distribution plot of PF magnitude and colour bar in the unit dB/m with the reference power of $10^{-12}\ W$.

Table 5.14: Net PF around excitation force and crack tips of cantilever plate with two cracks excited by 100 Hz force (cracks perpendicular to the x axis).

Measurement location	**Net PF (dB)**
Around excitation force	62.955
Around upper tip of the first crack	26.727
Around lower tip of the first crack	27.894
Around upper tip of the second crack	29.071
Around lower tip of the second crack	24.033

Table 5.15: Net PF in intact plates computed at the same locations as those of crack tips (the second crack perpendicular to the x axis located at (0.5, 1.06)).

Excitation frequency	Net PF in clamped plate (dB)		Net PF in cantilever plate (dB)	
	Lower tip location of the second crack	Upper tip location of the second crack	Lower tip location of the second crack	Upper tip location of the second crack
20 Hz	-38.491	-39.185	29.149	29.262
100 Hz	2.879	1.735	22.190	22.339

The same as the cases of the crack parallel to the x axis, the second crack perpendicular to the x axis is moved from the position (0.5, 1.06) to the positioin (0.5, 0.74). All parameters used in the power flow computation are exacly the same as used before. It is also assumed that the first and the second cracks are identical. The model of this cracked plate is illustrated in Figure 5.16. The 20 and 100 Hz point excitation forces are located at (0.5, 0.2).

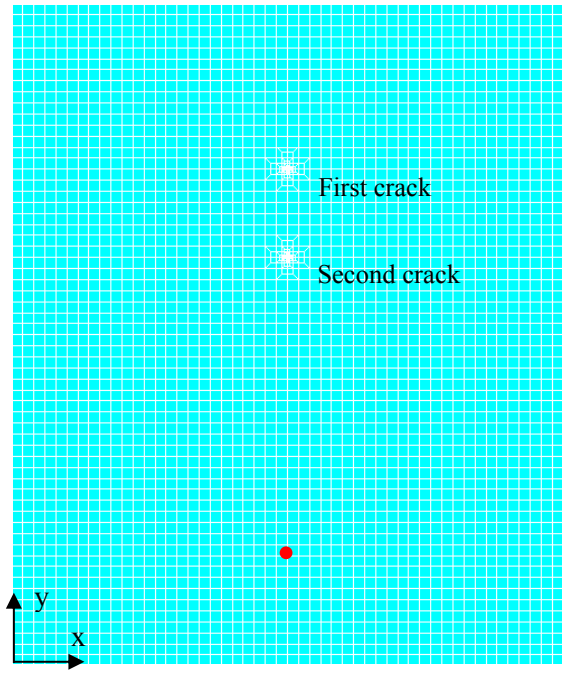

Figure 5.16: Model of plate with two cracks perpendicular to the x axis when the second crack is moved to (0.5, 0.74).

The results of the power flow are presented in the forms of the vector and power distribution plots in Figures $5.17 - 5.20$. Comparing (a) and (b) of Figures $5.17 - 5.20$ to those in Fiures $5.12 - 5.16$ indicates that the change in the postions of the second cracks does not affect the patterns of the power flow at the areas around and out of the first cracks. The characteristics of the power flow patterns around the second cracks at the new position ((c) of Figure $5.17 - 5.20$) are similar to those of the first cracks. (d) of Figrues

$5.17 - 5.20$ illustrate the power distribution plots which are able to clearly show the magnitude of the power flow at each location on the plates.

The same as the cases of the crack parallel to the x axis, the tips of the second cracks at the new postion on the clamped plates have the larger magnitudes of the net power flow than those of the second cracks at the old position. This can be seen by comparing the results in Tables $5.16 - 5.19$ to those in Tables $5.11 - 5.14$. However, this is not true for the case of the cantilever plates. For the cantilever plate excited by the $20\ Hz$ force, the net power flow magnitudes at both tips of the second crack at $(0.5,\ 0.74)$ are smaller than those counterparts at the old location. The other cantilever plate loaded by the $100\ Hz$ force has the lower net power flow around the upper tip of the second crack at $(0.5,\ 0.74)$ than that of the crack at the old position, but it possesses the higher net power flow around the lower tip than that of the crack at the old position. The net power flow magnitudes around the input excitation force and around the tips of the first cracks are not changed much when the second cracks are moved to $(0.5,\ 0.74)$.

The magnitudes of the net power flow at the crack tips of the second cracks in Tables $5.16 - 5.19$ are larger than those at the same locations on the coresponding intact plates which are presented in Table 5.20.

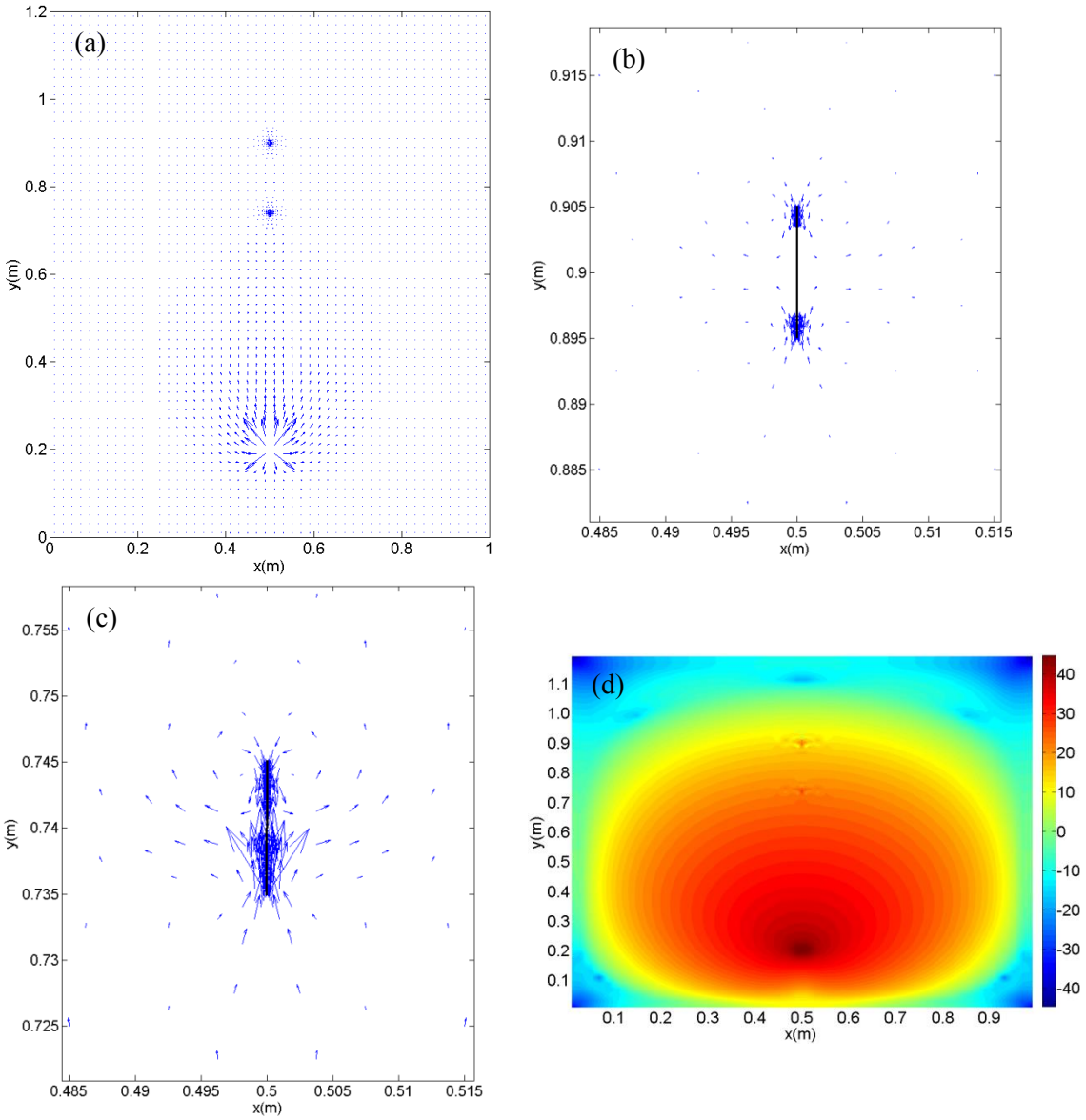

Figure 5.17: PF in the clamped plate with two cracks perpendicular to the x axis at $f_e = 20\ Hz$ when the second crack is at (0.5, 0.74): (a) PF vector plot; (b) zoomed-in version at first crack; (c) zoomed-in version at second crack; (d) power distribution plot of PF magnitude and colour bar in the unit dB/m with the reference power of $10^{-12}\ W$.

Table 5.16: Net PF around excitation force and crack tips of clamped plate with two cracks excited by 20 Hz force when the second crack is at (0.5, 0.74) (cracks perpendicular to the x axis).

Measurement location	**Net PF (dB)**
Around excitation force	33.016
Around upper tip of the first crack	-12.660
Around lower tip of the first crack	-9.993
Around upper tip of the second crack	-8.228
Around lower tip of the second crack	-4.490

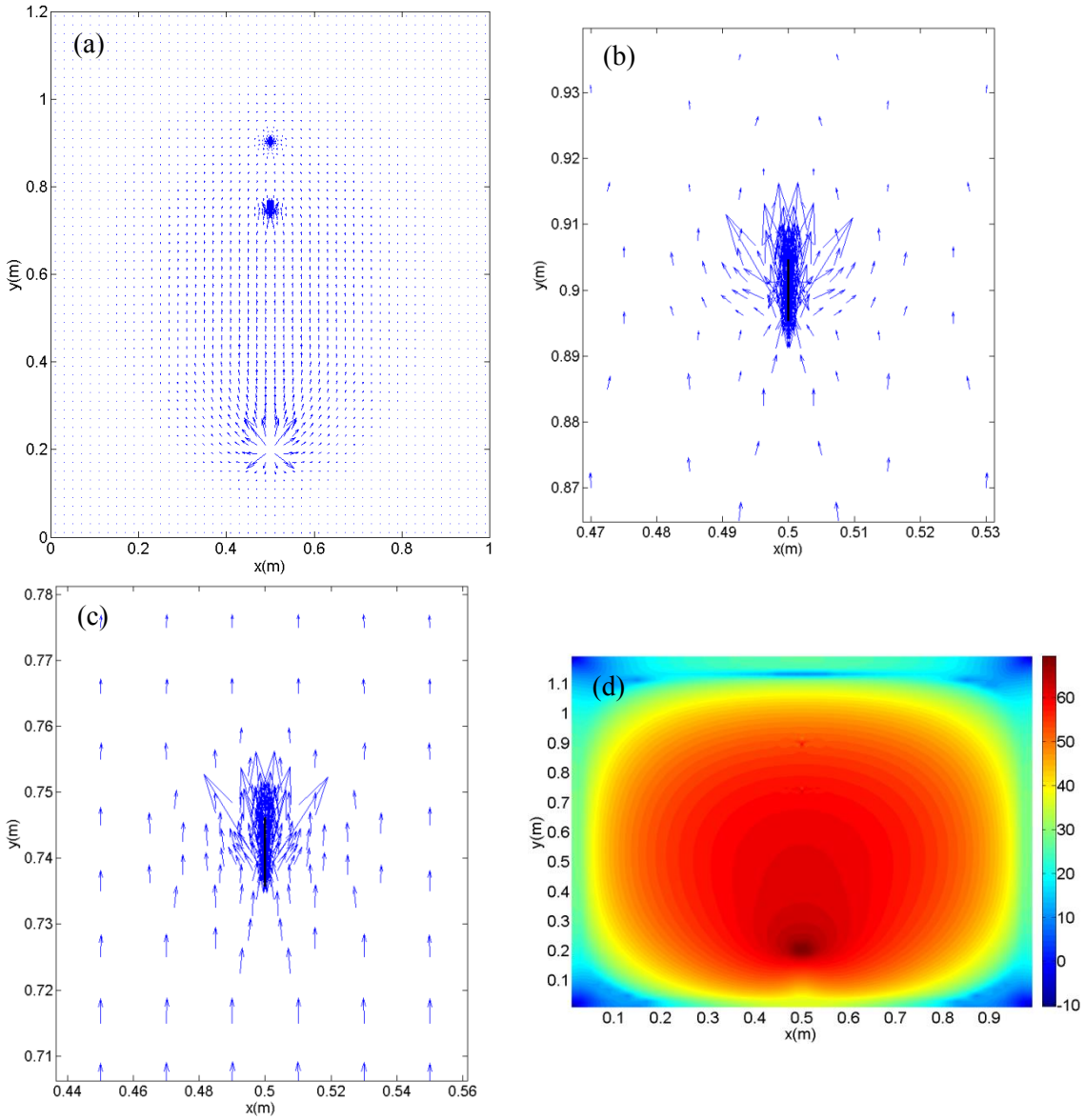

Figure 5.18: PF in the clamped plate with two cracks perpendicular to the x axis at $f_e = 100\ Hz$ when the second crack is at (0.5, 0.74): (a) PF vector plot; (b) zoomed-in version at first crack; (c) zoomed-in version at second crack; (d) power distribution plot of PF magnitude and colour bar in the unit dB/m with the reference power of $10^{-12}\ W$.

Table 5.17: Net PF around excitation force and crack tips of clamped plate with two cracks excited by 100 Hz force when the second crack is at (0.5, 0.74) (cracks perpendicular to the x axis).

Measurement location	**Net PF (dB)**
Around excitation force	57.691
Around upper tip of the first crack	21.785
Around lower tip of the first crack	25.261
Around upper tip of the second crack	20.394
Around lower tip of the second crack	27.999

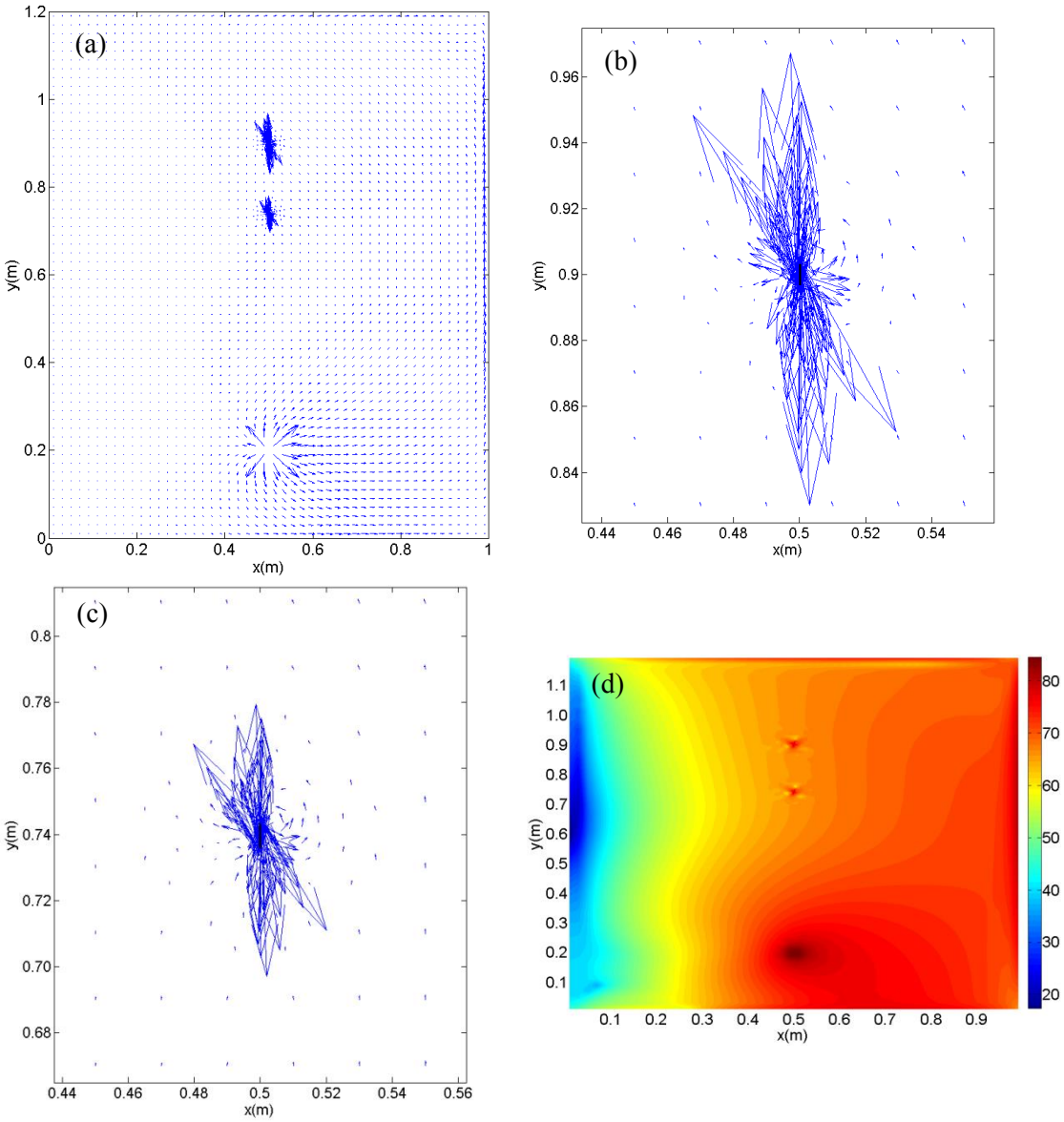

Figure 5.19: PF in the cantilever plate with two cracks perpendicular to the x axis at $f_e = 20\ Hz$ when the second crack is at (0.5, 0.74): (a) PF vector plot; (b) zoomed-in version at first crack; (c) zoomed-in version at second crack; (d) power distribution plot of PF magnitude and colour bar in the unit dB/m with the reference power of $10^{-12}\ W$.

Table 5.18: Net PF around excitation force and crack tips of cantilever plate with two cracks excited by 20 Hz force when the second crack is at (0.5, 0.74) (cracks perpendicular to the x axis).

Measurement location	**Net PF (dB)**
Around excitation force	72.884
Around upper tip of the first crack	43.919
Around lower tip of the first crack	44.155
Around upper tip of the second crack	41.614
Around lower tip of the second crack	41.726

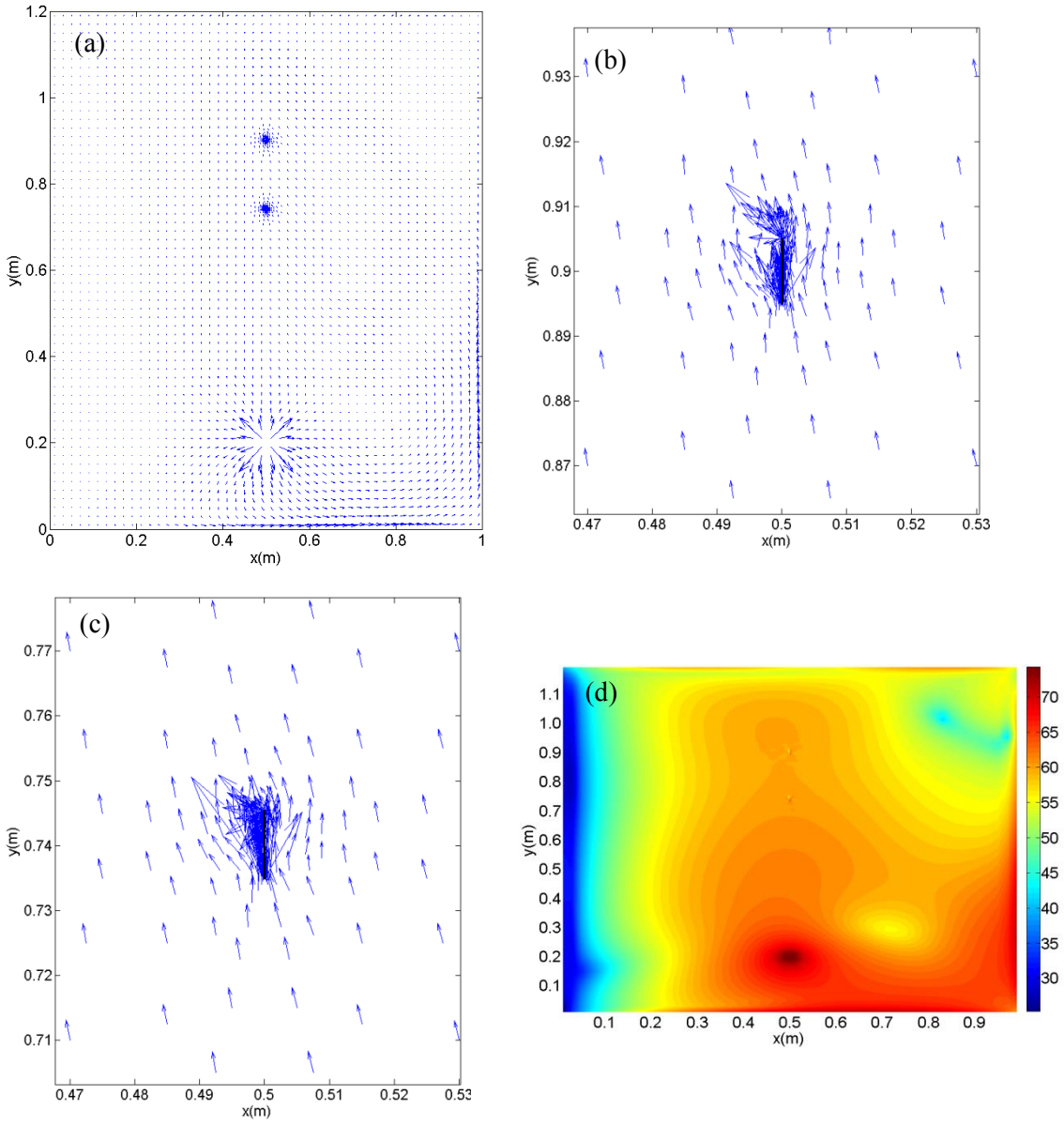

Figure 5.20: PF in the cantilever plate with two cracks perpendicular to the x axis at $f_e = 100\ Hz$ when the second crack is at (0.5, 0.74): (a) PF vector plot; (b) zoomed-in version at first crack; (c) zoomed-in version at second crack; (d) power distribution plot of PF magnitude and colour bar in the unit dB/m with the reference power of $10^{-12}\ W$.

Table 5.19: Net PF around excitation force and crack tips of cantilever plate with two cracks excited by 100 Hz force when the second crack is at (0.5, 0.74) (cracks perpendicular to the x axis).

Measurement location	**Net PF (dB)**
Around excitation force	62.956
Around upper tip of the first crack	26.741
Around lower tip of the first crack	27.890
Around upper tip of the second crack	26.550
Around lower tip of the second crack	29.324

Table 5.20: Net PF in intact plates computed at the same locations as those of crack tips (the second crack perpendicular to the x axis located at (0.5, 0.74)).

Excitation frequency	Net PF in clamped plate (dB)		Net PF in cantilever plate (dB)	
	Lower tip location of the second crack	Upper tip location of the second crack	Lower tip location of the second crack	Upper tip location of the second crack
20 Hz	-15.186	-15.543	28.701	28.758
100 Hz	21.321	21.1224	23.083	23.035

5.3 Effect of excitation frequency on net power flow

The magnitudes of the net power flow around the input force and the crack tips generated by the unit force with the excitation frequencies from 0 to 150 Hz are discussed in this section. Every parameter used in the computation is the same as that used in the previous sections. For the plate containing double cracks, the first cracks is located at (0.5, 0.9) and the second is at (0.5, 1.06). Figure 5.21 illustrates the magnitudes of the net power flow around the input force of the single- and double-cracked plates. It is shown from the figure that the net power flow values around the input forces of the plates containing one and two cracks are approximately the same for all cases. The highest net power flow of each mode is occurred at its natural frequency. Thus, there are 2 peaks of the clamped plates and 7 peaks of the cantilever plates appearing in the plots. The last two peaks of the cantilever plates are close to each other, so it may looks like they are in the same peak. It is also seen from Figure 5.21 that the effect of the presence of the second cracks on plate natural frequencies is negligible, since the natural frequencies of the single-cracked plates are still comparable to those of the plates with double cracks.

The next seven plots displayed in Figures $5.22 - 5.28$ are of the net power flow magnitudes around the tips of the cracks parallel and perpendicular to the coordinate x axis on the single-and double-cracked plates. It is worthily mentioned here again that the cracks on the single-cracked plates are located at the same position as those of the first cracks of the double-crack plates. From all of these figures, it can be observed that the differences of the net power flow magnitudes at both tips of the first cracks and the cracks on the single-cracked plate with the same orientation are very small, whereas the differences of those at the first and second cracks in the double-cracked plates are clearly inspected.

For the clamped plates (Figure 5.22), the net power flow values at both tips of each crack parallel to the x axis are equal due to the symmetries of the power flow patterns about the centre lines of the plates as shown earlier in the vector and power distribution plots. It is

indicated by Figure 5.23 and 5.24 that the net power flow values of all excitation frequencies at the lower tips of the cracks perpendicular to the x axis are more than those of the upper counterparts. This is due to the propagation paths of the power in the clamped plates that are parallel to the cracks. Therefore, the net power flow values are lower at the tips of the cracks located farther from the sources of power or the excitation force locations.

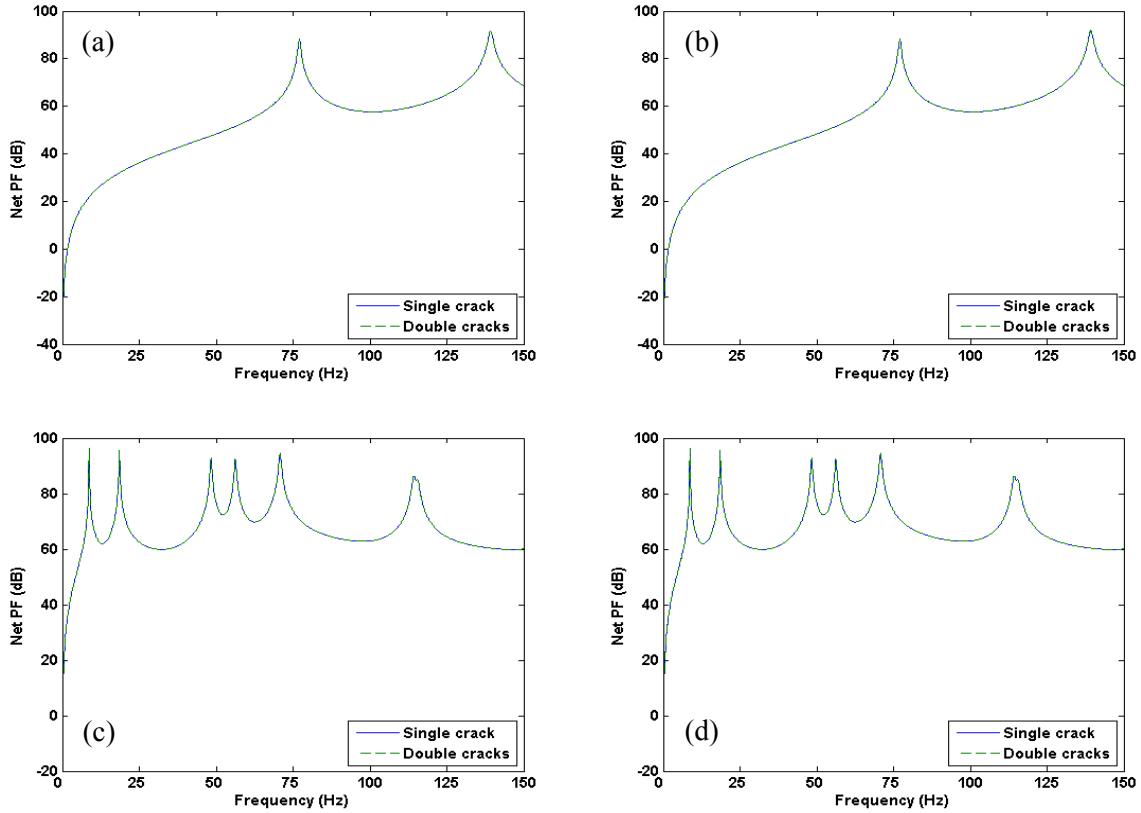

Figure 5.21: Net PF around excitation forces of plates: (a) clamped plate with one and two cracks parallel to the x axis; (b) clamped plate with one and two cracks perpendicular to the x axis; (c) cantilever plate with one and two cracks parallel to the x axis; (d) cantilever plate with one and two cracks perpendicular to the x axis.

For the cantilever plates (Figures 5.25-5.28), it can be observed that the differences of the net power flow magnitudes of the first and second cracks in each plot are lower than those of the clamped plates. The trends of the net power flow differences at the first and second cracks are not the same as those on the clamped plates. At the very low frequencies, the net power flow magnitudes at the tips of the first and second cracks are approximately the same. After the second resonance, the net power flow values of the second crack parallel to the x axis are slightly smaller than those of the corresponding first crack. At some

frequency ranges, the tips of the second crack perpendicular to the x axis have higher magnitudes of the net power flow than those of the first one that is located closer to the power source. This occurs due to the direction of power transmission in the cantilever plates as seen in the vector plots. The power from the sources transmits along the free end of the plates before going to the cracks.

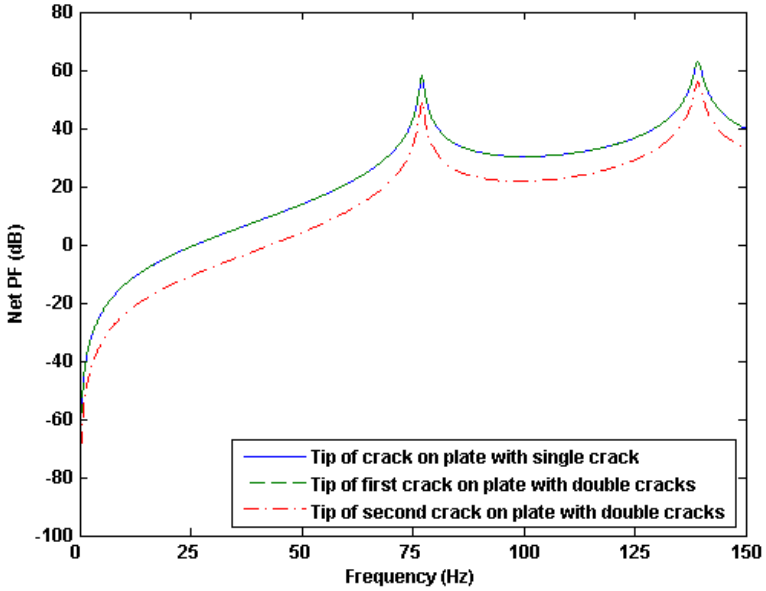

Figure 5.22: Net PF around crack tips of clamped plates with single and double cracks parallel to the x axis.

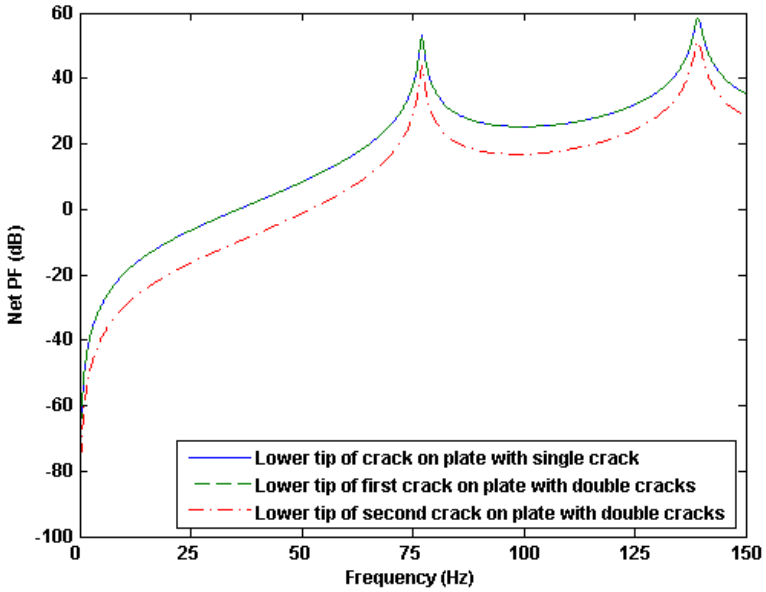

Figure 5.23: Net PF around lower crack tips of clamped plates with single and double cracks perpendicular to the x axis.

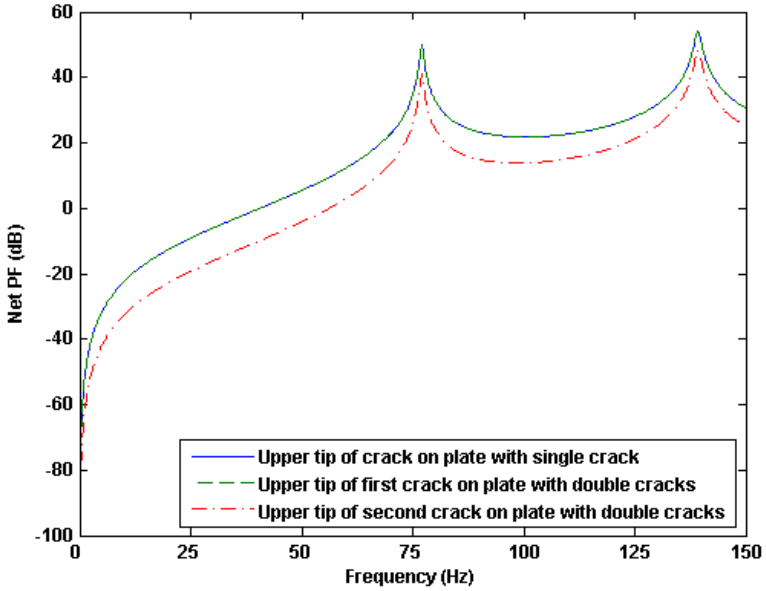

Figure 5.24: Net PF around upper crack tips of clamped plates with single and double cracks perpendicular to the x axis.

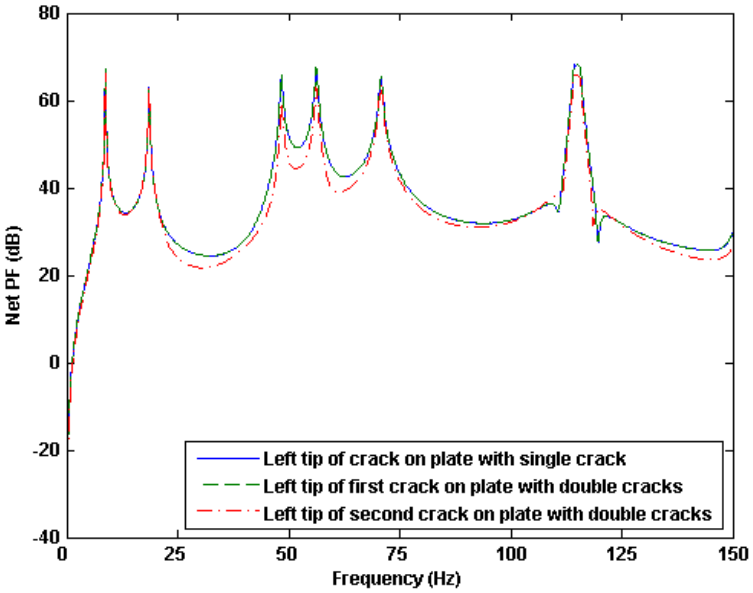

Figure 5.25: Net PF around left crack tips of cantilever plates with single and double crack parallel to the x axis.

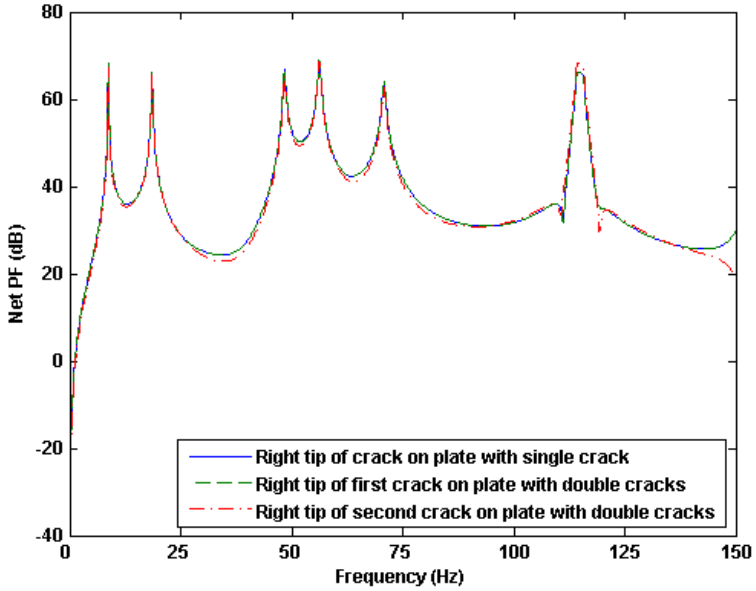

Figure 5.26: Net PF around right crack tips of cantilever plates with single and double crack parallel to the x axis.

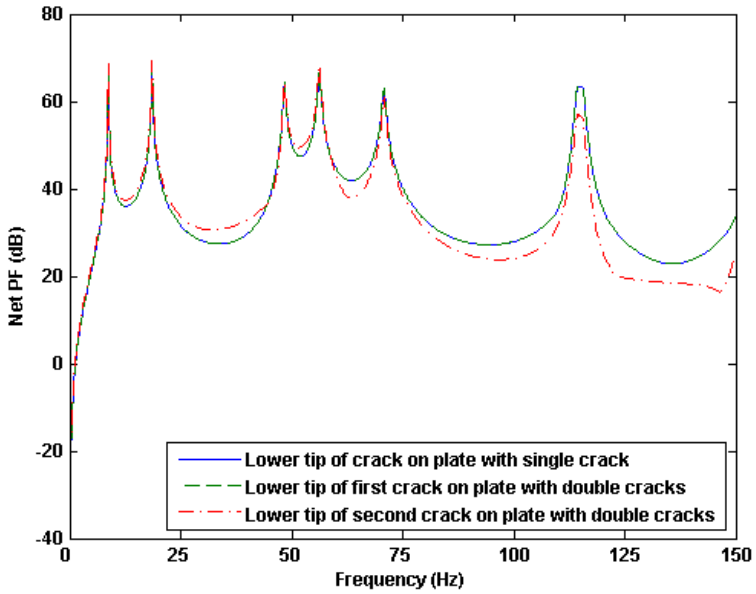

Figure 5.27: Net PF around lower crack tips of cantilever plates with single and double crack perpendicular to the x axis.

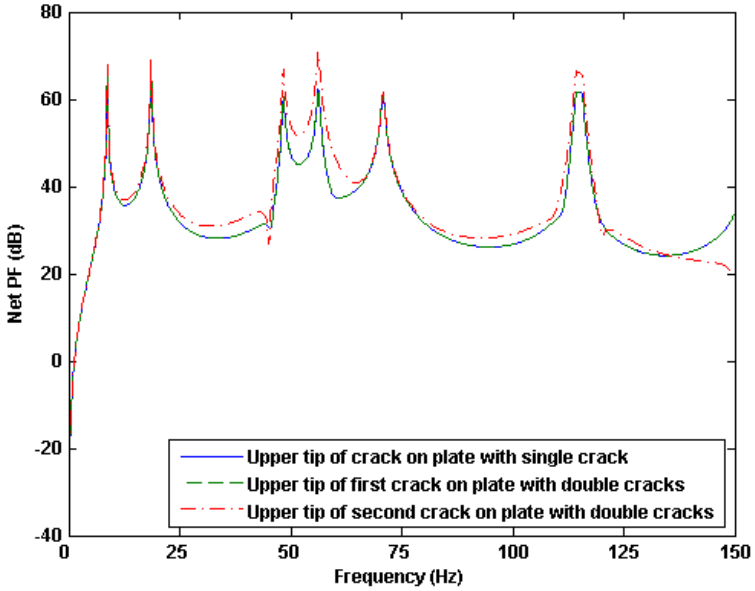

Figure 5.28: Net PF around upper crack tips of cantilever plates with single and double crack perpendicular to the x axis.

5.4 Power flow in plate containing three cracks

One more through-thickness crack is added to the plate. The geometry of the cracks is the same as that in the earlier sections, and three cracks on each plate are identical. The finite element models of the triple-cracked plates are shown in Figure 5.29.

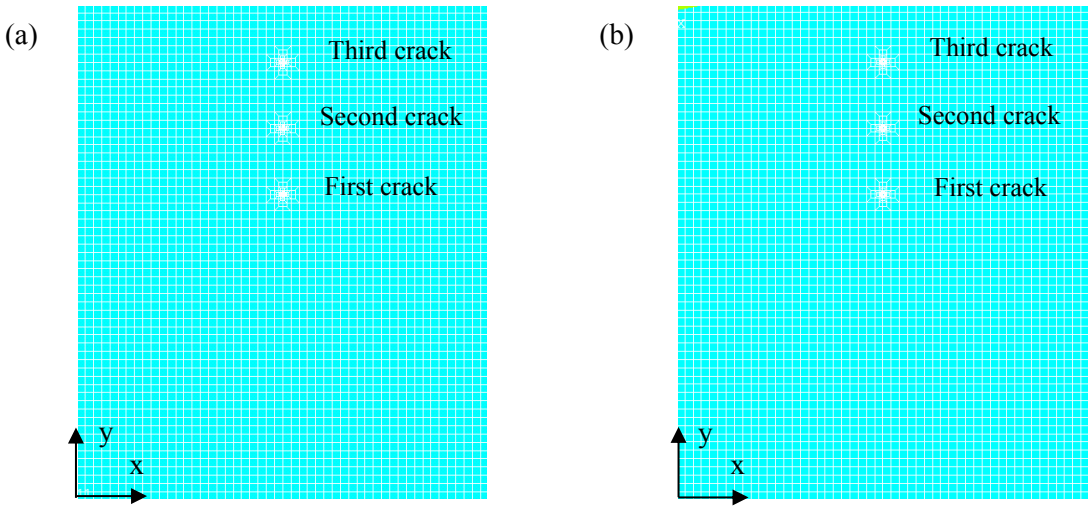

Figure 5.29: Models of triple-cracked plates: (a) cracks parallel to the x axis; (b) crack perpendicular to the x axis.

From the plate models, the second cracks are at the same location as those of the single cracked plates in Chapter 4. The first and the third cracks are at the locations of the second cracks in Section 5.2.1 and 5.2.2. The location of the excitation force is the same as before.

Table 5.21: Net PF around crack tips and excitation forces of plates containing three cracks parallel to the x axis

Plate/excitation frequency	First crack		Second crack		Third crack		Excitation force (dB)
	Left tip (dB)	Right tip (dB)	Left tip (dB)	Right tip (dB)	Left tip (dB)	Right tip (dB)	
Clamped plate/20 Hz	1.087	1.087	-4.278	-4.278	-14.383	-14.383	33.016
Clamped plate/100 Hz	32.806	32.806	30.278	30.278	21.846	21.846	57.693
Cantilever plate/20 Hz	37.765	41.584	38.393	42.182	38.397	42.081	72.882
Cantilever plate/100 Hz	32.760	32.415	32.629	31.703	32.111	32.129	62.958

Table 5.22: Net PF around crack tips and excitation forces of plates containing three cracks perpendicular to the x axis

Plate/excitation frequency	First crack		Second crack		Third crack		Excitation force (dB)
	Upper tip (dB)	Lower tip (dB)	Upper tip (dB)	Lower tip (dB)	Upper tip (dB)	Lower tip (dB)	
Clamped plate/20 Hz	-8.228	-4.501	-12.659	-9.992	-22.824	-20.019	33.016
Clamped plate/100 Hz	20.395	27.988	21.787	25.262	13.812	16.846	57.691
Cantilever plate/20 Hz	41.613	41.730	43.921	44.157	45.540	45.733	72.882
Cantilever plate/100 Hz	26.549	29.312	26.736	27.893	29.075	24.035	62.956

The values of the net power flow around the excitation forces and around the tips of the cracks parallel and perpendicular to the x axis are given in Tables 5.21 and 5.22. It can be observed from these tables that for the clamped plates, the values of the net power flow at the tips are directly proportional to the distance of the cracks from the excitation forces, but this relation is not valid for the net power flow in the cantilever plates. This trend is the same as that of the double-cracked plates shown earlier. The values of the net power flow around the crack tips and the excitation forces of the triple cracked plates are comparable to those of the cracks at the same location in single and double cracked plates. These results can show that the presence of the third minor cracks on the plates can significantly change the patterns and magnitudes of the power flow only at their locations. The patterns and magnitudes of the power flow at the uncracked locations are still comparable to those of the intact plates.

5.5 Summary

In this chapter, the power flow in the clamped and cantilever plates containing double and triple cracks is investigated. All of the cracks are assumed to have the same geometry. One of these cracks is located at the same position as those on the single cracked plates in Chapter 4. From the results, it can be concluded that the presence of the second and third small cracks on each plate does not affect the global pattern of the power flow. The significant changes in the power flow pattern and magnitude only occur at each crack location. At the other regions, the patterns and magnitudes of the power flow are analogous to those of the intact plates. Therefore, the location of each crack can be effectively revealed by the power flow.

The use of the FEM is advantageous to the power flow investigation in Chapter 4 and the present chapter since the elements at the region close to the crack can be refined and hence we can effectively observe the power flow patterns and magnitudes at the area near the crack. However, in practice, the location and severity of the crack are not known at the beginning, and types of measurement devices and size of measurement grids needed to be concerned. If the grid size is big when compared to the crack size, the location of the crack may not be shown successfully by the power flow. Hence, techniques that can enhance the inherent capability to detect damage of the power flow are required. These techniques will be introduced in the following chapters.

Chapter 6

Damage detection technique using power flow contours

6.1 Introduction

As seen from the earlier chapters, the local changes in the power flow can reveal the location of damage, and the changes in the power flow at the other regions are negligible. These results show the high potentials of the power flow to be used as a damage indicator for damage detection. In this chapter, a damage detection technique capable of detecting both damage location and severity in plate structures is introduced. The time-average power flow per unit length is used as a damage indicator based on the benefits of the local changes of the power flow at damage location stated earlier. The technique consists of two steps, which are the forward and reverse steps. The location and severity of damage are effectively revealed through power flow contour plots. The numerical case studies showing the effectiveness of the technique are completed using the FEM. Finally, the method for measuring the power flow relied on the transducer array and the finite difference method (FDM) is presented. Additionally, the simulation of the experimental measurements is performed to compare the power flows obtained from the FEM and the FDM.

6.2 Power flow computation scheme

As mentioned before, the computation of the power flow is carried out in the intact and damaged plates using the FEM throughout the chapter. Vibration responses of the plates i.e. displacement, velocity, and acceleration are obtained, and they are then transformed to stress and internal force components at the centroid of each element, which is necessary for the power flow calculation based on Equations (3.18) and (3.19). These two equations will produce the time-average vibrational power flow per unit length which will be labelled

as *power flow (PF)* in the chapter for the sake of convenience. The finite element codes for modelling the plates have been validated in the previous chapters.

6.3 Damaged plate modelling

6.3.1 Damage modelling

Damage will cause a local reduction in the structural stiffness at its location. Damage with higher severity can reduce more structural stiffness. The damage on the plate in this chapter is modelled based on this negative effect of damage on the structural stiffness. The method can be defined as *local stiffness reduction*, and it was previously employed in several works such as Wong et al. (2009) and Reddy and Swarnamani (2012). Propagation of the damage is neglected.

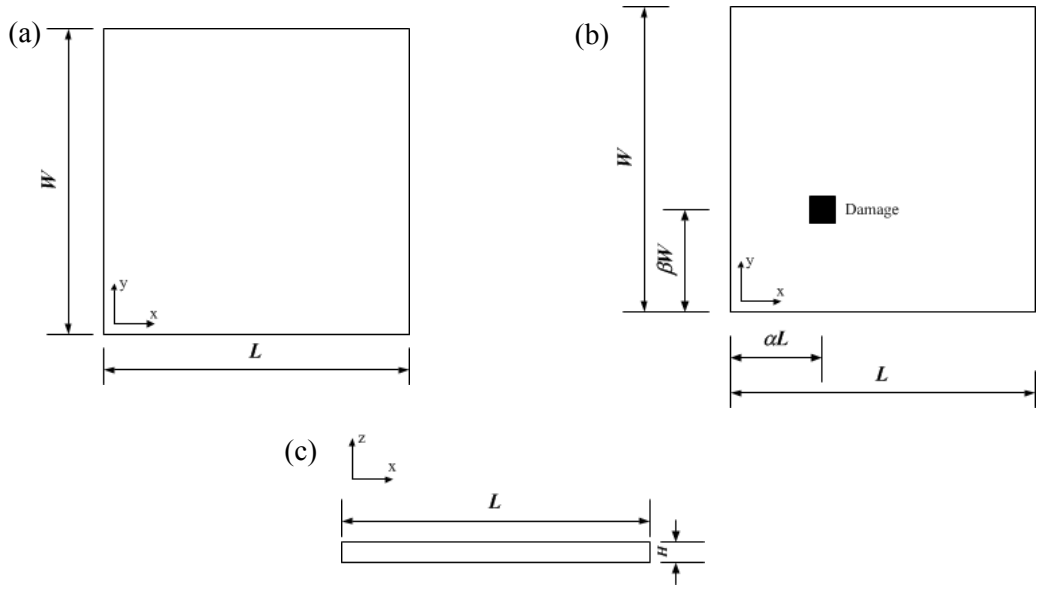

Figure 6.1: Thin plate model: (a) intact plate; (b) damaged plate; (c) plate thickness of intact and damaged plates.

The local stiffness method is used in conjunction with the FEM implemented by ANSYS to model damage at the specific location on the plate. At the location of the damage as shown in Figure 6.1(b), the element thickness is decreased to induce the stiffness reduction (see, Friswell and Penny (2002)), so it may be stated that the reduction in element thickness is directly proportional to the reduction in the local plate stiffness. More details of the damaged plate are given in the next section.

6.3.2 Intact and damaged plate models

The plate that will be used in case studies is a thin square plate (Figure 6.1). The locations of the excitation force and damage are defined by αL and βW, where L is plate length; W is plate width and α and β are dimensionless variables. However, only α and β are, hereinafter, used to show those locations, since the length and width of the plate are $1\,m$. The depth of damage, d, is normalised with the plate thickness, H, to obtain dimensionless damage depth, ζ. The geometry and material properties of the plate are given in Table 6.1. The plate contains constant structural damping ratio of 0.005, and the unit vertical excitation force is located at $\alpha = 0.5$ and $\beta = 0.05$. The shell elements having eight nodes per each in ANSYS are used to model the plate. Each element has 48 degrees of freedom, so 6 degrees of freedom, which are translations in the nodal x, y and z directions and rotations about the nodal x, y and z axis, is available at each node.

Table 6.1: Geometry and material properties of thin plates.

Length (L)	1.000 m
Width (W)	1.000 m
Thickness (H)	0.010 m
Young's modulus	210 GPa
Poisson's ratio	0.310
Mass density	7800 kg/m^3

The boundary conditions of the plate are given in Figure 6.2. The values of the power flow in the x and y directions in the intact simply supported plates composing of 1600 and 14400 shell elements are computed and given in Table 6.2. The first column of the table presents the locations on the plates where the power flow is calculated, and the second one shows the excitation frequencies of the input force. It can be seen that the values of the power flow generated by the same excitation frequency in both plates are approximately the same or slightly different. Therefore, discretising the plate into 1600 shell elements may be sufficient to produce accurate results of the power flow. This element number will be used to model the plates hereinafter in this chapter.

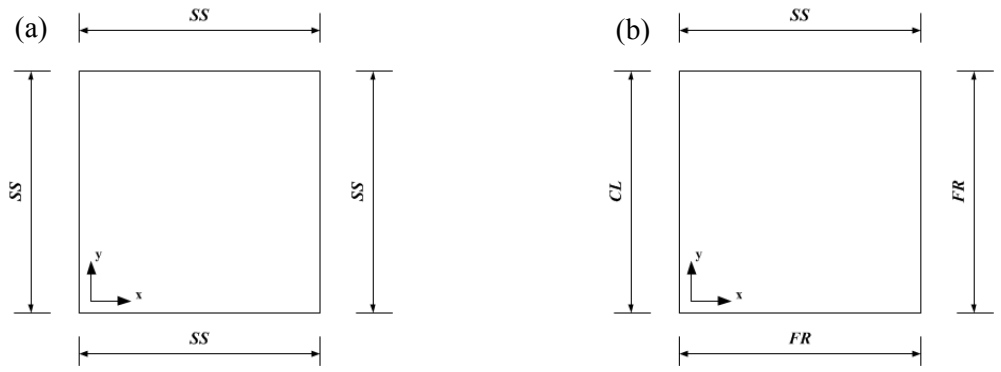

Figure 6.2: Boundary conditions used in case studies: (a) simply supported (SS); (b) mixed boundary conditions (CL = clamped, FR = free).

Table 6.2: Power flow in the intact simply supported plates created by different numbers of elements.

Computation location (α,β)	Number of elements	Excitation frequency (Hz)	Power flow in x direction (Watt/m)	Power flow in y direction (Watt/m)
(0.563,0.637)	1600	25	-4.54E-11	1.12E-09
		60	-2.82E-09	9.81E-08
		100	-3.39E-09	1.48E-07
	14400	25	-4.53E-11	1.12E-09
		60	-2.83E-09	9.83E-08
		100	-3.39E-09	1.48E-07
(0.188,0.287)	1600	25	-6.29E-10	1.49E-09
		60	-2.94E-08	7.29E-08
		100	-2.40E+08	5.82E-08
	14400	25	-6.30E-10	1.50E-09
		60	-2.94E-08	7.30E-08
		100	-2.41E-08	5.83E-08
(0.787,0.838)	1600	25	-5.52E-11	4.81E-11
		60	-4.39E-09	5.41E-09
		100	-6.61E-09	1.19E-08
	14400	25	-5.51E-11	4.82E-11
		60	-4.40E-09	5.43E-09
		100	-6.62E-09	1.20E-08

6.4 Sensitivity of power flow to damage

The sensitivities of the natural frequencies, mode shapes, and the power flow are compared. It is noted that the main purpose of this comparison is to show the sensitivities to damage of three aforementioned damage indicators when they are used without any other techniques to support or enhance their capabilities. The power flow is the

combination of force and velocity components, so it has the potential to be inherently more sensitive to damage.

The simply supported plates mentioned in Section 6.3.2 containing the damage at the locations $(\alpha, \beta) = (0.4875, 0.3125)$ and $(0.6125, 0.7625)$ with ζ varied from 0.1 to 0.4 are used as the specimens in the comparisons. The natural frequencies are the global properties of the plate, while the transverse displacements of the mode shapes and the power flow values are calculated locally at the damage locations.

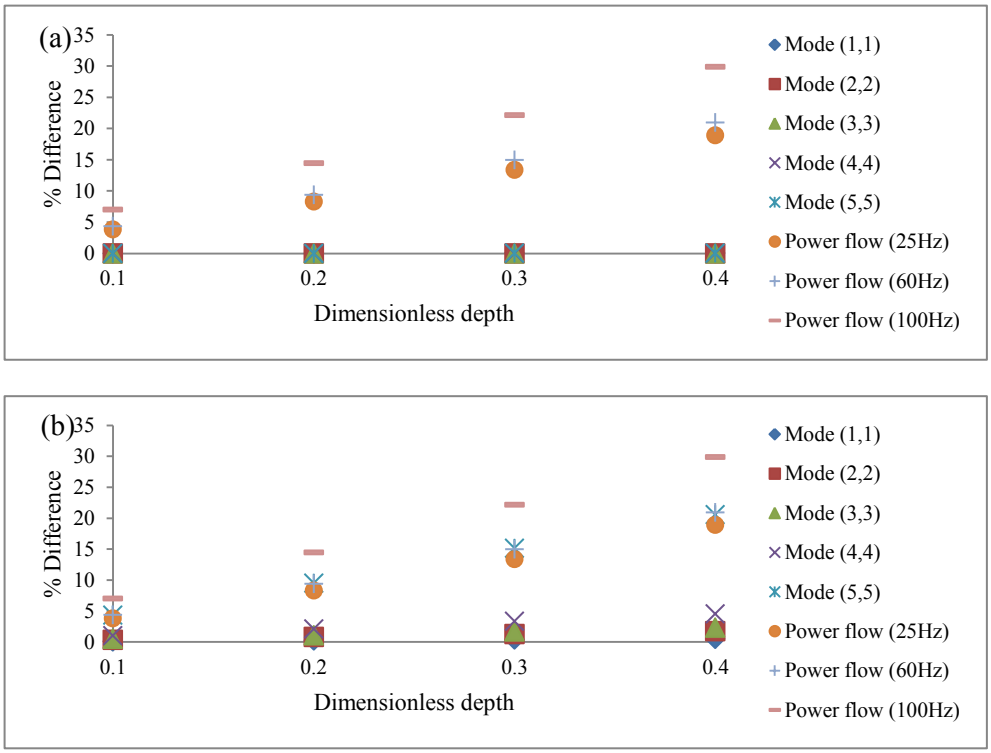

Figure 6.3: Percentage differences between natural frequencies, mode shapes and PFs of intact and damaged simply supported plates with damage at $(\alpha, \beta) = (0.6125, 0.7625)$: (a) PFs and natural frequencies; (b) PFs and mode shapes.

Figures 6.3 and 6.4 show the percentage differences between the natural frequencies of the flexural modes, the displacements of the mode shapes, and the power flow values induced by a unit force with the excitation frequencies of 25, 60 and 100 Hz. The values of the intact plate are used as the references. It can be seen clearly that the power flow is significantly more sensitive to the changes in damage depth than the natural frequencies, even the one of mode (5, 5) which is as high as approximately 1223 Hz. For the mode shapes, although the sensitivities of the mode shapes of the high-frequency mode, mode (5, 5), are comparable to those of the power flow values induced by some excitation

frequencies, mode shapes of high-frequency modes are difficult to be predicted experimentally. The other mode shapes are shown to be less sensitive than the power flow.

The patterns of the power flow in the intact and damaged simply supported plates and the plates with the mixed boundary conditions are presented in Figure 6.4. The power flow in each plate is generated by the forces with the excitation frequency of 100 Hz. The damage is located at (α, β) = (0.4875, 0.3125) of each damaged plate. The dimensionless damage depth, ζ, is 0.1 for the simply supported plate and 0.4 for the plate with the mixed boundary conditions. It can be inspected clearly that the power flow patterns of the simply supported plates and the plates with the mixed boundary conditions are different. For both boundary types, the powers transmit out of the locations of the input forces which have the highest power flow magnitudes shown by the dark-red colour, and their magnitudes are continuously reduced when they propagate away from their sources as seen in Chapters 4 and 5. The magnitudes of the power flows are high at the free ends of the plates with the mixed boundary conditions.

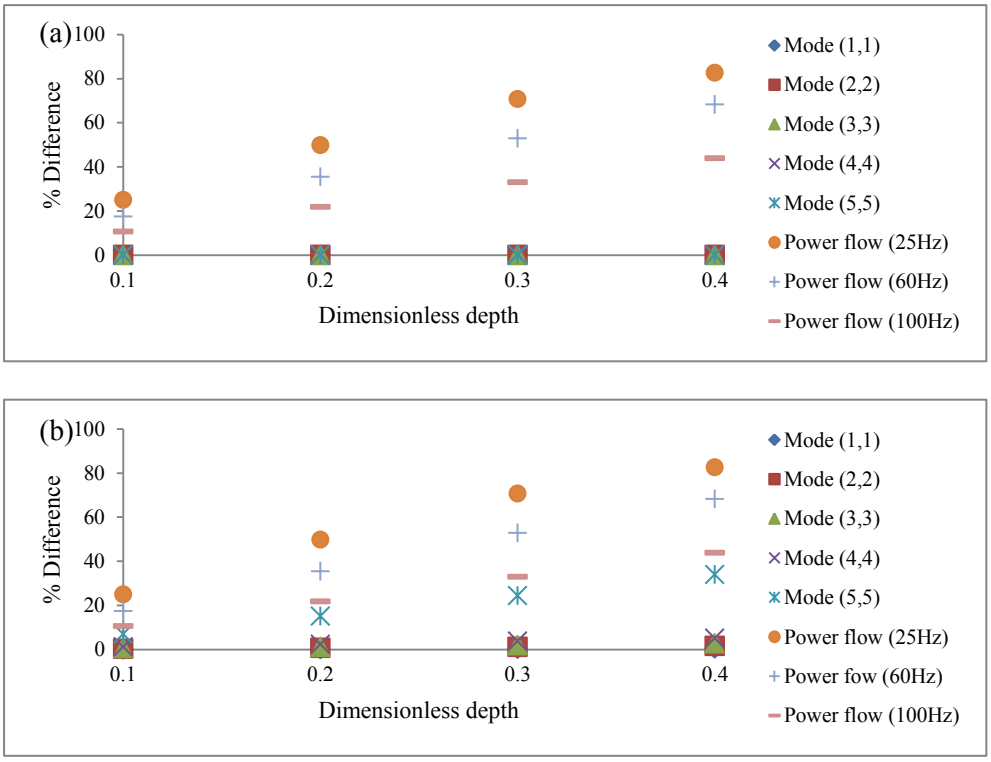

Figure 6.4: Percentage differences between natural frequencies, mode shapes and PFs of intact and damaged simply supported plates with damage at (α, β) = (0.4875, 0.3125): (a) PFs and natural frequencies; (b) PFs and mode shapes.

The locations of the damages can be noticed clearly from the abrupt changes in the power flow patterns in the damaged plates (Figures 6.5(b) and (d)) when comparing with those of the intact counterparts shown in their left hand sides. These pattern changes occur only at the damage locations. At the other places on the plates, the power flow patterns are the same for both intact and cracked plates. The results in Figure 6.5 can confirm the high sensitivity of the power flow to damage.

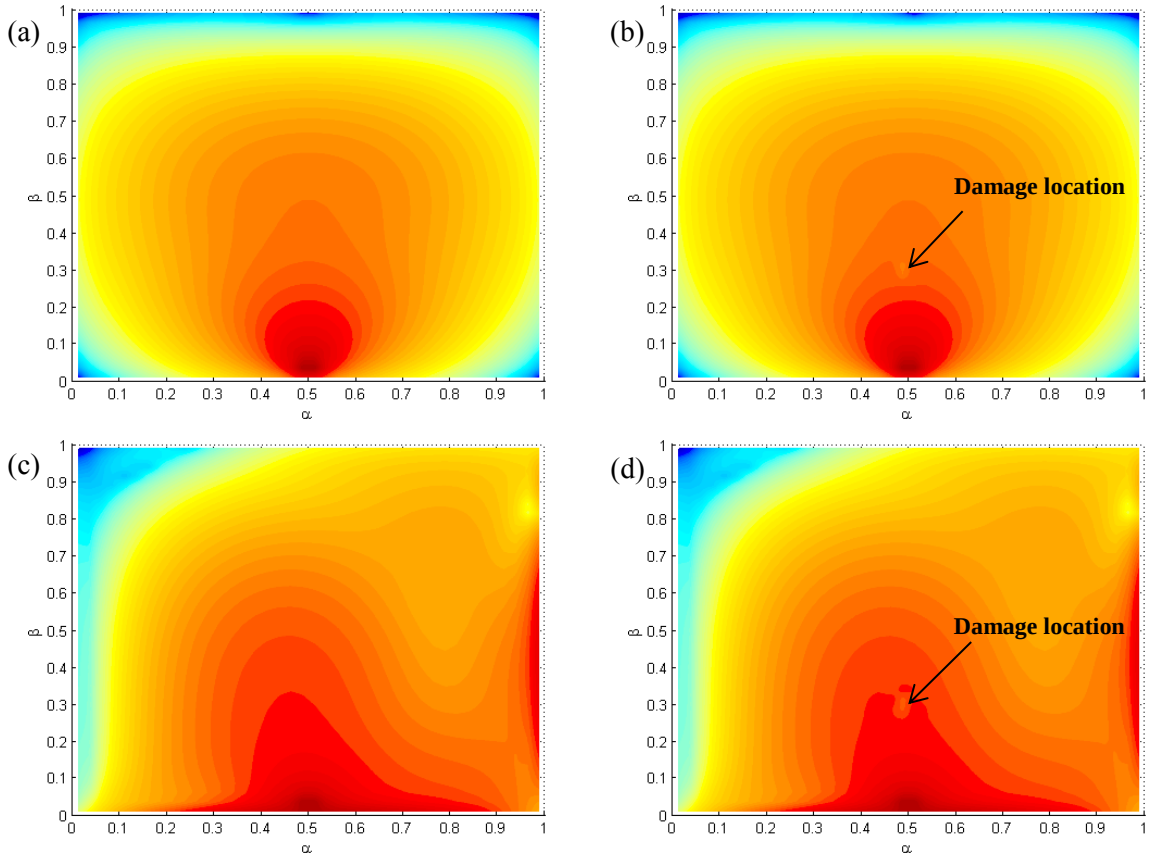

Figure 6.5: PF patterns: (a) intact simply supported plate excited by 100 Hz frequency; (b) damaged simply supported plate with damage at $(\alpha, \beta) = (0.4875, 0.3125)$ excited by 100 Hz frequency; (c) intact plate with mixed boundary conditions excited by 100 Hz frequency; (d) damaged mixed boundary condition plate with damage at $(\alpha, \beta) = (0.4875, 0.3125)$ excited by 100 Hz frequency.

6.5 Damage detection technique

The concepts of the technique to use an intersection of three power flow contour lines to present location and severity of damage on a plate structure are presented in this section. The technique comprises of two main steps which are power flow database creation (forward step) and detection of damage location and severity (reverse step). Previously, the damage detection technique using contour plots based on natural frequencies of the damaged beam was introduced by Li et al. (2005). As seen from the previous section, the natural frequency is not very sensitive to the changes in damage depth so that result errors may occur in the cases of very small damages, or the cases of two damages having very similar depths. In addition, the natural frequency contours in this reference cannot deal with the damage at the nodes of their vibration modes.

6.5.1 Power flow database creation (Forward step)

A square plate having the geometry and material properties presented in Table 6.1 is used to model a damaged plate. As mentioned in Section 6.3, the damage is generated on the plate by reducing the stiffness of the plate at the location of the damage. From Figure 6.1, the location of damage is defined by αL and βW, where α and β are dimensionless variables. The plate is discretised into 1600 eight-node shell elements. Since both the length and the width of the plate are equal to $1\,m$, the dimensionless variables α and β can be used directly to show locations of the damage on the plate, the power flow measurement points, and the excitation force.

In the considered case, a unit excitation point force is placed at $\alpha = 0.5$ and $\beta = 0.025$. The power flow is computed from the consecutive 20 elements (in line parallel to the x coordinate) which have their centroids located at the positions from $\alpha = 0.2625$ and $\beta = 0.0625$ (first point) to $\alpha = 0.7375$ and $\beta = 0.0625$ (last point). The position of the damage will range from $(\alpha, \beta) = (0.0125, 0.0875)$ to $(\alpha, \beta) = (0.9875, 0.9875)$ based on the element centroid. It is noted that the locations of the excitation force and the number of the measurement points and their locations are not restricted, but they must be the same as those used in the reverse step that will be discussed in the next section.

Since the power flows in the x and y directions at each measurement point are the vector quantities, the magnitude of the power flow created by the summation of these two vectors can be obtained by

$$|\langle \boldsymbol{P}(x,y;t)\rangle_t| = \sqrt{\langle P_x(x,y;t)\rangle_t{}^2 + \langle P_y(x,y;t)\rangle_t{}^2} \tag{6.1}$$

where $\boldsymbol{P}$ is the power flow magnitude. The numerical integration, Trapezoidal rule, is employed to complete the integration for these power flow magnitudes obtained from 20 consecutive points, since the power flow can only be measured at a discrete point of the centroid of each element (see, Gavrić and Pavić (1993)). The result obtained from this integration is designated as *net power flow (net PF)* having the unit of Watt (W).

The depth of the damage, d, is normalised by dividing it with the plate thickness, H. This dimensionless depth is represented by ζ. Thus, ζ can be expressed as $\zeta = d/H$. Dimensionless net power flow is generated by dividing the net power flow obtained from the damaged plate, P_d, by the net power flow from the intact counterpart, P_{int}, so it can be written as Dimensionless net power flow (DNPF) = P_d/P_{int}. This DNPF is determined at the measurement points when the damage having ζ from 0 (no damage) to 1 (damage depth equal to plate thickness) is located at each location around the plate, within the range mentioned earlier. This damage location is assumed to be relied on the location of the centroid of each element. The excitation frequency, f_e, is then changed to another one, and the same procedure of the DNPF determination as mentioned above is then performed again. At least three excitation frequencies are required in this forward step. These three excitation frequencies can be any. However, they should not be close to each another to avoid errors that may occur when the DNPFs obtained from the excitation frequencies are almost the same.

All of the DNPFs of three excitation frequencies obtained from the aforementioned procedure are collected as a power flow database. The flowchart of this procedure is shown in Figure 6.7(a). Consequently, it may be stated that the quantity of the DNPF obtained from the damaged plate excited by an excitation frequency is dependent on three dimensionless parameters, α, β and ζ of the damaged plate.

Examples of the DNPFs obtained from the damaged plates with all edges simply supported and mixed boundary conditions are shown in Figure 6.6. Each surface plot contains the

DNPFs of the specific f_e obtained from the measurement points mentioned previously, while the position of the damage with a specific ζ will change from being at the first element to the last element of the plate. Thus, the DNPF at each position on the surface plots is the one obtained from the measurement points when the damage is located at that position.

These surface plots of the data in the power flow database will also display the characteristic of the power flow when the damage is placed at each position on the plate. It can be observed from Figure 6.6 that the huge differences between P_d and P_{int} occur when the damage is located near the excitation force of each plate. The trend of this difference at each position is increased when ζ and/or f_e grows up.

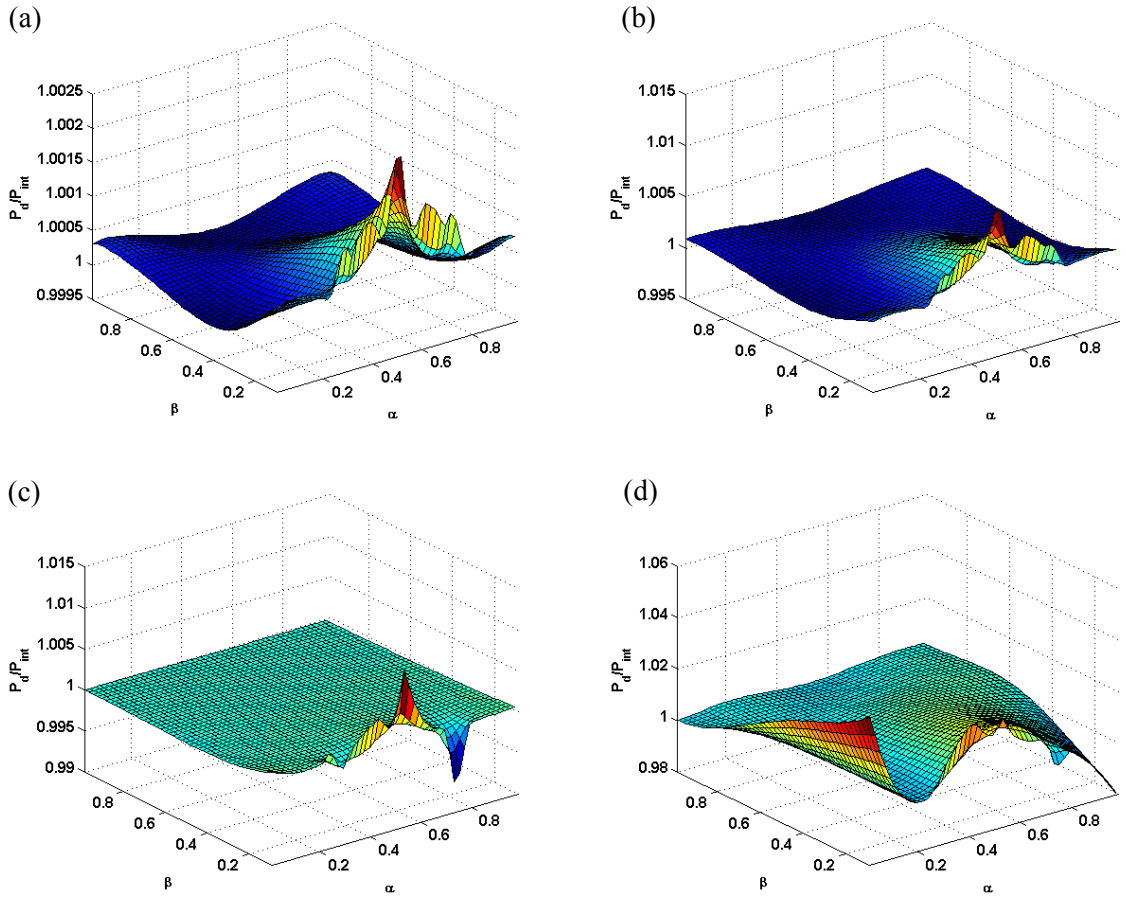

Figure 6.6: DNPF: (a) simply supported plate $f_e = 25\ Hz, \zeta = 0.10$; (b) simply supported plate $f_e = 25\ Hz, \zeta = 0.30$; (c) mixed boundary conditions $f_e = 25\ Hz, \zeta = 0.10$; (d) mixed boundary conditions $f_e = 60\ Hz, \zeta = 0.10$.

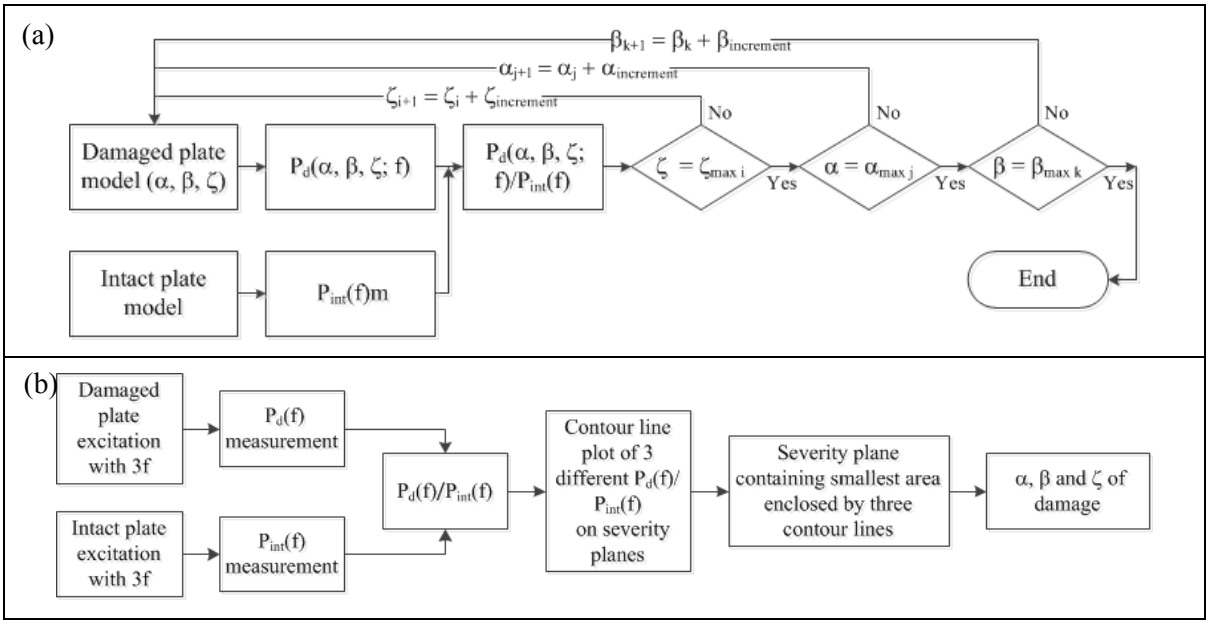

Figure 6.7: Flowchart presenting the procedures for damage detection: (a) power flow database creation or forward step; (b) damage detection or reverse step.

6.5.2 Detection of damage location and severity (Reverse step)

In this section, the power flow database created in Section 6.5.1 is used in conjunction with contour plots to identify damage location and severity on the damaged plate. The procedure to do this is in reverse to that of the power flow database creation in Section 6.5.1. The DNPFs of three f_e measured experimentally from the tested plate having the possibility to contain damage is used to determine the dimensionless parameters, α, β and ζ which will reveal the information of the damage location and severity. Thus, it may be stated that, for this reverse step, the parameters, α, β and ζ are dependent on the measured DNPFs. In this chapter, the DNPFs for the reverse step are obtained from numerical computations (FEM).

Apart from the surface plots (Figure 6.6), the data in the power flow database can also be displayed using contour plots, as shown in Figure 6.8. Each contour plot of each f_e and ζ is designated as *severity plane*. Therefore, there are three sets of the severity planes categorised by three f_e, and each set contains the DNPFs when the damage with ζ is located at different locations on the plate. It is worth to mention again that $\zeta = 0$ means it has no damage on the plate, and $\zeta = 1$ means the depth of damage equals to the plate thickness.

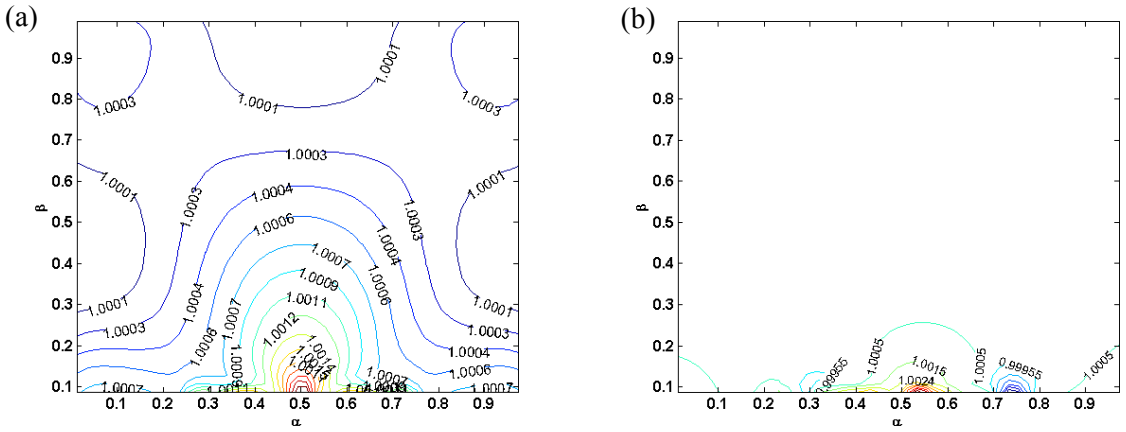

Figure 6.8: Contours of DNPFs: (a) simply supported plate: $f_e = 25\ Hz, \zeta = 0.10$; (b) mixed boundary conditions :$f_e = 25\ Hz, \zeta = 0.10$.

To obtain the location and severity of the damage, the unit force with three f_e which are the same as those used in the forward step, is required to generate power flow in the tested plate. Thus, three values of the DNPFs are obtained. It is noted that the locations of the excitation force and measurement points must also be the same as those used in the forward step. These three DNPFs are then used as inputs to the severity planes of their corresponding f_e. The severity planes returns the values that are matched with the input DNPFs, and shows as contour lines. After that, the contour lines on the severity planes with the same ζ of each f_e are combined.

An example of the combination of the severity planes with the same ζ of each f_e is illustrated in Figure 6.9. The location of the centroid of the smallest enclosed area created by these three contour lines will show the location of the damage, and the combined severity plane on which the smallest area is will present the damage severity. For a square plate having the length and the width of $1\ m$ as the one used in the case studies in this chapter, the values of α and β can directly represent the locations of the damage. The summary of the procedure for completing this damage detection mentioned above is summarised in the flowchart shown in Figure 6.7(b).

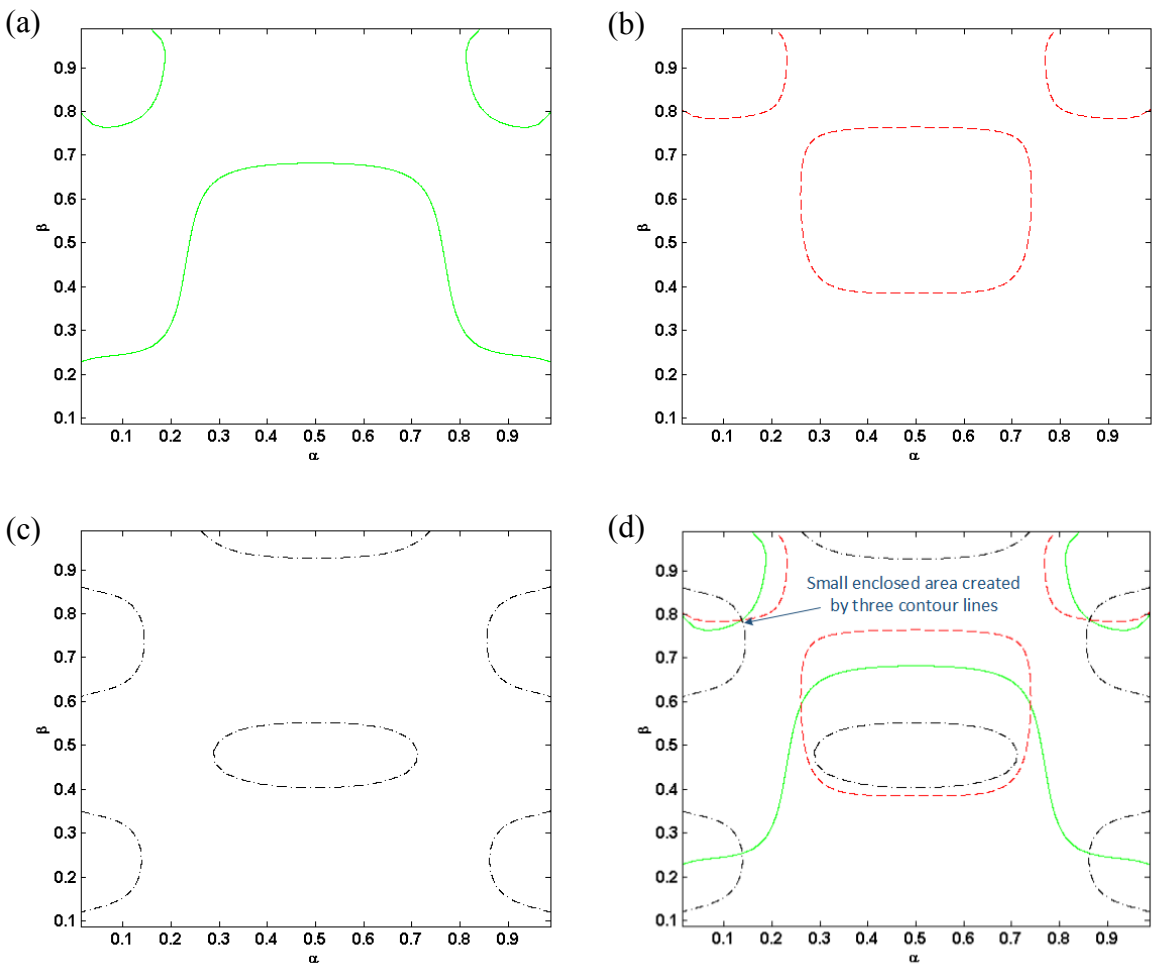

Figure 6.9: Contour plots of DNPFs on severity planes: (a) severity plane of $f_e = 25\ Hz$ and $\zeta = 0.10$; (b) severity plane of $f_e = 60\ Hz$ and $\zeta = 0.10$; (c) severity plane of $f_e = 100\ Hz$ and $\zeta = 0.10$; (d) combined severity plane.

6.6 Applications of damage detection technique

The effectiveness of the proposed damage detection technique based on power flow contour plots is presented through a number of case studies of damaged plates with all edges simply supported and mixed boundary conditions. Both forward and reverse steps of all case studies are completed using finite element simulation implemented by ANSYS.

6.6.1 Plate with all edges simply supported

The damage having the dimensionless depth, ζ, of 0.10 and located at $\alpha = 0.2875$ and $\beta = 0.5125$ is modelled on the simply-supported plate. It is assumed that these damage location and severity are unknown before. The DNPFs induced by the excitation frequencies of 25 Hz, 60 Hz and 100 Hz are obtained from the plate as inputs of the reverse step of the proposed damage detection technique. These excitation frequencies have to be the same as those used in the forward step. It is noted that in real cases, these three DNPFs are obtained from experimental measurements of the tested plate having potential to contain damage.

After inputting to the reverse step, these three values of DNPF are plotted as contour lines on the severity planes of ζ to find the plane that contains the smallest enclosed area generated by these three contour lines of the DNPFs. The centroid of this small enclosed area will give the location of the damage. The contour lines of these three DNPFs on the severity planes of $\zeta = 0.10$, 0.30 and 0.50 are shown in Figure 6.10 as examples of the results. The green solid line is of the DNPF at 25 Hz, while the red dashed line and black dash-dot lines are of the DNPFs at 60 and 100 Hz, respectively.

It can be observed that there is no small enclosed area created by three contour lines in the severity planes of $\zeta = 0.30$ and 0.50. Two identical small enclosed areas present in the severity plane of $\zeta = 0.10$ at $(\alpha, \beta) = (0.2875, 0.5125)$ and $(\alpha, \beta) = (0.7125, 0.5125)$. The left one in the red circle is the actual damage location, whereas the other on the right is the unreal one occurring due to the symmetries of the boundary condition, the excitation force and the measurement point locations about the centre line of the plate parallel to y axis. This unreal damage location can be eliminated by moving the excitation force or the measurement points toward one edge of the plate or changing the plate boundary condition. From the results of this case study, the damage location and severity revealed by the

proposed damage detection technique are exactly the same as those simulated on the plate at the beginning.

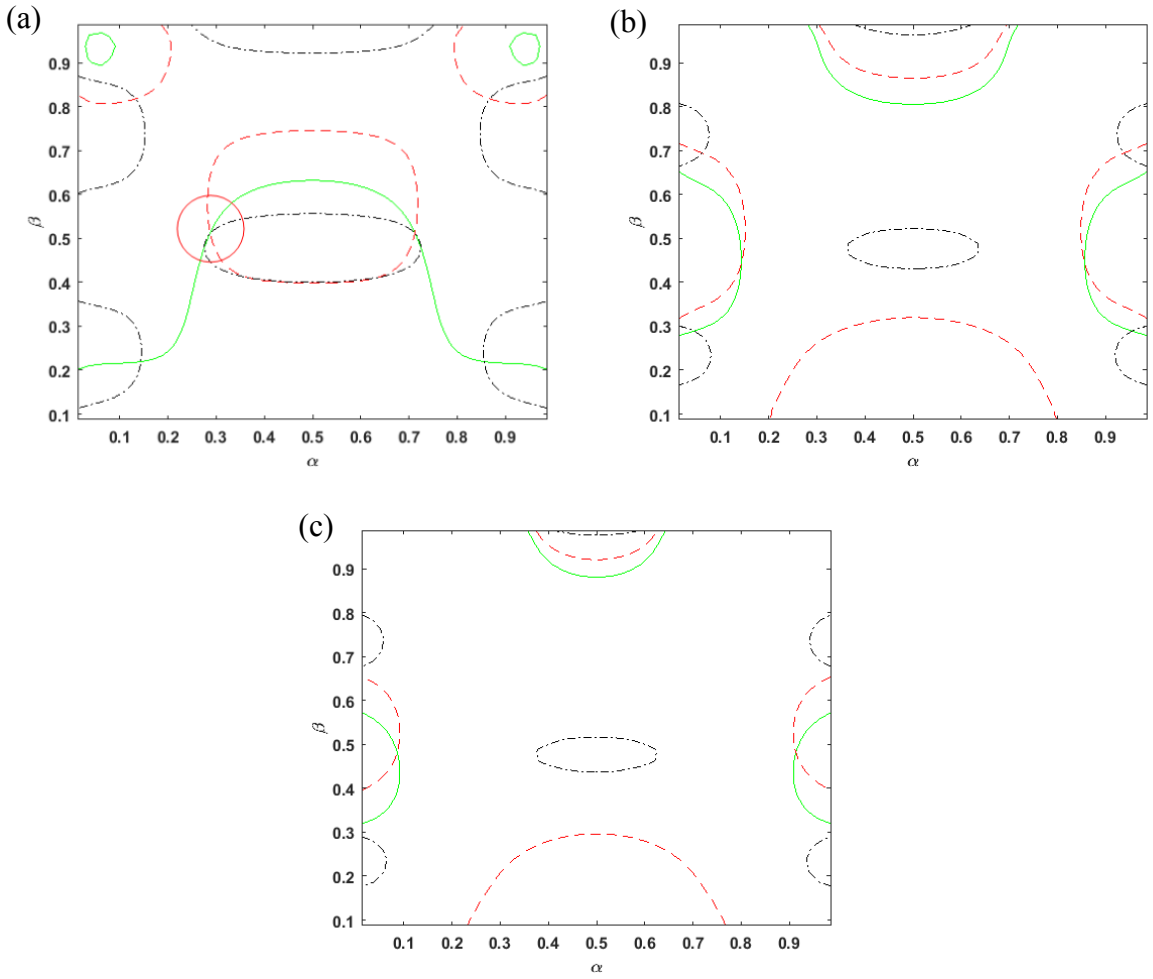

Figure 6.10: Contour plots on severity planes of DNPFs in damaged plate with simply supported boundary condition ($\alpha = 0.2875, \beta = 0.5125$): (a) severity plane of $\zeta = 0.10$; (b) severity plane of $\zeta = 0.30$; (c) severity plane of $\zeta = 0.50$.

The second case study of the simply supported plate is also presented. All of the parameters used in the computation are the same as the previous case, except the damage location which is changed to be at $\alpha = 0.8625$ and $\beta = 0.7875$, instead.

Figure 6.11 displays two smallest enclosed area of the DNPF contour plots on the severity plane of $\zeta = 0.1$ at the location (α, β) = (0.1372, 0.7875) and (α, β) = (0.8625,0.7875). The right one in the red circle is of the real damage location. The unreal location still presents here due to the aforementioned symmetries. There is no small enclosed area on the other two severity planes. The damage location and severity illustrated by Figure 6.11(a) are identical to those simulated on the plate. The proposed damage detection technique works

effectively with the plate having all edges simply supported. Only the drawback of the unreal location occurred due to the symmetries of the excitation force and measurement locations are needed to be overcome.

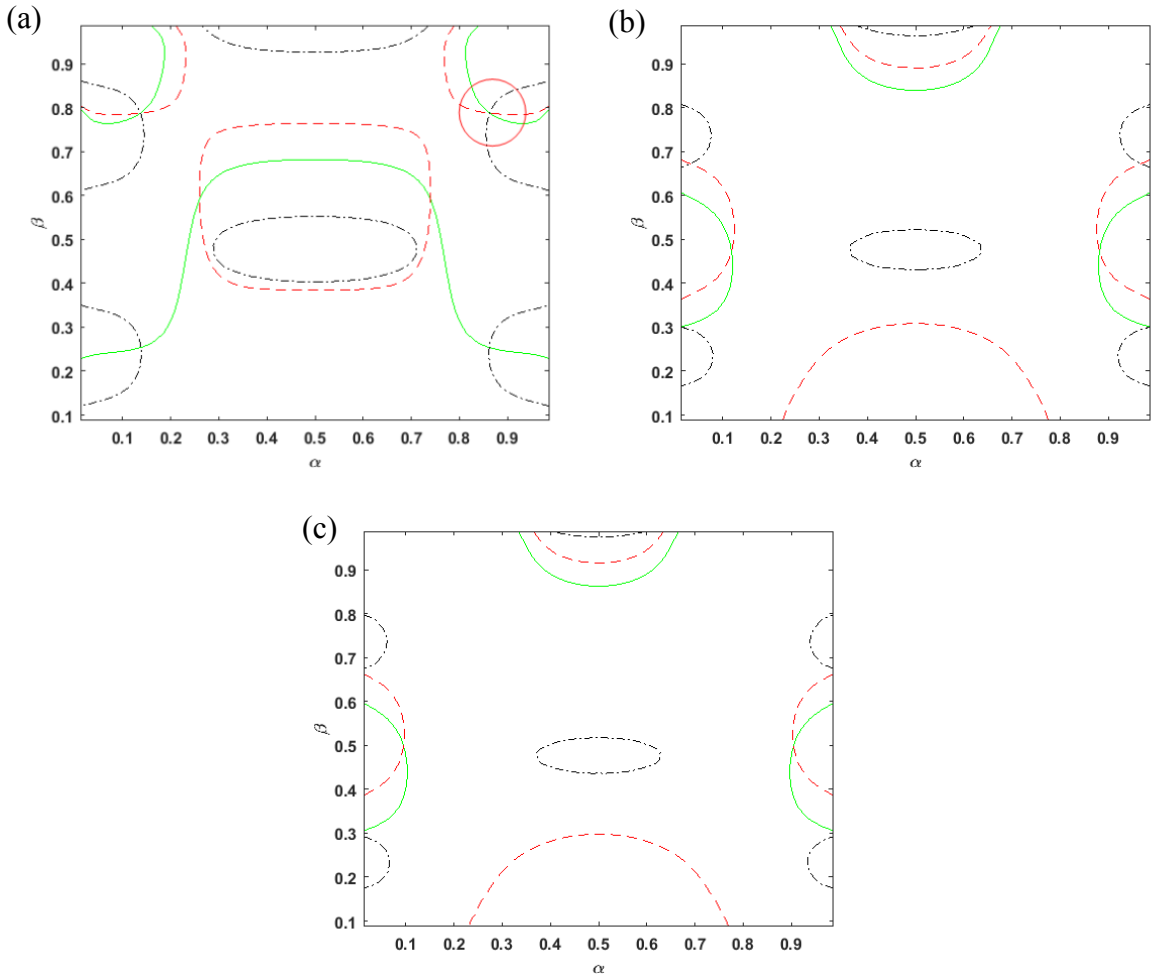

Figure 6.11: Contour plots on severity planes of DNPFs in damaged plate with simply supported boundary condition ($\alpha = 0.8625, \beta = 0.7875$): (a) severity plane of $\zeta = 0.10$; (b) severity plane of $\zeta = 0.30$; (c) severity plane of $\zeta = 0.50$.

6.6.2 Mixed boundary conditions

The first and the second case studies mentioned above are the cases of the plates with the symmetric boundary conditions (all edges simply supported). In other word, they have the same boundary condition at two parallel edges. The mixed boundary conditions of the plate are not symmetric. Only one small enclosed area will be created on the correct severity plane. The damage with dimensionless depth, ζ, of 0.10 is simulated at $\alpha = 0.2875$ and $\beta = 0.5125$.

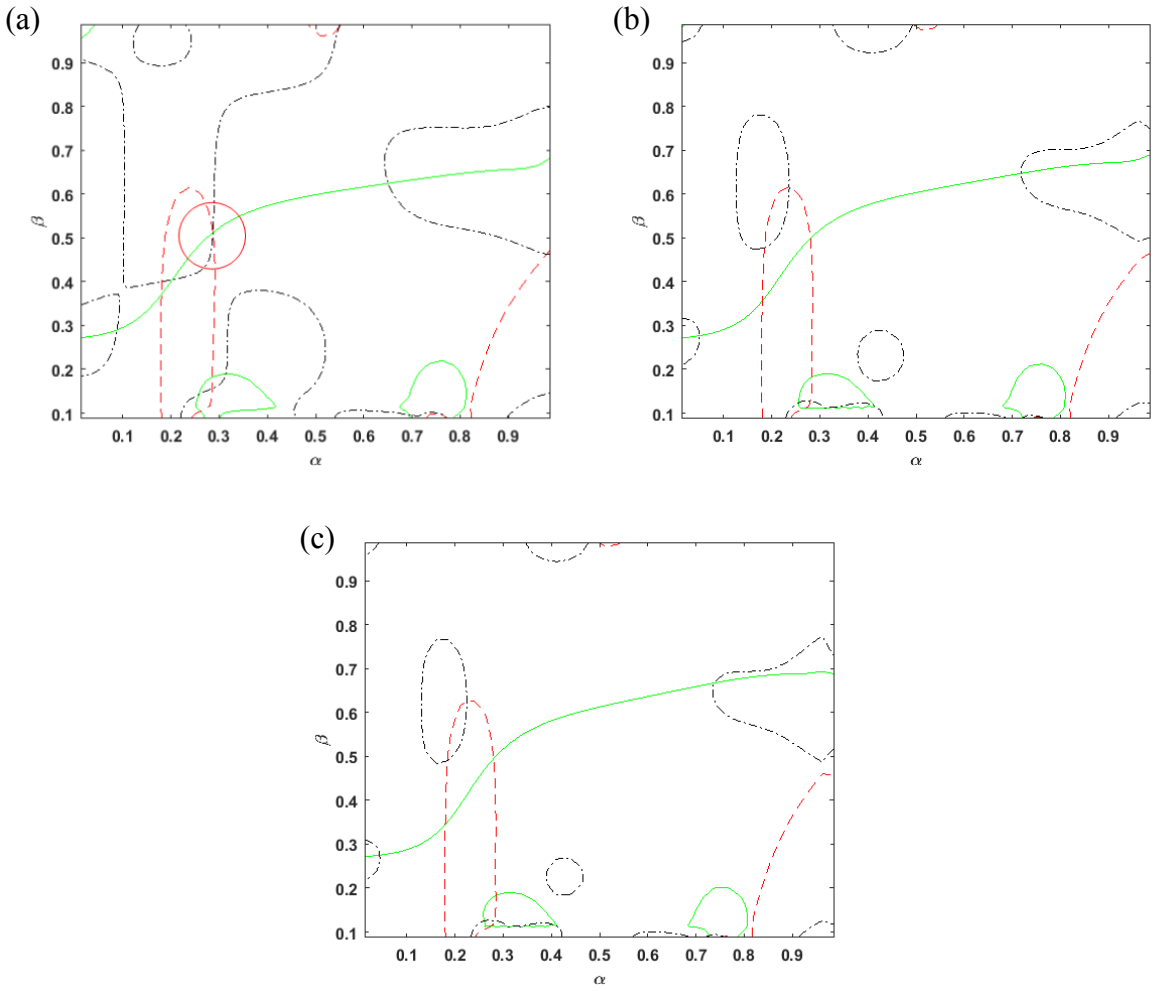

Figure 6.12: Contour plots on severity planes of DNPFs in damaged plate with mixed boundary conditions ($\alpha = 0.2875, \beta = 0.5125$): (a) severity plane of $\zeta = 0.10$; (b) severity plane of $\zeta = 0.30$; (c) severity plane of $\zeta = 0.50$.

Three severity planes containing the DNPF contour lines are shown in Figure 6.12. The DNPFs of 25 Hz, 60 Hz and 100 Hz are presented by green solid line, red dashed line and black dash-dot line, respectively. Due to the non-symmetric boundary conditions, only one small enclosed area appears on the severity plane of the damage depth ($\zeta = 0.10$). The location of the damage is the point at the centre of the small area in the red circle. It is shown to be at $\alpha = 0.2875$ and $\beta = 0.5125$ which is the same as the location of the damage simulated on the plate at the beginning.

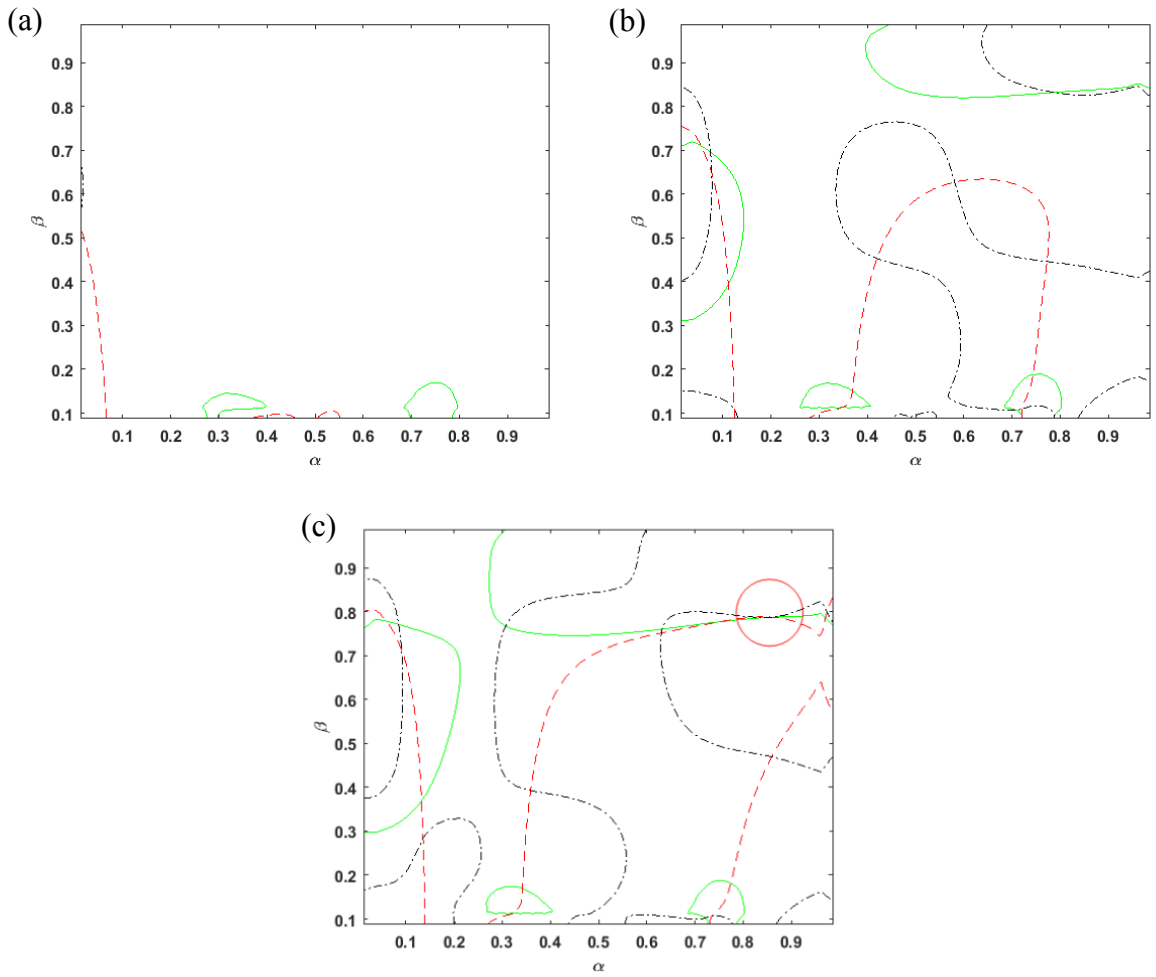

Figure 6.13: Contour plots on severity planes of DNPFs in damaged plate with mixed boundary conditions ($\alpha = 0.8625, \beta = 0.7875$): (a) severity plane of $\zeta = 0.10$; (b) severity plane of $\zeta = 0.30$; (c) severity plane of $\zeta = 0.50$.

The second case study for the plate with the mixed boundary conditions is also carried out. The damage having $\alpha = 0.8625$, $\beta = 0.7875$ and $\zeta = 0.50$ is initially simulated on the plate. The examples of the severity planes are shown in Figure 6.13. It is seen that the damage location and depth obtained from one of the severity planes shown in Figure 6.13 are $\alpha = 0.8625$, $\beta = 0.7875$ and $\zeta = 0.5$ which are identical to those of the simulated damage on the plate. For the cases of the plate with the mixed boundary conditions, only one smallest area that shows the damage location appears on the severity plane that tells the damage severity. Changing boundary condition of the plate to the non-symmetric one can eliminate the occurrence of the unreal small enclosed area, even though the symmetries of the excitation and measurement locations about the centre line of the plate are still not fixed.

6.6.3 Elimination of unreal damage location

It is seen from the case of the simply supported plate that the symmetries of the boundary conditions and the locations of the excitation force and measurement points lead to the symmetry of the DNPF contour plots which produces two identical small enclosed areas on the correct severity plane of damage depth. In this section, a case study of the simply supported plate, when the excitation force is moved from the position at $\alpha = 0.5$ and $\beta = 0.025$ to a new position out of the centre line of the plate parallel to the y axis is examined.

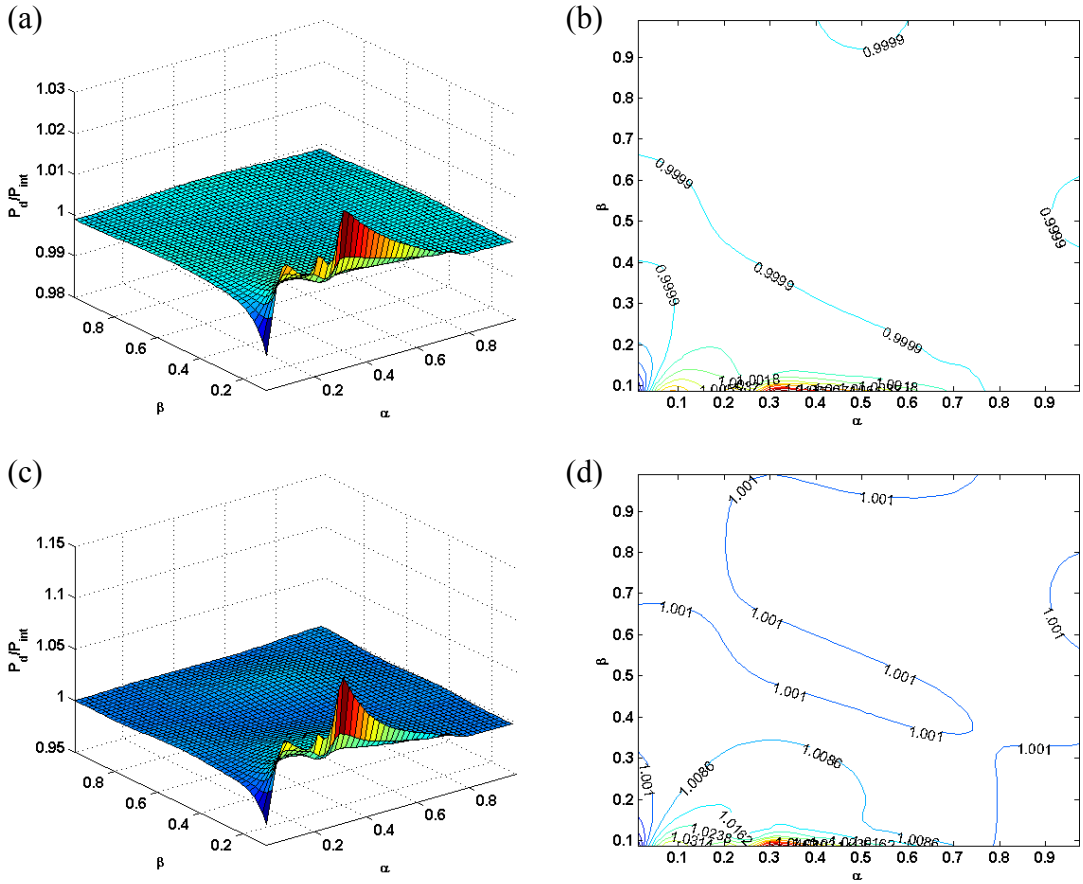

Figure 6.14: DNPFs in damaged plate with all edges simply supported excited by unit excitation force at $\alpha = 0.025$ and $\beta = 0.025$; (a) and (b) are surface and contour plots of $f_e = 60\ Hz$ and $\zeta = 0.1$; (c) and (d) are surface and contour plots of $f_e = 100\ Hz$ and $\zeta = 0.4$.

The unit excitation force is moved toward the corner of the plate to locate at the position $\alpha = 0.025$ and $\beta = 0.025$. The measurement points are still kept in the same positions as before. The power flow database is created based on the procedure in the flow chart in Figure 6.7. The DNPFs of the simply supported plate in the surface and contour plots are

shown in Figure 6.15 as the examples of the power flow database. It is seen from the figure that once the excitation force are moved to the new position, the symmetries of the power flow patterns in both surface and contour plots are disappeared. These contour plots are combined together to create the severity plane of each ζ.

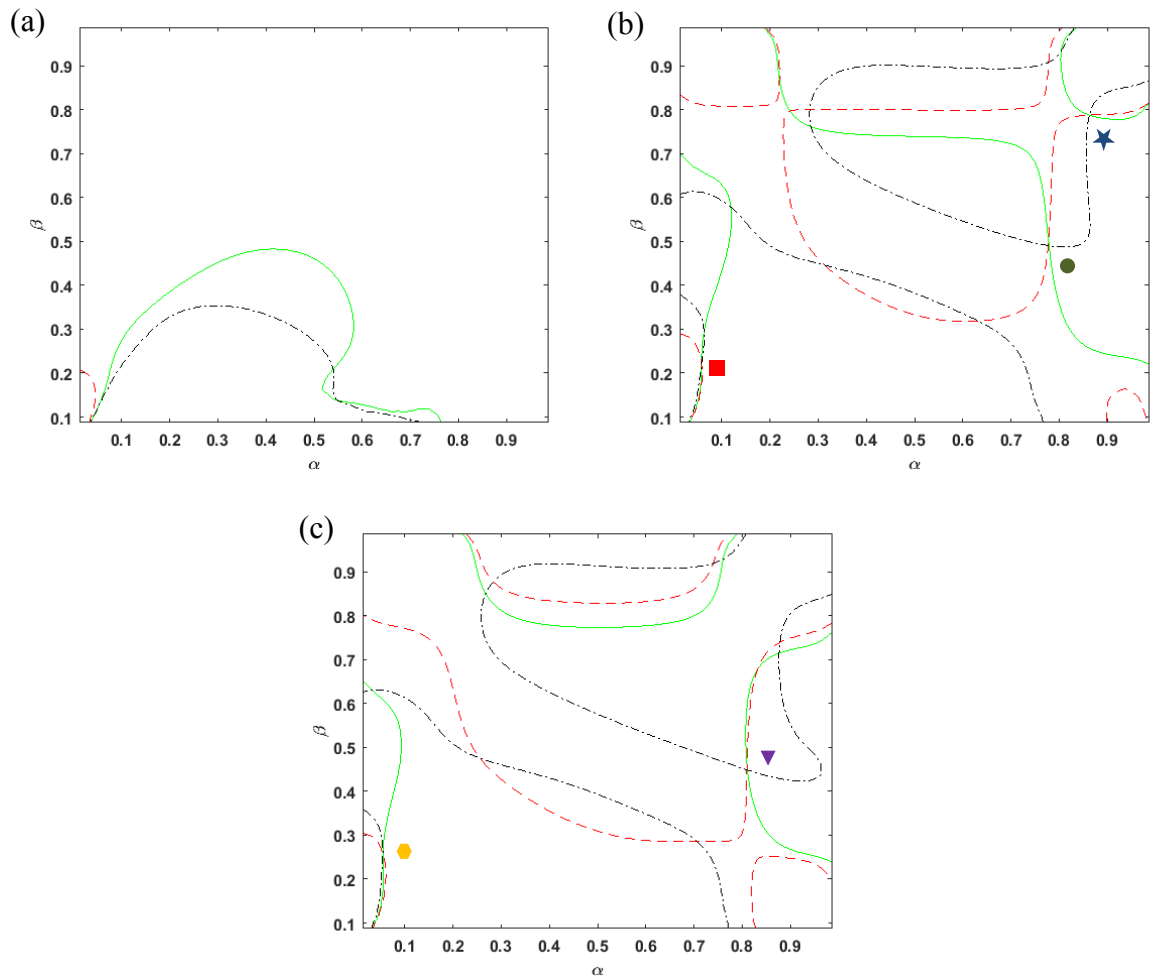

Figure 6.15: Contour plots on severity planes of DNPFs in damaged simply-supported plate ($\alpha = 0.8625, \beta = 0.7875$) excited by unit force at the plate corner: (a) severity plane of $\zeta = 0.11$; (b) severity plane of $\zeta = 0.32$; (c) severity plane of $\zeta = 0.40$.

For the case study, the damage with $\zeta = 0.32$ located at $\alpha = 0.8625$ and $\beta = 0.7875$ is simulated on the plate. This information of the damage is assumed to be unknown at this point. Three DNPFs are obtained from the damaged plate. The DNPFs are then plotted in the severity planes to obtain the location and severity of the damage. It can be observed from Figure 6.15 that two contour plots of the severity planes, which are in Figures 6.15(b) and (c), seem to contain five small enclosed areas. The coloured shapes are put at the locations of these small areas to label them. Only the smallest area will be selected as an

indicator of the damage location and the severity plane containing this area will give the severity of the damage.

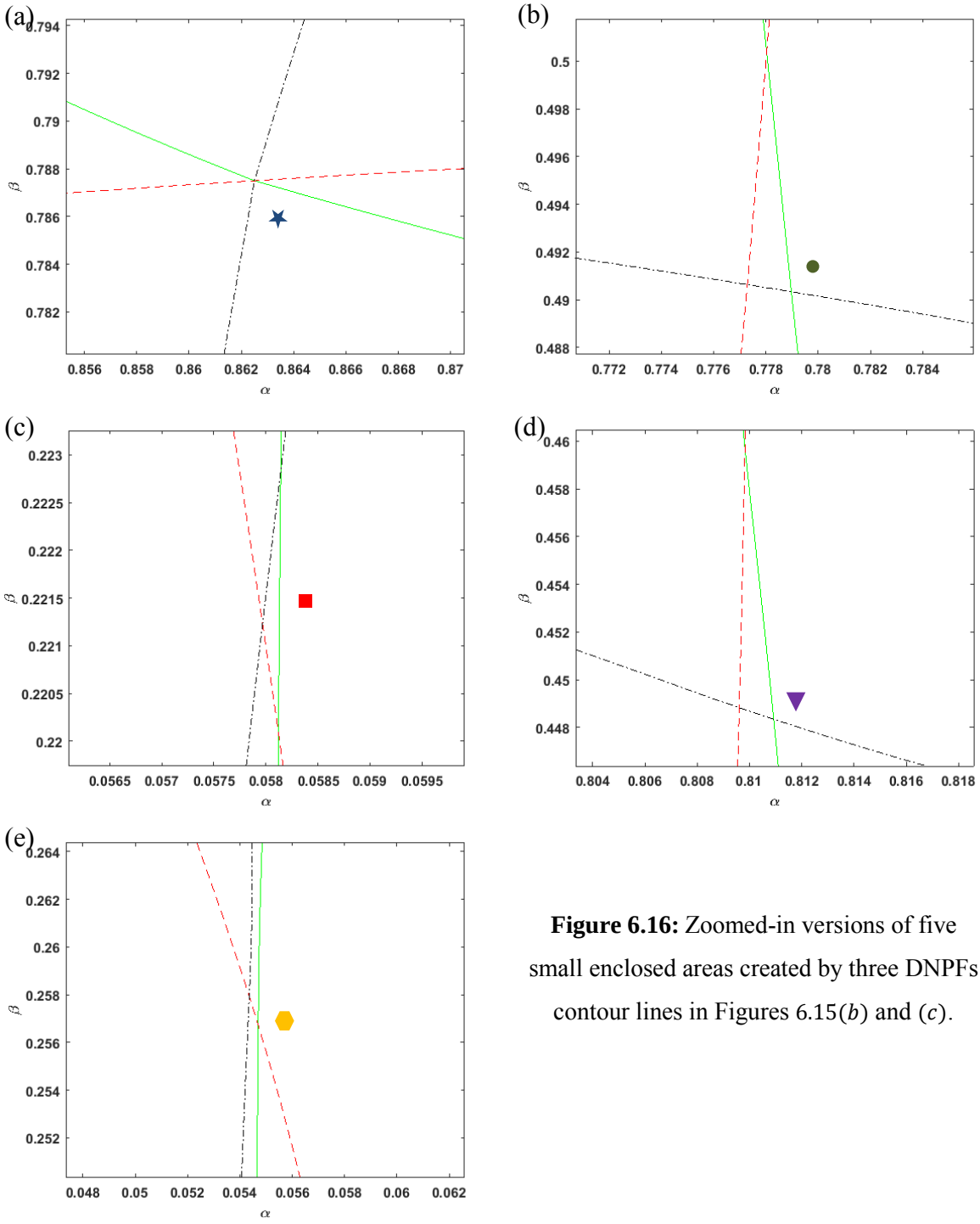

Figure 6.16: Zoomed-in versions of five small enclosed areas created by three DNPFs contour lines in Figures 6.15(b) and (c).

Figure 6.16 displays these small enclosed areas in the zoomed-in versions of those in Figures 6.15(b) and (c). The enclosed area labelled by the blue star is shown to be the smallest one, and it gives the location of the damage at $\alpha = 0.8625$ and $\beta = 0.7875$. This location is on the severity plane of $\zeta = 0.32$ (Figure 6.15(b)). Hence, the location of the

damage revealed by the severity plane is the same as the location of the damage on the plate before completing the damage detection.

This case study can prove that the symmetry of the DNPF pattern due to the symmetry of the plate boundary condition can be eliminated by changing the location of the excitation force to be out of the centre line of the plate. As stated earlier, one more way to solve this problem is to move the measurement points to another position. However, a case study connected to this solution is not included in the paper.

6.7 Method to enhance contrast of severity plane

As shown earlier, the proposed damage detection technique reveals the location of the damage using a small enclose area produced by three contour lines on the correct severity plane. Sometimes, when there are more than one enclose area appears on the severity plane, it may be difficult to distinguish which one is the smallest. To overcome this problem, a standard Bayesian average and an error function (see, Giannini et al. (2013)) is employed to magnify the indicator of damage location. This error function is adapted to be used for the power flow. It can be expressed as

$$ER_{f_e}(\alpha,\beta) = \frac{P_{f_e}(\alpha,\beta) - P_{f_e}^m}{\bar{B}} \tag{6.2}$$

where $ER_{f_e}(\alpha,\beta)$ is the error function of the DNPF of each excitation frequency; $P_{f_e}(\alpha,\beta)$ is the DNPF at each location on the plate; $P_{f_e}^m$is the DNPF obtained from the measurement points on the damaged plate; subscript f_e denotes the excitation frequency; superscript m shows the value from measurement; and $\bar{B}$ is the standard Bayesian average which is written as

$$\bar{B} = \frac{\sum_{e=1}^{E} P_{f_e,e}(\alpha,\beta) - \sum_{s=1}^{S} P_{f_e,s}^m}{E+S} \tag{6.3}$$

where e is the element number; E is the maximum element number; s is the number of measurement; and S is the maximum of measurement number. It is noted that e is related to the non-dimensional location, α and β of each element on the plate.

$ER_{f_e}(\alpha,\beta)$ at each location of the plate is computed. Since three excitation frequencies are used in this damage detection technique, three sets of $ER_{f_e}(\alpha,\beta)$ are obtained from Equation (6.2) for each used excitation frequency. These three sets are then processed based on the expression (see, Giannini et al. (2013))

$$k(\alpha,\beta) = \sqrt{\sum_{f_e} ER_{f_e}(\alpha,\beta)^2} \tag{6.4}$$

and these $k(\alpha,\beta)$ are plotted in a surface plot to reveal the damage location.

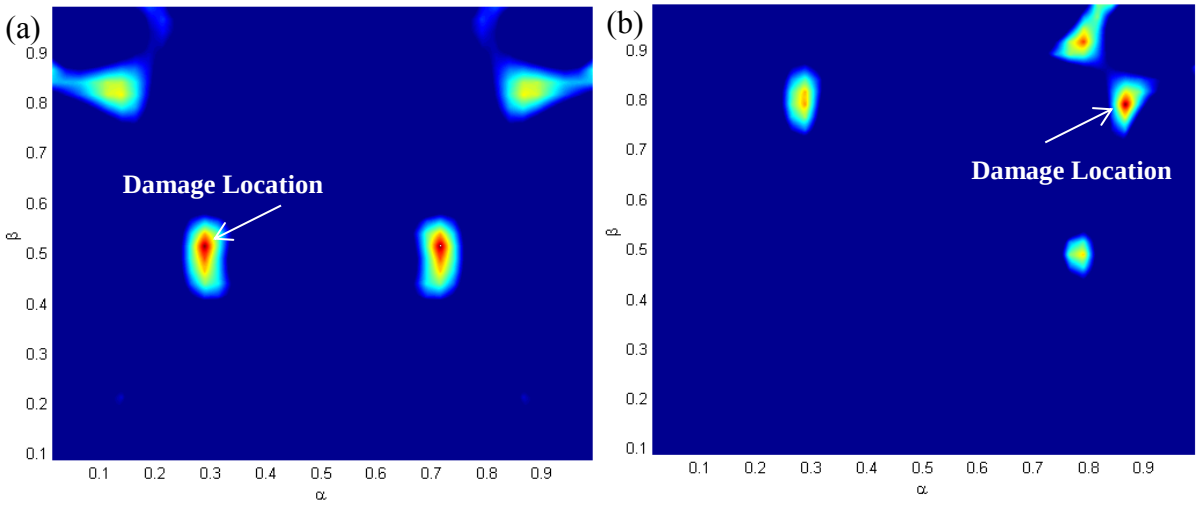

Figure 6.17: Damage location presented by standard Bayesian average and error function: (a) simply-supported plate with damage having $\zeta = 0.10$, $\alpha = 0.2875$ and $\beta = 0.5125$; (b) simply-supported plate (excitation force at the plate corner) with damage having $\zeta = 0.32$, $\alpha = 0.8625$ and $\beta = 0.7875$.

Figure 6.17(a) and (b) show the surface plots of the results of the same case studies as presented in Figure 6.10(a) and 6.15(b), respectively, created by Equation (6.4). It can be observed that the locations of the damages are illustrated correctly by the dark-red dots. Two dark-red dots are in Figure 6.17(a) due to the symmetry of the boundary condition (all edges simply supported) and the locations of the excitation force and measurement points, as stated before in Section 6.6. The left one is the correct location of the damage which is at $\alpha = 0.2875$ and $\beta = 0.5125$. This result is comparable to that presented in Figure 6.10(a). There is only one dark-red dot appear on the plot in Figure 6.17(b), since the location of the excitation force is moved to the corner of the plate. This dark-red dot is at $\alpha = 0.8625$ and $\beta = 0.7875$ which is consistent to the results in Figure 6.15(b). Moreover, the location of the damage is magnified, and it can be noticed easily without the

use of a zoomed-in version as done for Figure 6.15(b). The surface plot of the results from the standard Bayesian average and the error function may be used more efficiently than the contour plot in term of presenting the location of the damage.

6.8 Influences of noise and limitation of severity planes

In a practical situation, the uncertainty of the damage detection technique may occur due to several sources, such as human errors, errors from transducers, and environmental effects. For numerical simulation, uncertainty is usually simulated by adding artificial noise to the system (see, for example, Huh et al. (2011)). Monte Carlo simulation can also be employed to determine values contaminated by a random error (see, for example, Giannini et al. (2013)).

In this section, the random white Gaussian noise (WGN) is separately added to each velocity signal used to calculate P_d and P_{int} and hence the values of the DNPF for the case studies in Section 6.6. Additionally, the values of the DNPF induced by the frequencies of 25, 60 and 100 Hz are separately calculated, so they are contaminated by different sets of random noise with the same SNR. This set up aims to simulate the situation when the damage detection technique is carried out in random environments.

The simply supported plates containing the damage with $\zeta = 0.10$ located at $(\alpha, \beta) = (0.2875, 0.5125)$ and its intact counterpart are used in the study of noise effect. A set of 1000 samples of the contaminated DNPFs per excitation frequency is collected to observe the influence of noises with the signal to noise ratio (SNR) of 80 and 40. The averages of the contaminated DNPFs and their standard deviations are then determined.

Table 6.3: Comparison of averaged contaminated DNPFs and pure DNPFs.

Excitation frequency (Hz)	SNR = 80		SNR = 40	
	Percentage difference (%)	Standard deviation	Percentage difference (%)	Standard deviation
25	6.56E-04	4.62E-05	2.56	0.23
60	6.93E-04	2.95E-05	3.09	0.28
100	7.20E-04	4.32E-05	2.73	0.31

Table 6.3 shows the percentage differences of the contaminated and pure DNPFs (without noise) and the obtained standard deviations. It can be observed from the table that the differences between averages of the DNPFs contaminated by noise with SNR = 80 and

those without noise are negligible, and the standard deviations are also small. This means that the mean values of the contaminated DNPFs are almost the same as the pure DNPFs, and the majority of the contaminated DNPFs are close the means. However, once the power of noise is increased to reach the SNR = 40, the differences and the standard deviations are significantly increased.

Table 6.4: Location and severity of damage predicted by DNPFs with and without noise contamination.

SNR	DNPF	Predicted damage location and severity ($\alpha, \beta;\ \zeta$)
Without noise	-	(0.2875, 0.5125; 0.10)
80	Averaged	(0.2982, 0.5010; 0.10)
80	Maximum	(0.2980, 0.5295; 0.13)

The averaged values of the contaminated DNPFs of the SNR equal to 80 shown in Table 6.4 are used as the inputs for the reverse step of the damage detection method. For this time it is also assumed that the increment of the severity planes is 0.01. Therefore, it will be 11 severity planes for ζ in the range from 0.1 to 0.2. This setup aims to observe the effectiveness of the damage detection method when the number of the severity planes or the size of the power flow database is limited. It may be inconvenient to generate a very large power flow database in practice. The results are presented in Figure 6.18. The smallest enclosed area is appeared on the severity plane of $\zeta = 0.10$ and α and β obtained from this plane are 0.2982 and 0.5010, respectively as shown in the red circle.

Figure 6.19 illustrates the result when using the maximum values of the DNPF obtained from the 1000 samples per excitation frequency to predict the location and severity of the damage. The smallest enclosed area occur on the severity plane of $\zeta = 0.13$. This plane gives α and β as 0.2980 and 0.5295, respectively as shown in the red circle. These results of the damage location and severity produced by the averaged and maximum values of the contaminated DNPF are still not far from those obtained by the pure signals as seen from Table 6.4. The results also show that the limitation of the severity planes does not significantly affect the accuracy of the damage detection method since the centroid of the smallest enclosed area is still be able to present acceptable results.

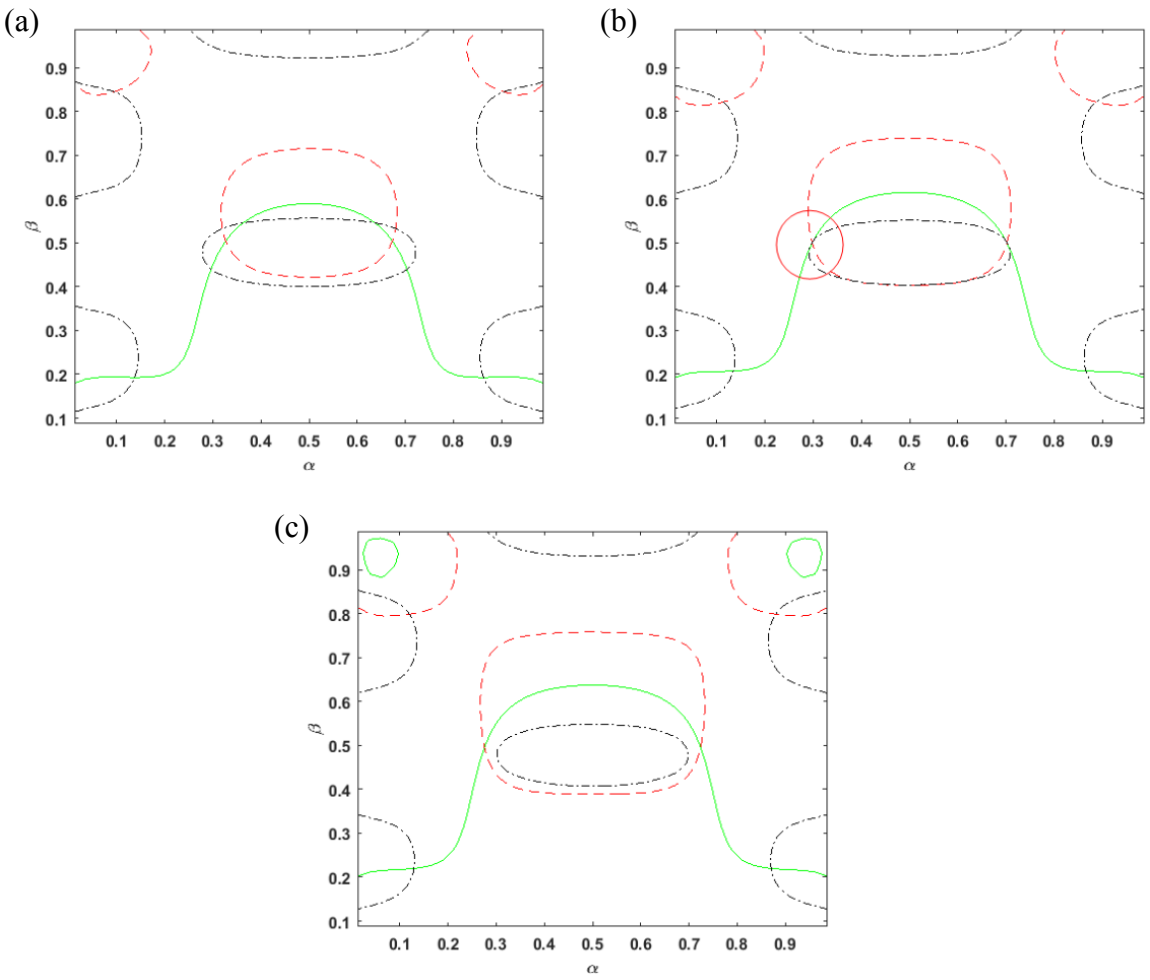

Figure 6.18: Contour plots on severity planes of averaged contaminated DNPFs (SNR = 80) in damaged simply-supported plate ($\alpha = 0.2875, \beta = 0.5125$): (a) severity plane of $\zeta = 0.09$; (b) severity plane of $\zeta = 0.10$; (c) severity plane of $\zeta = 0.11$.

The damage location and severity cannot be obtained by the averaged data of the SNR equal to 40 because their errors are significant. In order to reduce the influence of noise on the DNPF, P_d and P_{int} have to be measured in the same environment. A few power flow measurement points are sufficient to obtain the DNPF for the forward and reverse steps of the damage detection method. Reduction of these power flow measurement points can decrease the accumulation of the error from noise at each of them. Experimental studies and model updating of the damage detection method will be in the next phase of the work.

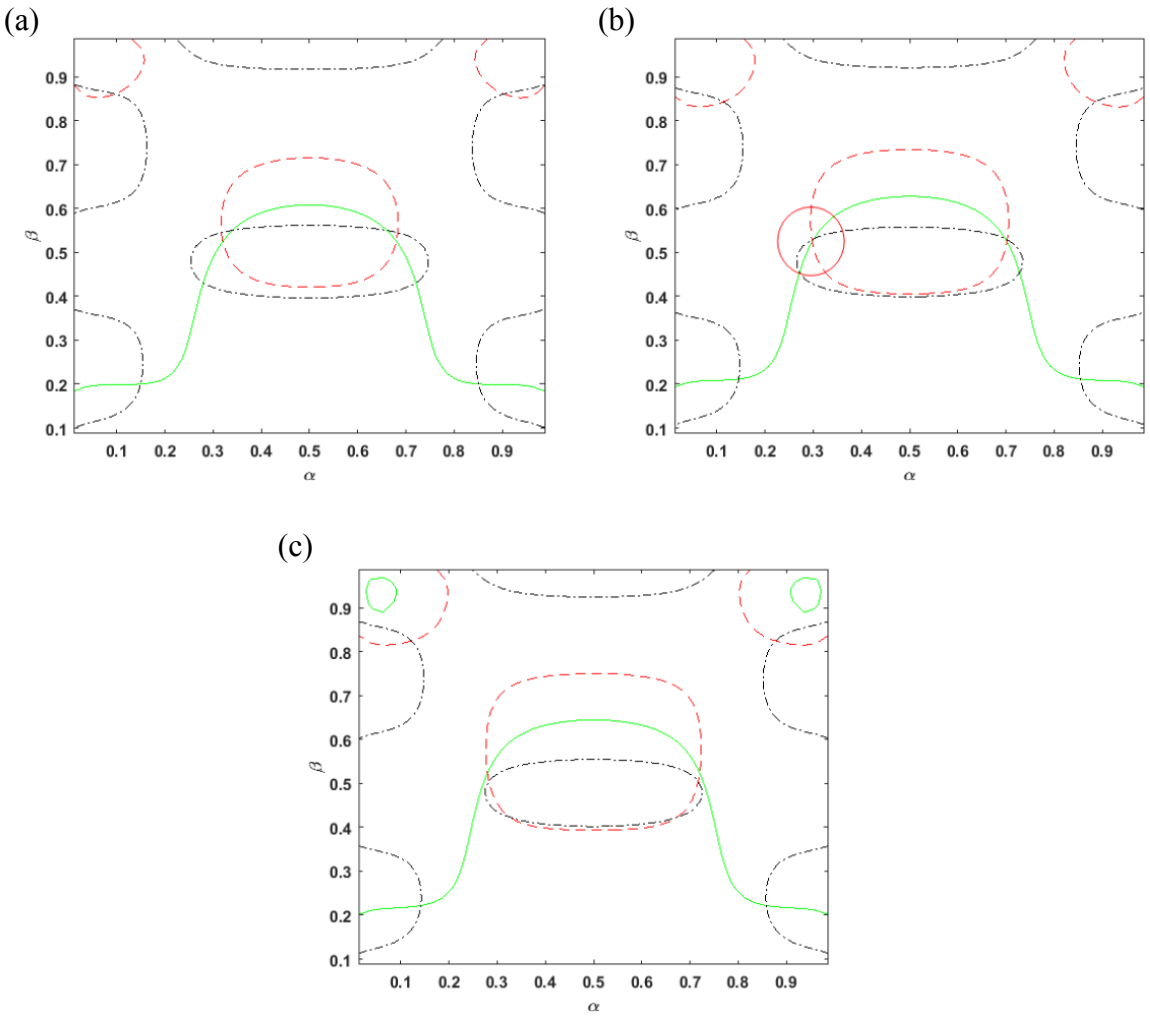

Figure 6.19: Contour plots on severity planes of maximum contaminated DNPFs (SNR = 80) in damaged simply-supported plate ($\alpha = 0.2875, \beta = 0.5125$): (a) severity plane of $\zeta = 0.12$, (b) severity plane of $\zeta = 0.13$, (c) severity plane of $\zeta = 0.14$.

6.9 Power flow measurement for damage detection

In practice, the proposed damage detection technique requires an experimental measurement to measure the power flow in the tested plate for using as inputs of the reverse step of the technique. As mentioned before, the technique employs the FEM to perform the power flow data collection in forward step, and the measured power flow from the tested plate is then used in the reverse step to obtain damage location and severity. This section will provide the brief details of power flow experimental measurement using the eight-point transducer method as discussed before in Chapter 3 for the reverse step of the damage detection technique. Furthermore, the eight-point array measurement is simulated, and the power flow results are compared with those obtained directly from the FEM.

6.9.1 Power flow measurement procedure for damage detection

The procedure for performing the power flow experimental measurement using the eight-point measurement array to obtain inputs of the reverse step of the damage detection technique is summarised as follows:

a) Preparing eight accelerometers for measuring vertical acceleration the tested structure and a shaker for generating driving force.
b) Estimating coherence functions between excitation force and accelerations to find the cut-off frequency. The excitation frequency should be higher than the cut-off frequency to minimise the interference of noise between force and acceleration. Three excitation frequencies used for the measurements have to be the same as those used in the forward step.
c) Determining the suitable distance between accelerometers and arranging them in the form of eight-point measurement array (Figure 3.2(b)).
d) Measuring accelerations at these eight measurement points simultaneously.
e) Using the finite difference method (FDM) to calculate the power flow from the measured accelerations.
f) Obtaining three values of the power flow from three excitation frequencies.
g) Plotting these three power flow values as contour lines on the severity planes obtained from the forward step. The centroid of the smallest region created by the contour lines shows the location of the damage, and the severity plane on which this region is will tell us the damage severity.

6.9.2 Theory of eight-point power flow measurement array

The power flow in a thin plate can be measured using a set of sensors such as accelerometers attached to the plate in the pattern called *Measurement array*. In this section, the eight-point measurement array which was firstly introduced by Pavić (1976) is presented. This array is presented schematically in Figure 3.2(b). The black circles and black squares in the figure represent the locations of the transducers. Vibration responses of the plate at these locations are captured, and the FDM is employed to determine the power flows in both x and y directions at the position shown by the cross sign in the figure.

The equations of the power flow in a plate were previously presented in Equations (3.18)-(3.21). Only the real part of the power flow is focused on. The terms of the complex membrane forces can be neglected since the values of the membrane forces are very low when compared to the other parameters in the equations. Therefore, Equations (3.20) and (3.21) will be used to determine the power flow based on the FDM in this section. Each term in Equation (3.20), which is of the power flow in the x direction, can be written based on the FDM when $T = 2\pi/\omega$ as

$$-\frac{\omega}{2}\Im\{\tilde{Q}_x\tilde{W}^*\} \cong -\frac{D\omega}{4\Delta^3}\Im\big[\tilde{W}_1\tilde{W}_3^* + \tilde{W}_1\tilde{W}_6^* + \tilde{W}_2\tilde{W}_3^* + \tilde{W}_2\tilde{W}_6^* - \tilde{W}_3\tilde{W}_4^* + \tilde{W}_3\tilde{W}_5^* - 10\tilde{W}_3\tilde{W}_6^* + \tilde{W}_3\tilde{W}_7^* + \tilde{W}_3\tilde{W}_8^* + \tilde{W}_4\tilde{W}_6^* - \tilde{W}_5\tilde{W}_6^* + \tilde{W}_6\tilde{W}_7^* + \tilde{W}_6\tilde{W}_8^*\big] \tag{6.5}$$

$$-\frac{\omega}{2}\Im\{\tilde{M}_x\tilde{\Phi}_y^*\} \cong \frac{D\omega}{4\Delta^3}\Im\big[\tilde{W}_1\tilde{W}_3^* - \tilde{W}_1\tilde{W}_6^* + 2\tilde{W}_3\tilde{W}_6^* - \tilde{W}_3\tilde{W}_8^* + \tilde{W}_6\tilde{W}_8^*\big] + \frac{D\omega\nu}{4\Delta^3}\Im\big[\tilde{W}_2\tilde{W}_3^* - \tilde{W}_2\tilde{W}_6^* - \tilde{W}_3\tilde{W}_4^* - \tilde{W}_3\tilde{W}_5^* + 4\tilde{W}_3\tilde{W}_6^* - \tilde{W}_3\tilde{W}_7^* - \tilde{W}_4\tilde{W}_6^* - \tilde{W}_5\tilde{W}_6^* + \tilde{W}_6\tilde{W}_7^*\big] \tag{6.6}$$

$$-\frac{\omega}{2}\Im\{\tilde{M}_{xy}\tilde{\Phi}_x^*\} \cong \frac{D\omega(1-\nu)}{8\Delta^3}\Im\big[\tilde{W}_2\tilde{W}_5^* - \tilde{W}_2\tilde{W}_7^* - \tilde{W}_4\tilde{W}_5^* + \tilde{W}_4\tilde{W}_7^*\big] \tag{6.7}$$

where $D = EH^3/12(1-\nu^2)$ is the flexural rigidity; E is the Young's modulus; H is the plate thickness; ν is the Poisson' s ratio; Δ is the twice grid size; $\Im$ represents the imaginary part; $\tilde{W}$ is the complex amplitude of vertical displacement measured by the transducer at each point and $*$ is the complex conjugation. The power flow in the x direction is

consequently obtained by substituting Equations (6.5), (6.6) and (6.7) into Equation (3.20). This result is equal to that obtained from Equation (3.5). For the power flow in the y direction, the positions of the transducers shown by the squares in Figure 3.2(b) are used, and Equations (6.6) and (6.7) are multiplied by -1. These terms are then substituted into Equation (3.21) to obtain the power flow in the y direction.

6.9.3 Simulation of eight-point array measurement

The power flow measurements of the damaged plates based on the eight-point array and FDM is simulated using ANSYS. The geometry and material properties of the plates are identical to those given in Table 6.1. A unit excitation force is placed at (α, β) = (0.5000, 0.0300). A set of the transducer is assumed to be arranged in the same pattern as shown in Figure 3.2(b). The size of the grid is assumed to be $0.01\,m$, so Δ is equal to $0.02\,m$. Accuracy of the FDM mainly depends on Δ. A smaller Δ will generate more accurate results. However, for an experimental measurement, the suitable Δ can be selected from a trade-off to prevent the occurrence of phase mismatch errors (see, Mandal (2006) and Huh et al. (2015)). The power flow is measured from three positions which are (α, β) = (0.0950, 0.0350), (0.105, 0.0350) and (0.1150, 0.0350). The magnitudes of these three power flows are computed using Equation (6.1), and then the net power flow is obtained by employing the Trapezoidal rule. The net power flows of damaged plates are consequently divided by the ones of the intact plates to obtain the DNPFs.

The DNPFs obtained directly from the FEM and the eight-point array measurement based on the FDM are given in Table 6.5. The percentage differences are computed by using the DNPFs obtained from the FEM as the references. It can be seen that the DNPFs from the FEM and the FDM are approximately the same. These measured DNPF data of three excitation frequencies are used for the reverse step to detect damage location and severity.

Table 6.5: DNPFs obtained from FDM and FEM.

Damage location and depth $(\alpha, \beta; \zeta)$	Excitation frequency 25Hz			Excitation frequency 60Hz			Excitation frequency 100Hz		
	FDM	**FEM**	**% Dif**	**FDM**	**FEM**	**% Dif**	**FDM**	**FEM**	**% Dif**
(0.505, 0.715; 0.1)	0.9992	0.9994	0.02	0.9998	0.9999	0.01	1.0009	1.0002	0.07
(0.375, 0.315; 0.1)	0.9990	1.0009	0.19	0.9992	0.9999	0.07	0.9935	0.9999	0.64
(0.845, 0.635; 0.1)	1.0001	0.9994	0.07	0.9997	0.9999	0.02	1.0002	0.9999	0.03
(0.505, 0.715; 0.3)	0.9991	0.9985	0.06	0.9992	0.9995	0.03	1.0022	1.0008	0.14
(0.375, 0.315; 0.3)	0.9995	1.0022	0.27	0.9992	0.9998	0.06	1.0027	1.0012	0.15
(0.845, 0.635; 0.3)	1.0014	0.9999	0.15	0.9995	0.9998	0.03	0.9994	1.0002	0.08

6.10 Summary

The concepts of the damage detection technique based on the power flow capable of detecting location and severity of damage on plate structures are introduced. The proposed technique employs three values of the DNPF induced by three excitation frequencies to form the power flow contours. The damage location and severity are revealed by the centroid of the small enclosed area generated by three contour lines of the DNPF values. The effectiveness of the proposed technique is shown through various numerical studies of the simply supported plate and the plate with the mixed boundary conditions. The presented case studies can confirm the sensitivity of the power flow, which is used as a damage indicator for the damage detection technique. The method to enhance the contrast of the plot to show the location and severity of the damage more clearly is also presented to reduce difficulty that may occur when there are more than one small enclosed areas presented in a contour plot. Finally, the eight-point power flow measurement array based on the FDM used for power flow experimental measurement is presented. This method is used to estimate the DNPF values for the reverse step of the proposed damage detection technique, or used for power flow database building. The DNPF values obtained from the numerical simulation of the measurement array are analogous to those from the FEM.

Chapter 7

Nonlinear power flow surface fitting for crack detection in beams

7.1 Introduction

Chapters 4, 5 and 6 have dealt with the linear vibrational power flow in damaged structures, and it has been shown in those chapters that the sensitivity of the power flow to structural damage is high. In reality, the early-age structural damage is usually in the form of a breathing fatigue crack which can induce nonlinearity in dynamic behaviours of structures. It is worthwhile to detect damage at its early stage before it is enlarged and cause structural failure. In this chapter, nonlinear power flows generated by a breathing crack in a cantilever beam is investigated. The degree of the nonlinearity of the power flow is used in conjunction with the curve fitting to build a crack detection technique having ability to detect the occurrence of the crack and reveal the approximate crack location and severity. The technique consists of the forward and reverse steps. The FEM is employed to compute the power flow, and show the effectiveness of the proposed crack detection technique.

7.2 Power flow computation scheme

Based on the FEM, the cracked cantilever beams are modelled using solid elements and three-dimensional contact elements at the crack faces. For these three-dimensional elements, components of stress and velocity outputs are directly given at the nodes of each element. Thus, the instantaneous vibrational power flows per unit area in three directions of the Cartesian coordinates of each node can be computed using Equations (3.14)-(3.16).

Generally, for beam structures, P_y and P_z are negligible when compared to P_x, which is the instantaneous power flow per unit area in the direction parallel to the length of the beams;

therefore, only P_x is frequently of interest. When the stress and velocity components are in the complex forms, only the real part of the instantaneous power flow per unit area will be focused on. Equation (3.14) is then rewritten as

$$P_x = -\Re\{\tilde{\sigma}_{xx}\}\Re\{\dot{\tilde{u}}\} - \Re\{\tilde{\tau}_{xy}\}\Re\{\dot{\tilde{v}}\} - \Re\{\tilde{\tau}_{xz}\}\Re\{\dot{\tilde{w}}\} \tag{7.1}$$

where P_x is the instantaneous vibrational power flow per unit area; $\Re$ denotes the real part; and the term with $\sim$ is complex.

To obtain the instantaneous net power flow in a cross section of the beam, the instantaneous power flows per unit area at the nodes on that cross section are numerically integrated. For the sake of convenience, the instantaneous net power flow in each cross section of the beam will be labelled as *power flow (PF)* throughout the chapter. The power flow can be written mathematically as

$$P_{x,net} = \int_A \left(\left(-\Re\{\tilde{\sigma}_{xx}\}\Re\{\dot{\tilde{u}}\} - \Re\{\tilde{\tau}_{xy}\}\Re\{\dot{\tilde{v}}\} - \Re\{\tilde{\tau}_{xz}\}\Re\{\dot{\tilde{w}}\}\right)\right) dA \tag{7.2}$$

More details of the beam finite element modelling and the power flow computation are discussed in the upcoming sections of this chapter.

7.3 Finite element model of cracked beam

7.3.1 Cracked beam geometry and material properties

The cracked beam that will be used for case studies in this chapter is a cantilever beam having one end fixed and the other free (Figure 7.1.). The geometry and material properties of the cracked steel beam are provided in Table 7.1.

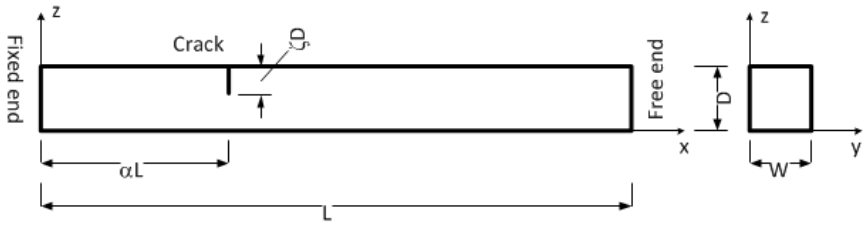

Figure 7.1: Schematic model of cracked cantilever beam.

The crack is in the form of a breathing crack which can be open and closed depending on the excitation force. The length of the crack is equal to the beam width (W). The crack

faces are assumed to be frictionless. Initially, the crack is closed, so both crack faces touch each other. Nonlinearity of the power flow of the cracked beam is generated due to abrupt changes in beam stiffness when the crack is open and closed, and when the crack faces contact each other. From Figure 7.1, α and ζ are the dimensionless values of the crack location and crack depth, respectively.

Table 7.1: Geometry and material properties of cracked beam used in the validation process.

Length (L)	0.400 m
Width (W)	0.020m
Thickness (D)	0.020 m
Young's modulus	210 GPa
Poisson's ratio	0.300
Mass density	7850 kg/m^3
Damping ratio	0.03

The FEM is employed to model the cracked beam by discretising it into a number of small 20-node solid elements. This modelling is completed using ANSYS. The interaction between crack faces, when the crack is closed, is generated by 8-node contact and target elements.

7.3.2 Contact problem based FEM

Nonlinear responses of a cracked beam can occur due to abrupt changes in the structural stiffness when two crack faces come into or out of contact with each other. These two crack faces can be labelled as *contactor* and *target*. As mentioned before, the crack can be open (non-contact) and closed (in contact) depending on the excitation force. The interaction of the contactor and target may be divided into three states (Figure 7.2).

When the crack is open, no traction occurs on the contactor and target since they do not touch each other. Thus, it can be stated that (Bouboulas and Anifantis, 2013)

$$R_i^a = R_i^b = 0 \; ; i = 1,2,3 \tag{7.3}$$

$$g^{ab} > 0 \tag{7.4}$$

where R is the traction at the point of contact; superscript a and b denotes the points on the contactor and target, respectively; i shows the local coordinate systems of the contactor

and target; 3 represents the nodal axis normal to the surface with the positive pointing outward the surface of the target; 1 and 2 represent the other two orthogonal axes and g is the gap between contact points on contactor and target. This state can be called *non-contact state*.

When the points a and b on the contactor and target contact each other and stick together, so the tangential traction at the contact point is zero. Total normal traction at the contact point is also zero. This state can be called *sticking state*, and it can be written as (see, Deng et al. (2015))

$$R_i^a = R_i^b = 0\,; i = 1,2 \tag{7.5}$$

$$R_i^a + R_i^b = 0\,; i = 3 \tag{7.6}$$

$$g^{ab} = 0 \tag{7.7}$$

The other state is called *sliding state* which occurs when two bodies not only contact but also slide on each other. Since it is assumed to have no friction on the surfaces of both crack faces, tangential traction at the contact point and total normal tractions are still zero. Therefore, Equations (7.5), (7.6) and (7.7) can also be used for this state.

The gap between the pair points, g^{ab}, can be written as

$$g^{ab} = g_0^{ab} + \left(u_i^a - u_i^b\right);\ i = 3 \tag{7.8}$$

where $g_0^{ab}$is the initial gap between point a and b; and u is the displacement.

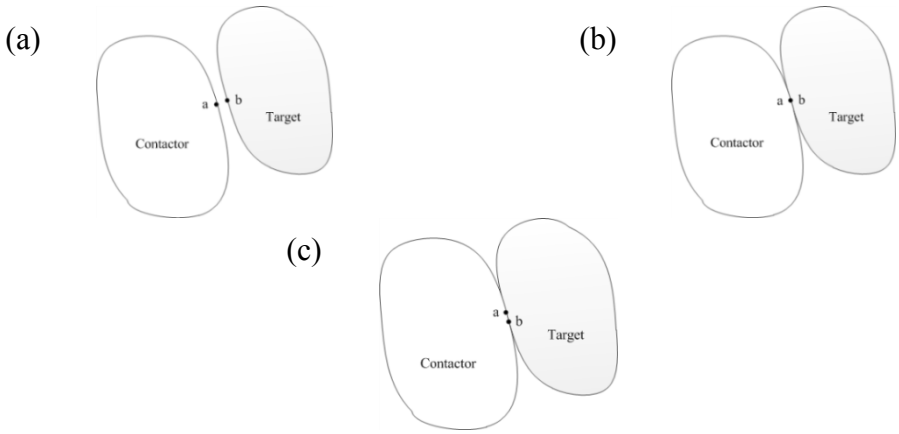

Figure 7.2: Contact states: (a) non-contact state; (b) sticking state; (c) sliding state.

At time $t + \Delta t$, the normal traction at the pair points when the crack is in the sticking and sliding states can be expressed as

$$^{t+\Delta t}(\Delta R_i^a) + {}^{t+\Delta t}\left(\Delta R_i^b\right) = 0\,; i = 3 \tag{7.9}$$

and the gap between the pair points when two bodies do not contact is

$$^{t+\Delta t}\left(g^{ab}\right) = {}^{t}\left(g^{ab}\right) + \left[\left({}^{t}(u_3^a) + {}^{t+\Delta t}(\Delta u_3^a)\right) - \left({}^{t}\left(u_3^b\right) + {}^{t+\Delta t}\left(\Delta u_3^b\right)\right)\right] \tag{7.10}$$

The solution of the governing equation in dynamic analysis employs the implicit integration, namely, Newmark method. Additionally, the iterative procedure, namely Newton-Raphson method, is also used to solve the nonlinear governing equation of the cracked beam. Thus, at the time $t + \Delta t$ and the iteration k, the equation can be expressed as (see, Bathe (1996))

$$\mathbf{M}^{t+\Delta t}\ddot{\mathbf{U}}^k + \mathbf{C}^{t+\Delta t}\dot{\mathbf{U}}^k + {}^{t}\mathbf{K_T}\Delta\mathbf{U}^k = {}^{t+\Delta t}\mathbf{F} - {}^{t+\Delta t}\mathbf{R}^{k-1} \tag{7.11}$$

where k is the iteration; $\mathbf{M}$, $\mathbf{C}$ and $\boldsymbol{K_T}$ are respectively the mass, damping and tangent stiffness matrices; $\mathbf{F}$ is the external force vector; $\mathbf{R}$ is the nodal force vector; $\Delta\mathbf{U}$ is the increment of the nodal displacement vector, which can be obtained from

$$\hat{\mathbf{K}}_\mathbf{T}\Delta\mathbf{U}^k = \Delta\hat{\mathbf{F}}^{k-1} \tag{7.12}$$

where $\hat{\mathbf{K}}_\mathbf{T}$ is the function of tangent stiffness matrix, mass matrix and damping matrix; $\Delta\hat{\mathbf{F}}$ is the nodal force vector and contributions from inertia and damping.

The displacement vector, $^{t+\Delta t}\mathbf{U}^k$, can then be evaluated using

$$^{t+\Delta t}\mathbf{U}^k = {}^{t+\Delta t}\mathbf{U}^{k-1} + \Delta\mathbf{U}^k \tag{7.13}$$

The iteration process keeps running until the sufficiently small $\Delta\hat{\mathbf{F}}$ and $\Delta\mathbf{U}$ is obtained.

7.3.3 Cracked beam finite element modelling

Validation

This section aims to confirm that the ANSYS finite element codes used to model the cracked beam are created correctly. To complete this task, the cracked cantilever beam in the work of Andreaus and Baragatti (2011) is remodelled using ANSYS finite element code. The solid elements containing 20 nodes per each is used to model the cracked cantilever beam having the geometry and material properties as those given in Table 7.2. The beam is discretised into 1600 solid elements, so it is totally 32000 nodes. At the crack faces, the eight-node contact and target elements are attached to induce responses due to the interaction between both crack faces when the beam is excited by an external force. These crack faces are assumed frictionless. The contact algorithm is selected as the augmented Lagrangian method. This algorithm determines the exact Lagrange multipliers, such as contact tractions, using iterative series of penalty updates. It was evidenced by Chati et al. (1997) that a singularity in the stress field at the vicinity of the crack tip does not affect natural frequencies of transverse mode of a beam. Therefore, quarter-point elements are not used at the tips of the crack in the beam model.

Table 7.2: Geometry and material properties of cracked beam used in the validation process.

Data	Andreaus and Baragatti (2011)
Length (L)	0.300 m
Width (W)	0.020 m
Thickness (D)	0.020 m
Young's modulus	206.8 Gpa
Mass density	7850 kg/m
Poisson's ratio	0.300

A natural frequency of a cracked beam can be calculated from the bilinear frequency equation which is expressed as (see, Andreaus and Baragatti (2011))

$$f_b = \frac{2 f_c f_o}{f_c + f_o} \tag{7.14}$$

where f_b is the bilinear frequency or natural frequency of breathing cracked beam, f_c is the natural frequency of the beam when the crack is closed, which may be assumed to be equal to the natural frequency of the intact beam (see, Giannini et al. (2013) and Shen and Chu (1992)), and f_o is the natural frequency of the beam when the crack is open. It has been

shown in the work of Andreaus and Baragatti (2011) that the bilinear frequencies of the cracked cantilever beam are not sensitive to the presence of a crack, especially when the crack is small or located far away from the fixed end of the beam.

Table 7.3 gives the bilinear frequencies of the first transverse mode presented in the work of Andreaus and Baragatti (2011), and those obtained by the author from ANSYS. The last column of the table contains the percentage differences of the latter from the former ones. It is seen that the differences in the bilinear frequencies from both sources are small. Increasing element number will produce results that are closer to those obtained from the analytical solution (see, Öz (2000)). However, the computational load will also increase.

Table 7.3: Bilinear frequencies of cracked beam obtained from Andreaus and Baragatti (2011) and ANSYS.

Crack		**Results from Andreaus and Baragatti (2011)**	**Present work from ANSYS**	**%Dif**
Position (α)	**Depth (ζ)**			
0.083	0.1	182.40	184.02	0.89
	0.3	177.90	178.44	0.30
	0.5	160.00	163.44	2.15
0.267	0.1	182.90	184.70	0.99
	0.3	178.50	181.46	1.66
	0.5	170.00	173.71	2.18
0.467	0.1	183.20	184.90	0.93
	0.3	182.00	183.74	0.95
	0.5	176.70	180.52	2.16

The acceleration responses of the same cracked beam are also determined using ANSYS. A $100\,N$ harmonic driving force is located at the free end of the beam. The acceleration responses of the beams are also obtained at this point. The acceleration responses are taken from the harmonic analysis with the substep of $50f_e$ substeps per second, where f_e is the excitation frequency. The time-domain responses are then transformed to frequency responses using the Fourier transformation.

In Figure 7.3(a), the Fourier spectrum of the acceleration responses, when the crack with $\alpha = 0.267$ and $\zeta = 0.500$ (selected from Table 7.3), and the excitation frequency is set to half the first bilinear frequency of the beam, is presented. This Fourier spectrum plot is comparable to that obtained by Andreaus and Baragatti (2011) shown in Figure 7.3(b), although the difference of the bilinear frequencies in Table 7.3 is highest when compared to the others. It can also be seen from the Fourier spectrum that apart from the excitation

frequency, which is 86.855 Hz, the peaks of the responses are also occurred at 173.71 Hz, 260.56 Hz, and 347.42 Hz. This nonlinear phenomenon is named *super-harmonic resonance* which occurs due to the nonlinearity generated by the breathing crack in the beam. Since the power flow is heavily dependent on vibration responses as seen from Equation (7.1), it also behaves nonlinearly if the responses are nonlinear. Thus, the super-harmonic resonance also occurs for the nonlinear power flow.

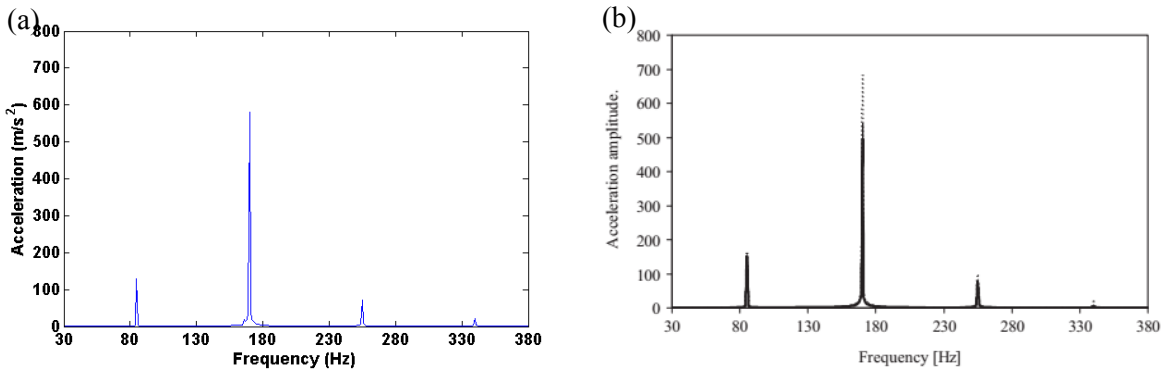

Figure 7.3: Fourier spectrum of an acceleration response of cracked beam containing crack with $\alpha = 0.267$ and $\zeta = 0.500$: (a) obtained from ANSYS by the author; (b) obtained by Andreaus and Baragatti (2011).

Cracked cantilever beam model

The geometry and material properties of the cantilever beams used for the power flow investigation are given in Table 7.1. The convergences of the bilinear frequencies of the cracked beams are studied to select the proper number of the elements used to model the cracked beams.

It can be seen from Table 7.4 that the first bilinear frequencies of the cracked beams decrease when the elements are smaller. However, the reductions of the bilinear frequencies stop when the number of the solid elements is changed from 2560 to 4800 elements. Thus, the cracked beams consisting of 2560 elements may be sufficient to produce acceptably accurate results. It should be noted that even though, finer elements can generate more accurate results, the more computational cost will be consumed. Since the study of stress intensity or beam responses occurred locally at the crack tips is not included herein, the quarter-point element is not used in this cracked beam modelling. The finite element model of the cracked beam is provided schematically in Figure 7.4. Cartesian coordinates of the model originate at the fixed end of the beam.

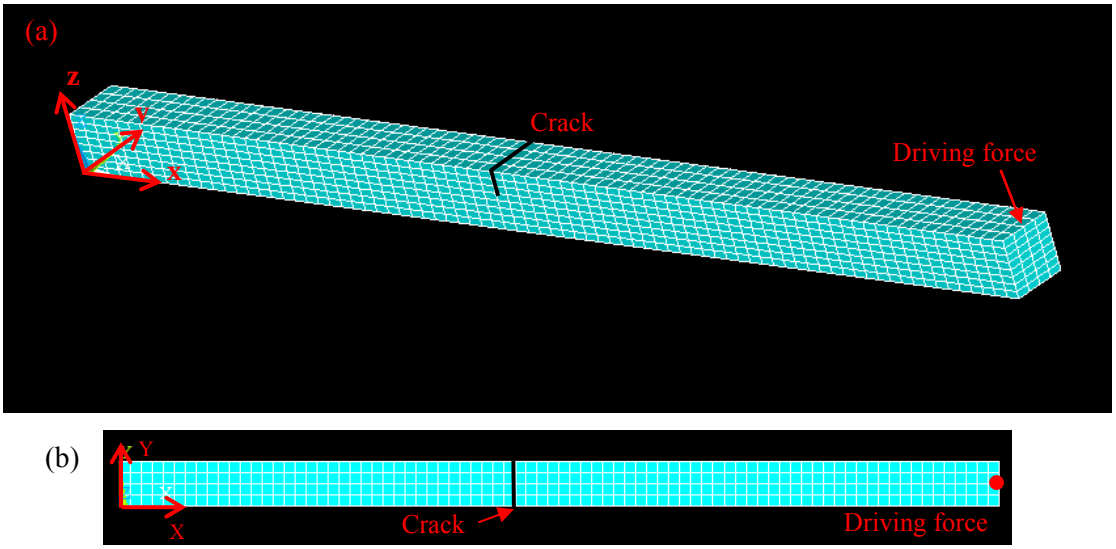

Figure 7.4: Finite element mesh of cracked cantilever beam model: (a) overall beam; (b) top view.

Table 7.4: Convergence studies of bilinear frequencies of cracked beams.

Crack		Number of solid elements	First bilinear frequency (Hz)
Position (α)	**Severity (ζ)**		
0.15	0.50	160	100.73
		320	99.83
		640	99.53
		1280	99.51
		2560	99.09
		4800	99.09
0.25	0.50	160	102.58
		320	101.89
		640	101.68
		1280	101.66
		2560	100.54
		4800	100.54
0.50	0.50	160	105.69
		320	105.41
		640	105.35
		1280	105.33
		2560	105.21
		4800	105.20

7.3.4 Results of power flow from finite element models

In order to check the accuracy of the power flow obtained using the numerical integration to integrate the nodal results on the cross section of the beam, as stated in Section 7.2, the finite element models of the cracked beams composing of 2560 and 4800 elements shown in the previous section are used to calculate the power flow based on Equation (7.2). The

crack having the depth of $\zeta = 0.50$ is located at $\alpha = 0.15$. The excitation point force with the magnitude of $100\,N$ is placed at the position shown in Figure 7.4. The excitation frequency, f_e, is equal to half of $99.09\,Hz$. This $99.09\,Hz$ is the first bilinear frequency of both cracked beams (see Table 7.4). The power flow is calculated for the cross sections of the beams at $x = 0.38\,m$ ($\alpha = 0.95$). The numerical integration, Trapezoidal rule, as used earlier in Chapters 4 and 5, is used in this chapter again to determine the power flow of the aforementioned cross sections.

Figure 7.5 displays the time-domain responses of the power flow taken from the 2560- and 4800-element beams. It can be observed from this figure that the aspects of the power flow responses obtained from both beams are approximately the same. Hence, the 2560-element beam is more efficient to be used in the computation, as the beam modelled with the finer elements consumes higher computational costs.

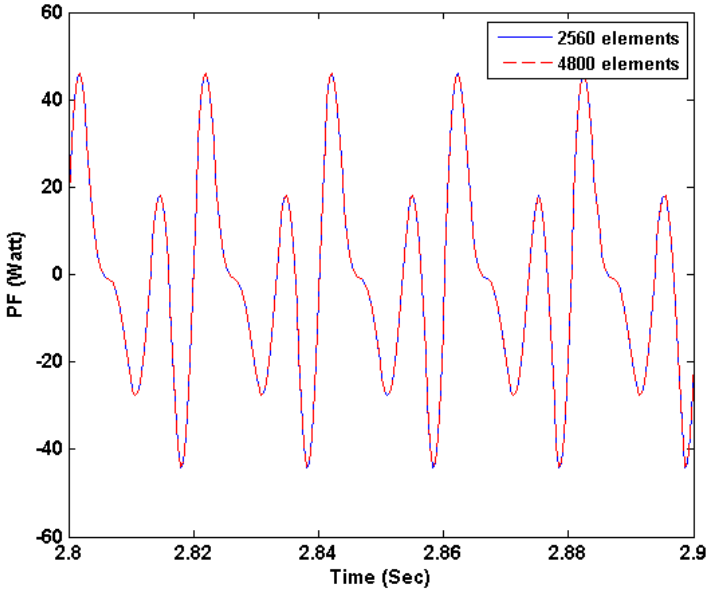

Figure 7.5: PF in cracked beams ($\alpha = 0.15$, $\zeta = 0.50$) consisting of 2560elements and 4800elements.

7.4 Power flow in intact and cracked beams

This section presents the behaviours of the power flow in intact and cracked beams, with the material properties and geometry given in Table 7.1. The excitation force and its location are the same as those in Section 7.3.4. The values of the power flow are obtained for the cross section of the beam at $x = 0.38\ m$ ($\alpha = 0.95$). For the cracked beam, the super-harmonic resonance, which occurs when the beam is excited by one half and one third of its first bilinear frequency, will be discussed. The other nonlinear phenomenon called *sub-harmonic resonance* which will occur when a bilinear frequency is the submultiple of the excitation frequency of the cracked beam is not focused on in this chapter.

7.4.1 Power flow in intact beam

The excitation frequencies, f_e, of the intact beam are $f_1/2$, where f_1 is the first natural frequency of the intact beam. f_1 is equal to $106.24\ Hz$, so f_e of the beam is $53.12\ Hz$. Figure 7.6 shows the time-domain and frequency-domain responses of the power flow induced by that excitation frequency. These plots are composed of $50 f_e$ substeps per one second. The Fourier transformation is employed to transform the responses in the time domain to those in the frequency domain. From the time-domain plot, the power flow is in the form of simple harmonic. It is seen from the frequency-domain plot that the peak is shifted to double of the excitation frequency. This feature occurs due to the result of the multiplication between two complex terms (see, Xing and Price (1999)). Equation (7.2) can be rewritten as

$$\begin{aligned} P_{x,net} = \frac{1}{2}\int_A \Big(& -\Re\left\{\left(\tilde{\bar{\sigma}}_{xx}\dot{\tilde{\bar{u}}}\right)e^{4i\pi ft} + \left(\tilde{\bar{\sigma}}_{xx}\dot{\tilde{\bar{u}}}^*\right)e^{4i\pi ft}\right\} \\ & - \Re\left\{\left(\tilde{\bar{\tau}}_{xy}\dot{\tilde{\bar{v}}}\right)e^{4i\pi ft} + \left(\tilde{\bar{\tau}}_{xy}\dot{\tilde{\bar{v}}}^*\right)e^{4i\pi ft}\right\} \\ & - \Re\left\{\left(\tilde{\bar{\tau}}_{xz}\dot{\tilde{\bar{w}}}\right)e^{4i\pi ft} + \left(\tilde{\bar{\tau}}_{xz}\dot{\tilde{\bar{w}}}^*\right)e^{4i\pi ft}\right\}\Big)\, dA \end{aligned} \tag{7.15}$$

where $\bar{\cdot}$ on each term denotes its amplitude; $*$ is the conjugation; e is the exponential; f is the excitation frequency; and t is time.

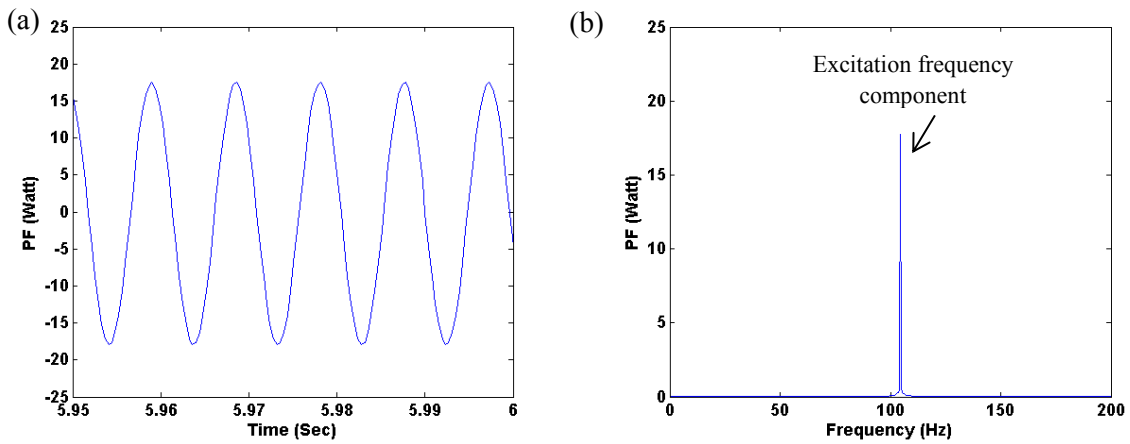

Figure 7.6: PF in intact beams when $f_e = \frac{1}{2} f_1$: (a) time-domain plot; (b) Fourier spectrum.

7.4.2 Super-harmonic resonance of power flow

Second-order superharmonic

The super-harmonic resonance occurs when the cracked beam is subjected to an excitation frequency having its integral multiple in the range of a bilinear frequency of the beam. In this section, the second order superharmonic of the first bilinear frequency, $f_{b,1}$, of the cracked beams is presented. Thus, the excitation frequencies can be stated as $f_{b,1}/2$. The number of the substep in one second is taken as $25 f_{b,1}$.

Table 7.5: Case studies of second-order super-harmonic resonance.

Crack		First bilinear frequency (Hz)	Figure
Position	**Severity**		
0.025	0.125	105.91	7.7(a)-(b)
	0.375	101.02	7.7(c)-(d)
0.200	0.125	106.14	7.8(a)-(b)
	0.375	103.28	7.8(c)-(d)
0.450	0.125	106.22	7.9(a)-(b)
	0.375	105.57	7.9(c)-(d)

The case studies of the second-order superharmonic and the figures illustrating the results are summarised in Table 7.5. It can be seen from the table that the bilinear frequencies of the beams are heavily dependent on the locations and severities of the cracks. It may be stated that the bilinear frequency reduces when the distance between the crack and the fixed end of the beam decreases. When the location of the crack is unchanged, the bilinear frequency reduces with increasing of crack severity.

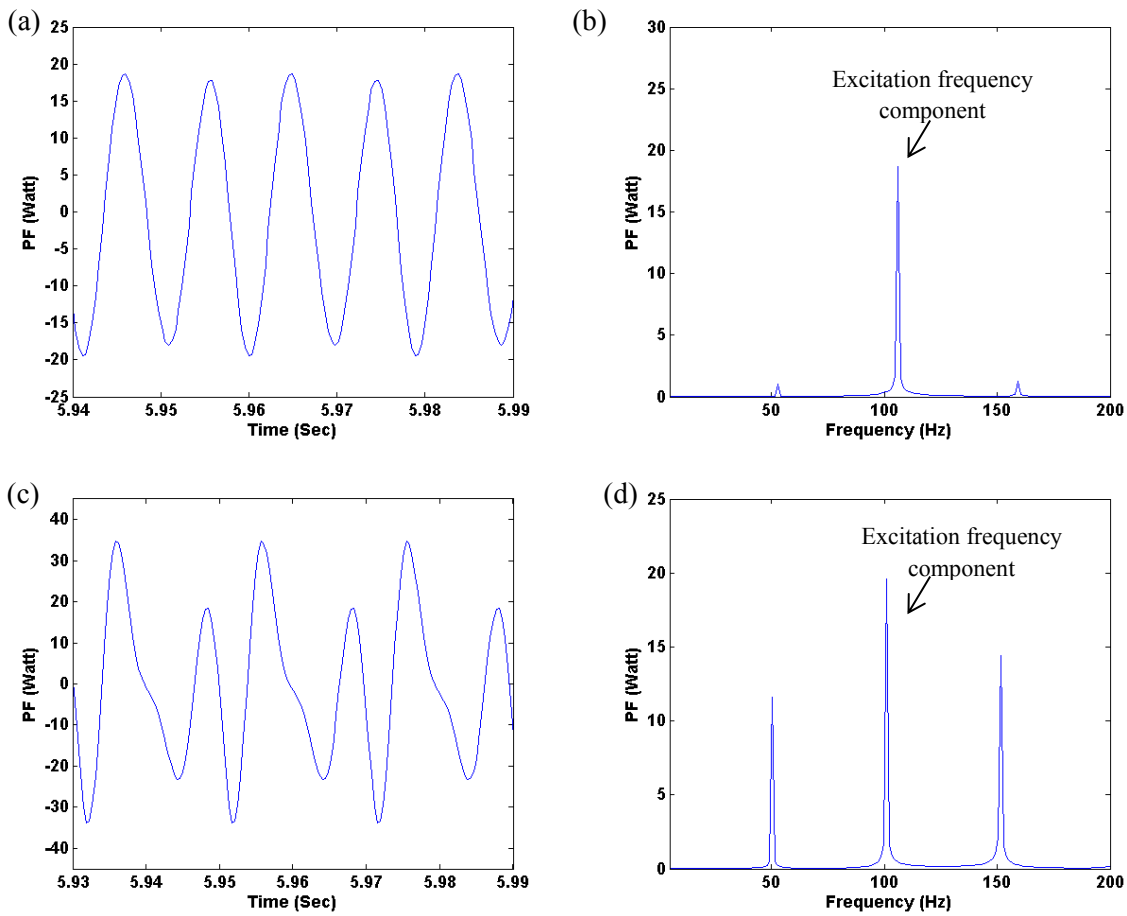

Figure 7.7: PF in cracked beams when $f_e = \frac{1}{2} f_{b,1}$: (a)-(b) time-domain plot and Fourier spectrum of case $\alpha = 0.025$, $\zeta = 0.125$; (c)-(d) time-domain plot and Fourier spectrum of case $\alpha = 0.025$, $\zeta = 0.375$.

From Figures 7.7 – 7.9, it is seen that the time-domain power flow responses are periodic but not time harmonic. Additionally, there is more than one peak presenting in each Fourier spectrum. Following Equation (7.15), the peaks of the excitation frequency components are double of the input excitation frequency. The other peaks occur due to the nonlinearity induced by the breathing cracks. The abrupt changes in the beam stiffness, when the cracks are open and closed, create impulses to superimpose on the primary responses of the beams (see, Atkinson and Heflinger (1956)).

The occurrence of a breathing fatigue crack on the beam can be detected by the nonlinearity of the power flow. Once the presence of the crack is known, the next task is to identify the crack location and severity. The location and severity of the crack may be predicted using a degree of nonlinearity of the power flow. The degree of nonlinearity of

the power flow in each case can be inspected from either the aspect of the time-domain power flow or the peaks of the super-harmonic resonances in the Fourier spectrum plot.

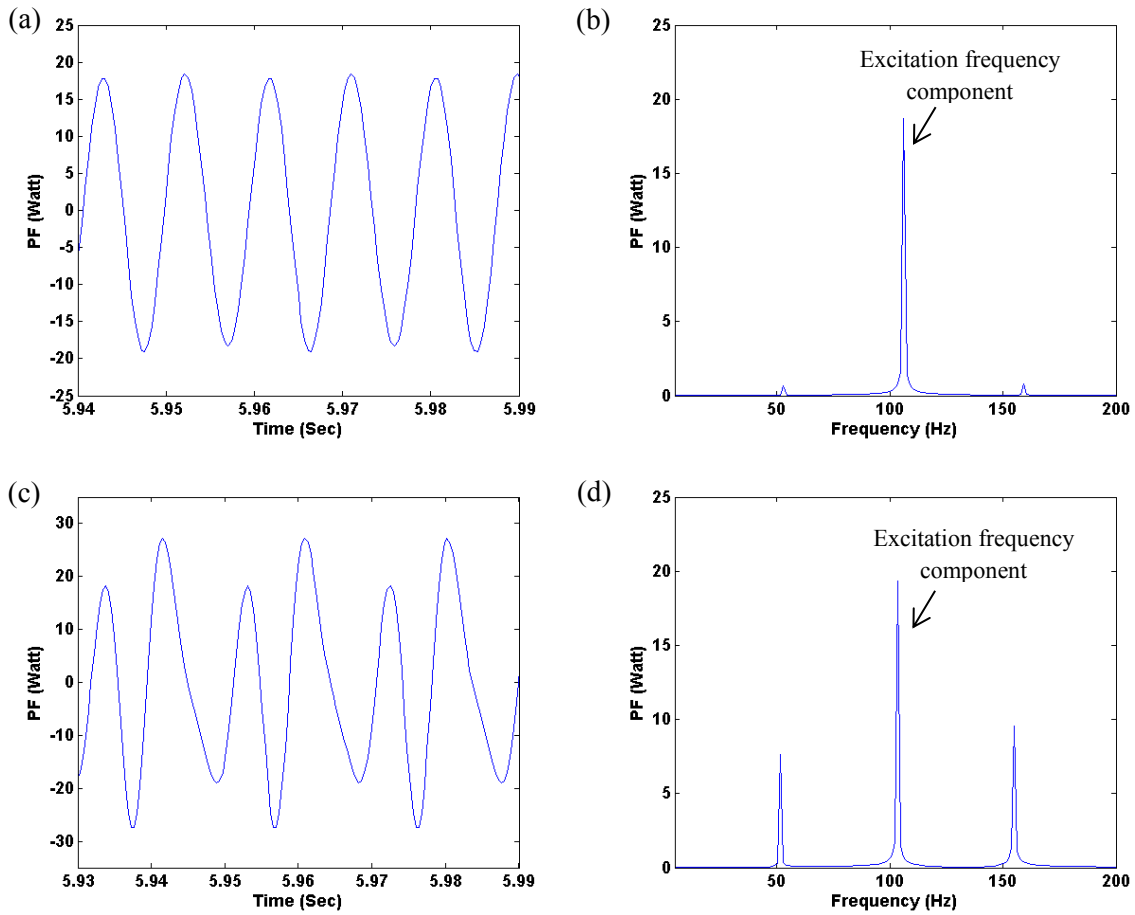

Figure 7.8: PF in cracked beams when $f_e = \frac{1}{2} f_{b,1}$: (a)-(b) time-domain plot and Fourier spectrum of case $\alpha = 0.200$, $\zeta = 0.125$; (c)-(d) time-domain plot and spectrum of case $\alpha = 0.200$, $\zeta = 0.375$.

Comparing (a) and (b) of Figures $7.7 - 7.9$ to one another reveals that the degree of nonlinearity reduces when the location of the crack with the same severity is moved far away from the fixed end of the beam. This reduction can be noticed from the differences of the successive response amplitudes in one cycle of the time-domain plots, and the differences between the peak heights of the excitation frequency components and the super-harmonic components. Higher degree of nonlinearity belongs to the cases with higher difference of consecutive time-domain amplitudes, and smaller difference of the peaks in a Fourier spectrum plot. The reduction in the nonlinearity degree due to the crack location moving away from the fixed end of the beam can be seen more clearly when the severity of the crack increases (see (c) and (d) of Figures $7.7 - 7.9$).

When the location of the crack is fixed, and the severity is varied instead, the trend of the nonlinearity degree can be archived in another manner. From Figures $7.7-7.9$, a comparison can be made with (a) and (c) of each figure, or (b) and (d) of each figure. It is seen from the comparison that the degree of nonlinearity increases with increasing in the crack severity.

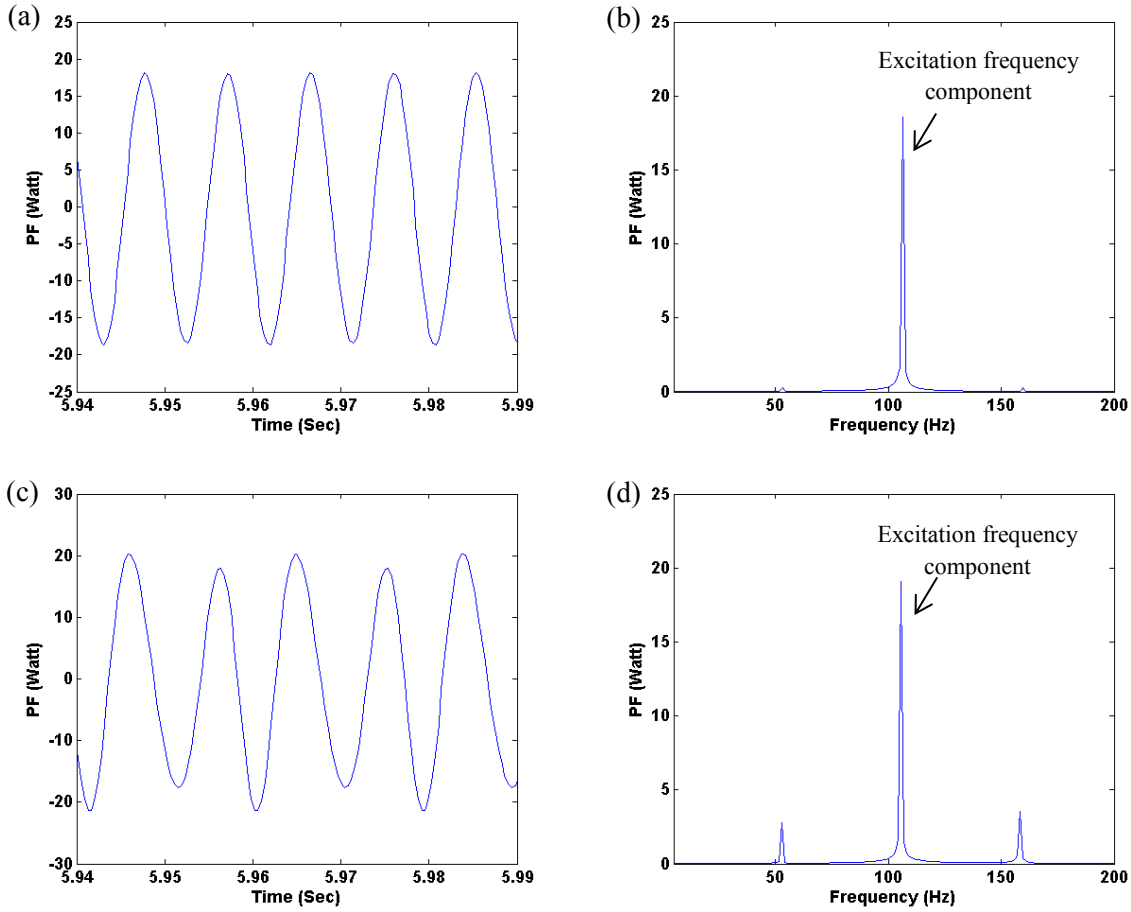

Figure 7.9: PF in cracked beams when $f_e = \frac{1}{2} f_{b,1}$: (a)-(b) time-domain plot and Fourier spectrum of case $\alpha = 0.450$, $\zeta = 0.125$; (c)-(d) time-domain plot and spectrum of case $\alpha = 0.450$, $\zeta = 0.375$.

Third-order superharmonic

The system will undergo the third-order super-harmonic resonance when it is subjected to an excitation force with a single frequency equal to one-third of a bilinear frequency.

Table 7.6: Case studies of third-order super-harmonic resonance.

Crack		First bilinear frequency (Hz)	Figure
Position	**Severity**		
0.025	0.125	105.91	7.10(a)-(b)
	0.375	101.02	7.10(c)-(d)
0.200	0.125	106.14	7.11(a)-(b)
	0.375	103.28	7.11(c)-(d)

In this section, the cracked beam is excited by $f_e = f_{b,1}/3$. The case studies of the third-order superharmonic are shown in Table 7.6.

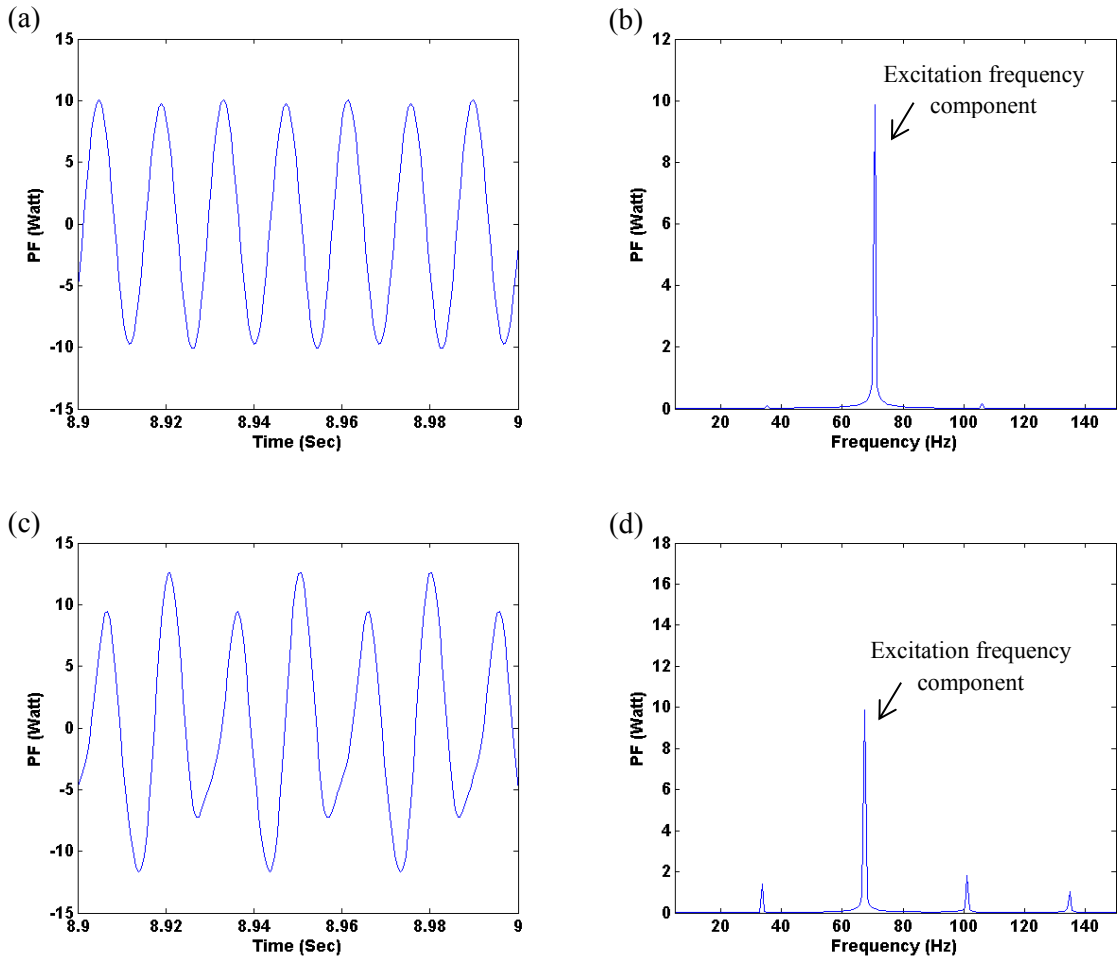

Figure 7.10: PF in cracked beams when $f_e = \frac{1}{3} f_{b,1}$: (a)-(b) time-domain plot and Fourier spectrum of case $\alpha = 0.025$, $\zeta = 0.125$; (c)-(d) time-domain plot and spectrum of case $\alpha = 0.025$, $\zeta = 0.375$.

It can be inspected from Figures 7.10 and 7.11 that the nonlinearity degrees follow the same trend as that of the second-order counterpart shown in the previous section. The higher degree belongs to the beam with the crack located closer the fixed end, and the one having more severity.

Comparing the results of the same cases of the third-order and second-order superharmonics illustrates that the nonlinearity degree of the previous one is lower than that of the latter. This is because, for the third-order superharmonic, the impulse caused by the sudden changes in beam stiffness has a longer time to die out (see, Atkinson and Heflinger (1956)), so its effect on the primary response is lower than that of the second-order counterpart. This means that the components of the second-order resonances in the Fourier spectrum plots can be inspected more clearly. Hence, only the super-harmonic resonance of the second order is selected to be used for crack detection which will be discussed in the upcoming section.

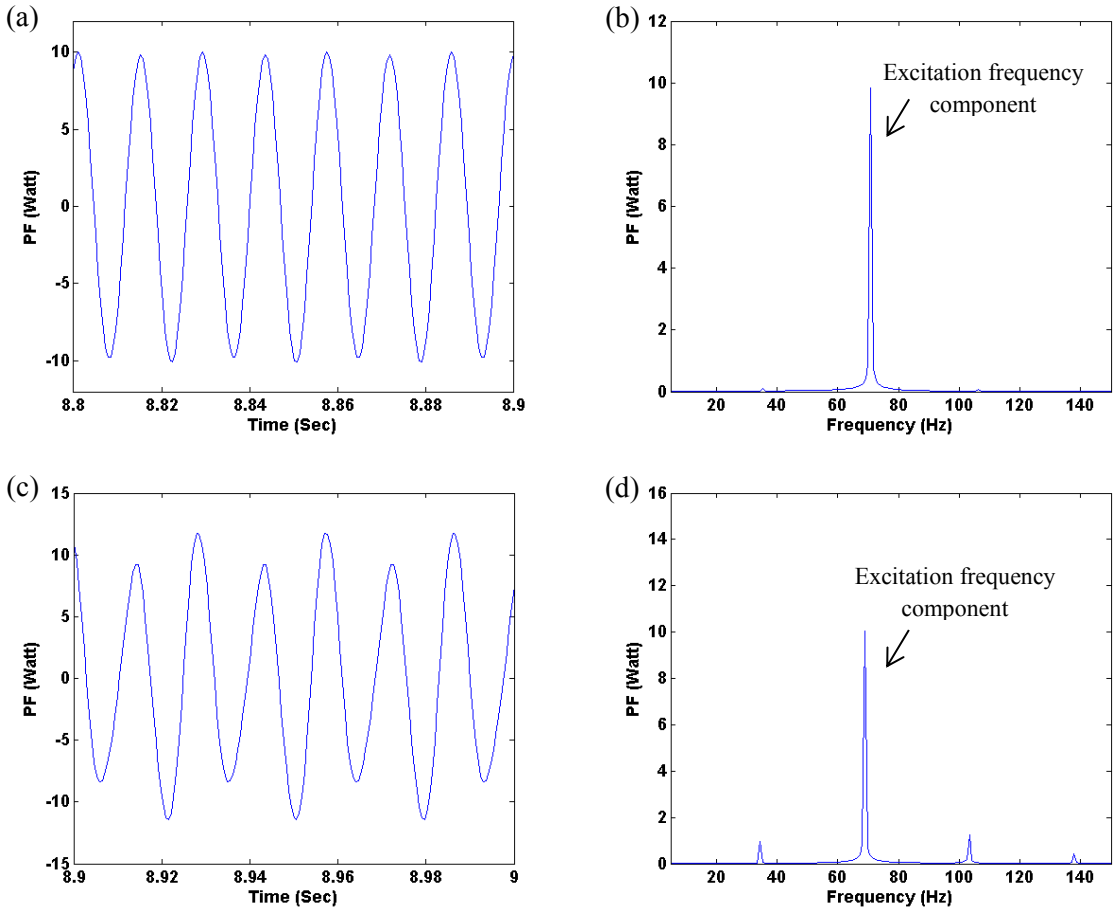

Figure 7.11: PF in cracked beams when $f_e = \frac{1}{3} f_{b,1}$: (a)-(b) time-domain plot and Fourier spectrum of case $\alpha = 0.200$, $\zeta = 0.125$; (c)-(d) time-domain plot and spectrum of case $\alpha = 0.200$, $\zeta = 0.375$.

7.4.3 Effect of crack on global power flow in beam

As seen from the results in Section 7.4.2, the time-domain responses of the power flow are periodic at the steady state. In each cycle of the power flow responses, there are one higher amplitude and lower amplitude. This trend happens to both positive and negative amplitudes of the power flow responses. In this section, two consecutive positive and negative amplitudes in each cycle at the steady states of the time-domain power flow obtained from each location on the cracked beams are presented in Figures 7.12 and 7.13, where higher and lower in the brackets mean higher and lower amplitudes when comparing these two consecutive amplitudes to each other. Figure 7.12 is the cases of the cracks with $\alpha = 0.025$, and $\zeta = 0.125$ and 0.375, while those of the cracks with $\alpha = 0.450$, and $\zeta = 0.125$ and 0.375 are in Figure 7.13. The y axis of each graph is the power flow amplitudes, whereas the x axis presents the beam length where the fixed end is at 0.

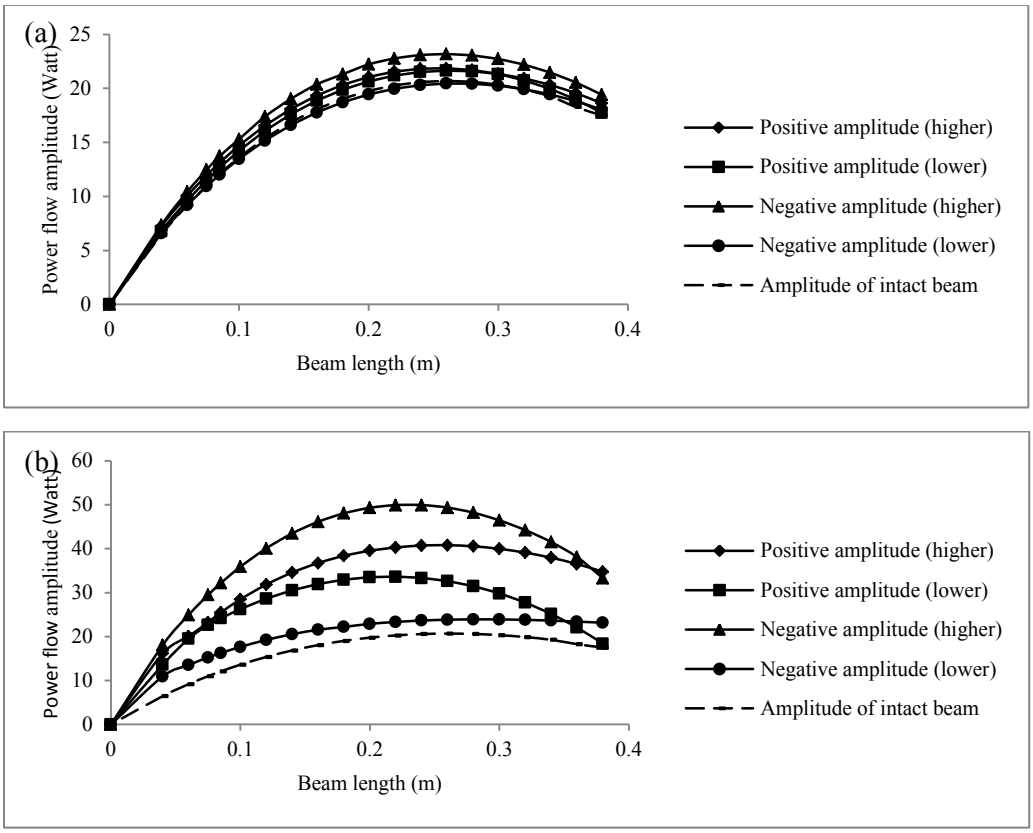

Figure 7.12: Trend of PF amplitudes in cracked beam when $f_e = \frac{1}{2} f_{b,1}$: (a) case $\alpha = 0.025$, $\zeta = 0.125$; (b) case $\alpha = 0.025$, $\zeta = 0.375$.

The amplitudes of the power flow in the intact beam are also plotted in these two figures. For the case of the intact beam, the power flow response is in a simple harmonic form, so all amplitudes are consistent.

It can be observed from these two figures that the breathing cracks globally affect the power flow amplitudes. The significant changes in the power flow magnitudes from that of the intact beam occur not only in the region close to the crack but also the other positions. Due to these results, the damage index based on linear time-average power flow, such as the one proposed in the work of Huh et al. (2011), may not successfully locate the crack.

The differences between the power flow amplitude of the intact beam at each location and those of the cracked beam can be inspected more clearly when the nonlinearity degree is higher. Thus, the higher differences are of the case of the crack located closer to the fixed end of the beam, or the case of the larger crack severity.

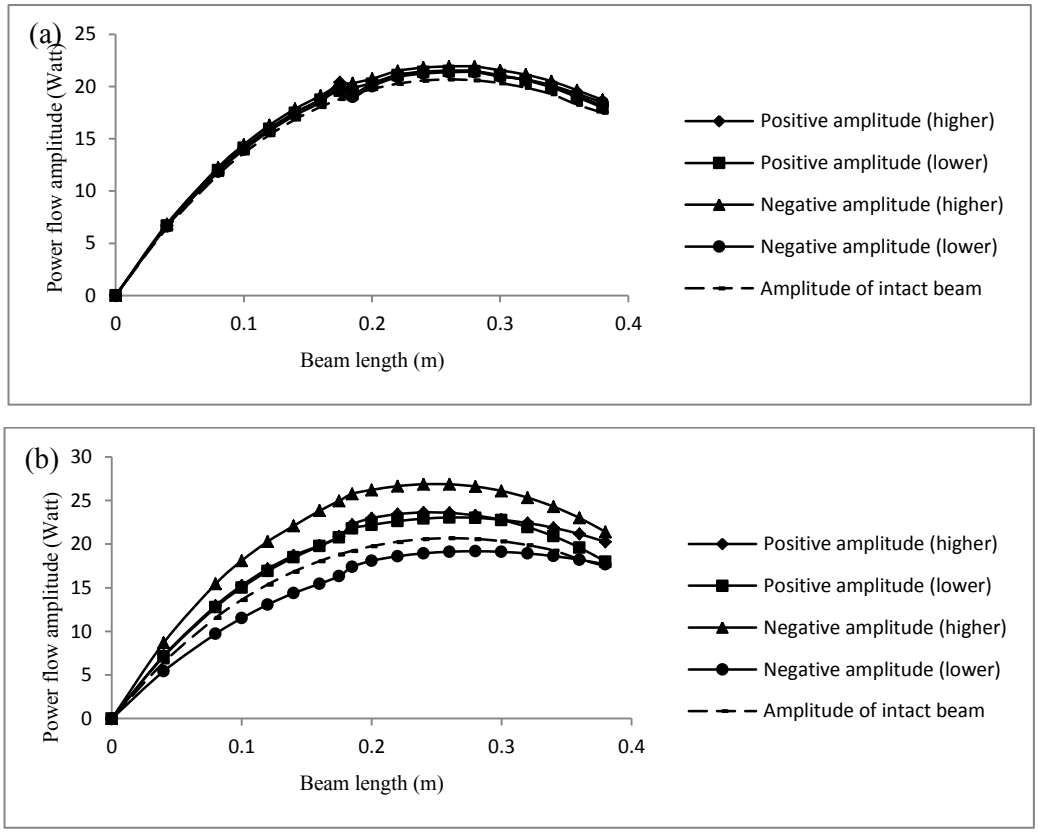

Figure 7.13: Trend of PF amplitudes in cracked beam when $f_e = \frac{1}{2} f_{b,1}$: (a) case $\alpha = 0.450$, $\zeta = 0.125$, (b) case $\alpha = 0.450$, $\zeta = 0.375$.

Moreover, it is also seen from the figures that the amplitudes of the power flow abruptly change at the locations of the cracks due to the interaction between the crack faces. This clapping of two crack faces can also generate the power flow, and it can be another source of the power flow of the cracked beams, apart from the input excitation forces (see, Semperlotti and Conlon (2010) and Romano et al. (2013)).

7.5 Crack detection technique

As seen earlier, the nonlinearity degree of the power flow increases when the crack is moved closer to the fixed end of the beam. The degree of nonlinearity also increases when the crack is deeper. These features can be used to estimate location and severity of a crack in a cantilever beam.

7.5.1 Sensitivity of power flow compared to strain energy

Before going further to the crack detection technique, the sensitivity of the power flow to the presence of a breathing crack on the beam compared with strain energy is investigated. Strain energy is the energy stored after structures deflected due to one or more external forces. It can be written mathematically as (see, Eraky et al. (2015))

$$S = \frac{1}{2}\int_V \left(\sigma_{xx}\epsilon_{xx} + \sigma_{yy}\epsilon_{yy} + \sigma_{zz}\varepsilon_{zz} + \tau_{xy}\gamma_{xy} + \tau_{xz}\gamma_{xz} + \tau_{yz}\gamma_{yz}\right)dV \tag{7.16}$$

where S is the strain energy; σ and ϵ are the dynamic stress and strain; τ and γ are the shear stress and strain; subscripts x, y and z denotes the directions of stress and strain; and V is the volume of the observed component.

For a uniform beam like structure in bending, Equation (7.16) can be reduced to (see, Gavin (2012))

$$S_{beam} = \frac{1}{2}\int_V \sigma_{xx}\,\epsilon_{xx}dV \tag{7.17}$$

where S_{beam} is the strain energy in beams; σ and ϵ are the dynamic stress and strain in the x direction of the beam in Figure 7.1; and V is the volume of the observed component.

The numerical integration, Trapezoidal rule, is employed to determine the strain energy in an observed volume since the FEM provides results of the stress and strain at discrete points. The time-domain responses of the strain energy and the power flow taken from the same cracked beams are shown in Figure 7.14. The power flow is obtained from the same location as that in Section 7.4.2, while the strain energy is the one stored in the beam in the volume between the beam cross section at $x = 0.37\ m$ to $x = 0.38\ m$.

It is seen from Figures 7.14(b) and (d) that the time-domain responses of the strain energy are periodic. Since it is a product of stress and strain components pointing to the same direction, the values of the strain energy are ≥ 0. Comparing (a) to (b) and (c) to (d) show that the patterns of the power flow change from the simple-harmonic form more than those of the strain energy.

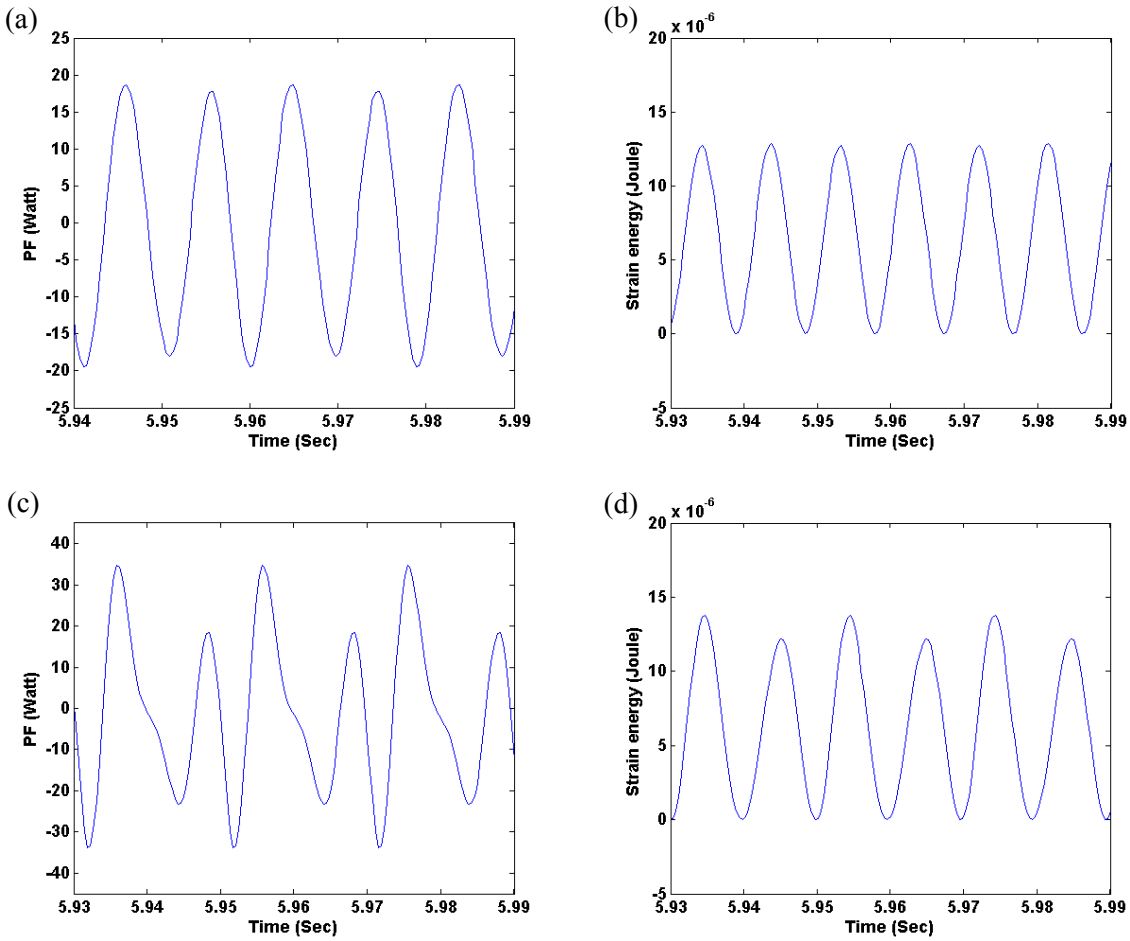

Figure 7.14: PF and strain energy in cracked beams when $f_e = \frac{1}{2} f_{b,1}$: (a) PF time-domain plot of case $\alpha = 0.025$, $\zeta = 0.125$; (b) strain energy time-domain plot of case $\alpha = 0.025$, $\zeta = 0.125$; (c) PF time-domain plot of case $\alpha = 0.025$, $\zeta = 0.375$; (d) strain energy time-domain plot of case $\alpha = 0.025$, $\zeta = 0.375$.

7.5.2 Nonlinear power flow indices

The nonlinear power flow indices able to show the degree of the nonlinearity of the power flow from the time-domain and Fourier spectrum plots are introduced in this section. As stated before, the time-domain responses of the nonlinear power flow are periodic but not time harmonic. This is because the successive amplitudes in one cycle of each time-domain response are not equal. The difference between those amplitudes can present the degree of the nonlinearity of the power flow. From Figure 7.15(a), it can be written as

$$NAD = |A_{nh} - A_{nl}| \tag{7.18}$$

$$PAD = \left|A_{ph} - A_{pl}\right| \tag{7.19}$$

where NAD and PAD represent the negative and positive amplitude differences, respectively; A_{nh} is the higher negative amplitude; A_{nl} is the lower negative amplitude; A_{ph} is the higher positive amplitude; and A_{pl} is the lower positive amplitude. Higher differences between these consecutive amplitudes mean higher nonlinearity degree of the power flow.

Alternatively, the differences between the peaks of the spectra created by the primary resonance and those created by super-harmonic resonance can also reveal the nonlinearity degree of the power flow (Figure 7.15(b)).

$$SPD = |P_h - P_l| \tag{7.20}$$

where SPD represents the difference of peaks of super-harmonic and primary resonances in spectrum plot; P_h is the peak of the primary resonance; and P_l is the peak generated by super-harmonic resonance. The lower difference between these two peaks means higher degree of nonlinearity of the power flow.

As seen earlier, for the intact beam, the time-domain power flow is in the form of a simple harmonic, so the values of NAD, PAD and SPD are equal to zero.

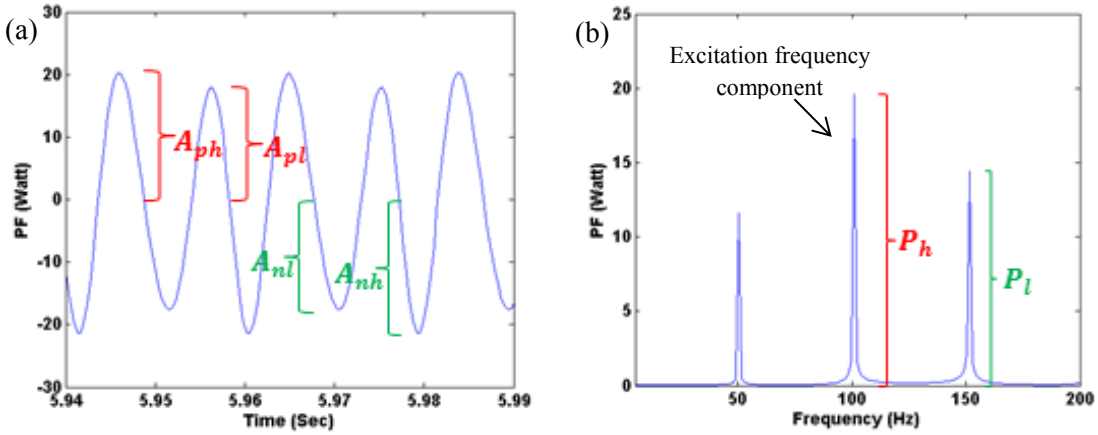

Figure 7.15: Measurements of NAD, PAD, and SPD.

7.5.3 Forward and reverse steps of crack detection technique

Detecting a crack in a structure requires solutions to solve forward and reverse problems since the location and severity of the crack are not known at the beginning. This can be defined as forward and reverse steps of a crack detection technique, respectively. By taking the benefit of the nonlinearity degrees in conjunction with the polynomial equations extracted from the surface fitting, the forward and reverse problems can be tackled to obtain approximate location and severity of the crack.

Forward step

The NADs, PADs, and SPDs of the cracked beam excited by $f_e = f_{b,1}/2$ obtained from Equations (7.18), (7.19) and (7.20) are given in Table 7.7. The global trend of the nonlinearity degree can be inspected from this table. The forward problem of the crack identification technique is to generate surface fitting plots by using the data of the NADs, PADs, and SPDs. These surface fitting plots are created using polynomial equations with the specific coefficients.

The surface fitting plots of the NADs, PADs and SPDs are presented in Figure 7.16. The red marks on the surface plots are the points of the real data. It is seen that the data of the NADs and PADs fit well with the surface plots. For the SPD fitting plot, it contains a small region of the surface that do not fit satisfactorily with the real data. The reason for this will be shown in Case study 3 of Section 7.5.4. This negative aspect can be overcome by increasing the amount of the real data in this region.

From the surface fitting plots, the global trends of the power flow nonlinearity, when the crack location and severity are changed, can be observed more clearly than inspecting from Table 7.7. The degree of the nonlinearity reduces proportionally to the distance of the crack from the fixed end of the beam. The nonlinearity degree is also increased with the increase in the crack severity. The changes in the nonlinearity degree of the cracks located beyond the half length of the beam (from the fixed end) are not significant when compared to those close to the fixed end.

Table 7.7: NADs, PADs, and SPDs of cracked beam with different crack locations and severities.

Location (α)	**Severity (ζ)**	**NAD**	**PAD**	**SPD**
0.050	0.250	5.883	4.135	13.988
	0.375	10.456	14.615	6.390
	0.500	17.239	34.334	3.920
0.150	0.250	4.542	2.716	15.162
	0.375	9.032	10.130	9.317
	0.500	15.594	26.044	1.099
0.250	0.250	3.340	1.875	16.282
	0.375	7.618	6.489	11.974
	0.500	12.036	18.041	5.163
0.375	0.250	1.902	0.990	17.402
	0.375	5.048	3.343	14.783
	0.500	9.631	9.459	10.001
0.500	0.250	0.873	0.568	18.109
	0.375	2.769	1.487	16.798
	0.500	6.070	3.930	14.300
0.600	0.250	0.400	0.279	18.484
	0.375	1.431	0.540	17.838
	0.500	3.016	1.465	16.681
0.700	0.250	0.207	0.003	18.700
	0.375	0.397	0.256	18.479
	0.500	1.294	0.394	18.030

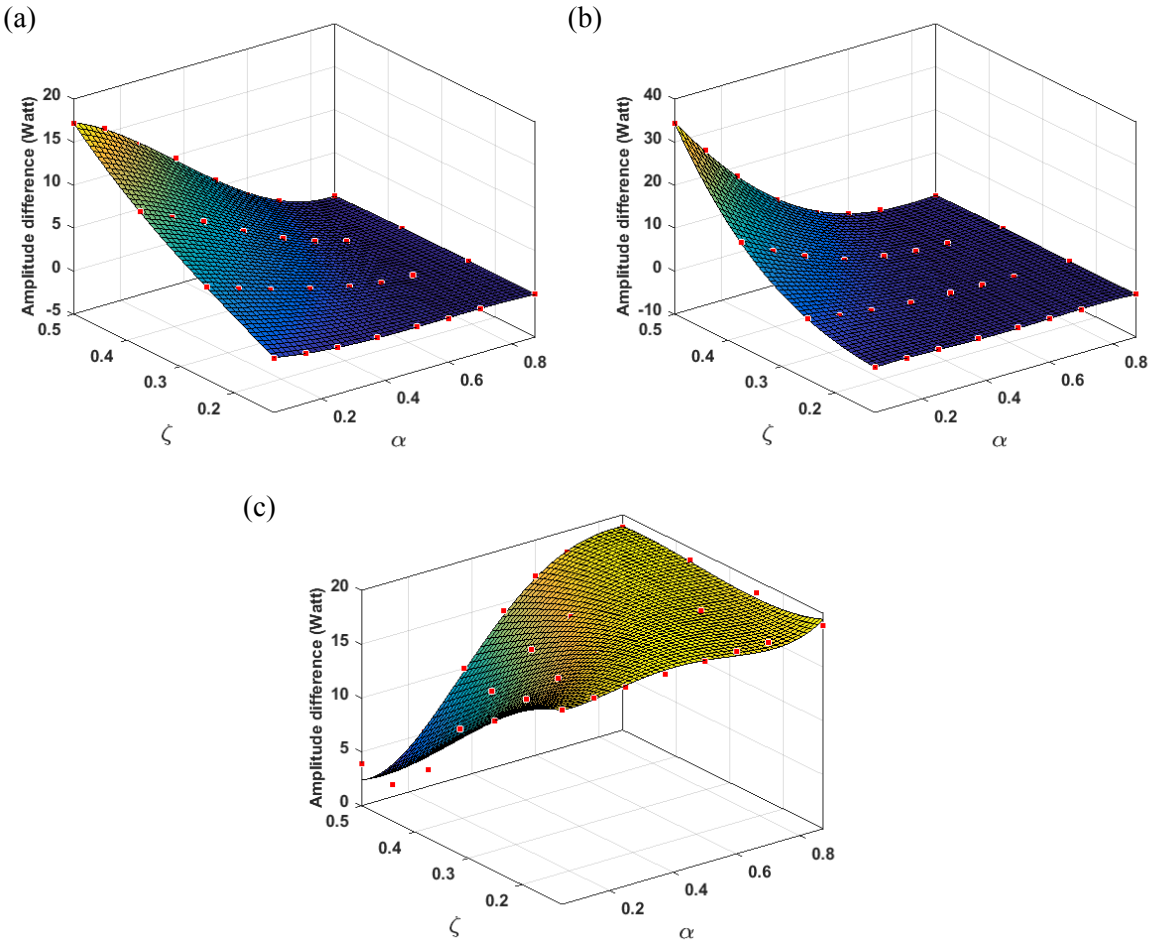

Figure 7.16: Surface fitting of amplitude and peak differences taken from second-order super-harmonic resonance: (a) NADs; (b) PADs; (c) SPDs.

The orders of the polynomial equations of the surface fitting plots are selected as the fourth order for the crack location, α, and the third order for the crack severity, ζ. Hence, the polynomial equations of the surface plots presented in Figure 7.16 are

$$NAD = K_1\alpha^4 + K_2\alpha^3\zeta + K_3\alpha^2\zeta^2 + K_4\alpha\zeta^3 + K_5\zeta^3 + K_6\alpha\zeta^2 + K_7\alpha^2\zeta + K_8\alpha^3 + K_9\zeta^2 + K_{10}\alpha\zeta + K_{11}\alpha^2 + K_{12}\alpha + K_{13}\zeta + K_{14} \tag{7.21}$$

$$PAD = M_1\alpha^4 + M_2\alpha^3\zeta + M_3\alpha^2\zeta^2 + M_4\alpha\zeta^3 + M_5\zeta^3 + M_6\alpha\zeta^2 + M_7\alpha^2\zeta + M_8\alpha^3 + M_9\zeta^2 + M_{10}\alpha\zeta + M_{11}\alpha^2 + M_{12}\alpha + M_{13}\zeta + M_{14} \tag{7.22}$$

$$SPD = N_1\alpha^4 + N_2\alpha^3\zeta + N_3\alpha^2\zeta^2 + N_4\alpha\zeta^3 + N_5\zeta^3 + N_6\alpha\zeta^2 + N_7\alpha^2\zeta + N_8\alpha^3 + N_9\zeta^2 + N_{10}\alpha\zeta + N_{11}\alpha^2 + N_{12}\alpha + N_{13}\zeta + N_{14} \quad (7.23)$$

where K_n, M_n and N_n are the coefficients of the polynomial equations given in Table 7.8.

Table 7.8: Coefficients of polynomial equations**.**

n	K_n	M_n	N_n
1	0.25674	-37.79600	90.15334
2	121.36117	-23.29289	-254.66333
3	-110.58869	474.81494	286.98715
4	-124.63274	-401.93076	-517.52187
5	85.69785	317.52528	303.12872
6	172.28739	-396.88247	270.74783
7	-79.73014	-82.73891	144.91751
8	-21.94561	68.56172	-111.34186
9	-47.32306	12.26092	-295.08442
10	-79.13159	90.63801	-43.82524
11	23.75602	-32.14847	43.85555
12	-0.03227	0.88687	-5.29848
13	44.76150	-6.42628	44.74984
14	-3.33894	0.30429	16.67240

Reverse step

The reverse problem is to solve Equations (7.21), (7.22) and (7.23) to obtain the values of α and ζ, which are the location and severity of the crack, respectively. The NAD, PAD and SPD are measured from the tested beam, and used as inputs of the reverse step by substituting into Equations (7.21), (7.22) and (7.23). Two from these three equations are required in each computation.

The nonlinear system solver in MATLAB, based on the Trust-region-reflective method (see, Coleman and Li (1996a) and Coleman and Li (1996b)) is employed to solve these equations numerically. This solver is designated as *Non-linear least square solver* since it minimises the sum of squares of a function. Thus, it can be expressed mathematically as (see, Sagara and Fukushima (1991))

$$\min_{x,y} f(x,y) \equiv \frac{1}{2}\|\boldsymbol{F}(x,y)\|_2^2 = \frac{1}{2}\sum_{i=1}^{m} F_i(x,y)^2 \;;\; l_x \le x \le u_x,\; l_y \le y \le u_y \quad (7.24)$$

where $\boldsymbol{F}(x_1, x_2) = [F_1(x_1, x_2), F_2(x_1, x_2), \ldots, F_m(x_1, x_2)]^T$is the objective functions of the optimisation; x and $y \in \mathbb{R}^n$; $\mathbb{R}^2$ is the two-dimensional real coordinate space and l and u are the lower and upper bounds, respectively.

An iterative method is required to solve a nonlinear problem. Following the Gauss-Newton iterative method, the subproblem at the current iteration k of Equation(7.24) can be written as

$$\min_{s\in\mathbb{R}^n} \frac{1}{2}\|F(x_k, y_k) + J(x_k, y_k)s\|_2^2 \tag{7.25}$$

where $J(x, y)$ is the Jacobi; and s is the trial step. This subproblem may be rearranged to be in the form of the Trust region subproblem as (see, Sagara and Fukushima (1991))

$$\min_{s\in\mathbb{R}^n} \left\{ g_k^T s + \frac{1}{2} s^T B_k s \;\; such\ that\ \|Ds\|_2 \leq \Delta_k \right\} \tag{7.26}$$

where g is the gradient of f at the current iteration k; B is the Hessian matrix; $\Delta_k > 0$ is the trust region radius; and D is the diagonal scaling matrix to keep the iterates within the specific range of the problem. Equation (7.26) is solved to determine the trial steps, s, that satisfies the condition $f(x + s_x, y + s_y) < f(x, y)$. Otherwise, the region of trust is shrunk, and the trial step repetition is performed.

Getting back to Equation (7.21), (7.22) and (7.23), the measured NAD, PAD and SPD on the left-hand side of the equations are moved to the right, so these three equations are in the form of the objective function, F_i, α and ζ that make f optimised i.e. closest to zero are searched by the nonlinear solver based on Equations (7.24) and (7.26). The solver will give only one pair of roots per one input initial point, so more than one initial point may be needed to obtain the correct roots.

7.5.4 Application of the crack identification technique

The forward and reverse steps of the crack detection technique in the previous section are applied to several case studies in this section. The location of the crack on the beam is defined by α, and its severity represented by the crack depth, and will be defined by ζ.

Case study 1: Crack location and severity of $\alpha_r = 0.450$ and $\zeta_r = 0.375$

The real location, α_r, and severity, ζ_r, of the crack are respectively 0.450 and 0.375. It is assumed that the location and severity of the crack are not known before. The time-domain response and the spectrum of the power flow obtained from the cracked beam are presented in Figures 7.9(c) and (d). The NAD, PAD, and SPD used as inputs of the reverse step are determined from the results in these figures.

Firstly, the NAD and PAD are used to determine α and ζ. They are substituted into Equations (7.21) and (7.22). The coefficient of each term presented in Table 7.8 is also input to the equations. The equations are then solved using the nonlinear system solver provided by MATLAB. The lower and upper bounds of the solver are set to be fit within the ranges of α and ζ used to create the surface fitting plots as $[\alpha_{lb}, \zeta_{lb}] = [0.04, 0.10]$ and $[\alpha_{ub}, \zeta_{ub}] = [0.70, 0.50]$, where the subscripts lb and ub represent lower and upper bounds, respectively. These specific upper and lower bounds will eliminate the roots of the solver that are not in the observed ranges (out of the ranges of the beam length or depth). A number of initial values of the crack location, α_{int}, and depth, ζ_{int}, for the solver are the random values obtained from a uniform distribution within the lower and upper bounds of the solver stated above. For the case studies in this Chapter, 100 random values of α_{int} and ζ_{int} are used. These bounds and initial values are kept constant for every case study in this section.

Table 7.9: α and ζ obtained from polynomial equations of NAD and PAD ($\alpha_r = 0.450, \zeta_r = 0.375$).

No.	Location (α)	Severity (ζ)
1	0.153	0.225
2	**0.341**	**0.306**

From Table 7.9, two pairs of results are obtained from the solver. The second pair, in bold, is closer to the real crack location and severity.

Following this, the NAD and SPD are used. Equations (7.21) and (7.23) are taken part in the computation. Similar to the former case, there are two pairs of results achieved from the solver, and the second pair is closer to α_r and ζ_r.

Table 7.10: α and ζ obtained from polynomial equations of NAD and SPD ($\alpha_r = 0.450, \zeta_r = 0.375$).

No.	Location (α)	Severity (ζ)
1	0.135	0.219
2	**0.375**	**0.326**

Lastly, it is the turn of the PAD and SPD as shown in Equations (7.22) and (7.23). The obtained roots of these equations are in Table 7.11. The second pair is closest to α_r and ζ_r.

Table 7.11: α and ζ obtained from polynomial equations of PAD and SPD ($\alpha_r = 0.450, \zeta_r = 0.375$).

No.	Location (α)	Severity (ζ)
1	0.095	0.212
2	**0.425**	**0.362**

It is seen from all of the above results that the upper and lower bounds of the solver can effectively eliminate the roots of the solver that are not in the ranges of the beam length and depth. Therefore, only two pairs of the roots are obtained for each pair of the coefficient combination, and one of them gives the approximate crack location and severity. Even though the crack detection technique cannot pinpoint the precise location and severity of the crack, it can reveal rough information of the crack that can help us to ease the process of crack identification in beam structures.

Case study 2: Crack location and severity of $\alpha_r = 0.200$ and $\zeta_r = 0.125$

The computation process and the parameters used in the calculation are the same as those for Case study 1. The NAD, PAD, and SPD are obtained from the time-domain and spectrum plots of the power flow in Figure 7.8(a) and (b). α and ζ computed from each combination are presented in Table 7.12. The ones of each combination closest to α_r and ζ_r are in bold.

Table 7.12: α and ζ obtained from polynomial equation of NAD, PAD and SPD ($\alpha_r = 0.200$, $\zeta_r = 0.125$).

Combination	No.	Location (α)	Severity (ζ)
NAD & PAD	**1**	**0.145**	**0.124**
	2	0.523	0.251
NAD & SPD	**1**	**0.157**	**0.125**
PAD & SPD	**1**	**0.221**	**0.152**
	2	0.490	0.293

Case study 3: Crack location and severity of $\alpha_r = 0.050$ and $\zeta_r = 0.500$

The power flow data is collected from the cracked beam, and presented through the time- and frequency-domain plots as shown in Figure 7.17. The NAD, PAD, and SPD are then obtained from this figure. It can be observed from the values of the NAD, PAD, and SPD that the nonlinearity created by the crack is huge, since the crack is located near the fixed end of the beam, and its severity is also large. In practice, these α_r and ζ_r are still unknown at this point. However, it may be estimated from the high degree of nonlinearity that there is a crack with high severity at the position near the fixed boundary of the beam.

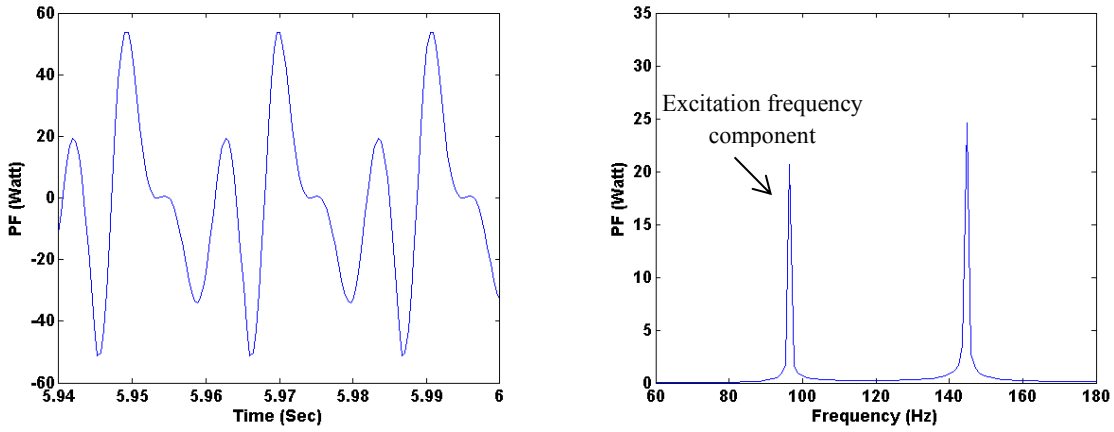

Figure 7.17: Time-domain plot and Fourier spectrum of the PF of case $\alpha = 0.050, \zeta = 0.500$.

From Table 7.13, the combination of NAD and PAD generates only one pair of α and ζ. The solver cannot determine the results for the other two combinations. The reason for this may be known from the surface fitting plot of the SPD in Figure 7.16(c). The area of the surface around $\alpha = 0.050$ and $\zeta = 0.500$ is not fitted properly with the data. The trend of the SPD data at this small region is varied due to the high degree of the power flow nonlinearity that generates higher peak of the super-harmonic component in the Fourier spectrum plot than that of the excitation frequency counterpart (see Figure 7.17).

Table 7.13: α and ζ obtained from NAD, PAD and SPD ($\alpha_r = 0.050, \zeta_r = 0.500$).

Combination	No.	Location (α)	Severity (ζ)
NAD & PAD	**1**	**0.055**	**0.499**
NAD & SPD	1	n/a	n/a
PAD & SPD	1	n/a	n/a

From all of the case studies shown above, it can be summarised as follows:

- The presence of a fatigue crack on the beam can be informed by time-domain and Fourier spectrum plots of the nonlinear power flow.
- The crack detection technique can effectively predict the approximate location and severity of a crack on the beam.
- The crack detection technique can ease the process of crack identification. The approximate crack location and severity will scope down the region on the beam that has to be observed during the crack identification process.
- Errors in curve fitting plots may be occurred due to very high nonlinearity degree when a crack with high severity located close to the fixed end of the beam. To overcome this drawback, more data points of the NAD, PAD and SPD are required for the curve fitting plot.

7.5.5 Signal with noise contamination

In a practical situation, it may be difficult to avoid effects of noise on the accuracy of the crack detection technique. To observe the effects on results from numerical simulations, noise in the form of random artificial white Gaussian noise (WGN) can be added to the signal. The power of this kind of noise is related to that of the signals by a signal-to-noise ratio (SNR).

The white Gaussian noises with the SNR of 50, 20 and 10 are added to the pure power flow signals of Case studies 1 and 2 in the previous section. These contaminated signals are shown in Figures 7.18 and 7.19. The effects of noise can be seen clearly from the time-domain plots of the signals contaminated by the noises with the SNR of 20 and 10. It can also be observed from Figure 7.19(f) that the small peak of the super-harmonic component of the crack with small depth located closed to the fixed end of the beam can still be seen although the noise power is high.

Since the contaminated time-domain responses of the power flow in Figures 7.18 and 7.19 are not periodic, so the NAD and PAD of each response cycle are not equal, the averages of the NAD and PAD taken from 10 sets of the consecutive amplitudes are used to predict crack location and severity. The approximate crack locations and severities obtained from the signals with the SNR of 20 and 50 are shown in Table 7.14. The solver cannot determine the results of the contaminated signal with the SNR of 10, due to huge errors of the NAD, PAD and SPD obtained from the contaminated signal.

Table 7.14: α and ζ obtained from the power flow contaminated by noise.

Case study	SNR	NAD & PAD		NAD & SPD		PAD & SPD	
		$\boldsymbol{\alpha}$	$\boldsymbol{\zeta}$	$\boldsymbol{\alpha}$	$\boldsymbol{\zeta}$	$\boldsymbol{\alpha}$	$\boldsymbol{\zeta}$
1	20	0.211	0.229	0.208	0.238	0.176	0.230
	50	0.303	0.287	0.220	0.250	0.193	0.241
		0.169	0.231				
2	20	n/a	n/a	0.355	0.228	n/a	n/a
				0.435	0.271		
	50	0.145	0.124	0.101	0.118	0.143	0.130
				0.638	0.391	0.542	0.338

It is seen from Table 7.14 that for the case study 1 with the SNR equal to 50, the lowest differences between the pair of α and ζ from the real data are 33% and 23%, respectively, and they are 28% and 0.8%, respectively, for the case study 2. When the power of noise is increased to the SNR equal to 20, the lowest differences are 53% and 39% for the case study 1, and 77% and 82% for the case study 2. Unsurprisingly, the errors of the results are increased when the power of noise increases.

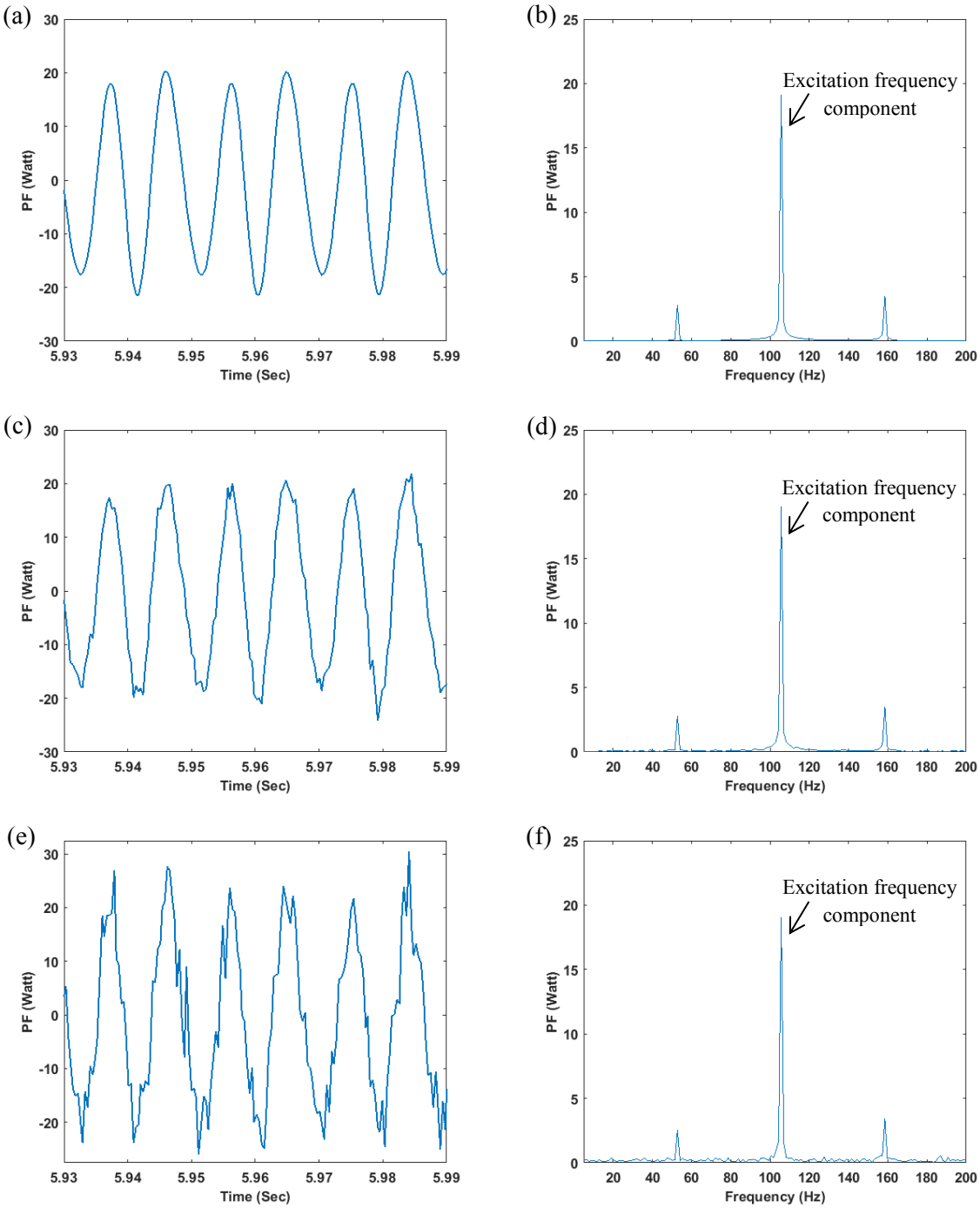

Figure 7.18: Time-domain plot and spectrum of the PF of case $\alpha = 0.450, \zeta = 0.375$ with noise contamination: (a)-(b) SNR = 50; (c)-(d) SNR = 20; (e)-(f) SNR = 10.

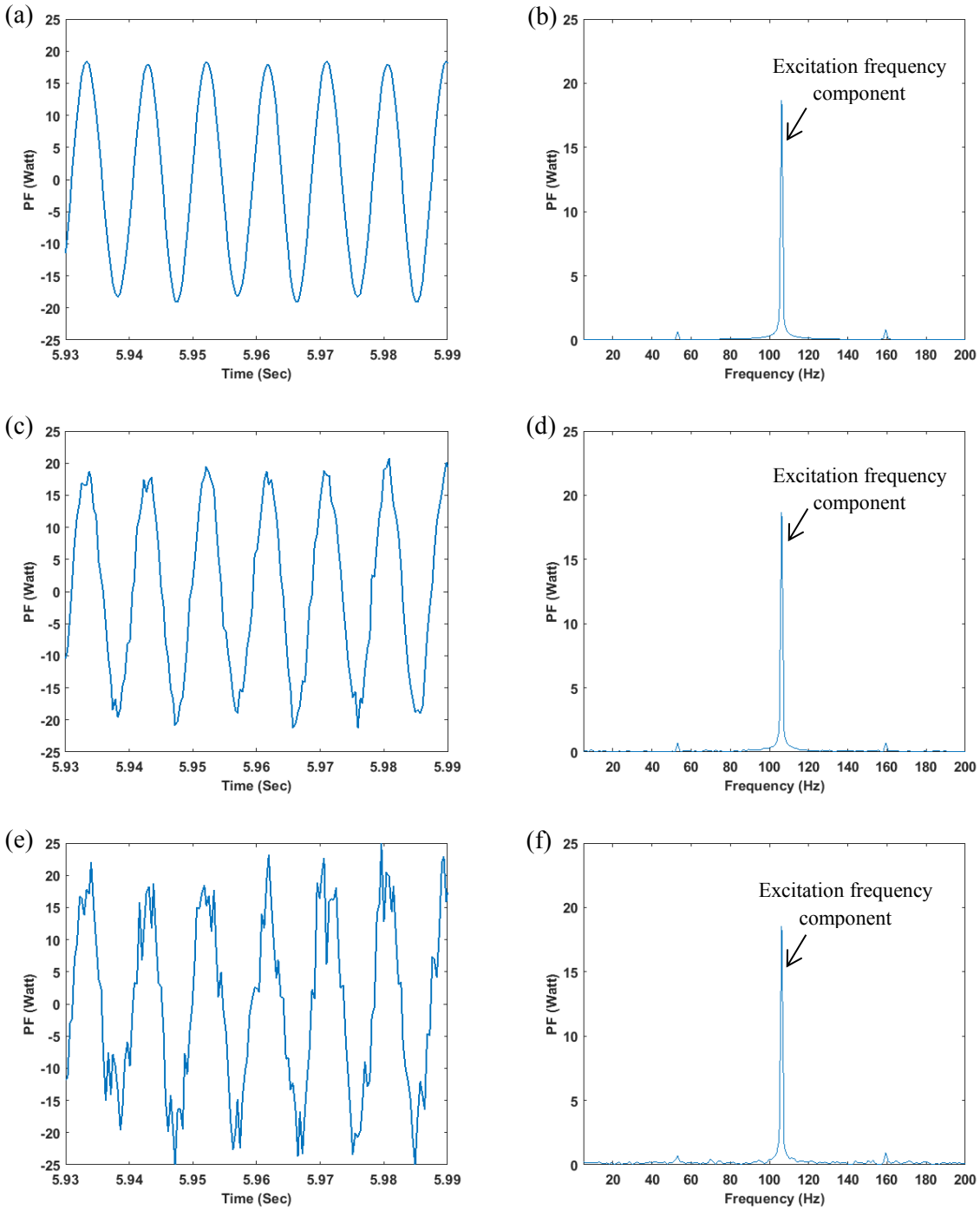

Figure 7.19: Time-domain plot and spectrum of the PF of case $\alpha = 0.200, \zeta = 0.125$ with noise contamination: (a)-(b) SNR = 50; (c)-(d) SNR = 20; (e)-(f) SNR = 10.

7.6 Summary

The super-harmonic resonance of the PF in a cracked cantilever beam has been studied in this chapter. This phenomenon can be inspected from the time-domain and Fourier spectrum plots of the power flow. The nonlinearity degree of the power flow is estimated from the height differences of two consecutive amplitudes in the time-domain plot, or the height difference between the peaks of the excitation frequency and super-harmonic components in the Fourier spectrum plot. This degree is reversely proportional to the distance of the crack from the clamped end of the beam. On the other hand, it is directly proportional to crack severity. Therefore, the deep crack located close to the clamped end can generate the power flow with a high nonlinearity degree.

The trends of the nonlinearity degrees measured from time-domain responses (NADs and PADs) and frequency-domain responses (SPDs), when the crack location and severity are varied, are employed as the tools for the crack detection technique. This technique is composed of two steps which are forward and inverse steps. In the forward step, only a few data of the NADs, PADs and SPDs are required for building surface fitting plots giving polynomial equations and their coefficients. The polynomial equations are then solved numerically by the nonlinear equation solver based on the optimisation algorithm in the reverse step to obtain the approximate location and severity of the crack.

The proposed crack detection technique can inform us the presence of a crack on the beam, and it can effectively estimate location and severity of the crack, without the need of the data from the corresponding intact counterparts. Moreover, only the power flow measured from a measurement point is used as an input for the reverse step. Although, the technique cannot pinpoint the exact crack location and severity, the process of crack detection will be more relaxed if the approximate location and severity are known.

Chapter 8

Multiple crack detection technique using nonlinear power flow indices

8.1 Introduction

This chapter presents the aspects of the super-harmonic resonances when more than one crack occurs in a cantilever beam. Comparisons between the nonlinear power flow behaviours of the single- and multiple-cracked beams are made. The crack detection technique for beam-like structures based on the proposed nonlinear power flow damage indices (DIs) is also introduced herein. This technique can deal with both single and multiple cracks on a beam. The provided case studies show that the crack detection technique is sensitive to small breathing cracks, although it is interfered by noise. Furthermore, the proposed technique can perform without knowledge of the corresponding intact structure.

8.2 Power flow computation scheme

Since the solid finite elements are used again to model cracked beams, Equation (7.2) is employed to compute nonlinear vibrational power flow in the cracked beams. In this chapter, two forms of nonlinear vibrational power flow are obtained. The first one is the instantaneous net vibrational power flow, the same as in Chapter 7, for presenting the degree of the nonlinearity of the power flow in single- and multiple-cracked beams, and for building the DIs for crack detection. The second form is the time-average net vibrational power flow which is obtained using Equation (8.1), and used directly as a damage indicator. The abilities of the time-average net vibrational power flow and the DIs to detect cracks on cantilever beams are discussed. For the sake of convenience, in this chapter, the instantaneous net vibrational power flow will be designated as *power flow (PF)*, and *time-average power flow (TPF)* will represent the time-average net vibrational power flow.

The time-average power flow can be expressed mathematically as

$$\bar{P}_{net} = \frac{\omega}{2\pi}\int_0^{2\pi/\omega}\int_A \left(-\Re\{\tilde{\sigma}_{xx}\}\Re\{\dot{\tilde{u}}\} - \Re\{\tilde{\tau}_{xy}\}\Re\{\dot{\tilde{v}}\} - \Re\{\tilde{\tau}_{xz}\}\Re\{\dot{\tilde{w}}\}\right) dAdt \tag{8.1}$$

where ω is the radian frequency of the excitation force; and t is time. Thus, it may be stated that the time-average power flow is obtained by integrating the power flow over a period of time and divide the result by that period. Equation (3.17) cannot be employed to determine the time-average power flow because the solid elements do not provide internal forces and moments at the centroids of the elements.

8.3 Cracked cantilever beam modelling

8.3.1 Model description

The cracked beam model used in this chapter is a cantilever beams containing single and multiple breathing cracks (Figure 8.1). Its geometry and material properties of the beam are given in Table 8.1. From Figure 8.1, the Cartesian coordinates of the beam are placed at their fixed end. The cracks are modelled on both sides of the beams that perpendicular to the z axis. The dimensionless crack location on the top side of the beam is represented by α_i, while that of the bottom sides is β_j. The dimensionless depths of the top- and bottom-side cracks are represented by ζ_i and ζ_j, respectively. The subscripts i and j show the crack number when there are multiple cracks on the top or bottom sides. When only one crack appears on each side, these subscripts are neglected. A harmonic driving force is input to the beams at the free end.

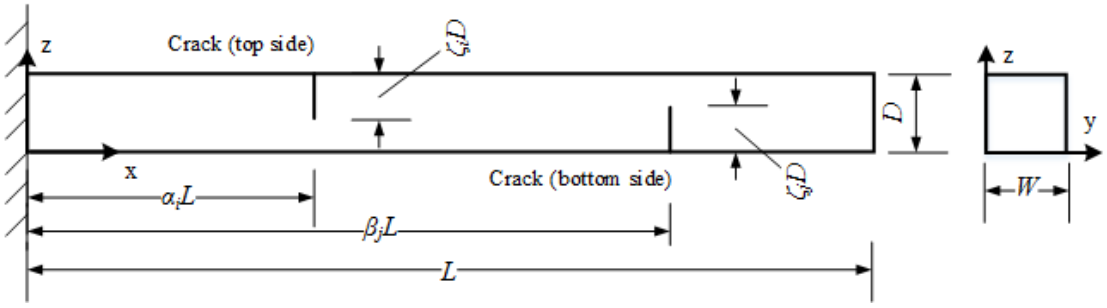

Figure 8.1: Schematic model of cracked cantilever beam.

The same as in Chapter 7, the cracked beam is simulated using the FEM implemented by the codes of the finite element software, ANSYS. The breathing cracks can be open and

closed depending on the excitation force input to the beam. This leads to nonlinear dynamic behaviour of the beams due to abrupt changes in their stiffness during opening and closing of the cracks. It is assumed that there is no friction on both crack faces, and at the initial point, the cracks are closed, so both crack faces contact each other. Additionally, the cracks are also assumed non-propagating. More details of the finite element model of the beam will be mentioned in the following sections.

Table 8.1: Geometry and material properties of cracked cantilever beam.

Length (L)	0.400 m
Width (W)	0.020m
Thickness (D)	0.020 m
Young's modulus	210 GPa
Poisson's ratio	0.300
Mass density	7850 kg/m^3
Damping ratio	0.03

8.3.2 Finite element model

The element type used to model the cracked beams is a 20-node solid element in ANSYS. The breathing cracks on the beams are created by the use of coincident nodes on two crack faces, so these crack faces can move apart and move back to touch each other when the beam is subject to dynamic excitation force. Interactions between these two crack faces are simulated using the theory of the contact problem of two elastic bodies (see Section 7.3.2). Therefore, the eight-node contact and target elements are attached on the crack faces capturing responses when the crack faces create their interactions, such as clapping and sliding. Since local stress intensity at the crack tips is not focused on, the singularity elements may not be used in this cracked beam modelling.

As stated before in Chapter 7, the bilinear frequencies of the cracked beam can be determined using (see, Andreaus and Baragatti (2011))

$$f_b = \frac{2f_c f_o}{f_c + f_o} \tag{8.2}$$

where f_b is the natural frequency of the cracked beam, f_c is the natural frequency of the beam when the cracks are closed, which may be assumed to be equal to the natural

frequency of the intact beam, and f_o is the natural frequency of the beam when the cracks are open.

The ANSYS finite element codes of the cracked beams have been validated in Chapter 7. The number of the solid elements used to model the cracked beams is 2560 elements. This number is selected on the results of the convergence study given in Table 7.4 in the previous chapter.

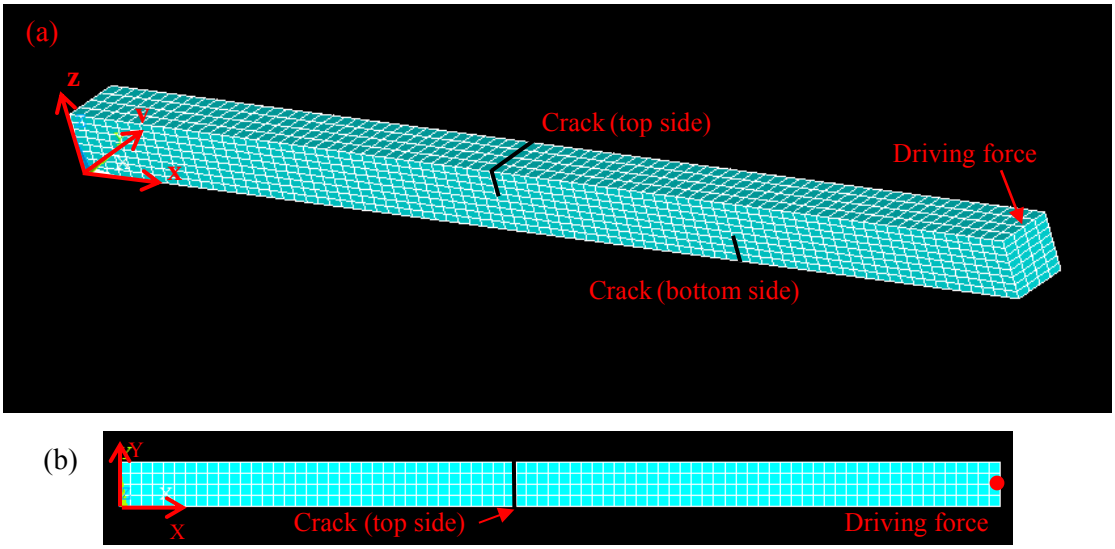

Figure 8.2: Finite element mesh of cracked cantilever beam model: (a) overall beam; (b) top view.

Figure 8.2 displays the finite element model of the cantilever beam containing one breathing crack on its top side, and another one on the bottom side. The coordinates of the beam are at the fixed end, and the driving force is at the free end of the beam. Figure 8.2(b) illustrates the top view of the cracked beam model with the z axis points out of the paper.

8.4 Nonlinear vibrational power flow

The super-harmonic resonance will occur when a cracked beam is subjected to an excitation frequency in the range of its natural frequency divided by an integer. This phenomenon also includes in the nonlinear power flow responses. To observe the super-harmonic resonance in the power flow responses, the cracked beams will be excited by halves of their first mode bilinear frequencies. It is noted that for the beam containing double cracks, the first crack is the one closer to the fixed end of the beam. The first bilinear frequencies of the beams with single and double breathing cracks are given in Table 8.2. These bilinear frequencies are determined using Equation (8.2).

Table 8.2: Bilinear frequencies of beams with single and double cracks.

No.	First crack (α, ζ)	Second crack (α, ζ)	First bilinear frequency (Hz)
1	0.025, 0.125		105.91
2	0.025, 0.375		101.02
3	0.200, 0.125		106.14
4	0.200, 0.375		103.28
5	0.025, 0.125	0.200, 0.125	105.63
6	0.025, 0.375	0.200, 0.375	98.66

Figures 8.3 – 8.5 demonstrate the time-domain plots and the Fourier spectra of the power flow obtained for the beam cross section at $x = 0.38\,m$. The first and second rows of each figure, (a) – (d), are the cases of the beams with single crack, while the last row, (e) and (f), is of the beam containing both the cracks of the first and second rows. It is seen that the time-domain power are periodic but not time harmonic. Apart from the peak of the excitation frequency, there are more peaks occurring in each Fourier spectral. These additional peaks are occurred due to the nonlinear vibration characteristic called the super-harmonic resonance as discussed earlier in Chapter 7.

A degree of the nonlinearity of the power flow may be evaluated by the differences of the consecutive amplitudes or the differences of the peaks of the excitation frequency component and one of the super-harmonic components (Figure 7.15). Comparing the first and second rows of each figure shows that the nonlinearity degree of the power flow depends on the location of the crack. The crack located close to the fixed end of the beam can generate a higher degree of the nonlinearity. When comparing the first and second rows of Figure 8.3 to those of Figure 8.4, it can be observed that the degree of the nonlinearity is also dependent on the depth of the crack. The deeper crack can cause the higher nonlinearity.

It can also be observed from Figures 8.3 and 8.4 that when the second crack presents on the beam, the degree of the nonlinearity is higher. However, the amplitudes and the peaks of the power flow in the last row of Figure 8.5 are comparable to those shown in the first row of the same figure, since the second crack is located far away from the fixed end of the beam, and its effect on the power flow behaviour is small although its depth is large.

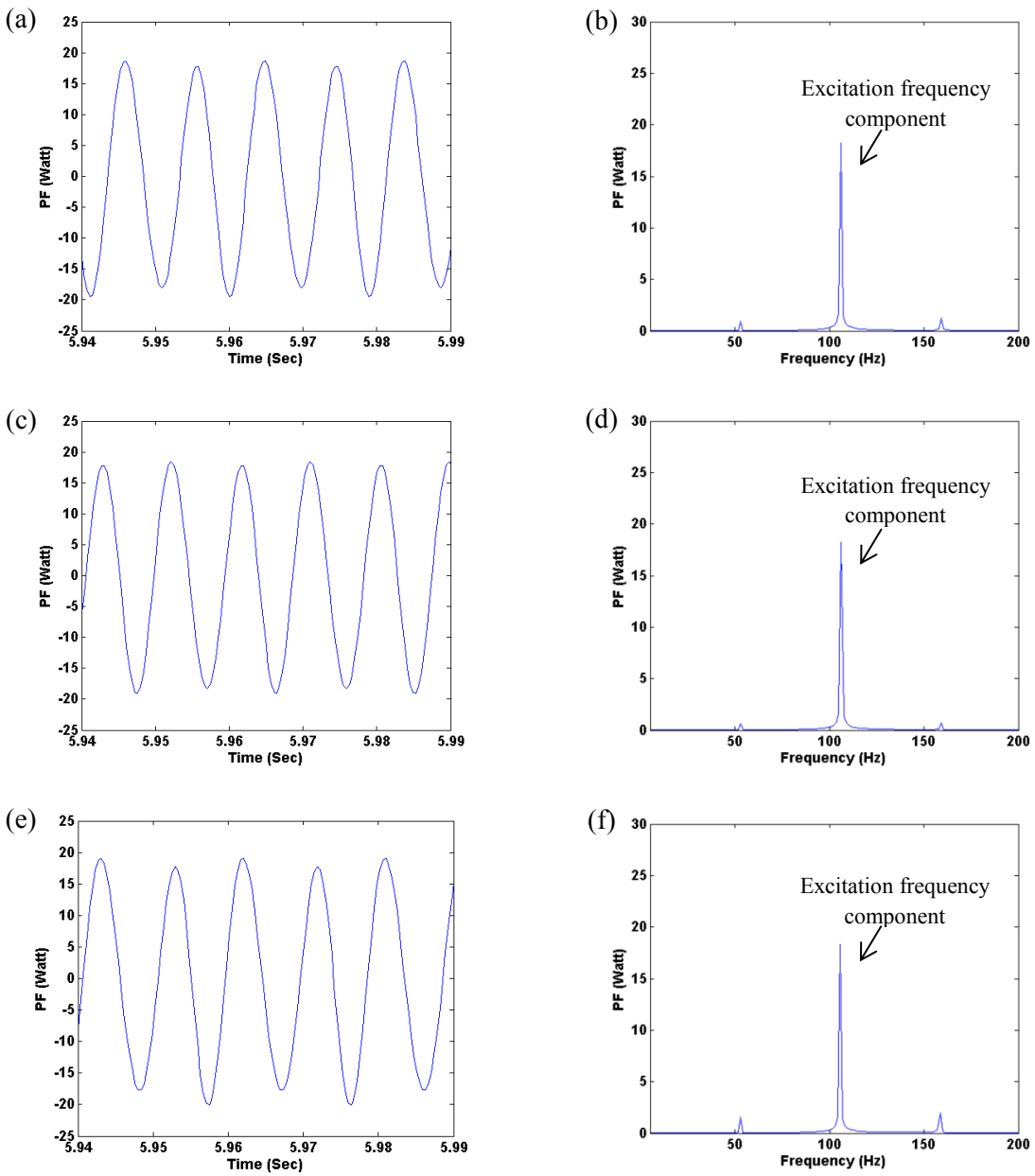

Figure 8.3: Time-domain plots and Fourier spectra of the PF in beams with single and double cracks: (a)-(b) $(\alpha, \zeta) = (0.025, 0.125)$; (c)-(d) = $(\alpha, \zeta) = (0.200, 0.125)$; (e)-(f) $(\alpha, \zeta) = (0.025, 0.125)$ and $(0.200, 0.125)$.

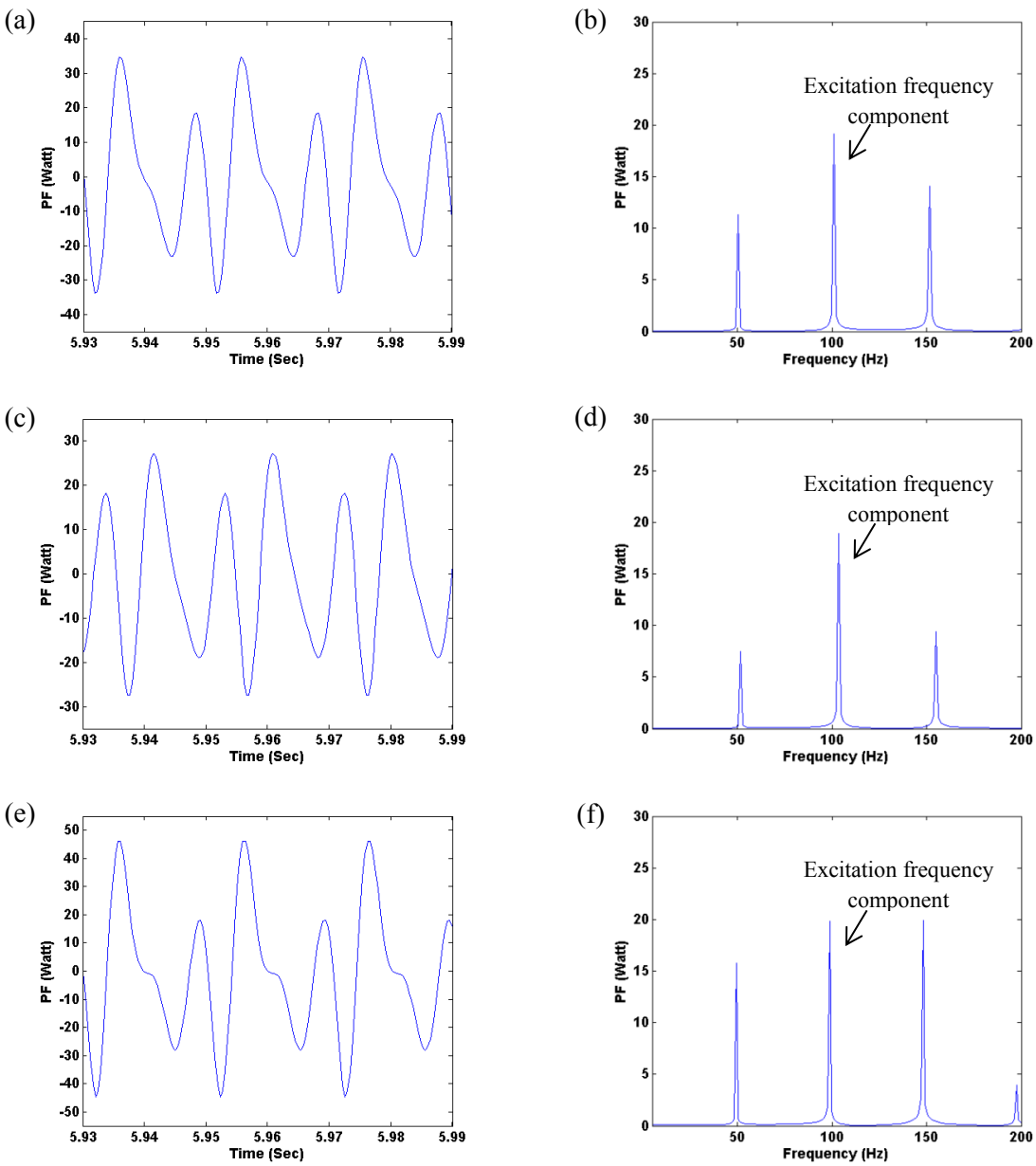

Figure 8.4: Time-domain plots and Fourier spectra of the PF in beams with single and double cracks: (a)-(b) $(\alpha, \zeta) = (0.025, 0.375)$; (c)-(d) = $(\alpha, \zeta) = (0.200, 0.375)$; (e)-(f) $(\alpha, \zeta) = (0.025, 0.375)$ and $(0.200, 0.375)$.

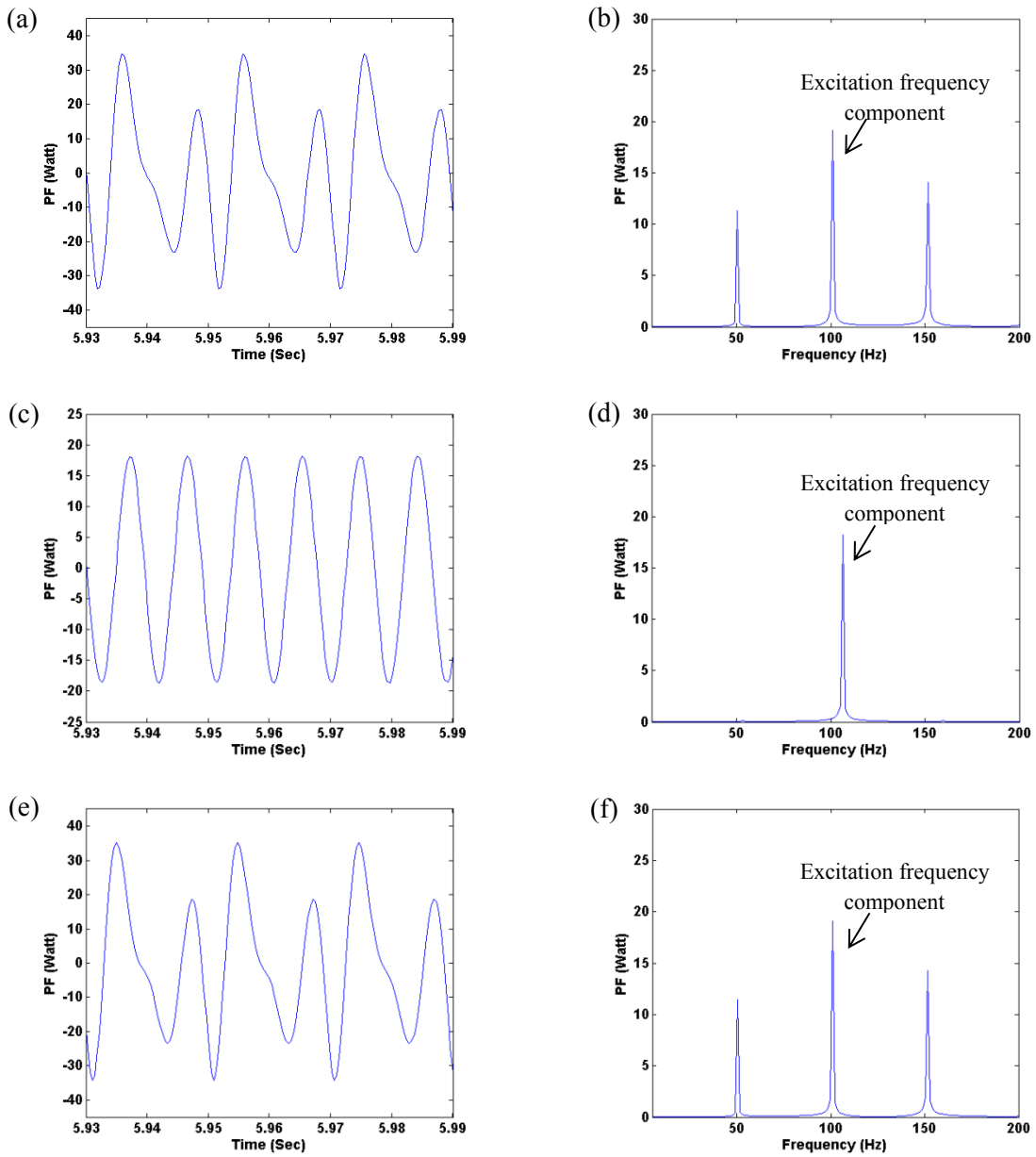

Figure 8.5: Time-domain plots and Fourier spectra of the PF in beams with single and double cracks: (a)-(b) $(\alpha, \zeta) = (0.025, 0.375)$; (c)-(d) = $(\alpha, \zeta) = (0.800, 0.375)$; (e)-(f) $(\alpha, \zeta) = (0.025, 0.375)$ and $(0.800, 0.375)$.

8.5 Application to crack detection

8.5.1 Time-average power flow for crack detection

As stated in Section 8.2, the amount of the power flow averaged over one period of time is defined as the time-average power flow. In this section, the time-average power flow is computed at each position throughout the cracked beams based on Equation (8.1). The layout of the power flow computation points on the beam is shown in Figure 8.6. The computation points are represented by the small black rectangles.

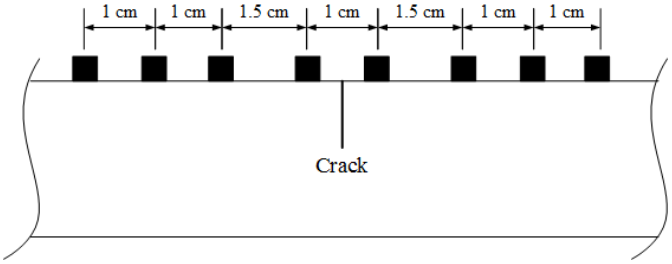

Figure 8.6: Layout of PF measurement points.

The distance between two measurement points is $1\,cm$. Only the one next to the computation points at the crack location is set as 1.5 cm to make all computation points fit with the node locations of the finite element model. It is noted that the positions of the computation points in Figure 8.6 are not the positions of the sensors for measuring the power flow in an experiment. The distance between each measurement point is also not the distance between two sensors. The suitable sensor spacing range in experimental measurement is dependent on the wavenumber (see, Huh et al. (2011)).

The intact and cracked beams are excited by the f_e equal to $f_1/2$ and $f_{b,1}/2$, respectively, where f_1 is the first natural frequency of the intact beam and $f_{b,1}$ is the first bilinear frequency of the cracked beam. The quantity of the time-average power flow in the intact beam (Figure 8.7(a)) increases smoothly from the free end until the vicinity of the beam's mid-point, and then smoothly decreases to zero at the fixed end of the bam.

Once a breathing crack occurs in the beam, the quantity of the time-average power flow at the crack location is abruptly changed. Figures 8.7(b) and (c) contain the plots of the time-average power flow at the crack locations and their vicinities. The solid line, dotted line and dashed lines in (b) are of the cracks located at (α, ζ) equal to (0.200, 0.125), (0.450, 0.125) and (0.800, 0.125), respectively, while in (c), ζ of the cracks is changed from 0.125

to 0.375. It can be observed that the changes of the time-average power flow at the cracks close to the fixed end of the beam (solid lines) are small, and cannot be seen clearly, when compared to those of the other two cracks in the same plot.

From the results in Figure 8.7, the sensitivity of the time-averaged power flow to the breathing cracks is varied with the crack location. A powerful indicator for crack detection has to be consistently sensitive to the cracks at every location on the beam. In the next section, the DIs that are more sensitive to the cracks is proposed.

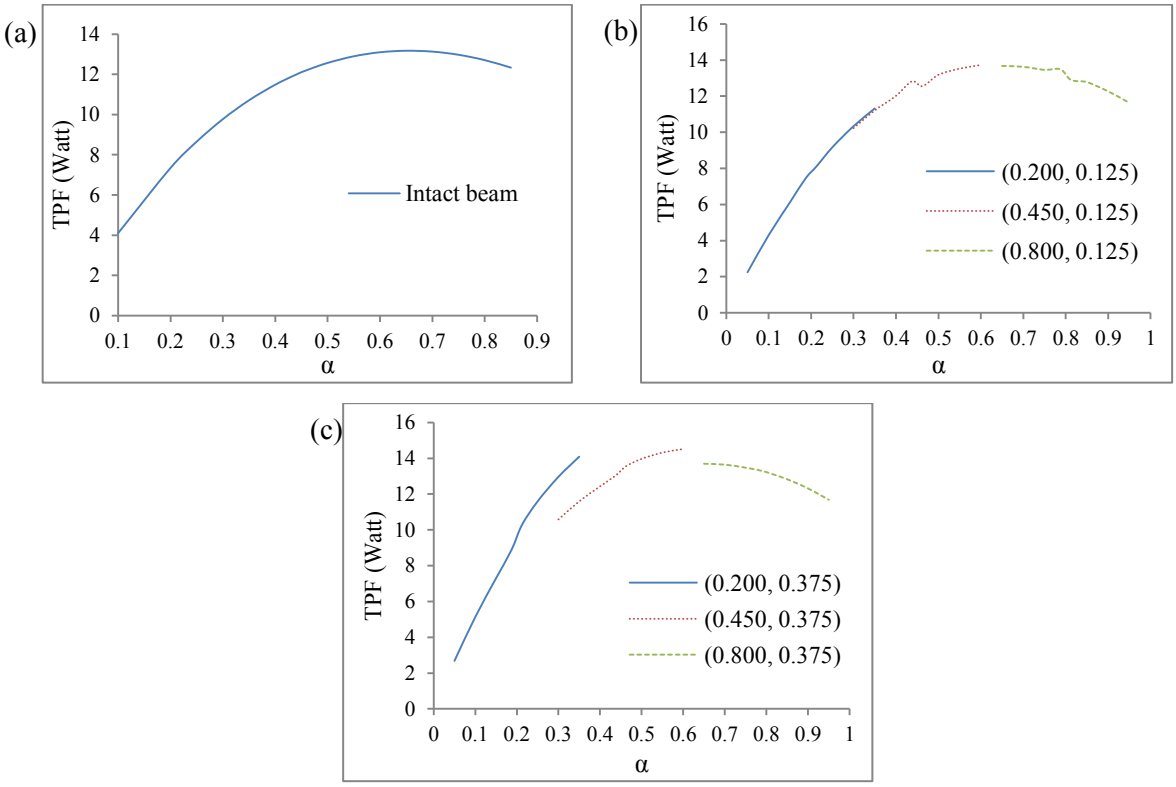

Figure 8.7: TPF in intact and cracked beams: (a) intact beam, (b)-(c) cracked beam with (α, ζ) presented in the graph.

8.5.2 Crack detection technique using power flow damage indices

The differences between two consecutive amplitudes of the time-domain responses of the nonlinear power flow at their steady states are used to build damage indices (DIs) for crack detection. From Figure 8.8, we will have two damage indices from the positive and negative amplitudes. Moreover, the combination of the damage indices from the positive and negative amplitudes can also be employed as another damage index. All of these damage indices are given as

$$DI_p = \left[\frac{A_{p,h} - A_{p,l}}{A_{p,h}}\right] \times 100 \tag{8.3}$$

$$DI_n = \left[\frac{|A_{n,h}| - |A_{n,l}|}{|A_{n,h}|}\right] \times 100 \tag{8.4}$$

$$DI_T = DI_p + DI_n \tag{8.5}$$

where DI is the damage index; A is the amplitude; and the subscripts p, n, h, l and T denote the positive, negative, higher, lower, and total, respectively. It is noted that one pair of positive and negative consecutive amplitudes, as shown in Figure 8.8, may not be sufficient when the technique is performed in real environments that contain noise. This point will be discussed in Section 8.5.4.

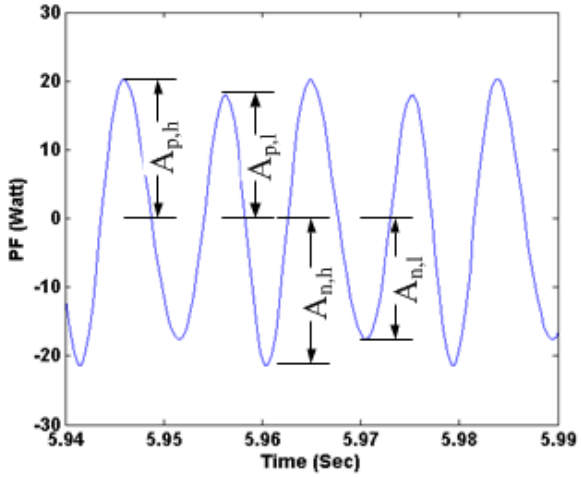

Figure 8.8: Positive and negative consecutive amplitudes for DIs.

To complete crack detection using this technique, the above DIs at the locations on the tested beam based on the layout in Figure 8.6 are evaluated. The DIs are then plotted against the dimensionless crack locations, α and β, to reveal crack location.

8.5.3 Case studies of crack detection

Single crack cases

The DIs shown in Equations (8.3), (8.4) and (8.5) are applied to the case studies of the beam with a breathing crack. Figure 8.9 shows the results when the locations and depths of the crack are (α, ζ) = (0.200, 0.100), (0.200, 0.125) and (0.200, 0.250). The location of the

crack is fixed, while the crack depth is varied to observe the effectiveness of the indices. The red arrows in the plots point to the real locations of the cracks.

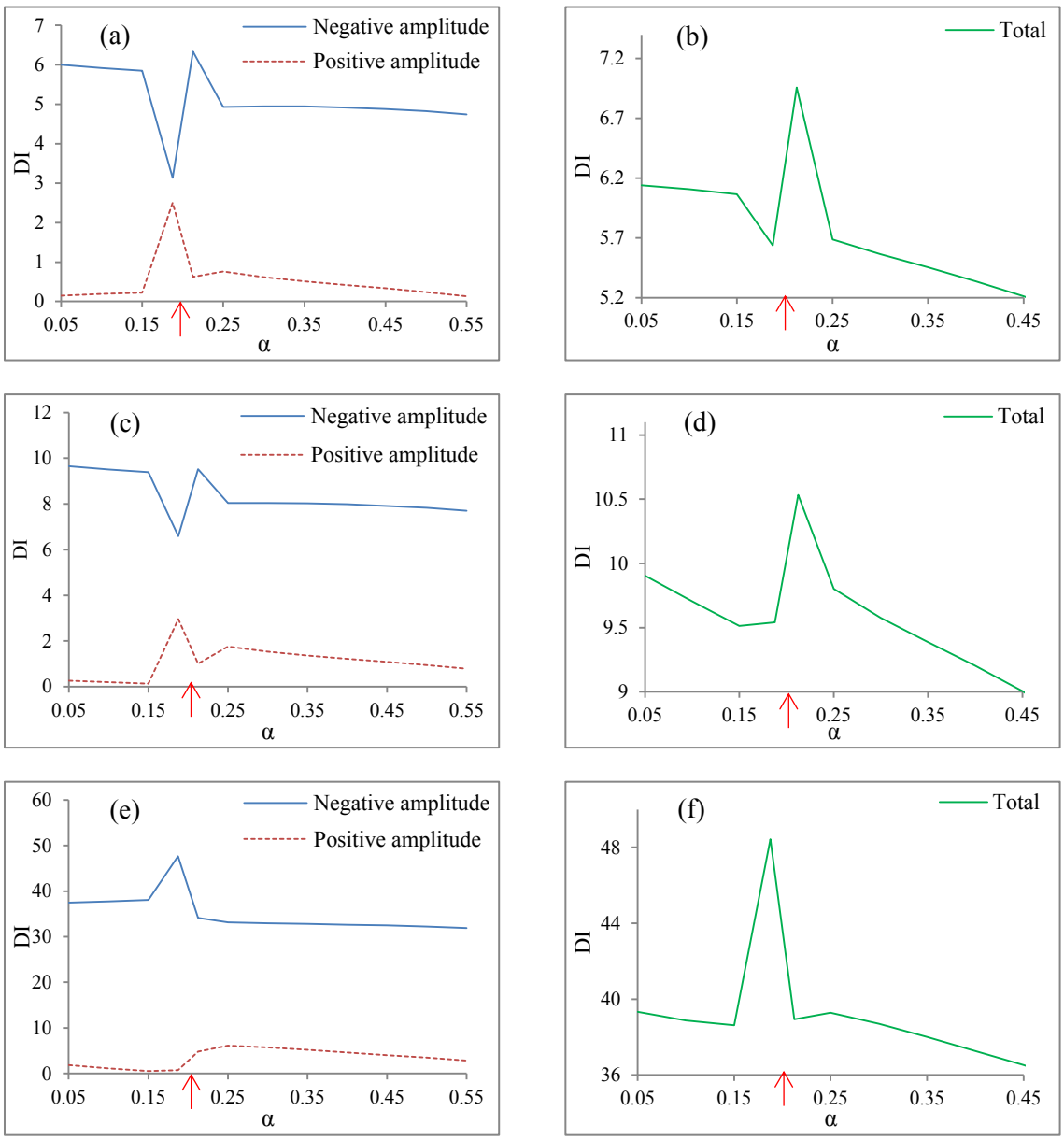

Figure 8.9: DIs of cracked beam: (a)-(b) $(\alpha, \zeta) = (0.200, 0.100)$; (c)-(d) $(\alpha, \zeta) = (0.200, 0.125)$; (e)-(f) $(\alpha, \zeta) = (0.200, 0.250)$.

It is seen from each plot that the values of both negative and positive amplitude indices abruptly change at the location of the crack. At the other locations, the graphs of the DIs are almost straight. Thus, we can know the location of the crack by the peaks of the indices occurred in each plot. One more point that we can observe from these plots of the positive and negative indices is that the difference of the index from the negative amplitudes, DI_n, and the one from the positive amplitudes, DI_p at the same location, is directly proportional

to the depth of the crack, so this may be used to approximately predict the level of crack severity. Furthermore, when this difference is low, the sudden change of the DIs and hence the crack location can be inspected more clearly from the plots.

The right column in Figure 8.9 presents the locations of the cracks obtained from the total damage index, DI_T, or the combination of the negative and positive amplitude indices. It can be observed that the crack locations shown by the DI_T can be seen more clearly than those presented by the DI_n and DI_p, especially for the case of the crack with $(\alpha, \zeta) = (0.200, 0.250)$.

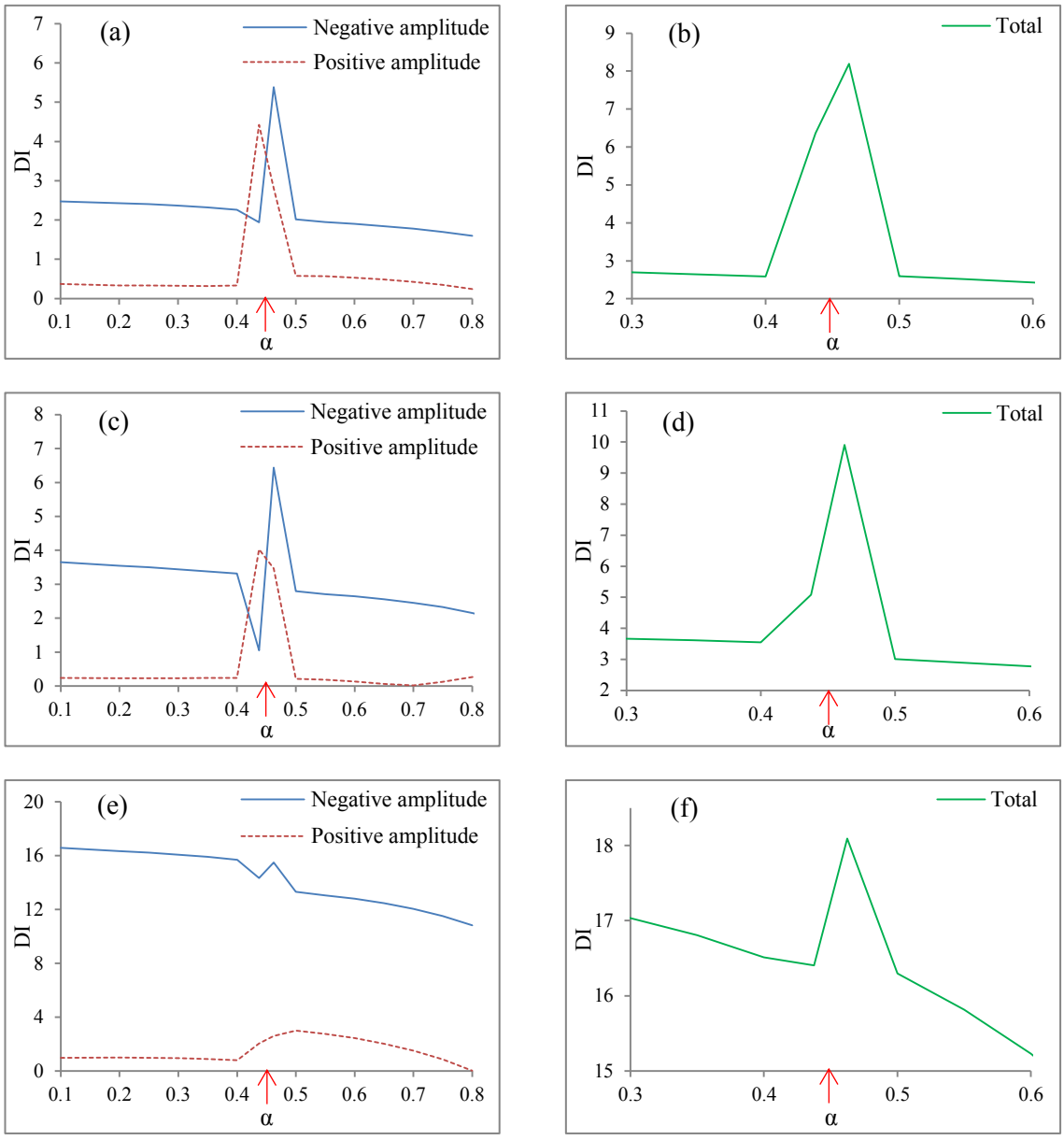

Figure 8.10: DIs of cracked beam: (a)-(b) $(\alpha, \zeta) = (0.450, 0.100)$; (c)-(d) $(\alpha, \zeta) = (0.450, 0.125)$; (e)-(f) $(\alpha, \zeta) = (0.450, 0.250)$.

Figures 8.10 and 8.11 show the results of the other two cases with α equal to 0.450 and 0.800. ζ is varied with the same trend as that of the first case. From the results, the significant changes of the DIs are at the location of the crack, so the proposed crack detection technique can still work well when the crack is changed to locate at the middle of the beam and the place close to the free end. The changes in the values of the DI_T are still higher than those of the other two indices.

Comparing each plot of DI_n and DI_p in Figures 8.9, 8.10 and 8.11 to one another shows that when the depth of the crack is kept constant the difference of the DI_n and DI_p is reversely proportional to the distance of the crack from the fixed end of the beam. As seen from Figure 8.11 of the crack located farthest from the fixed end, the differences of the DI_n and DI_p in all plots are as low as less than 5.0.

In summary, the points that we can obtain from the plots in Figures 8.9, 8.10 and 8.11 are as follows:

- The proposed crack detection technique can work successfully with a breathing crack having different depths, and located at different locations;
- The location of the crack is revealed by the abrupt changes in damage indices, and these changes can be noticed more clearly in the cases of the cracks with smaller depths, so the technique can be deal with cracks at early ages that can be difficult to be noticed by humans' naked eyes;
- The difference between the DI_n and DI_p in each plot is varied with crack depth and location, so once the location is known, crack depth can be approximately predicted;
- The combination of the DI_n and DI_p to be the DI_T can enhance the ability to present the crack location of the crack detection technique.

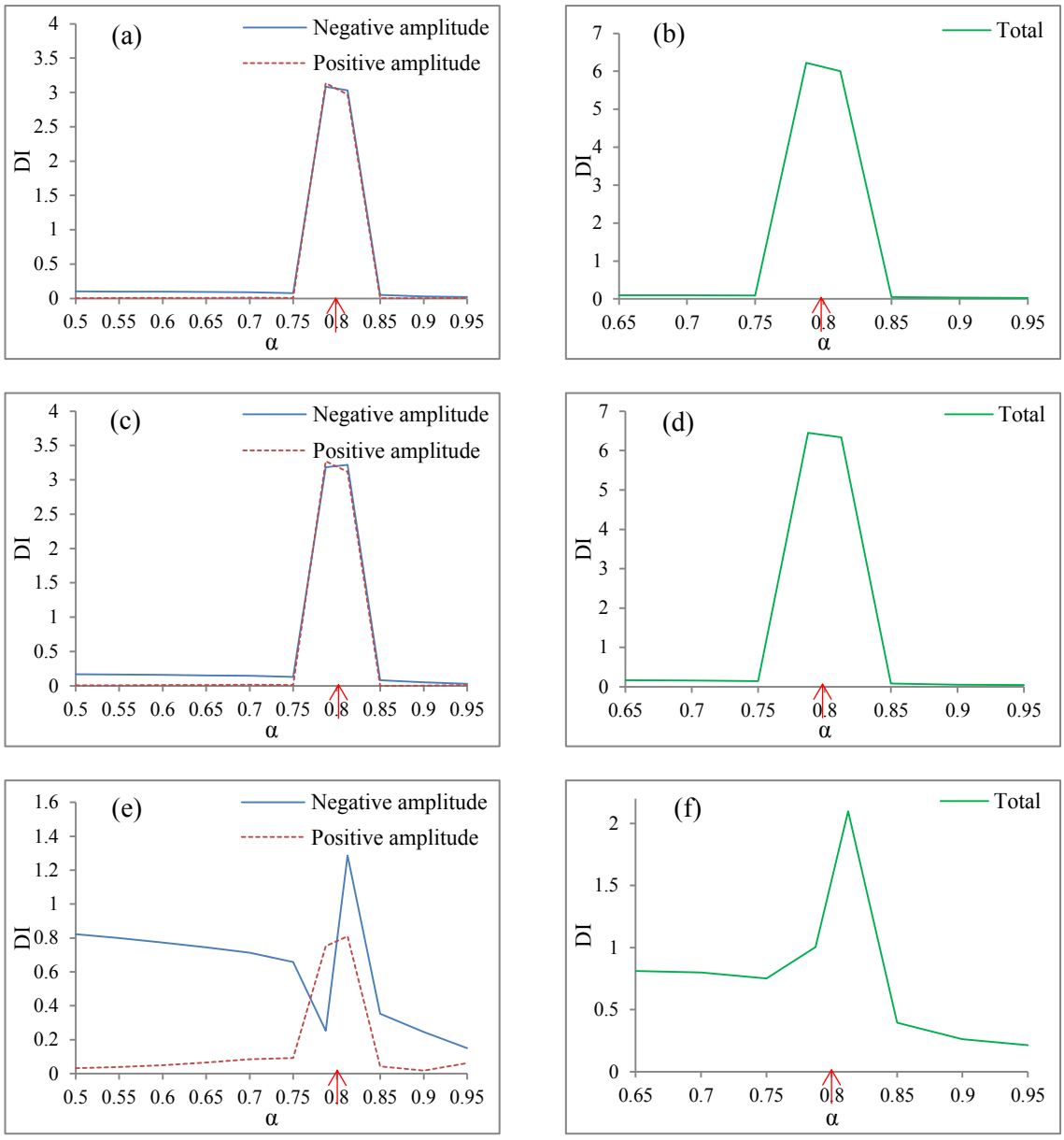

Figure 8.11: DIs of cracked beam: (a)-(b) $(\alpha, \zeta) = (0.800, 0.100)$; (c)-(d) $(\alpha, \zeta) = (0.800, 0.125)$; (e)-(f) $(\alpha, \zeta) = (0.800, 0.250)$.

Double crack cases

The cases of double cracks are divided into two sub-cases which are the cases of both cracks located on top side of the beam, and the cases of one crack on top and the other on the bottom side. It is worthily mentioned again that α represents the location of the cracks on the top side of the beam, whereas β is the location of the crack on the bottom side. The depths of both top and bottom cases are denoted by ζ. The red solid-line and green dashed-line arrows point to the real locations of the first and second cracks, respectively.

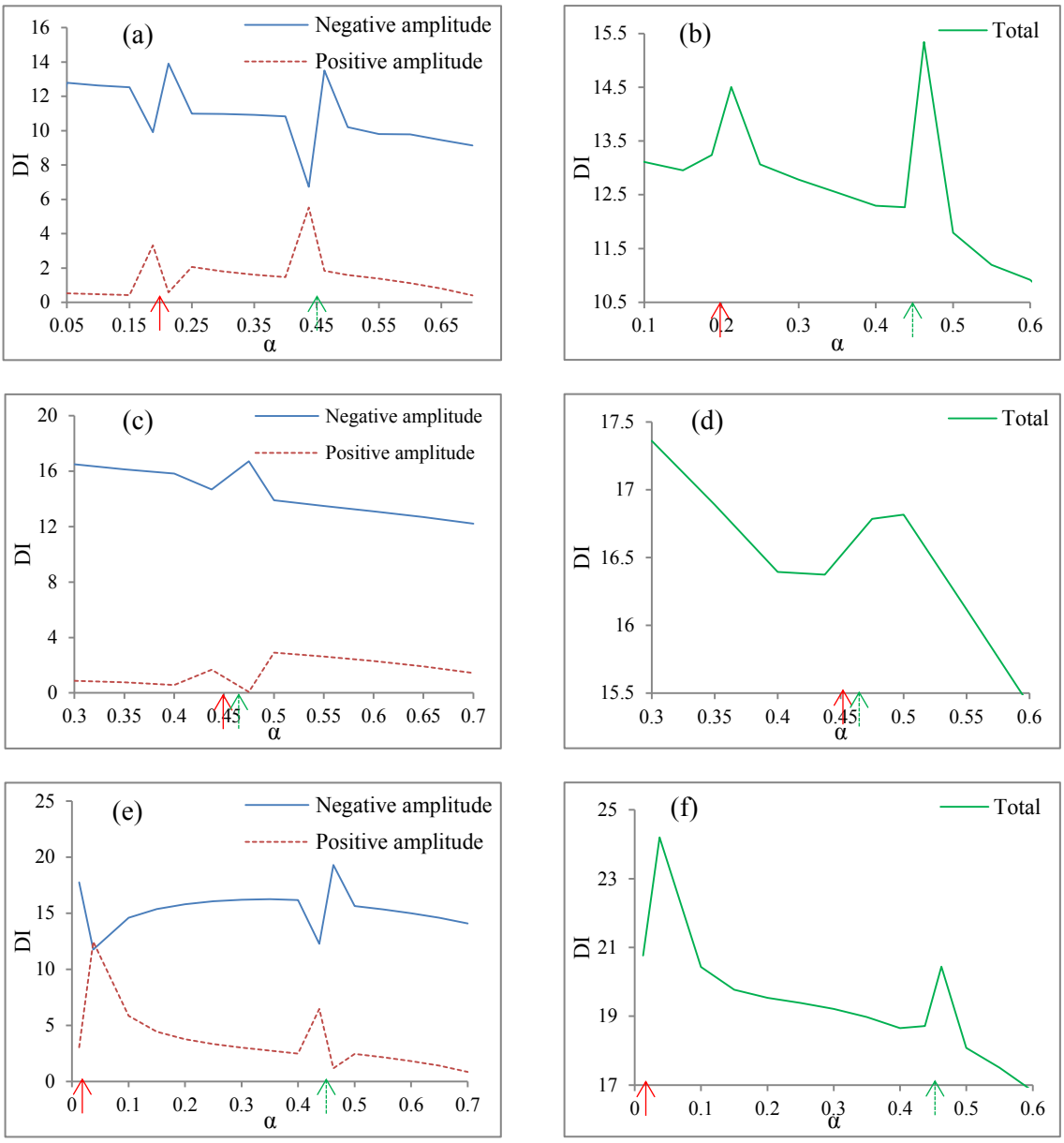

Figure 8.12: DIs of beam containing double cracks on top side only: (a)-(b) first crack: $(\alpha, \zeta) = (0.200, 0.125)$, second crack: $(\alpha, \zeta) = (0.450, 0.125)$; (c)-(d) first crack: $(\alpha, \zeta) = (0.450, 0.250)$, second crack: $(\alpha, \zeta) = (0.463, 0.125)$; (e)-(f) first crack: $(\alpha, \zeta) = (0.025, 0.125)$, second crack: $(\alpha, \zeta) = (0.450, 0.125)$.

Figure 8.12 shows the results of the double crack cases when all the cracks are on the top side of the beam, and located at the different locations. It is seen that both locations of the cracks in each beam are effectively revealed by the DIs, even for the cases of two cracks located close to each other shown in Figure 8.12(c) and (d), and the crack located close to the fixed end of the beam shown in Figure 8.12(e) and (f). However, the peaks of the DIs

at the locations of two cracks close to each other are not as sharp as those of the other cases, and the precise location of each crack cannot be revealed.

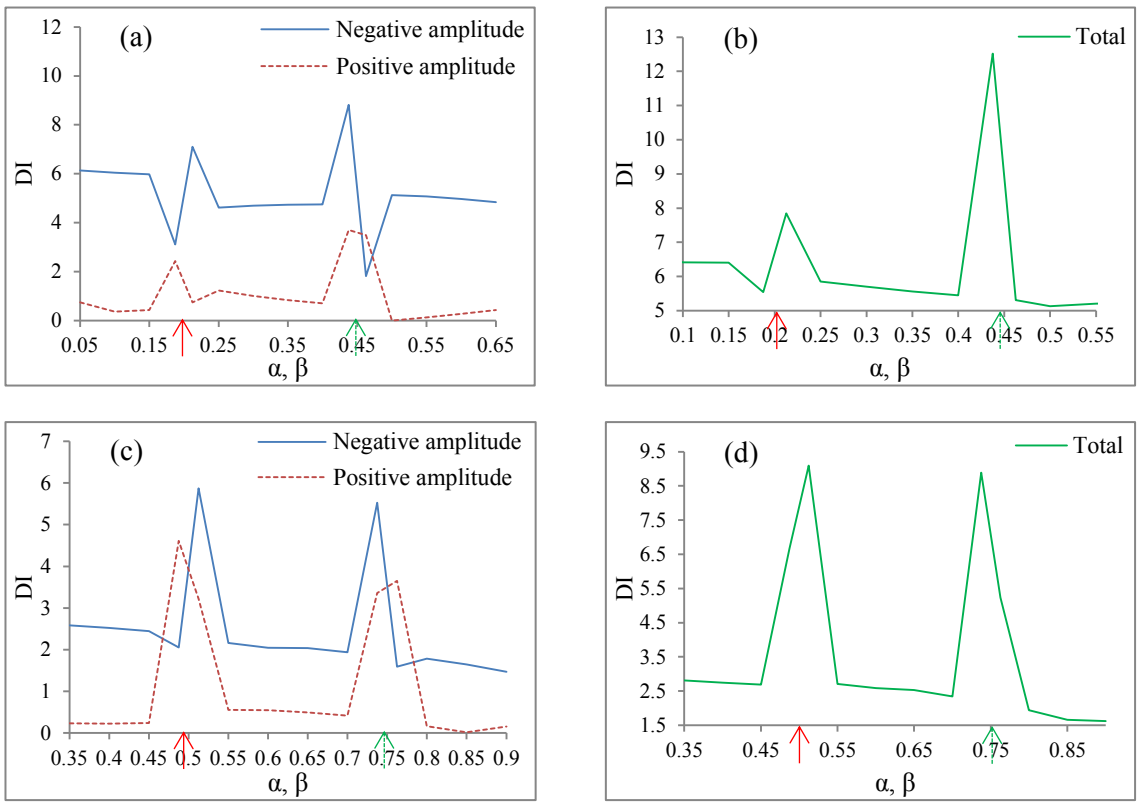

Figure 8.13: DIs of beam containing double cracks on top and bottom sides: (a)-(b) first crack on top side: $(\alpha, \zeta) = (0.200, 0.125)$, second crack on bottom side: $(\beta, \zeta) = (0.450, 0.125)$; (c)-(d) first crack on top: $(\alpha, \zeta) = (0.500, 0.125)$, second crack on bottom: $(\beta, \zeta) = (0.750, 0.125)$.

The cases of the two cracks located on the different sides of the beam are presented in Figure 8.13. The horizontal axis of each plot shows α and β which are the dimensionless locations of the cracks on top and bottom sides of the beam, respectively. The locations of both cracks can still be revealed by the proposed technique. However, the DIs cannot show the side of the beam on which the cracks are.

From all of the results in this section, it can be summarised as follows:

- The crack detection technique can accurately predict the locations of double cracks;
- The cracks close to each other can be detected by the technique, but the precise location of each crack cannot be obtained;
- The technique can detect the crack located at every location on the beam;
- The locations of the cracks on both sides of the beams can be revealed by the technique; however, the technique cannot show which side of the beam the crack is;

- The relationship between the differences of the DI_n and DI_p, and the crack depth cannot be used to estimate the severity of the crack in the cases of multiple cracks.

8.5.4 Influence of noise

The results shown in the previous section are numerically computed, so there is no influence from the environment, such as noise, on the collected power flow data. In this section, to observe the influence of noise on the proposed crack detection technique, the random white Gaussian noise (WGN) is separately added to the power flow signal obtained from each computation point before it is used to estimate the DIs. The power of the noise is represented by the signal-to-noise ratio (SNR).

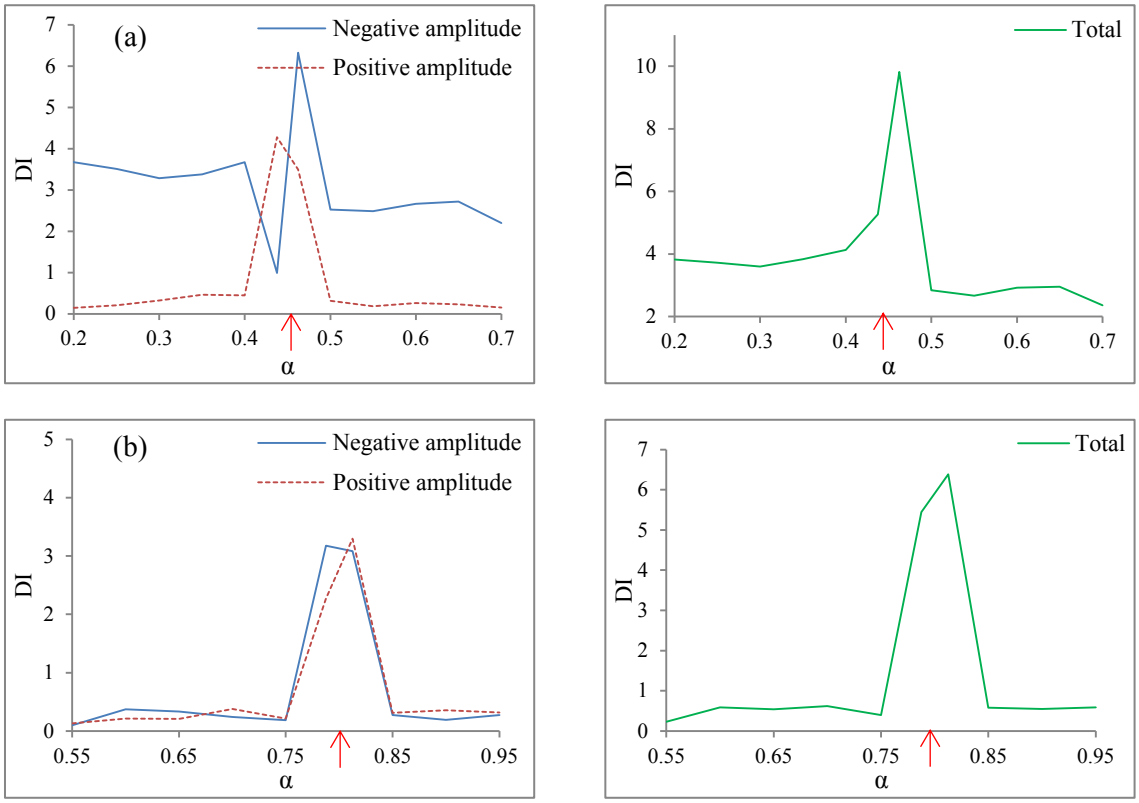

Figure 8.14: DIs with SNR = 50: (a)-(b) $(\alpha, \zeta) = (0.450, 0.125)$; (c)-(d) $(\alpha, \zeta) = (0.800, 0.125)$.

The DIs are estimated using Equations (8.3), (8.4) and (8.5). Due to the effect of noise, the amplitudes of each cycle of the power flow signal at the steady state are not equal. Therefore, the averages of 20 negative and positive amplitude differences of the power flow signal are used as the numerators of Equations (8.3) and (8.4), and the averages of 20 corresponding higher positive and negative amplitudes are used as the denominators of the equations. This is because if using only one negative and positive difference, it may lead to

huge errors in the results of crack detection when the technique has to be carried out in a noisy environment.

Figure 8.14 presents the DIs obtained from the power flow signals contaminated by the noise with the SNR = 50, while Figure 8.15 shows the cases of the noise with the double higher SNR, SNR = 25. It can be seen that the graphs of the DIs at the locations out of the cracks are not as straight as those of the cases without noise shown in Section 8.5.3, especially in the cases of SNR = 25. For the cases of the SNR = 50, the locations of the cracks can be inspected from all of the DIs. However, when the ratio of signal and noise is increased to the SNR = 25, only the peaks of the DI_T showing the crack locations can be inspected, since the heights of the other peaks out of the crack locations caused by the noise are almost alike, and much lower than the ones showing the crack locations. This is an important advantage of the DI_T, compared to DI_n and DI_p, when the damage detection technique has to be performed in a noisy environment.

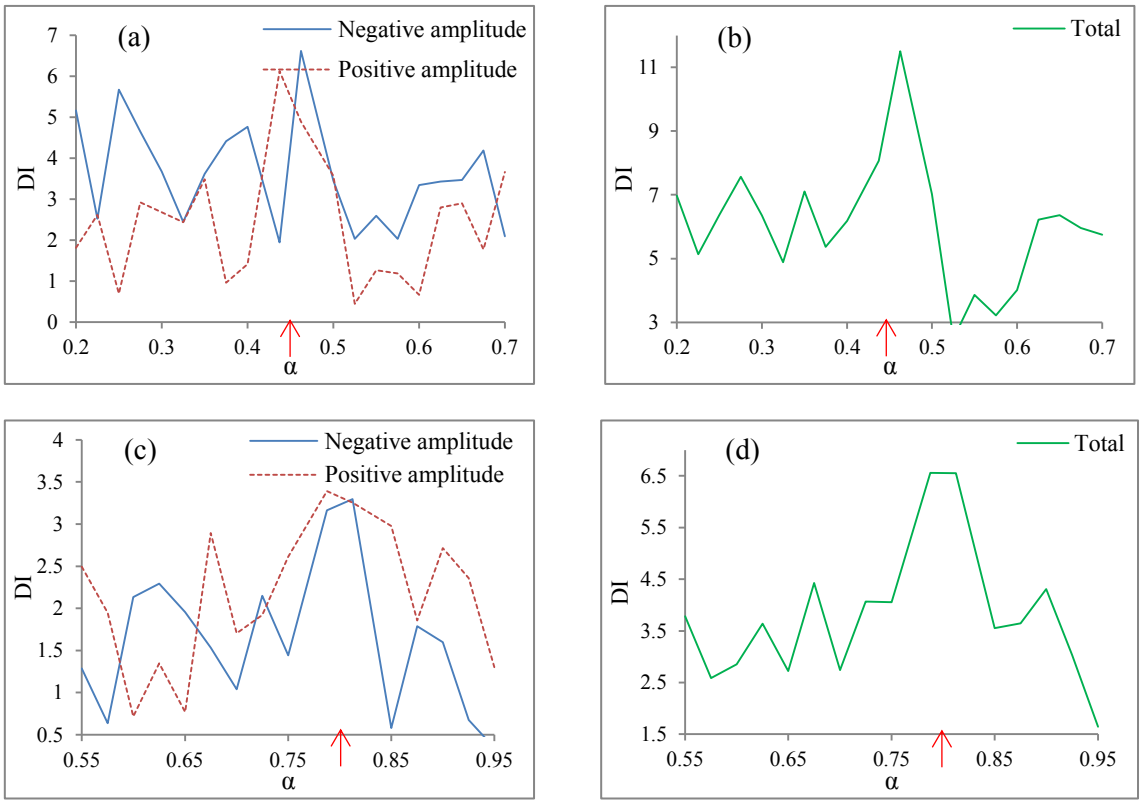

Figure 8.15: DIs with SNR = 25: (a)-(b) $(\alpha, \zeta) = (0.450, 0.125)$; (c)-(d) $(\alpha, \zeta) = (0.800, 0.125)$.

A simple method to enhance the sharpness of the peak of the DI_T showing crack location is to increase all the values of the DI_T in the plot exponentially. In Figure 8.16, the values raised to the power of 6 of the DI_T in Figures 8.15(b) and (d) are shown. It is seen that the

levels of the peaks occurred due to the noise are reduced, and only the highest peaks at the crack locations are presented clearly. This can occur due to the fact that the peaks created by noise are much lower than that induced by a crack, although the power of noise is as high as that of the SNR= 25.

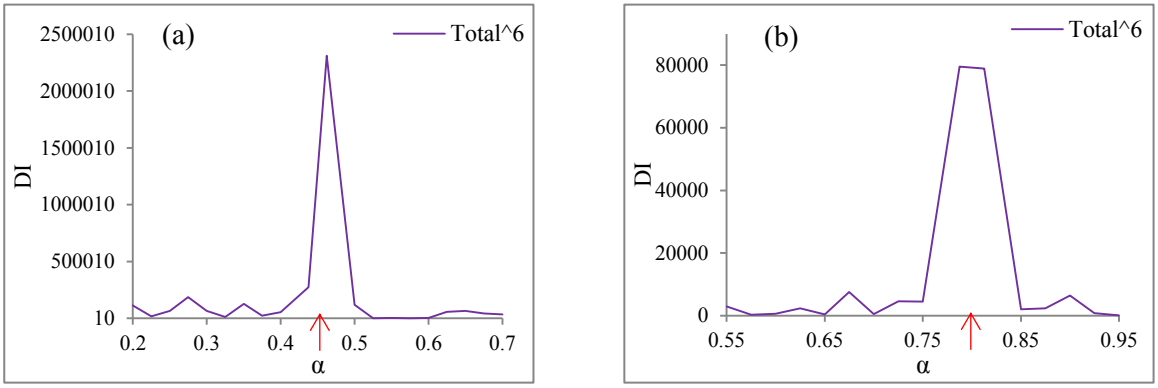

Figure 8.16: DI_T raised by the exponent of 6: (a) $(\alpha, \zeta) = (0.450, 0.125)$; (b) $(\alpha, \zeta) = (0.800, 0.125)$.

8.6 Summary

The super-harmonic resonances of the nonlinear power flow in the cantilever beams containing single and multiple breathing cracks were shown. The nonlinearity degree of the power flow can be evaluated from the time-domain plots and the Fourier spectra of the nonlinear power flow at the steady state. This degree is highly dependent on location and severity of the breathing cracks on the beams, and it is increased when the number of cracks on the beam is increased.

The crack detection technique using the power flow damage indices (DIs) based on the time-domain responses of the nonlinear power flow was also introduced. These DIs can effectively reveal the locations of single and multiple breathing cracks on the beams although the cracks have low severity and locate far away from the fixed ends of the beams. It was also shown that the DIs still work well in the environments with moderate noise. Hence, the proposed crack detection technique has high potential to be used in early-age fatigue crack detection. One more advantage of the crack detection technique is no requirement of knowledge of the corresponding intact beam for the process of crack detection.

Chapter 9

Conclusion & future work

The thesis focuses on investigating the linear and nonlinear characteristics of the power flow in damaged structures and developing the techniques for detecting damage using the power flow as a damage indicator. Following the introduction of the thesis that given in Chapter 1, the literature review of non-destructive damage detection (NDD) techniques was rigorously made and presented in Chapter 2. In Chapter 3, the concepts of the power flow, as well as its engineering applications and determination methods, were provided. Chapters 4 and 5 proposed the investigations on the power flow characteristics in the plates containing single and multiple through-thickness cracks, while the technique to detect damage location and severity in plate structures based on power flow contours was introduced in Chapter 6. In Chapter 7, the nonlinear characteristic of the power flow, namely super-harmonic resonance, created by a breathing fatigue crack was studied. The relationship between the degree of nonlinearity of the power flow and crack location and severity was employed to predict approximate location and severity of a breathing crack on the cantilever beam. The investigation of the nonlinear power flow was extended to the cases of the beams containing multiple breathing cracks in Chapter 8. In this chapter, the crack detection technique that can deal with multiple breathing cracks on beam structures was also introduced.

9.1 Conclusion

All objectives of the research stated in Chapter 1 have been fulfilled. The potential of the linear and nonlinear vibrational power flows to be employed as damage indicators for damage detection in beam and plate structures has been investigated. After the investigation, the techniques that can enhance the effectiveness of the power flows in detecting occurrence of damage, damage location, and damage severity have been proposed.

The results obtained in Chapters 4 and 5 indicate the positive points of the power flow in use for damage detection as follows:

- The significant changes of the power flow pattern and magnitude due to the presence of a through-thickness crack on a plate occur locally at the location of the crack. At the other regions of the cracked plate, the power flow pattern and magnitude are still comparable to those of the intact counterpart;
- The pattern and magnitude of the power flow at the crack location are dependent on the boundary conditions of the plate and the excitation frequency of the force that the plate is subjected to;
- The power flow is more sensitive to the crack perpendicular to its direction than the one parallel to the power transmission path, so the changes in the power flow pattern and magnitude at the location of the first-mentioned crack are more pronounced;
- The tips of the crack behave similarly to the sinks of power, so the power transmits toward them, and the magnitudes of power at the tips are high;
- The larger crack has higher magnitudes of the power flow at its tips than those of the smaller one;
- The presence of the second crack does not provide much effect to the global pattern and magnitude of the power flow, so the remarkable changes still occur only at the locations of the cracks.

Chapter 6 introduced a technique to detect damage location and severity in plate structures using the advantages from the local changes of the power flow at damage location as discussed in the former chapters and the power flow contours. The findings obtained from this chapter are as follows:

- The power flow is shown to be more sensitive to damage than the classical damage indicators such as natural frequencies and mode shapes;
- The intersection between three power flow contour lines on the correct severity plane can effectively reveal the location and severity of damage on a plate;
- The standard Bayesian average can effectively enhance the contrast of the intersection point on the severity plane, so the location of damage can be inspected more clearly;
- Once the power flow database has been collected in the forward step, only three power flow data of three excitation frequencies measured from the tested plate are required as

inputs for the technique to predict the location and severity of damage, and the power flow database can be kept for using again with the same type of plates.

The nonlinear phenomenon of the power flow in a cracked cantilever beam, namely super-harmonic resonance, has been studied in Chapter 7, and a crack detection technique based on the nonlinearity of the power flow has also been introduced. The findings gained from this chapter are as follows:

- The super-harmonic resonance of the power flow occurs when the cracked beam is excited by the excitation frequency having its integral multiples in the range of bilinear frequencies of the beam;
- The super-harmonic resonance is induced by the sudden changes in beam stiffness due to the breathing crack. These stiffness changes create the impulse that superimposes on the primary responses of the beam;
- The degree of nonlinearity of the power flow is dependent on the location and severity of the breathing crack. This degree can be evaluated from the time-domain plot and Fourier spectrum of the power flow. The nonlinearity degree is directly proportional to the crack depth but reversely proportional to the distance of the crack from the fixed end of the beam;
- The crack detection technique based on the nonlinearity degree of the power flow and the surface fitting plots can effectively estimate the approximate location and severity of the breathing crack;
- Once the curve fitting plots are obtained, they can be kept to be used again with the same type of beams;
- Comparing to the technique presented in Chapter 6, this crack detection technique can deal with more realistic damage, breathing fatigue crack, which usually arises on real structures in operations, without knowledge of the corresponding intact beam. In addition, a much smaller database is required in the forward step of the technique, and only one power flow data from the tested beam is needed for the reverse step to obtain the approximate crack location and severity.

In Chapter 8, the trend of the power flow nonlinearity degree when multiple breathing cracks present on a cantilever beam has been discussed. The power flow damage indices (DIs) for detecting single and multiple breathing cracks have also been proposed in the chapter. The results achieved from the chapter give rise to the findings as follows:

- The nonlinearity degree of the power flow is directly proportional to the amount of the breathing cracks on the beam;
- The negative, DI_n, and positive, DI_p, damage indices obtained from the time-domain response of the power flow can effectively reveal the crack locations of both single and multiple cracks on the beam. The cracks can be on both top and bottom sides of the beam. These indices are sensitive to low-severity breathing cracks, so they can be used to detect early-age fatigue cracks on real beam structures. Moreover, the difference of the DI_n and DI_p may be used to estimate the severity of the single crack;
- The total damage index (DI_T), which is the combination of the DI_n and DI_p, can sharpen the peak of the graph at the crack location, so this location can still be seen clearly although the crack detection technique is performed in the environment with noise;
- Comparing to the crack detection technique in Chapters 6 and 7, this technique does rely on a power flow database, so it is not specific to only one type of beams. The crack detection technique in Chapter 8 can pinpoint the locations of multiple cracks, whereas those in the previous two chapters are fixed with only single damage.

In summary, the non-destructive damage detection (NDD) techniques capable of revealing the results up to Level 3 have been developed based on the sensitivities to damage of the linear and nonlinear power flows, realistic damage(s) and the size of the database. Hence, the primary aim of the research mentioned in the earliest chapter has been reached.

9.2 Future work

A number of works recommended to be completed in the future are provided as follows:

- The concepts of the NDD techniques based on the power flow have been rigorously discussed in the thesis, and their effective applications have also been presented through several numerical case studies with and without the effects of noise, and the results are very encouraging. The next phase of the work should be to carry out experimental studies of the proposed NDD techniques. For the techniques relied on databases obtained from finite element models, a model updating method has to be employed to reduce the inaccuracies in the finite element models that may happen due to many reasons such as simplification in the modelling, material properties, and boundary conditions;

- The severity of the breathing cracks in the thesis is represented by the crack depth. The length of the cracks is always equal to the beam width. In reality, a breathing crack may occur at only the edge of the beam. Therefore, the further research should go into the sensitivity of the power flow to edge breathing cracks on beams. The crack length will be another parameter to show the crack severity;
- The sub-harmonic resonance of the nonlinear power flow in cracked beams is still left for further investigations. More detailed studies of the super-harmonic resonance of the nonlinear power flow induced by single and multiple breathing cracks are worthily performed;
- Investigations on the nonlinear power flow in other types of cracked structures, such as cylinders, for crack detection, are desirable to be carried out in the future.

Appendix

A. Power flow directions near plate boundaries

Due to the significant differences between the power flow values at the sources of the power and the crack tips and those at the other locations of the plates, the vector arrows at some regions, especially those near the plate boundaries that are far away from the power sources, in the power flow vector plots in Chapters 4 and 5 cannot be inspected clearly. This section will show the zoomed-in versions of those vector plots at the boundaries of both intact and corresponding damaged plates. Therefore, the power flow directions shown by the vector arrows can be compared. It is noted that only the plots of the damaged plates with the cracks parallel to the x axis will be displayed here since the directions of the power flow at the locations far away from the cracks of the plates with the cracks perpendicular to the x axis are approximately the same.

Intact plates

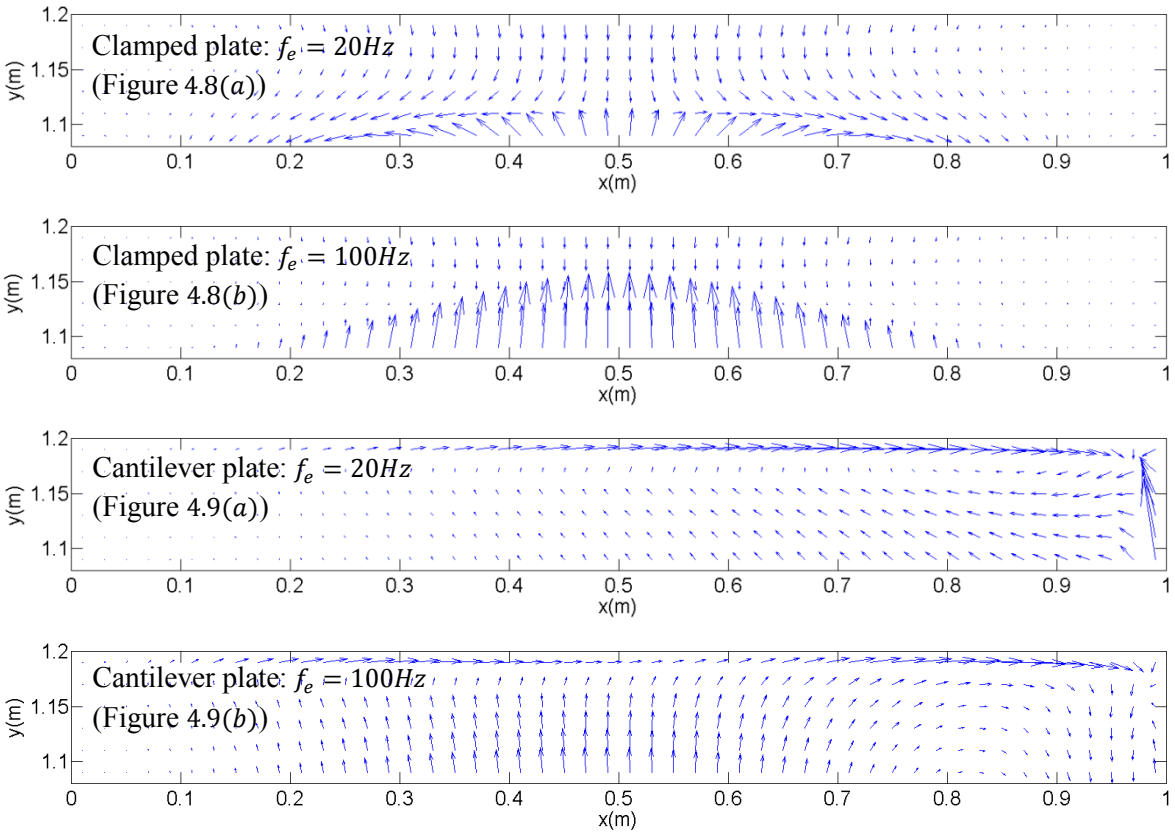

Damaged plates

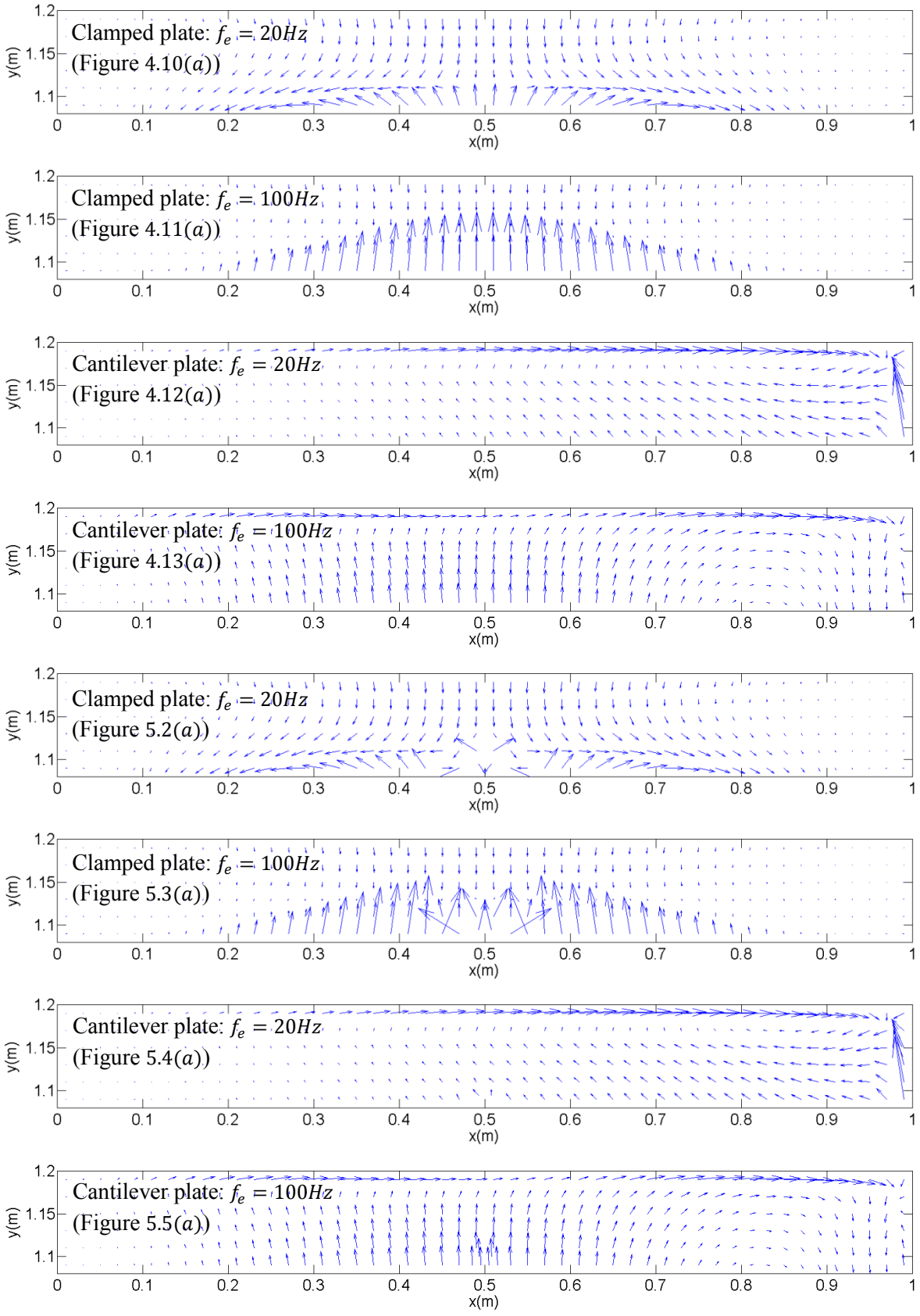

From the zoomed-in versions of the vector plots in Chapters 4 and 5 presented above, it can be seen clearly that the power flow directions at the regions near the boundaries of the intact plates are identical to those of the corresponding damaged counterparts. For the zoomed-in versions of Figures 5.2(a), 5.3(a), 5.4(a) and 5.5(a), which are of the plates containing two cracks, the directions of the power flow are changed only at the locations near the second cracks located at (x, y) = (0.5, 1.06).

B. List of publication

- P. Boonpratpai, Y.P. Xiong, Investigation of vibrational power flow patterns in damaged plate structures for damage localisation, Proceedings of the 5th International Conference on Marine Structures (MARSTRUCT 2015), Southampton, UK, 25-27 March 2015, pp. 115-122.

Bibliography

Aggelis, D. G. & Matikas, T. E., 2012. Effect of plate wave dispersion on the acoustic emission parameters in metals. *Computers & Structures,* Volume 98-99, pp. 17-22.

Aggelis, D. G. & Shiotani, T. M. S. H. A., 2009. Acoustic emission and ultrasound for damage characterisation of concrete elements. *ACI Materials Journal,* 106(6), pp. 509-514.

Ai, Q., Liu, C. X., Chen, X. R., He, P. & Wang, Y., 2010. Acoustic emission of fatigue crack in pressure pipe under cyclic pressure. *Nuclear Engineering and Design,* 240(10), pp. 3616-3620.

Alleyne, D. N. & Cawley, P., 1992. The interaction of lamb waves with defects. *IEEE Transactions on Ultrasonics,* Volume 39, pp. 381-397.

Alobaidi, W. M., Alkuam, E. A., Al-Rizzo, H. M. & Sandgren, E., 2015. Applications of ultrasonic techniques in oil and gas pipeline industries: A review. *Americal Journal of Operations Research,* Volume 5, pp. 274-287.

Anderson, T. L., 2005. *Fracture mechanics fundamentals and applications.* 3 ed. Boca Raton: Taylor & Francis Group.

Andreaus, U. & Baragatti, P., 2011. Cracked beam identification by numerically analysing the nonlinear behaviour of the harmonically forced response. *Journal of Sound and Vibration,* Volume 330, pp. 721-742.

Andreaus, U. & Baragatti, P., 2012. Experimental damage detection of cracked beams by using nonlinear characteristics of forced response. *Mechanical Systems and Signal Processing,* Volume 31, pp. 382-404.

Andreaus, U. & Casini, P., 2016. Identification of multiple open and fatigue cracks in beam-like structures using wavelets on deflection signals. *Continuum Mechanics and Thermodynamics,* 28(1), pp. 361-378.

Andreaus, U., Casini, P. & Vestroni, F., 2007. Non-linear dynamics of a cracked cantilever beam under harmonic excitation. *International Journal of Non-Linear Mechanics ,* Volume 42, pp. 566-575.

Aoki, K. & Suga, Y., 1999. Application of artificial neural network to discrimination of defect type in automatic radiographic testing of welds. *ISIJ International,* 39(10), pp. 1081-1087.

Armon, D. & Ben-Haim, Y. B. S., 1994. Crack detection in beams by rank-ordering of eigenfrequency shifts. *Mechanical Systems and Signal Processing,* 8(1), pp. 81-91.

Arruda, J. R. F. & Mas, P., 1998. Localising energy sources and sinks in plates using power flow maps computed from laser vibrometer measurements. *Shock and Vibration,* Volume 5, pp. 235-253.

Atkinson, C. P. & Heflinger, L. O., 1956. Subharmonic and superharmonic oscillations of a bilinear vibrating system. *Journal of the Franklin Institute,* 262(3), pp. 185-190.

Barber, M., 2013. *Great Yarmouth suspension bridge disaster memorial unveiled.* [Online] Available at: http://www.bbc.co.uk/news/uk-england-norfolk-24240357 [Accessed 12 October 2016].

Bathe, K. J., 1996. *Finite element procedures.* Upper Saddle River, New Jersey: Prentice Hall.

Boonpratpai, P. & Xiong, Y. P., 2015. *Investigation of vibrational power flow patterns in damaged plate structures for damage localisation, MARSTRUCT 2015: The 5th International Conference on Marine Structures.* Southampton, Taylor & Francis Group, pp. 115-123.

Bouboulas A., S. & Anifantis, N. K., 2010. Finite element modelling of a vibrating beam with a breathing crack: observations on crack detection. *Structural Health Monitoring,* 10(2), pp. 131-145.

Bouboulas, A. S. & Anifantis, N. K., 2013. Three-dimensional finite element modelling of a vibrating beam with a breathing crack. *Archive of Applied Mechanics,* 83(2), pp. 207-223.

Carneiro, G. N. & Ribeiro, P., 2015. Vibrations of beam with a breathing crack and large amplitude displacements. *Journal of Mechanical Engineering Science,* 0(0), pp. 1-21.

Cawley, P., 2001. Non-destructive testing - current capabilities and future directions. *Proceedings of the Institution of Mechanical Engineers, Part L,* Volume 215, pp. 213-223.

Cawley, P. & Adams, R., 1979. The location of defects in structures from measurements of natural frequencies. *Journal of Strain Analysis,* 14(2), pp. 49-57.

Chati, M., Rand, R. & Mukherjee, S., 1997. Modal analysis of a cracked beam. *Journal of Sound and Vibration,* 207(2), pp. 249-270.

Chen, J. S. & Wang, R. T., 2014. Wave propagation and power flow analysis of sandwich structures with internal absorbers. *Journal of Vibration and Acoustics,* Volume 136, pp. 041003-1-041003-8.

Chen, X. & Li, B., 2007. Acoustic emission method for tool condition monitoring based on wavelet analysis. *International Journal of Advanced Manufacturing Technology,* 33(9-10), pp. 968-976.

Chillara, V. K. & Lissenden, C. J., 2016. Review of nonlinear ultrasonic guided wave nondestructive evaluation: theory, numerics, and experiment. *Optical Engineering,* 55(1).

Chinchalkar, S., 2001. Determination of crack location in beams using natural frequencies. *Journal of Sound and Vibration,* 247(3), pp. 417-429.

Choi, W. J., Xiong, Y. P. & Shenoi, R. A., 2009. Power flow analysis for a floating sandwich raft isolation system using a higher-order theory. *Journal of Sound and Vibration,* Volume 319, pp. 228-246.

Cieślik, J., 2004. Vibration energy flow in rectangular plates. *Journal of Theoretical and Applied Mechanics,* 42(1), pp. 195-212.

Coleman, T. F. & Li, Y., 1996a. An interior trust region approach for nonliner minimisation subject to bounds. *SIAMJ. Optimisation,* 6(2), pp. 418-445.

Coleman, T. F. & Li, Y., 1996b. On the convergence of interior-reflective Newton methods for nonlinear minimisation subject to bounds. *Mathematical Programming,* Volume 67, pp. 189-224.

Cornwell, P., Doebling, S. W. & Farrar, C. R., 1999. Application of the strain energy damage detection method to plate-like structures. *Journal of Sound and Vibration,* 224(2), pp. 359-374.

Cornwell, P., Doebling, S. W. & Farrar, C. R., 1999. Application of the strain energy damage detection method to plate-like structures. *Journal of Sound and Vibration,* 224(2), pp. 359-374.

Cremer, L., Heckl, M. & Petersson, B. A. T., 2005. *Structure-borne sound: structural vibrations and sound radiation at audio frequencies.* New York: Springer.

Cuschieri, J. M., 1990. Vibration transmission through periodic structures using a mobility power flow approach. *Journal of Sound and Vibration,* 143(1), pp. 65-74.

Daley, M. J. & Hambric, S. A., 2005. Simulating and measuring structural intensity fields in plates induced by spatially and temporally random excitation. *Journal of Vibrationn and Acoustics,* 127, pp. 451-457.

Dassios, K. G., Kordatos, E. Z. & Aggelis, D. G., 2013. Crack Growth Monitoring in Ceramic Matrix Composites by Combined Infrared Thermography and Acoustic Emission. *Journal of the American Ceramic Society,* 97(1), pp. 251-257.

de Wrachien, D. & Mambretti, S., 2009. *Dam-break problems, solutions and case studies.* 1 ed. Southampton: WIT Press.

Deng, Q., Li, C. G. & Tang, H., 2015. A smooth system of equations approach to complementarity problems for frictionless contacts. *Mathematical Problems in Engineering,* Volume 2015, pp. 1-9.

Deutsch, S., 1979. A preliminary study of the fluid mechanics of liquid penetrant testing. *Journal of Research of the National Bureau of Standards,* 84(4), pp. 287-292.

Dimaroganas, A. D., 1996. Vibration of cracked structures: A state of the art review. *Engineering Fracture Mechanics,* 55(5), pp. 831-857.

Douka, E., Loutridis, S. & Trochidis, A., 2004. Crack identification in plates using wavelet analysis. *Journal of Sound and Vibration,* Volume 270, pp. 279-295.

Dowling, S., 2015. *What caused the Space Shuttle Columbia disaster?.* [Online]
Available at: http://www.bbc.com/future/story/20150130-what-caused-the-columbia-disaster
[Accessed 12 October 2016].

Eraky, A., Anwar, A. M. S. A. & Abdo, A., 2015. Damage detection of flexural structural systems using damage index method-Experimental approach. *Alexandria Engineering Journal,* Volume 54, pp. 497-507.

Friswell, M. I. & Penny, J. E. T., 2002. Crack modelling for structural health monitoring. *Structural Health Monitoring,* 1(2), pp. 139-148.

Furukawa, A., Otsuka, H. & Kiyono, J., 2006. Structural damage detection method using uncertain frequency response functions. *Computer-Aided Civil and Infrastructure Engineering,* Volume 21, pp. 292-305.

Gavin, H. P., 2012. *Review of strain energy methods and introduction to stiffness matrix methods of structural analysis,* North Carolina: Civil and Environmental Engineering, Duke University.

Gavrić, L. & Pavić, G., 1993. A finite element method for computation of structural intensity by the normal mode approach. *Journal of Sound and Vibration,* 164(1), pp. 29-43.

Gholizadeh, S., Leman, Z. & Baharudin, B. T. H. T., 2015. A review of the application of acoustic emission technique in engineering. *Structural Engineering and Mechanics,* 54(6), pp. 1075-1095.

Giannini, O., Casini, P. & Vestroni, F., 2013. Nonlinear harmonic identification of breathing cracks in beams. *Computers and Structures,* Volume 129, pp. 166-177.

Gittings, J., 2002. *Crash plane broke up in mid-air.* [Online]
Available at:
https://www.theguardian.com/business/2002/may/27/theairlineindustry.internationalnews
[Accessed 12 October 2016].

Goyder, H. G. D. & White, R. G., 1980a. Vibrational power flow from machines into built-up structures, part I: Introduction and approximate analyses of beam and plate-like foundations. *Journal of Sound and Vibration,* 68(1), pp. 59-75.

Goyder, H. G. D. & White, R. G., 1980b. Vibrational power flow from machines into built-up structures, part II: Wave propagation and power flow in beam-stiffened plates. *Journal of Sound and Vibration,* 68(1), pp. 77-96.

Goyder, H. G. D. & White, R. G., 1980c. Vibrational power flow from machines into built-up structures, part III: Power flow through isolation systems. *Journal of Sound and Vibration,* 68(1), pp. 97-117.

Gudmundson, P., 1982. Eigenfrequency changes of structures due to cracks, notches or other geometrical changes. *Journal of the Mechanics and Physics of Solids,* 30(5), pp. 339-353.

Hambric, S. A., 1990. Power flow and mechanical intensity calculations in structural finite element. *Journal of Vibration and Acoustics,* Issue 542-549, p. 112.

Hensman, J. et al., 2011. Spatial scanning for anomaly detection in acoustic emission testing of an aerospace structure. *Mechanical Systems and Signal Processing,* 25(7), pp. 2462-2474.

Hu, H. & Wu, C., 2009. Development of scanning damage index for the damage detection of plate structures using modal strain energy method. *Mechanical Systems and Signal Processing,* Volume 23, pp. 274-287.

Hu, H., Wu, C. & Lu, W. J., 2011. Damage detection of circular hollow cylinder using modal strain energy and scanning damage index methods. *Computers and Structures,* Volume 89, pp. 149-160.

Huh, Y. C., Chung, T. Y., Lee, J. W. & Kim, J. K., 2015. Damage identification in plates using vibratory power estimated from measured accelerations. *Journal of Sound and Vibration,* Volume 336, pp. 106-131.

Huh, Y. C. et al., 2011. Damage detection in beams using vibratory power estimated from the measured accelerations. *Journal of Sound and Vibration,* Volume 330, pp. 3645-3665.

Israr, A. et al., 2009. Analytical modelling and vibration analysis of partially cracked rectangular plates with different boundary conditions and loading. *Journal of Applied Mechanics,* Volume 76, pp. 1-9.

Jemielniak, K. & Arrazola, P. J., 2008. Application of AE and cutting force signals in tool condition monitoring in micro-milling. *CIRP Journal of Manufacturing Science and Technology,* 1(2), pp. 97-102.

Jhang, K. Y., 2009. Nonlinear ultrasonic techniques for non-destructive assessment of micro damage in material: A review. *International Journal of Precision Engineering and Manufacturing,* 10(1), pp. 123-135.

Jones, S., 2014. *Friday marks 7 years since I-35W bridge collapse.* [Online] Available at: http://minnesota.cbslocal.com/2014/08/01/friday-marks-7-years-since-i-35w-bridge-collapse/ [Accessed 11 October 2016].

Kayat, R. A., 2012. *The hotel New World collapse (March 15, 1986).* [Online] Available at: https://failures.wikispaces.com/Hotel+New+World+Collapse [Accessed 12 October 2016].

Keshtgar, A. & Modarres, M., 2013. Acoustic emission-based fatigue crack growth prediction. *Reliability and Maintainability Symposium (RAMS), 2013 Proceedings-Annual.*

Khadem, S. E. & Rezaee, M., 2000. Introduction of modified comparison functions for vibration analysis of a rectangular cracked plate. *Journal of Sound and Vibration,* 236(2), pp. 245-258.

Khoo, L. M., Mantena, P. R. & Jadhav, P., 2004. Structural damage assessment using vibration modal analysis. *Structural Health Monitoring,* 3(2), pp. 177-194.

Kim, J. T., Ryu, Y. S., Cho, H. M. & Stubbs, N., 2003. Damage identification in beam-type structures: frequency-based method vs mode-shape-based method. *Engineering Structures,* Volume 25, pp. 57-67.

Kral, Z., Horn, W. & Steck, J., 2013. Crack Propagation Analysis Using Acoustic Emission Sensors for Structural Health Monitoring Systems. *The Scientific World Journal,* Volume 2013.

Kwon, H. W., Hong, S. Y., Lee, H. W. & Song, J. H., 2011. Power flow boundary element analysis for multi-domain problems in vibrational built-up structures. *Journal of Sound and Vibration,* 330(26), pp. 6482-6494.

Langley, R. S., 1989. Application of the dynamic stiffness method to the free and forced vibrations of aircraft panels. *Journal of Sound and Vibration,* 135(2), pp. 319-331.

Langley, R. S., 1992. A wave intensity technique for the analysis of high frequency vibrations. *Journal of Sound and Vibration,* 159(3), pp. 483-502.

Lee, H. P., Lim, S. P. & Khun, M. S., 2006. Diversion of energy flow near crack tips of a vibrating plate using the structural intensity technique. *Journal of Sound and Vibration,* Volume 296, pp. 602-622.

Lee, U. & Shin, J., 2002. A frequency response function-based structural damage identification method. *Computers and Structures,* Volume 80, pp. 117-132.

Lee, Y. S. & Chung, M. J., 2000. A study on crack detection using eigenfrequency test data. *Computers and Structures,* Volume 77, pp. 327-342.

Lele, S. P. & Maiti, S. K., 2002. Modelling of transverse vibration of short beams for crack detection and measurement of crack extension. *Journal of Sound and Vibration,* 257(3), pp. 559-583.

Li, B., Chen, X. F., Ma, J. X. & He, Z. J., 2005. Detection of crack location and size in structures using wavelet finite element methods. *Journal of Sound and Vibration,* Volume 285, pp. 767-782.

Li, K., Li, S. & Zhao, D. Y., 2010. Investigation on vibration energy flow characteristics in coupled plates by visualisation techniques. *Journal of Marine Science and Technology,* 18(6), pp. 907-914.

Li, T. Y., Liu, J. X. & Zhang, T., 2004. Vibrational power flow characteristics of circular plate structures with peripheral surface crack. *Journal of Sound and Vibration,* Volume 276, pp. 1081-1091.

Li, T. Y., Zhang, W. H. & Liu, T. G., 2001. Vibrational power flow analysis of damaged beam structures. *Journal of Sound and Vibration,* 242(1), pp. 59-68.

Li, T. Y., Zhu, X., Zhao, Y. & Hu, X. F., 2009. The wave propagation and vibrational energy flow characteristics of a plate with a part-through surface crack. *International Journal of Engineering Science,* Volume 47, pp. 1025-1037.

Li, Y. J. & Lai, J. C. S., 2000. Prediction of surface mobility of a finite plate with uniform force excitation by structural intensity. *Applied Acoustics,* Volume 60, pp. 371-383.

Li, Y. & Xiong, Y. P., 2015. *Power flow analysis and dynamic performance of a nonlinear vibration energy harvesting system coupled to a SD oscillator.* Hawaii, USA, International Society of Offshore and Polar Engineers, pp. 1049-1053.

Liao, T. W. & Ni, J., 1996. An automated radiographic NDT system for weld inspection: Part I - Weld extraction. *NDT & E International,* 29(3), pp. 157-162.

Liao, T. W. & Li, Y., 1998. An automated radiographic NDT system for weld inspection: Part II - Flaw detection. *NDT & E International,* 31(3), pp. 183-192.

Lin, T. K., Hung, S. L. & Huang, C. S., 2012. Detection of damage location using a novel substructure-based frequency response function approach with a wireless sensing system. *International Journal of Structural Stability and Dynamics,* 12(4), pp. 1-24.

Linjama, J. & Lahti, T., 1992. Estimation of bending wave intensity in beams using the frequency response technique. *Journal of Sound and Vibration,* 153(1), pp. 21-36.

Lucassen, J. & Tempel, M. V. D., 1972. Longitudinal waves on visco-elastic surfaces. *Journal of Colloid and Interface Science,* 41(3), pp. 491-498.

Luk, B. L. & Chan, A. H. S., 2007. Human factors and ergonomics in dye penetrant and magnetic particles nondestructive inspection methods. *Engineering Letters,* 15(1).

Lu, Q., Ren, G. & Zhao, Y., 2002. Multiple damage location with flexibility curvature and relative frequency change for beam structures. *Journal of Sound and Vibration,* 253(5), pp. 1101-1114.

Lyall, S., 2010. *In BP's record, a history of boldness and costly blunders.* [Online] Available at: http://www.nytimes.com/2010/07/13/business/energy-environment/13bprisk.html?_r=0 [Accessed 11 October 2016].

Lysmer, J. & Waas, G., 1972. Shear waves in plane infinite structures. *Journal of the Engineering mechanics Division,* Volume 98, pp. 85-105.

Mace, B. R. & Shorter, P. J., 2000. Energy flow models from finite element analysis. *Journal of Sound and Vibration,* 233(3), pp. 369-389.

Mandal, N. K., 2006. A complete description of intensity fields of thin isotropic plates for flexural waves in general field conditions. *Trends in Applied Sciences Research,* 1(6), pp. 553-563.

Mandal, N. K. & Biswas, S., 2005. Vibration power flow: A critical review. *The Shock and Vibration Digest,* 37(1), pp. 3-11.

Manjula, K., Vijayarekha, K. & Venkatraman, B., 2014. Weld flaw detection using various ultrasonic techniques: A review. *Journal of Applied Sciences,* 14(14), pp. 1529-1535.

Martín, J. G., Gil, J. G. & Sánchez, E. V., 2011. Non-Destructive Techniques Based on Eddy current Testing. *Sensors,* Volume 11, pp. 2525-2565.

Masserey, B., 2006. *Ultrasonic surface crack characterisation using Rayleigh waves,* Zurich: Swiss Federal Institute of Technology.

Mitcheson, P. D. et al., 2008. Energy harvesting from human and machine motion for wireless electronic devices. *Proceedings of the IEEE,* 96(9), pp. 1457-1486.

Muthumari, S. & Singh, A., 2011. Review of various ultrasonic techniques employed in modern industries. *International Journal of Engineering Science and Technology (IJEST),* 3(4), pp. 3078-3085.

Nair, A. & Cai, C. S., 2010. Acoustic emission monitoring of bridges: Review and case studies. *Engineering Structures,* Volume 32, pp. 1704-1714.

Noiseux, D. U., 1970. Measurement of power flow in uniform beams and plates. *Journal of the Acoustical Society of America,* 47(1), pp. 238-247.

Ohno, K. & Ohtsu, M., 2010. Crack classification in concrete based on acoustic emission. *Construction and Building Materials,* 24(12), pp. 2339-2346.

Öz, M. R., 2000. Calculation of the natural frequencies of a beam-mass system using finite element method. *Mathematical & Computational Applications,* 5(2), pp. 67-75.

Pandey, A. K. & Biswas, M., 1994. Damage detection in structures using changes in flexibility. *Journal of Sound and Vibration,* Volume 169, pp. 3-17.

Pandey, A. K., Biswas, M. & Samman, M. M., 1991. Damage detection from changes in curvature mode shapes. *Journal of Sound and Vibration,* 145(2), pp. 321-332.

Park, N. G. & Park, Y. S., 2003. Damage detection using spatially incomplete frequency response functions. *Mechanical Systems and Signal Processing,* 17(3), pp. 519-532.

Park, N. G. & Park, Y. S., 2005. Identification of damage on a substructure with measured frequency response functions. *Journal of Mechanical Science and Technology,* 19(10), pp. 1891-1901.

Pavić, G., 1976. Measurement of Structure borne wave intensity, part I: formulation of the methods. *Journal of Sound and Vibration,* 49(2), pp. 221-230.

Pavić, G., 1987. Structural surface intensity: An alternative approach in vibration analysis and diagnosis. *Journal of Sound and Vibration,* 115(3), pp. 405-422.

Pearson, C. & Delatte, N., 2006. Collapse of the Quebec Bridge, 1907. *Journal of Performance of Constructructed Facilities,* 20(1), pp. 84-91.

Peng, Z. K., Lang, Z. Q. & Billings, S. A., 2007. Crack detection using nonlinear output frequency response functions. *Journal of Sound and Vibration,* Volume 301, pp. 777-788.

Pinnington, R. J. & White, R. G., 1981. Power flow through machine isolators to resonant and non-resonant beams. *Journal of Sound and Vibration,* 75(2), pp. 179-197.

Ratcliffe, C. P., 1997. Damage detection using a modified Laplacian operator on mode shape data. *Journal of Sound and Vibration,* 204(3), pp. 505-517.

Reddy, D. M. & Swarnamani, S., 2012. Damage detection and identification in structures by spatial wavelet based approach. *International Journal of Applied Science and Engineering,* 10(1), pp. 69-87.

Rice, J. R. & Levy, N., 1972. The part-through surface crack in an elastic plate. *Journal of Applied mechanics,* pp. 185-194.

Rizos, P. F., Aspragathos, N. & Dimarogonas, A. D., 1990. Identification of crack location and magnitude in a cantilever beam from the vibration modes. *Journal of Sound and Vibration,* 138(3), pp. 381-388.

Romano, P. Q., Conlon, S. C. & Smith, E. C., 2013. Investigation of contact acoustic nonlinearities on metal and composite airframe structures via intensity based health monitoring. *J. Acoust. Soc. Am.,* 133(1), pp. 186-200.

Rucevskis, S., Janeliukstis, R., Akishin, P. & Chate, A., 2016. Mode shape-based damage detection in plate structure without baseline data. *Structural Control and Health Monitoring,* Volume 23, pp. 1180-1193.

Rucevskis, S. & Wesolowski, M., 2010. Identification of damage in a beam structure by using mode shape curvature squares. *Shock and Vibration,* Volume 17, pp. 601-610.

Rucka, M., 2011. Damage detection in beams using wavelet transform on higher vibration modes. *Journal of Theoretical and Applied Mechanics,* 49(2), pp. 399-417.

Ruotolo, R., Surace, C., Crespo, P. & Storer, D., 1996. Harmonic analysis of the vibrations of a cantilevered beam with a closing crack. *Computers & Structures,* 61(6), pp. 1057-1074.

Rytter, A., 1993. *Vibration based inspection of civil engineering structures,* Aalborg: Department of Building Technology and Structural Engineering, Aalborg University, PhD Thesis.

Saavedra, P. N. & Cuitiño, L. A., 2001. Crack detection and vibration behaviour of cracked beams. *Computers and Structures,* Volume 79, pp. 1451-1459.

Sagara, N. & Fukushima, M., 1991. A hybrid method for the nonlinear least squares problem with simple bounds. *Journal of Computational and Applied Mathematics,* Volume 36, pp. 149-157.

Salawu, O. S., 1997. Detection of structural damage through changes in frequency: a review. *Engineering Structures,* 19(9), pp. 718-723.

Sampaio, R. P. C., Maia, N. M. M. & Silva, J. M. M., 1999. Damage detection using the frequency-responses-function curvature method. *Journal of Sound and Vibration,* 226(5), pp. 1029-1042.

Santhosh, N., Baskaran, V. & Amarkarthik, A., 2015. A review on front end conversion in ocean wave energy converters. *Frontiers in Energy,* 9(3), pp. 297-310.

Semperlotti, F. & Conlon, S. C., 2010. Structural damage identification in plates via nonlinear structural intensity maps. *J. Acoust. Soc. Am.,* 127(2), pp. 48-53.

Semperlotti, F., Wang, K. W. & Smith, E. C., 2009b. Localisation of a breathing crack using nonlinear subharmonic response signals. *Applied Physics Letters,* Volume 95.

Shafeek, H. I., Gadelmawla, E. S., Shafy, A. A. A. & Elewa, I. M., 2004. Assessment of welding defects for gas pipeline radiographs using computer vision. *NDT & E International,* Volume 37, pp. 291-299.

Shepherd, M. R., Conlon, S. C., Semperlotti, F. & Hambric, S. A., 2012. Structural intensity modelling and simulations for damage detection. *Journal of Vibration and Acoustics,* 134(5).

Shepherd, M. R., Conlon, S. C., Semperlotti, F. & Hambric, S. A., 2012. Structural intensity modelling and simulations for damage detection. *Journal of Vibration and Acoustics,* 134(5).

Shi, Z. Y., Law, S. S. & Zhang, L. M., 1998. Structural damage localisation from modal strain energy change. *Journal of Sound and Vibration,* 218(5), pp. 825-844.

Shi, Z. Y., Law, S. S. & Zhang, L. M., 2002. Improved damage quantification from elemental modal strain energy change. *Journal of Engineering Mechanics,* Volume 128, pp. 521-529.

Tamura, Y., 2009. *Wind-induced damage to buildings and disaster risk reduction, paper presented to The 7th Asia-Pacific Conference on Wind Engineering.* Taipei, 8-12 November.

Tanaka, M. & Bercin, A. N., 1998. Determination of crack location from changes in natural frequencies. In: M. Tanaka & G. S. Dulikravich, eds. *Inverse Problems in Engineering Mechanics.* s.l.:s.n., pp. 73-80.

Truitt, A. & Mahmoodi, S. N., 2013. A review on active wind energy harvesting designs. *International Journal of Precision Engineering and Manufacturing,* 14(9), pp. 1667-1675.

Vafai, A. & Estekanchi, H. E., 1999. A parametric finite element study of cracked plates and shells. *Thin-Walled Structures,* Volume 33, pp. 211-229.

Wang, G. & Liao, T. W., 2002. Automatic identification of different types of welding defects in radiographic images. *NDT & E International,* Volume 35, pp. 519-528.

Wang, Q. & Deng, X., 1999. Damage detection with spatial wavelets. *International Journal of Solid and Structures,* Volume 36, pp. 3443-3468.

Wang, Z. H., Xing, J. T. & Price, W. G., 2004. A study of power flow in a coupled plate-cylindrical shell system. *Journal of Sound and Vibration,* Volume 271, pp. 863-882.

Williams, E. G., Dardy, H. D. & Fink, R. G., 1985. A technique for measurement of structure-borne intensity in plates. *The Journal of the Acoustical Society of America,* 78(6), pp. 2061-2068.

Wong, W. O., Wang, X. Q. & Cheng, L., 2009. Modal power flow analysis of a damaged plate. *Journal of Sound and Vibration,* 320(1-2), pp. 3645-3665.

Xing, J. T. & Price, W. G., 1999. A power-flow analysis based on continuum dynamics. *Proc. R. Soc. Lond. A,* Volume 455, pp. 401-437.

Xiong, Y. P., Wang, X. P. & Xing, J. T. P. W. G., 2000. Hybrid active and passive control of vibratory power flow in flexible isolation system. *Shock and Vibration,* 7(3), pp. 139-148.

Xiong, Y. P., Xing, J. T. & Price, W. G., 2001. Power flow analysis of complex coupled systems by progressive approaches. *Journal of Sound and Vibration,* 239(2), pp. 275-295.

Xiong, Y. P., Xing, J. T. & Price, W. G., 2005a. Interactive power flow characteristics of an integrated equipment-nonlinear isolator-travelling flexible ship excited by sea waves. *Journal of Sound and Vibration,* 287(1), pp. 245-276.

Xiong, Y. P., Xing, J. T. & Price, W. G., 2005b. A power flow mode theory based on a system's damping distribution and power flow design approaches. *Proceedings of the Royal Society A: Mathematical, Physical and Engineering Science,* 461(2063), pp. 3381-3411.

Xu, R., 2011. *Why fracture and failure mechanics is so important? From Southwest Boeing 737 cracks to future Boeing 787 safety.* [Online]
Available at:http://imechanica.org/node/10052
[Accessed 11 October 2016].

Xu, X. D., Lee, H. P., Wang, Y. Y. & Lu, C., 2004. The energy flow analysis in stiffened plates of marine structures. *Thin-Walled Structures,* Volume 42, pp. 979-994.

Yan., Y. J., Cheng, L., Wu, Z. Y. & Yam, L. H., 2007. Development in vibration-based structural damage detection technique. *Mechanical Systems and Signal Processing,* Volume 21, pp. 2198-2211.

Yan, A. & Golinval, J. C., 2005. Structural damage localisation by combining flexibility and stiffness methods. *Engineering Structures,* Volume 27, pp. 1752-1761.

Yan, G., De Stefano, A., Matta, E. & Feng, R., 2013. A novel approach to detecting breathing-fatigue cracks based on dynamic characteristics. *Journal of Sound and Vibration,* Volume 332, pp. 407-422.

Yang, J., 2013. *Power flow analysis of nonlinear dynamical systems,* Southampton: Faculty of Engineering and the Environment, University of Southampton, PhD Thesis.

Yang, J., Xiong, Y. P., Xing, J. & T., 2013. Dynamics and power flow behaviour of a nonlinear vibration isolation system with a negative stiffness mechanism. *Journal of Sound and Vibration,* Volume 332, pp. 167-183.

Yang, J., Xiong, Y. P. & Xing, J. T., 2011. *Investigations on a nonlinear energy harvesting system consisting of a flapping foil and an electro-magnetic generator using power flow analysis.* Washington, DC, USA, Proceedings of the ASME 2011 International Design Engineering Technical Conferences & Computers and Information in Engineering Conference EDETC/CIE 2011, pp. 1-8.

Yang, J., Xiong, Y. P. & Xing, J. T., 2015. Power flow behaviour and dynamic performance of a nonlinear vibration absorber coupled to a nonlinear oscillator. *Nonlinear Dyn,* Volume 80, pp. 1063-1079.

Yang, Z. et al., 2013. A damage identification approach for plate structures based on frequency measurements. *Nondestructive Testing and Evaluation,* 28(4), pp. 321-341.

Zhao, J. & DeWolf, J. T., 1999. Sensitivity study for vibrational parameters used in damage detection. *Journal of Structural Engineering,* Volume 125, pp. 410-416.

Zhong, H. & Yang, M., 2016. Damage detection for plate-like structures using generalised curvature mode shape method. *J Civil Struct Health Monit,* Volume 6, pp. 141-152.

Zhu, X., Li, T. Y., Zhao, Y. & Liu, J. X., 2006. Structural power flow analysis of Timoshenko beam with an open crack. *Journal of Sound and Vibration,* Volume 297, pp. 215-226.

Zhu, X., Li, T. Y., Zhao, Y. & Yan, J., 2007. Vibrational power flow analysis of thin cylindrical shell with a circumferential surface crack. *Journal of Sound and Vibration,* Volume 302, pp. 332-349.

Zhu, X. Q. & Law, S. S., 2006. Wavelet-based crack identification of bridge beam from operational deflection time history. *International Journal of Solids and Structures*, Volume 43, pp. 2299-2317.